SOIL ENHANCEMENT BY FLUID INJECTION FOR
IN SITU TREATMENT OF CONTAMINATED SOIL

DAVID J. WALTER

SOIL ENHANCEMENT BY FLUID INJECTION

FOR

IN SITU TREATMENT OF CONTAMINATED SOIL

by

David J. Walter

A thesis submitted to the School of Graduate Studies

in partial fulfilment of the requirements for the degree of

Doctor of Philosophy

Faculty of Engineering and Applied Science

Memorial University of Newfoundland

October, 1999

St. John's   Newfoundland

ABSTRACT

Across North America, there are numerous sites where industrial, commercial or waste management activities have resulted in the release of a wide variety of contaminants into the ground. Many technologies used for *in situ* remediation of contaminants in soil and groundwater promote the movement of fluids through the subsurface to either treat the contaminant in place or to facilitate removal of the contaminant for surface treatment. The *in situ* treatment of contaminants located in low permeability soil is a particularly challenging problem. Existing *in situ* techniques for treating contaminants are generally ineffective in these soils and seldom used. The objective of this research has been to investigate a simple and low cost fluid injection technique that relies on a soil shearing mechanism to create an enhanced flow regime within the soil. An enhanced flow regime allows greater accessibility to contaminants and enables conventional *in situ* treatment technologies to be used more effectively over a broader range of soil conditions.

The research included an experimental program consisting of fluid injection tests carried out from vertical and horizontal wellbores, and numerical simulations of injection test results. Reduced scale injection tests were carried out in a geotechnical centrifuge and large scale field experiments were carried out at the former U.S. Naval Facility in Argentia, NF. The numerical modelling work also included the analysis of data from an injection test program carried out by others in a large calibration chamber.

The injection tests resulted in the formation of high permeability discontinuities within the soil surrounding the wellbore. Yielding due to shear was found to dominate under certain conditions, however, other mechanisms also occurred including porous flow without yielding, cavity expansion, and yielding in tension. The role that each of these mechanisms plays, is influenced by a complex interrelationship between physical and geotechnical parameters including pore and injection fluid properties, injection zone details, the soil stress state, permeability, constitutive behaviour, and structure.

ii

ACKNOWLEDGEMENTS

TABLE OF CONTENTS

CHAPTER 5 - NUMERICAL MODELLING OF FLUID INJECTION

LIST OF TABLES

LIST OF FIGURES

LIST OF ABBREVIATIONS AND SYMBOLS

Δ	change in, or incremental	c_u	undrained shear strength
γ'	buoyant unit weight	C_u	coefficient of uniformity
γ	bulk unit weight	c_v	coefficient of consolidation
ϕ'	effective friction angle	D	diameter
ϕ'_p	peak effective friction angle	e	void ratio
ϕ'_{cv}	constant volume eff. friction angle	e_1	principal strains (also e_2 and e_3)
κ	elastic slope in V-p' space	e_1^e	elastic component of principal strains
λ	plastic slope in V-p' space	e_1^p	plastic component of principal strains
μ	viscosity	e^{ps}	plastic shear strain hardening parameter
ν'	effective Poisson's ratio		
π	pi	e^{pt}	plastic tensile strain hardening parameter
ρ	density		
ρ'	buoyant density	E	energy
ρ_d	dry density	F	force
ρ_{sat}	saturated density	f^s	shear yield function
ρ_w	density of water	f^t	tensile yield function
σ	normal stress	g	acceleration due to gravity
σ'_1	maximum (or major) principal effective stress	G	shear modulus
σ'_2	intermediate principal effective stress	g^s	shear potential function
		g^t	tensile potential function
σ'_3	minimum (or minor) principal effective stress	G_s	specific gravity
		H	height of water column
σ'_θ	tangential effective stress	h_w	height of water column at well
σ'_h	horizontal effective stress	I_p	plasticity index
σ'_r	radial effective stress	k	hydraulic conductivity (permeability)
σ_t	tensile strength		
σ'_t	tensile effective stress		
σ_{nw}	tension limit of water	k_o	initial hydraulic conductivity
σ'_v	vertical effective stress	K	ratio of horizontal to vertical effective stress (see also K_o)
σ'_x	effective stress in the x direction		
σ'_y	effective stress in the y direction	K_a	absolute permeability
σ'_z	effective stress in the z direction	K_o	coefficient of lateral earth pressure at rest
τ	shear stress		
ψ	dilation angle	k_h	horizontal hydraulic conductivity
a	acceleration	K_I	stress intensity factors (also K_{II} and K_{III})
A	area		
B	bulk modulus	K_{Ic}	critical stress intensity factor
B_w	bulk modulus of water	K_{nc}	normally consolidated value of K_o
c'	effective cohesion	k_v	vertical hydraulic conductivity
C_c	coefficient of curvature	l	length

xxviii

m	an experimentally derived index property for soil
M	mass, or slope of critical state line in q-p' space
n	porosity, or scale factor
N	scaling factor
N_ϕ	$(1 + \sin \phi) / (1 - \sin \phi)$
N_ψ	$(1 + \sin \psi) / (1 - \sin \psi)$
OCR	over-consolidation ratio
p'	$(\sigma'_1 + \sigma'_2 + \sigma'_3)/3$
P_i	initiation pressure for a hydraulic fracture
P_e	excess pore pressure required to initiate yield
P_p	peak injection pressure measured at point of injection
P_r	closure pressure for a hydraulic fracture
q	$(\sigma_1 - \sigma_3)/2$
Q	flow rate
R	radius
Re	Reynold's number
r_w	radius at well
t	time
u	pore pressure, or velocity
V	velocity, or specific volume
w_l	liquid limit
w_p	plastic limit

CHAPTER 1 - INTRODUCTION

1.1   Background

Across North America, there are numerous sites where industrial, commercial or waste management activities have resulted in the release of a wide variety of contaminants into the ground. These contaminants may exist in many phases, some of which may be immiscible fluids that are denser than water (DNAPLs), immiscible fluids that are lighter than water (LNAPLs), vapour phase contaminants in the soil above the water table, and contaminants dissolved in the groundwater.

The presence of contaminants in soil or groundwater can pose a serious health hazard, and in recent years, there has been a concerted effort to develop processes and technologies that can be used *in situ* to remove or treat contaminants in soil and groundwater. The performance of many existing *in situ* treatment technologies is closely linked to the ease in which fluid movement can be promoted through the zone of soil in which the contaminant is located. Fluid movement may include vapour and/or liquid phase flow which is usually encouraged by the installation of some combination of extraction and/or injection wells placed either above or below the groundwater table.

The effectiveness of methods which rely on subsurface fluid flow to access the contaminated soil are largely influenced by the permeability of the soil. In pervious soils where fluids may

1

flow through the subsurface relatively quickly, conventional *in situ* remediation technologies are often successful in removing contaminants from the sub-surface or treating contaminants in place. For contaminants within low permeability soils, the ability of fluids to move through the subsurface is greatly reduced, and conventional *in situ* remediation techniques are severely limited in their effectiveness and seldom used.

1.2 Statement of the Problem

The *in situ* treatment of contaminants located in dense low permeability soil is a particularly challenging problem. Existing techniques for the *in situ* treatment of contaminants are generally ineffective in these soils. For these techniques to be successful, some process must be first carried out on the soil which will increase the porosity and connectivity between pores in the soil, and thus, enhance the ability of fluids to move through the pore space. This thesis describes research carried out to investigate an innovative means of increasing the porosity of soil using a fluid injection technique called soil shearing.

In the soil shearing process, fluid is injected into a wellbore to cause stress changes in the soil surrounding the well. The stress changes can cause the soil to yield, which can result in an increase in the soil porosity and the generation of shear bands within the soil. These zones of increased porosity and shear banding will help to increase the connectivity of naturally occurring fractures and may increase the bulk permeability of the soil. The physical changes

2

made to the soil structure may allow greater accessibility to contaminants located within the soil and enable conventional *in situ* treatment technologies to be used more effectively over a broader range of soil conditions.

There has been very little work carried out to date to investigate the geotechnical parameters that may influence the *in situ* shearing process in low stress environmental applications. A number of processes may occur during fluid injection including shearing, cavity expansion, tensile parting (hydraulic fracturing) and flow through the pore space. The role that each of these mechanisms may have during the fluid injection process is influenced by a complex interrelationship between physical and geotechnical parameters including pore fluid and injection fluid properties, injection zone details, the state of stress in the soil, absolute permeability of the soil, soil constitutive behaviour, and macro structure (see Figure 1.1). In order to evaluate the suitability of shearing for enhanced *in situ* treatment of contaminated soil and groundwater, it is desirable to first gain a better understanding of how the physical and geotechnical parameters shown in Figure 1.1 may influence the shearing process.

1.3   Objectives of Research Program

The overall objective of this research program was to develop a fundamental understanding of the mechanism of yield zone development due to fluid injection in overconsolidated low permeability soil. Specific objectives of the research were:

3

- to investigate how injection parameters will influence the injection process (i.e. well geometry and orientation, rate of injection, fluid viscosity and density, etc.);

- to investigate how geotechnical parameters will influence the injection process (i.e. in situ stress, friction angle, cohesion, dilation, permeability, etc.)

- to investigate the effect of shear induced permeability enhancement on the development of yield zones due to fluid injection; and

- to investigate the significance and relative contributions of shear and tensile yield mechanisms during the injection process.

These objectives were realized through a comprehensive research program that included experimental and numerical work components. The experimental work included large scale field tests and reduced scale physical model tests performed in a geotechnical centrifuge.

1.4   Scope of Research

The primary emphasis of the work carried out during this research program was to develop an understanding of the geotechnical processes involved with soil shearing. The research

4

program included both experimental and numerical work components.

During the experimental work component, injection tests were carried out to generate yield zones within the soil mass surrounding a wellbore. The injection tests were closely monitored and testing was performed to determine the effect of the process on the soil surrounding the wellbore. The experimental work included 16 reduced scale physical model experiments, and two large scale field experiments. Additionally, laboratory testing was carried out to determine geotechnical properties of the soil used in the experiments. The experimental portion of the research may be summarised as follows:

- Reduced scale physical model experiments were carried out on the large 5 m radius Acutronic 680-2 geotechnical centrifuge located at the C-CORE Centrifuge Centre. The physical models were tested on the centrifuge at accelerations of 25 and 50 g's, which allowed the prototype subsurface stress fields to be simulated in the model.

- Large scale field experiments were carried out at the Environmental Test Facility, located at the former United States Naval Forces Facility in Argentia, NF. The field testing program allowed the soil shearing process to be tested and evaluated under conditions similar to those that could be expected in a typical field situation.

- Geotechnical testing was carried out in the soils laboratories at C-CORE and Memorial University to determine strength and deformation properties and to

determine fluid flow characteristics of the soil used in the model tests and field experiments. Additional testing was performed to characterize the soil and obtain grain size distributions, Atterberg Limits, density, specific gravity, etc.

Experimental results were used to develop a numerical model for the soil shearing process. The numerical modelling component of this work included the analysis of data from an extensive laboratory injection test program carried out by others in a large calibration chamber. Numerical modelling of the shearing process was performed using the two-dimensional explicit finite difference code Fast Lagrangian Analysis of Continua (FLAC). A strain softening constitutive model was used to model the stress-strain response of the soil and full coupling was maintained between the mechanical response and fluid flow.

Only the geotechnical aspects of soil shearing were investigated during this research. No work was carried out to evaluate the effect of applying shearing in conjunction with one or more conventional *in situ* remediation technologies for the purpose of contaminant treatment/removal. Although this type of testing was outside the scope of this project, such testing would constitute a logical next step in the development of soil shearing as a commercial application.

1.5   Organization of Thesis

Chapter 2 of this thesis provides a review of existing literature that is relevant to soil shearing. The literature review includes a discussion of the background and geomechanical principles of soil shearing and discusses how the process may enhance the effectiveness of existing *in situ* techniques for treating contaminated soil.

The field experiments are described in Chapter 3. This chapter presents descriptions of the experimental setup and test methods, and a summary of test results from the experiments.

The centrifuge experiments are described in Chapter 4. This chapter presents descriptions of the experimental setup and test procedures, and provides a summary of test results.

Chapter 5 describes and presents the results of numerical simulations of the injection tests. The numerical model and the analysis technique are described and a summary is provided of parameters used for the analyses. The results of numerical modelling are presented for the field and centrifuge experiments, as well as for injection tests carried out by others.

A discussion of the results of the injection tests and numerical modelling is provided in Chapter 6 of this thesis. The mechanisms resulting from the injection process are discussed as are the key parameters which influence the failure mechanism.

Chapter 7 presents conclusions that arise from this research. Recommendations are made regarding possible directions for additional work.

Five appendices are included at the end of the thesis. Calibration data for instrumentation is provided in Appendix 1, Appendix 2 contains the results of soils testing, and Appendix 3 contains detailed results from the injection tests. Appendix 4 contains data from large scale injection tests in a calibration chamber. Appendix 5 contains results of the numerical modelling.

Injection Fluid
- injection ratio
- injection fluid viscosity
- unit weight of fluid
- use of proppant

Permeability of Soil
- particle size
- void ratio
- composition
- fabric
- saturation
- pore fluid properties

Injection Zone Details
- injection depth
- pre-formed slot
- injection interval

Fluid Injection Process

Soil Constitutive Behaviour
- strength (c', φ', γ')
- deformation (G, B, ψ)
- permeability increase

State of Stress in Soil
- stress history (OCR)
- stress ratio (K)
- unit weight (γ)

Stress Response
- pore pressure (Δu)
- total stress (Δσ)
- eff stress (Δσ')

Macro Structure of Soil
- homogeneity
- bedding

Mechanism
- cavity expansion
- yield in tension
- yield in shear

No Yielding
- flow through pore space

Figure 1.1. Factors influencing the failure mechanism during fluid injection

9

CHAPTER 2 - LITERATURE REVIEW

2.1   *In Situ* Treatment of Contaminated Soil

Traditionally, a large proportion of site cleanup operations have involved removal of the contaminated soil from the site by excavation, and either *ex situ* treatment of the soil or disposal in a secure landfill. In addition to being expensive, the "excavate and dispose" approach to dealing with contaminated soil usually creates a great deal of disturbance at a site, often causing industrial or business activities on the site to stop during the remediation process. Additionally, environmental regulations governing the handling and disposal of contaminated soil are becoming more stringent, making it even more expensive to rely on *ex situ* techniques for dealing with contaminated soil.

Current practice in the environmental industry is to minimize site disturbance and costs by relying, wherever possible, on *in situ* techniques for treatment of contaminated soil. Enormous progress has been made over the past 20 years in the development of effective new technologies for the *in situ* treatment of contaminated soils. For example, the VISITT 6.0 database (U.S. EPA, 1997a), compiled by the Technology Innovation Office within the U.S. EPA's Office of Solid Waste Emergency Response, lists 371 environmental technologies by 214 vendors. Of the technologies listed in the database, 170 are provided by 98 vendors for the *in situ* treatment of contaminated soil, sediment, groundwater, and non-aqueous phase liquids (NAPLs). The majority of the *in situ* technologies listed in the VISITT database utilize

treatment methods that can be grouped into thirteen categories:

1. Adsorption
2. Air sparging
3. Bioremediation
4. Bioventing
5. Chemical treatment
6. Dual phase extraction
7. Electrical separation
8. Soil flushing
9. Soil vapour extraction
10. Solvent extraction
11. Surfactant enhanced recovery
12. Thermally enhanced recovery
13. Vitrification

Nearly all of these technologies rely, to some extent, on promoting the movement of fluids through the subsurface. This is usually accomplished by means of wells installed within the zone of subsurface contamination (U.S. EPA, 1994). Depending on the nature of the contaminant, the soil characteristics, the location of the contaminant with respect to the groundwater table, and the treatment technology or technologies to be used; the cleanup process may be carried out from a combination of injection and extraction wells with well screens located either below, coincident with, or above the groundwater surface.

Where a contaminant is located within a relatively pervious soil, the effectiveness of *in situ* technologies in cleaning the soil is well demonstrated (U.S. EPA, 1990). For contaminants located within low permeability soil, *in situ* techniques are much less effective and are seldom used. Deposits of low permeability soils are widespread across much of Canada and the United States. Many of these deposits were formed directly by glaciers or as lacustrine deposits associated with large lakes of glacial meltwater. These deposits are often located at

11

the ground surface and range from several to many tens of metres in thickness.

A common feature of low permeability clay deposits is the presence of a weathered zone within a few metres of the ground surface, characterized by ubiquitous and hydraulically active fractures and root holes. Although nearly all of the bulk porosity of these soils occurs in the matrix between fractures, the main avenues for fluid flow are provided by naturally occurring fractures. The density of natural fractures decreases with depth below the surficial weathered zone, although they have been found to extend to depths as great as 6 m below ground surface in the Sarnia, Ontario area (Ruland et al., 1990) and to depths in excess of 10 m in the Canadian prairies (Keller et al., 1986).

In areas underlain by low permeability soils, the occurrence and distribution of contaminants in the subsurface is controlled by complex relationships involving multi-phase transport through the fracture network, diffusive transfer of contaminants between the fractures and adjacent matrix blocks, and sorption of the contaminants on solids associated with fracture surfaces and within the matrix (Parker et al., 1993).

Remediation measures that involve promoting fluid movement through naturally fractured clays are limited by the complexity of the fracture network and the associated physical limitations to fluid flow. Techniques have been developed that either change the physical structure of the soil by inducing fractures and thereby increase the connectivity between the pre-existing naturally occurring fractures; or by changing the orientation of a treatment well

12

to intersect more fractures and to access a greater volume of contaminated soil.

2.2 Physical Processes for Enhancing *In Situ* Treatment

2.2.1 Horizontal well technology

Horizontal and directional drilling is used extensively in the petroleum sector as a cost effective means of producing hydrocarbons from reservoirs through gravity drainage (Butler, 1992). The first directionally drilled horizontal wells for environmental remediation were installed in 1988 as part of horizontal extraction and injection remediation systems at the United States DOE Savannah River Site Integrated Site Technology Demonstration (U.S. EPA, 1997b). Directional drilling methods can create wellbores with almost any trajectory. Blind wells terminate in the subsurface. Continuous wells intersect the ground surface and are accessible at both ends. In the environmental industry, horizontal wells provide unique characteristics and advantages that can improve the effectiveness of established soil and groundwater cleanup technologies now using traditional vertical well techniques.

The steering capability associated with some horizontal well drilling techniques allows installation in areas containing underground utilities, vertical wells, and other subsurface obstructions. Horizontal wells can be installed beneath buildings and other structures, thereby accessing contaminated regions of soil that are generally inaccessible to vertical wells.

13

The use of horizontal wells may allow fewer wells to be used to achieve similar remediation goals as can be achieved with vertical wells. This is due to the greater surface area associated with the lengthwise screened area of horizontal wells. At locations where a contaminant is distributed within a broad flat layer of soil, horizontal screens provide greater surface area in contact with contaminated soil or groundwater, allowing more effective transfer of materials used for remedial treatment (e.g., nutrients and microbes for bioremediation treatments, air for air sparging, vacuum for vapour extraction, soil flushing materials, etc.).

The use of horizontal wells for environmental remediation is increasing. The number of horizontal wells installed in the United States for environmental remediation projects was 55 in 1994 and 117 in 1995 (Kaback and Oakley, 1996), and predicted to be more than 400 for 1996 (Wilson, 1995). Because horizontal wells for remediation are a recent innovation, there is only limited data available which compares the performance of horizontal and vertical wells. Two horizontal wells were installed for a pilot test at the U.S. Department of Energy Savannah River Site (U.S. EPA, 1997b). During this test, more than 16,000 lbs of solvents were extracted using a 300 ft long sparging well placed below the ground water table and a 200 ft long soil vapour extraction well located above the ground water table (Kaback and Oakley, 1996; Looney et al, 1991). A test carried out at the Alberta Gas Plant (Armstrong et al, 1995) indicated that one 60 m long horizontal well could provide the same areal coverage as 22 vertical wells. A sparging study using horizontal and vertical wells was carried out for the U.S. Army Corps of Engineers (Wade et al, 1996) at the Hastings East Industrial Park in Nebraska. The horizontal well used in the study had a sparging capacity of more than

14

10 times that of a vertical well under the same injection pressure.

In low permeability formations such as glacial till where naturally occurring vertical fractures provide the primary flow paths for fluid flow, a horizontal well may intersect more fractures than a vertical well. As with vertical wells, the effectiveness of horizontal wells decreases as the percentage of fine particles in the soils increases. In soil deposits where horizontal bedding or other heterogeneities are present, the effectiveness of horizontal wells may also be reduced. The U.S. EPA (1997b) reports that horizontal wells are most applicable for conducting remedial activities in pervious soils such as gravel, sand and silty sand. The costs increase dramatically in geologic environments that include clay, glacial till, or bedrock. The effectiveness of horizontal wells in low permeability soils could be increased if the well was utilized with a flow enhancement process such as hydraulic fracturing or soil shearing.

2.2.2 Hydraulic fracturing in rock

2.2.2.1 Petroleum sector applications

Economic development of hydrocarbon reservoirs with low intrinsic permeability has been a major goal of the petroleum sector over the last century. Hydraulic fracturing has been used by the petroleum industry for more than 50 years to improve the rate at which oil or gas is produced from a reservoir and to increase the total volume of hydrocarbon that can be

recovered from a reservoir (Gidley et al, 1989). The technology associated with hydraulic fracturing has been developed almost exclusively for use in conventional hydrocarbon reservoirs which consist primarily of cemented (sandstones) or crystalline (carbonate) rock.

The hydraulic fracturing process involves blending chemicals to make an appropriate fracturing fluid and then pumping the blended fluid into the pay zone at high enough rates and pressures to create a tensile parting in the rock which is "wedged" open and extended hydraulically. A fluid that contains no propping agent is first pumped to initiate the fracture and to establish propagation. A propping agent is then introduced (usually silica sand), which is carried into the fracture as it extends, and serves to hold the fracture open after the fracturing process is completed. A viscosifier is mixed with the injection fluid to reduce fluid loss (or leak-off) into the pore space of the rock and so that the proppant will remain in suspension in the injection fluid. Hubbert and Willis (1957), and Morgenstern and Vaughan (1963), defined a non-penetrating fluid as one that is unable to enter the pervious material around the section being tested, and which does not establish a pore-fluid pressure gradient. A penetrating fluid is a fluid such as water which produces an immediate response in the pore pressure in the proximity of the borehole and a pressure gradient is established.

Several factors have been identified that affect fracture propagation including: variations of the *in situ* stresses existing within different layers of rock, relative bed thickness of formations in the vicinity of the fracture, bonding between formations, variations in mechanical rock properties (including elastic modulus, Poisson's ratio, fracture toughness, and ductility) fluid

16

pressure gradients in the fracture, and variations in pore pressure from one zone to the next.

The *in situ* stress is generally considered to be the most important factor controlling hydraulic fracturing. The process of drilling a borehole in the ground and applying a fluid pressure in the borehole will change the vertical, radial and tangential stresses in the rock around the borehole (see Figure 2.1). It is widely accepted in the literature that hydraulic fracturing occurs when the minor principle effective stress becomes tensile with a magnitude exceeding the tensile strength of the rock, i.e. when $\sigma_3' + \sigma_t \leq 0$.

If the minor principal effective stress is in the vertical direction (σ_z' in Figure 2.1), the orientation of the resulting fracture will be horizontal. If the minor principal effective stress is in a direction tangential to the borehole (σ_θ' in Figure 2.1), the orientation of the resulting fracture will be horizontal. The *in situ* stress controls the fracture azimuth (Hubbert and Willis, 1957) and orientation, the vertical height growth, crushing of the proppant, and various other aspects of fracturing.

The pressure versus time record for an ideal hydraulic fracture test in rock is shown in Figure 2.2. The pressure increases as fracture fluid is pumped at the start of the test and the compressive stresses in the walls of the well are reduced until at some point they become tensile. When the tensile stress exceeds some critical value related to the tensile strength of the rock, a hydraulic fracture is initiated (Pi) and begins propagating. If pumping is stopped, the crack will extend until equilibrium (the instantaneous shut-in pressure) is obtained. The

17

closure pressure or crack re-opening pressure (Nolte, 1988) is the pressure required to re-open an existing fracture. In Figure 2.2, the closure pressure is designated as Pr. Hydraulic fracture tests are often used to estimate the magnitude of *in situ* stresses. For example, if a vertical fracture is produced, the pressure record obtained during the test can be used to estimate the magnitudes of the secondary principal stresses in the plane normal to the test hole axis. If a horizontal fracture is produced, not as much information can be derived.

Rock is predominantly a brittle material and most efforts to understand the behaviour of crack equilibrium and growth in rocks have relied on elastic, brittle fracture theories. Griffith (1921) advanced the first plausible theory of crack behaviour while studying the reasons for the low tensile strength observed in brittle materials such as glass. He suggested that the low tensile strength observed in glass was a result of the presence of cracks and used an energy approach to equate the work performed during extension of the crack to an energy ascribed to the newly created crack surface. Barenblatt (1962) proposed a cracking model that leads to the same crack-extension criterion as advanced by Griffith, but provided a means of dealing with unrealistic infinite stress development at the crack tip.

The most general and extensively used theory for hydraulic fracturing of rock is linear elastic fracture mechanics theory. The theory of linear elastic fracture mechanics is related to Griffiths (1921) theory, but was modified by Orowan (1952) and restated by Irwin (1957) to include energy dissipation processes such as plastic flow and micro-cracking. These factors are incorporated through stress intensity factors (K_I, K_{II} and K_{III}) which refer to different

18

modes of crack behaviour. A fracture will advance when its stress intensity reaches a critical value, K_{Ic}, which is known as the plane strain fracture toughness, and has been shown to be a measurable property for many engineering materials including metals, glass, ceramics, polymers and others.

Andreev (1995) presents a comprehensive discussion of failure mechanisms in rock, including the initiation and propagation of fractures. The relative positions of various failure mechanisms with respect to the Mohr-Coulomb failure criterion are plotted in Figure 2.3. In Figure 2.3, fracturing processes occur in a relatively small region near the origin where the minimum principal stress, σ_3, is tensile.

Numerical models used to predict fracture growth in petroleum reservoirs have been developed over a number of years and are well established. These models relate injection rate, time of treatment, and fluid leakoff with fracture width and length. There are two basic approaches used for two-dimensional modelling of fracture propagation in petroleum reservoirs. In both approaches, the fracture height is assumed to be constant and the dimensions that change are assumed to be the width and the length of the fracture. The Perkins-Kern (PK) model (1961) assumes that the fracture has an elliptical shape when viewed in the vertical plane, perpendicular to the long axis of the fracture. The Geertsma-de Klerk model (1969) assumes that the fracture takes a rectangular shape in the vertical plane and an approximately elliptical shape in the horizontal plane.

19

A number of three-dimensional (3D) fracture propagation models have been developed such as that by Cleary et al (1983). Most 3D fracture models assume that the fracture is planar and remains planar during propagation. There are some 3D models with curved fractures (Ingraffea et al, 1985), however, these models are generally very complex and computationally demanding. Three-dimensional models have several basic elements in common including a crack-opening model, a fluid flow model, a crack propagation criterion, and a fracture propagation algorithm.

One of the problems associated with evaluating how well these models can predict fracture initiation and growth is the inherent difficulty in observing the geometry adopted by fractures *in situ*. The most detailed descriptions of *in situ* hydraulic fractures have been obtained through experiments where fractures were formed using a dyed or similarly tagged fluid, and subsequently excavated to expose the surfaces on which fluid penetration has occurred (Tyler et al., 1977; Warpinski et al., 1982; Trevits et al., 1982). Other techniques for determining fracture growth and geometry include surface based micro-seismic arrays (Ito, 1981), down-hole based hydrophones, (Shuck, 1974) and three component geophones (Albright and Pearson, 1982; Leydecker, 1981). An alternative method that is particularly useful for determining the geometry of near surface fractures is through the deployment of an array of continuously recording shallow-borehole tiltmeters. The interpretive technique is based on conventional strain seismology methods for recovering the fracture parameters of buried slippage on active geological faults from observation of the surface deformation (Evans, 1983; Davis, 1983).

20

2.2.2.2 Other non-petroleum sector applications

Hydraulic fracturing has been associated with other non-petroleum related activities including the construction of water wells, the grouting of foundations for dams, and the generation of thermal energy.

In the case of grouting, the objective is primarily to decrease the permeability and sometimes to increase the strength of the foundation. Fractures may occur when excessive grouting pressures are used which may result in the consumption of excessive volumes of grout, permanent weakening of the rock, or an increase in permeability. Grouting of dam foundations using pressures high enough to cause the grout to flow out of the grout hole in concentrated streams by hydraulic fracturing has been understood and applied practically since before 1960 (Sherard, 1986). Morgenstern and Vaughan (1963) established a theoretical mechanism for determining the allowable grouting pressures in rock based on the Mohr-Coulomb failure criterion in terms of effective stresses.

Fracturing has been used for many years in the water well industry to increase the yield of water wells (Koenig, 1960a and 1960b; Stewart, 1978). Gale and MacLeod, (1995) presented the results of an investigation carried out to determine the potential for using hydraulic fracturing to increase the connectivity of naturally occurring fractures, and thus increase the productivity of water wells on the Avalon Peninsula and Eastern districts of Newfoundland.

21

Results from the hydraulic stimulation program demonstrated that well yields in many of the rock units in Newfoundland can be increased by low pressure hydraulic stimulation.

The generation of thermal energy from hot dry rocks uses hydraulic fracturing to create flow paths between two wells (Murphy, 1982). Water heated by passage through the hot rocks between the two boreholes is used to drive turbines for electrical power. Successful applications of this technology have been carried out in New Mexico (Murphy, 1982; Kerr, 1987), England (Kerr, 1987), France (Cornet et al., 1982) and Germany (Rummel and Kappelmeyer, 1982).

2.2.3 Hydraulic fracturing in soil

Hydraulic fracturing of uncemented particulate media (soil) has often been considered a process to safeguard against in geotechnical engineering practice. Since about 1970, it has been known that hydraulic fracturing has occurred inadvertently when the fluid pressure in borings drilled through the cores of embankment dams exceeds the adjacent embankment earth pressure (Sherard, 1970, 1973, and 1986). Inadvertent hydraulic fracturing was found to occur when excessive water pressures were used in field permeability testing (Bjerrum et al, 1972). It is generally accepted that concentrated leaks, such as those that ultimately led to the catastrophic failure of the Teton Dam, may result from hydraulic fractures created in earth dams due to reservoir water acting on the upstream face of the core (US Government,

22

1976; Jaworsky et al, 1981; Kulhawy and Gurtowski, 1976; Seed and Duncan, 1981).

Various researchers (Overy and Dean, 1986; Wright and Tan, 1991; Andersen et al, 1994) have investigated the occurrence of hydraulic fractures during the setting of conductors for offshore oil or gas wells. Setting the conductor at too shallow a depth may result in the drilling fluid pressure causing hydraulic fractures to develop in the soil adjacent the well, which could result in the drill hole caving, water entering the well, or loss of drilling fluid. Wright and Tan estimated the fracture initiation pressure based on several theories including a tensile parting mechanism, a shear failure mechanism and a cavity expansion mechanism. Andersen and others presented a new approach for calculating hydraulic fracture pressures which assumes a tensile parting mechanism; but considers non-linearity of the stress-strain properties of the soil, and pore pressure changes in the soil due to changes in total normal stress and shearing of the soil.

Hydraulic fracturing tests in soil have been proposed as a means of determining the magnitude of the *in situ* minor principal stress (Bjerrum and Andersen, 1972). Massarsch and Broms (1977) and Clark (1979) drew attention to the effect of soil fracturing due to pile driving in cohesive soils. During pile driving in clay, horizontal and vertical cracks may be formed in the plastic zone around the pile. The cracks can provide drainage channels to pervious layers and thereby significantly increase the rate of reconsolidation after driving. Massarsch (1978), indicated that hydraulic fractures may be produced during driving of sand drains which increases the effective drainage area, and thus the efficiency of the sand drain.

23

The creation of hydraulic fractures in uncemented reservoirs is a relatively new technology in the early stages of development (Been and Kosar, 1991). Although the techniques used to create hydraulic fractures in soils subjected to low stresses are similar to those used for hydraulic fracturing in highly stressed cemented rock, the mechanisms of fracturing in soil are very different and are not well understood. A major driving force behind the development of numerical models for fracture formation in uncemented reservoir materials, has been a need to enhance hydrocarbon production in oil sands deposits, such as those found in Alberta, Canada (Chhina and Agar, 1985). A significant obstacle to the development and use of fracture models has been the lack of reliable test data. A large joint industry laboratory testing project was carried out by Golder Associates Ltd. (1991, 1992, and 1994) to enhance the mathematical formulations of models by providing data to calibrate and verify fracture models. As part of this test program, high rate injection simulations were carried out in a large triaxial stress chamber on homogeneous sand impregnated with a highly viscous fluid.

In the last decade, fracturing has been introduced as a technique to enhance the effectiveness of conventional in situ remediation techniques for the cleanup of contaminated soil and groundwater (Leach et al, 1994; Frank and Barkley, 1995; Keffer et al, 1996; Murdoch et al, 1990; Schuring et al, 1995). Since its introduction, hydraulic fracturing has gained acceptance and is being used commercially in the environmental industry as a means of accessing contaminants in low permeability near surface soils (US EPA, 1997b).

A rather unique application of hydraulic fracturing was presented by Zyrmiak (1997), and

24

involved a project carried out to investigate the feasibility of using the technology to enhance leachate extraction from wells retrofitted into an existing municipal landfill. Preliminary results from the project indicate that, from one site alone, the use of the technology could result in potential long term leachate extraction cost savings of millions of dollars.

Work has been carried out (Piggott, 1995; Piggott and Elsworth, 1994, and Piggott, 1996) to investigate the potential for hydraulic fracturing to result in detrimental mobilization of target contaminants due to the fluid flow regime induced during fracture extension. Piggott (1996) concluded that the potential for mobilizing aqueous phase groundwater contaminants during hydraulic fracturing is relatively small and can be estimated as a function of the properties of the contaminated formation and the details of the proposed fracture treatment.

The methodology that has been adopted to model hydraulic fracturing in fine grained soils for remediation of contaminated sites has involved conventional fracture mechanics (Murdoch et al., 1991; Murdoch, 1993). Modelling of fracture growth in soils using numerical analyses developed for cemented geological materials has met with very limited success. The main reason for the poor performance of conventional fracture models is that they fail to consider the mechanical behaviour of soils as a particulate media. Unlike cemented reservoir rocks such as sandstone, soils are uncemented and the individual soil grains are not constrained by cementation. As fluid is injected into a dense sand or an overconsolidated clay, the mineral grains slide relative to each other, increasing the void space. These volume changes, termed shear dilation or contraction, can significantly alter the stress field and the resulting initiation,

25

propagation and orientation mechanism may be influenced more by shearing and less by tensile parting.

2.2.4 Soil shearing

Shearing has been identified as a prominent mechanism that occurs in addition to tensile parting during hydraulic fracturing of uncemented particulate media. Chhina and Agar (1985) noted that significant shear stresses may develop near the tip of advancing hydraulic fractures in oil sand deposits, and that the propagation may be due to both tensile parting and shear distortion. They indicate that shear deformation and material dilation during fracturing may cause sub-parallel and/or intersecting planes beyond the fracture tip that may or may not be hydraulically connected to the fluid-filled fracture. The authors identify cases where field evidence supports shearing as a mechanism during fracturing. These cases include hairline shear planes observed in cores taken from near fluid filled fractures where no trace of the fracture fluid was found in the hairline shear fractures; a drop in pore pressure observed in some observation wells during fracturing which may be due to shear dilation; and significant surface heave observed at some sites that cannot be explained by temperature and pressure effects but may be due to shear deformation and associated dilatancy.

Mori and Tamura (1987) investigated the relation between hydrofracturing pressure and the strength of various cohesive soils. Injection tests carried out in a triaxial fracturing device

26

resulted in the creation of vertical, inclined and horizontal fractures in the test specimens. Mori and Tamura postulated that it is shear failure near the borehole, rather than tensile failure, which initiates the hydraulic fracture of cohesive soils, irrespective of whether the fracture propagates in a horizontal or vertical direction.

Dusseault and Rothenberg (1988) discuss the role of shear dilatancy with respect to permeability enhancement in oil sands deposits. Fluid injection at hydraulic fracturing pressures results in shear band development in advance of hydraulic fractures, primarily in shallow reservoirs where the vertical stress is the smallest principal stress. The authors indicate that volume increases due to dilation are likely to increase the permeability due to widening of flow paths whereas the permeability increase due to shearing is a result of increased connectivity between flow paths.

Shear failure, rather than tensile parting, was reported as the dominant mechanism in experiments carried out by Golder Associates (1991, 1992, and 1994) as part of a joint industry laboratory study investigating hydraulic fracture propagation in oil sands. Large scale laboratory injection tests were carried out using Lane Mountain 125 sand with a viscous pore fluid in a 1.4 m diameter by 1 m high calibration chamber. The test chamber allowed principal stresses of up to 1000 kPa to be applied independently to the soil through a circumferential (σ_h) and upper (σ_v) cavity. Pore fluid pressure was applied to the sample through drainage ports in the base and top of the chamber. An injection well was located in the centre of the sample cavity. Flourescent dye was added to the fluid injected into the soil during the testing.

27

A total of 18 injection tests were carried out at different injection rates and with different boundary conditions. Following each test, the soil was excavated and the locations of dye traces and fractures were mapped. A single or closely spaced distribution of fractures oriented primarily perpendicular to the minimum principal stress was not generated in any of the experiments. Generally, the injection fluid was found roughly spherically about the injection zone transported by a network of intersecting fractures up to several square centimetres in area. The size of the fracture zone was found to be related to the volume of fluid injected and the distance the injected fluid travelled from the injection well during a test was 1 to 2 orders of magnitude greater than would occur if flow had taken place only through the pore space of the sand. It was concluded that shear failure was the dominant mechanism at the injection rates used in the test program.

During the drilling of a wellbore in a hydrocarbon reservoir, rock strata is removed by the cutting tool and replaced by drilling mud. If the hydrostatic pressure of the mud at the face of the wellbore is less than the *in situ* stress, the material will expand or swell into the wellbore. There will be plastic, or irrecoverable strains around the well caused by shear failure with elastic deformation at greater distance from the well (Kosar and Been, 1991). Plastic or "yield" zones around a well can also be caused by changes in pore pressures caused by radial flow into the soil or rock surrounding the wellbore, dynamic fluid pressure fluctuations during drilling and subsequent hydrocarbon production, and thermal stress induced by the temperature difference between the drilling fluid and the rock mass (Kwong and Kaiser, 1991).

28

It is interesting to note that shearing has been identified as a significant mechanism during hydraulic fracturing of soils, despite most fracturing projects using highly viscous injection fluids to maximize the ability to wedge and extend the fractures via a tensile parting mechanism. No attempts have been made to date, to design the injection process such that shearing will dominate. The amount of leak-off that occurs during fluid injection may influence the role of shear dilation or contraction. Leak-off into the soil will tend to increase the pore pressure and thus reduce the effective stress over a larger volume of soil. If the in situ stress condition of the soil is anisotropic, pore pressure increases may result in yielding and development of shear bands in the soil. If the soil is dilatant, the volume increase during shear increases the porosity and results in an increase in the permeability of the soil.

The development of shear bands in the soil plays an important role in the shearing process. Morgenstern and Tchalenko (1967) presented the results of early work carried out to examine the development of microscopic and macroscopic structures in kaolin clay under direct shear conditions. Particular attention was paid to investigating the shear-induced fabric which they concluded results from translation and rotation of particles rather than displacements across particles. No discontinuities were observed to appear during stable yielding to peak strength. Structures begin to appear at or near the peak strength. Kinking is the dominant mode of deformation in the production of major structures with many kink structures being comparable to full-scale geological structures.

The point where a shear band is initiated on a stress-strain curve is referred to as the

29

bifurcation point, and marks the onset of non-homogeneous deformation. Vardoulakis (1980) found the bifurcation point to be close to the peak of a stress-strain curve.

Strain softening and shear band formation of granular soils tested under multi-axial conditions was investigated by Chu et al. (1996). Strain path tests were carried out on sand in a multi-axial cell and a photographic technique was used to detect the initiation of shear bands. Strain softening was found to be path dependent. It can occur as shear band formation or it may occur without the development of any non-homogeneity. Shear band formation is not necessarily a consequence of boundary imperfections, but can occur as the inevitable response of a sample to certain stress states and shear paths

Oda and Kazama (1998) examined the microstructure of shear bands in relation to the mechanisms of dilatancy and failure of dense granular soils. Plane strain tests were carried out on Ticino and Toyura sand specimens. Following the tests, cross-sections were taken of shear bands which were then photographed using an x-ray technique and examined microscopically. Oda and Kazama concluded that shear band boundaries are curved rather than straight; that large voids appear along a shear band with void ratios sometimes exceeding the maximum void ratio determined by the Japanese standard method; there is significant particle rotation and orientation within the shear bands; and the thickness of the shear bands is about 7 to 8 times the particle diameter.

Numerical modelling of shear band formation is a challenging problem for geotechnical

engineers and requires the capability of modelling a strain weakening material and capturing the localized deformation during shear band development. Two general approaches have been used to model shear zone deformation with finite elements. The first approach involves modifying the stiffness of a bifurcating element to account for development of a shear band (Pietruszczak and Mroz, 1981). The second approach is to model the shear band in a discrete manner, modifying the mesh to accommodate the development of the shear band (Pastor et al, 1991). Most methods can only effectively model small deformations, large deformations will usually result in severe mesh distortion which, in turn, may result in numerical instability or inaccuracies.

Wan et al. (1992) presented a method by which a shear band in a geostructure can be modelled numerically. The model accounts for dissipation of energy, even with a vanishing zone of localization. Chan et al. (1997) introduced a contact band approach for kinematic modelling of shear zone deformation. This approach treats the top and bottom surface of the shear band as two contact surfaces with elements located between the two surfaces. The method requires a robust scheme of remeshing within the band, however, there are fewer problems associated with distorted elements.

The soils which may achieve the greatest permeability enhancement due to shearing may be low permeability soils that are heavily overconsolidated. Soil may become overconsolidated due to a number of processes, including soil deposition followed by glaciation, changes in water table elevation, dessication, aging, chemical alteration, or erosion. These soils, which

31

may include stiff clays, dense sands and glacial till, often exhibit very similar stress-deformation behaviour in that they will dilate when subjected to anisotropic loading or unloading at low confining stresses. Volume increase due to shear dilation will result in an increase in permeability.

Mori and Tamura (1986) carried out experiments where silicate and acrylamide grouts were introduced into the pore space of loose sands and medium dense sands and allowed to set prior to undergoing shear in a triaxial cell. Soil permeability was measured during shearing based on the flow of water through the soil. The authors noted that for dense samples, the coefficient of permeability began to increase at approximately 2% axial strain, probably due to the development of dilatancy induced flow channels in the specimen. A permeability increase was also observed in loose sand samples undergoing shear. The strain at which the permeability began to increase in the loose samples was substantially greater than for the dense samples. The results of these experiments indicated that shear displacement caused an increase in permeability of up to two orders of magnitude along the vertical axis of the specimens. There was a substantial increase in permeability even when the volumetric strain was negative. This suggests that shear distortion effects the fabric of the soil, altering flow channels and increasing the flow path connectivity within the soil. The effect of dilation would tend to enhance the permeability increase.

In oil sands, fluid injection is used to enhance the production of hydrocarbons from the reservoir. Kosar and Been (1991) noted that a significant porosity increase can occur around

a wellbore during injection as a result of unloading as the effective stress decreases. A fluid injection test was carried out on a dense sand sample from the Athabasca Oil Sands deposit in northern Alberta. The behaviour of Athabasca Oil Sands at a fracture face subjected to a stress path representative of a fluid injection and production cycle is shown in Figure 2.4. The porosity increases during fluid injection as the effective stress decreases due to unloading. Because of the dilatant behaviour of the soil, there is a porosity increase of about 2% while the soil is sheared under constant stress conditions. Much of the porosity increase is not recovered when the soil is reloaded to the *in situ* stresses during the production cycle. The authors conclude that the porosity increase due to shearing is likely to have a significant influence on the fluid flow characteristics of the soil adjacent a fracture.

Scott et al (1991) indicate permeability increases of up to 16% in Cold Lake oil sands specimens when the isotropic effective stress is -reduced to zero from an initial isotropic effective stress of 12 MPa. The authors concluded that permeability changes during isotropic unloading are a function of the degree of unloading, the initial porosity of the soil, and the stress path. It was suggested that permeability increases more rapidly when unloading occurs through increasing pore pressure rather than by decreasing total isotropic stress. The authors also noted that a permeability increase is expected in oil sand samples undergoing anisotropic unloading at low confining stresses. Permeability changes during anisotropic unloading are a function of the average mean effective stress, the shear strength of the soil, the grain compressibility, and mineralogy.

33

The Steam Assisted Gravity Drainage (SAGD) process is used for the enhanced recovery of heavy oil from oil sand reservoirs. SAGD is a special form of steam flooding where the movement of oil to a production well is caused by gravity and is approximately parallel to the interface which forms the boundary of a growing steam saturated zone, known as the steam chamber. Phase A trials of the SAGD process (Edmunds et al., 1992) were carried out at the Underground Test Facility, located near Fort McMurray, Alberta. Chalaturnyk and Scott (1995), Chalaturnyk (1996), and Chalaturnyk and Scott (1997) report that shearing is a major geomechanical factor in SAGD. The primary stress path identified by Chalaturnyk and Scott for SAGD is illustrated in Figure 2.5. Under initially anisotropic stress conditions, a pore pressure increase due to steam injection results in equal reductions of σ_1' and σ_3'. In p-q space, the stress path is horizontal because $(\sigma_1' - \sigma_3')$ remains constant, however, the stress ratio (σ_1' / σ_3') increases due to a reduction in σ_3'. Following the pore pressure injection stage, the horizontal stresses continue to increase due to thermal expansion of the reservoir within the developing steam chamber. For the SAGD process, it is the deformation response along this stress path that is of primary importance. Reservoir deformations due to shear stress and changes in mean effective stress result in dilation or contraction, which alters the porosity and the permeability of the formation. Chalaturnyk and Scott (1997) reported that changes in reservoir fluid pressure during tests of the SAGD process at the Underground Test Facility near Fort McMurray resulted in shear induced volume strains, increases in porosity, and 30% to 50% increases in the absolute permeability of the formation.

2.3 Summary

There is a demonstrated need within the environmental industry for *in situ* techniques that can be used to efficiently cleanup contaminants in low permeability soils. Of particular interest are techniques that can be used to enhance the fluid flow characteristics of the soil, and thus allow existing processes to be used in low permeability soils that are proven to work under high to moderate permeability conditions. One technique that has proven to be successful in enhancing the cleanup of low permeability soils is hydraulic fracturing. Although hydraulic fracturing is effective, it can be expensive to implement in that specialized materials and equipment are required for creating the viscous proppant laden injection fluids. There is experimental evidence suggesting that for hydraulic fracturing processes carried out in some soils, shearing is a dominant mechanism in addition to tensile parting. There has been no research carried out to date, which has been directed at investigating the factors governing the occurrence of shearing during the injection process. The primary advantage of shearing over fracturing is that the process is very inexpensive and, because a proppant is not used, the process does not require the use of any specialized equipment to apply. Research carried out to date indicates that shearing may potentially be used as an inexpensive means to enhance the *in situ* remediation of low permeability soil.
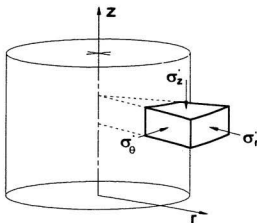
Figure 2.1. Stresses around a wellbore
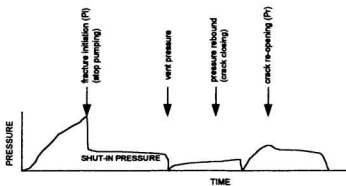
Figure 2.2. Pressure record for a hydraulic fracture test
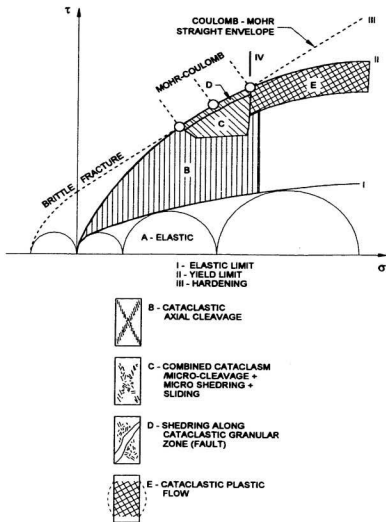
Figure 2.3. Location of failure processes on the Mohr diagram (after Andreev, 1995)

37
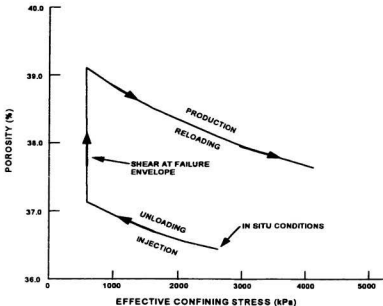
Figure 2.4. Porosity changes during anisotropic unloading and loading (after Kosar and Been, 1991)
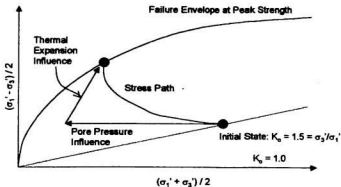
Figure 2.5. Major stress path during SAGD process (after Chalaturnyk and Scott, 1997)

38

CHAPTER 3 - FIELD EXPERIMENTS

3.1   General

This chapter presents the results of two field injection tests that were carried out at the
Environmental Test Facility (ETF) between June and October of 1997. The Environmental
Test Facility is a commercial organization that carries out large scale testing and verification
of soil and groundwater remediation technologies for the environmental industry. As part of
their infrastructure, ETF operates a two hectare full scale field testing site (Figure 3.1) which
is located at the former United States Naval forces base in Argentia, NF.

The first field experiment, FLDTST1, was carried out between June and July of 1997, and the
second field experiment, FLDTST2, was carried out between August and October of 1997.
Both field experiments were carried out in test beds constructed using recompacted glacial
till soil. Injection wells were installed in the compacted soil and instrumentation was installed
for monitoring pore pressures and ground deformations. The tests involved injecting dyed
water into wells while monitoring pore pressure development within the soil and soil
displacement at the ground surface. Following the experiments, the test beds were excavated
and the locations of dye traces found in the soil were mapped. The following sections provide
details of the test equipment and procedures used to carry out the injection tests, and presents
a short summary of data collected during the experiments.
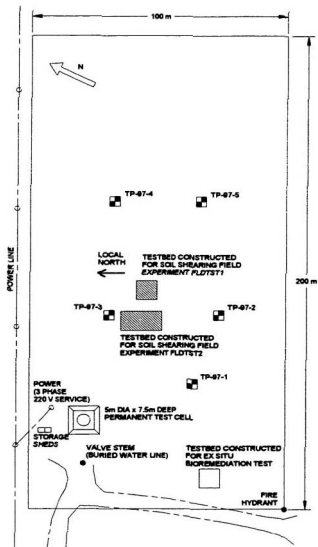
Figure 3.1. Field testing area - Environmental Test Facility

3.2   Test Bed Construction

3.2.1   Selection of test bed locations

The Environmental Test Facility controls two hectares of land on the former US Naval facility at Argentia which is used as a site for large scale field testing of *in situ* and *ex situ* soil and groundwater remediation technologies. Five test pits were excavated within the ETF field testing area in order to characterize the soil and determine the most suitable location for construction of test beds for the injection tests. A site plan showing the approximate locations of the test pits is presented in Figure 3.1. The test pits were excavated using a small backhoe. Test pit logs are included in Appendix 2.

The five test pits varied from 2.7 to 3.1 m in depth with similar soil conditions noted within all test pits. Generally, a thin zone of sand and gravel fill containing some silt was encountered at the ground surface which extended from 0.19 to 0.42 m in depth. A thin zone of organic topsoil, usually less than 0.1 m in thickness, underlies the fill. Underlying the topsoil layer was a dense to very dense brown weathered sand and gravel glacial till containing some silt and frequent cobbles and boulders. The amount of weathering decreased with depth, and was indicated by the colour changing from brown to grey. The test pits were generally dry, however, some granular lenses containing free water were encountered. Representative grain size distribution curves and moisture content test results for the till are included in Appendix 2.

The results of the field investigation indicated that the soil conditions were generally uniform across the test site. Level areas of the site, close to electricity and water supplies, were selected for construction of the test beds (see Figure 3.1).

A temporary survey control benchmark (designated SE) was established near the test beds by driving a spike into the remains of a former wooden power pole that had been cut off near the ground surface. The benchmark was given an arbitrary reference elevation of 100 m for use in elevation control during construction of the test beds and carrying out the field experiments. Elevations reported for the field experiments are referenced to the local benchmark elevation. A survey level was used for measurement of depth and elevation during construction and excavation of the test beds and during the field experiments.

A local coordinate system was established for each test bed with the centre of the test bed given the coordinates 0.0 m N and 0.0 m E. Grid lines were established with respect to the centre point to allow the locations of instrumentation and engineering measurements to be referenced by northing and easting to the local grid.

3.2.2   Test bed excavation

Excavation of test beds was carried out using small rubber-tired and tracked backhoes. Topsoil and organic materials were stripped from the ground surface prior to excavating the

test beds. Soil from the excavation was stockpiled adjacent the excavation for later use as backfill material.

The base of the test bed for *FLDTST1* was excavated to approximately 2.5 m below the original ground surface (base elevation 97.12 m in local reference system). The base of the excavation covered an area of about 3 m by 3 m. The approximate shape and dimensions of the excavation are shown in Figure 3.2.

The base of the test bed for FLDTST2 was excavated to approximately 3.9 m below the original ground surface (base elevation 95.91 m in local reference system). The base of the excavation covered an area of about 4 m by 8 m. The approximate shape and dimensions of the excavation are shown in Figures 3.3 and 3.4.

3.2.3   Backfill and compaction

The base of both test bed excavations were compacted prior to placement of backfill. Base compaction consisted of a minimum of three passes with a gasoline powered vibrating plate compactor. Thereafter, backfill was placed in 150 mm thick horizontal lifts, with each lift compacted by at least three passes of the compactor. Large cobbles and boulders were separated from the backfill material prior to compaction.

Following compaction of each lift, the density and moisture content of the soil were measured at two locations using a Troxler Model 3430 nuclear densimeter. For all density measurements, the probe depth was set to 150 mm and the time count was set at 1 minute. A summary of density and moisture content test results for both test beds is provided in Appendix 2.

Test bed FLDTST1 was backfilled and compacted to an average ground surface elevation of 99.1 m. Test bed FLDTST2 was backfilled and compacted to an average ground surface elevation of 98.7 m. Topographic surveys were carried out using a surveyors rod and level to determine the ground surface elevation of the test beds prior to the injection tests.

3.2.4 Injection wells

A vertical injection well was installed at coordinate 0 N, 0 E in test bed FLDTST1. The tip of the well was at elevation 97.12 m. The injection well was fabricated using 50 mm diameter schedule 40 PVC pipe. The lower 0.55 m of the well was screened using a commercially available well screen with 0.1" slots. The well screen was surrounded with #1 silica sand to a sand pack diameter of 0.15 m. The injection well was positioned prior to placement of backfill within the test bed and the soil was compacted in lifts around the well. The sand pack was temporarily contained around the well during placement of the backfill by setting the injection well within a 0.15 m diameter sheet metal tube which was filled with silica sand. The

44

sheet metal tube was then pulled up out of the soil as the height of the backfill increased around the exterior of the tube. When the backfill reached the top of the sand pack, the sheet metal tube was removed and additional backfill was placed and compacted up against the PVC injection well.

For FLDTST1, measures were taken to prevent leaks from occurring along the smooth interface between the PVC pipe and the soil. At three locations along the shaft of the injection well, silicone sealant was applied to the exterior of the pipe and a thin 0.25 m radius piece of polyethylene was clamped around the pipe over the silicone. The polyethylene sheet was then spread out horizontally and covered by the next lift of soil.

In test bed FLDTST2, a horizontal injection well was installed with the riser pipe located at coordinate 0.0 N, 2.0 W and a 3.0 m long horizontal screened section extending from 0.0 N, 1.5 W to 0.0 N, 1.5 E. The screen was fabricated with 0.1" slots. The elevation of the horizontal well was 96.29 m. The injection well was fabricated from 50 mm diameter schedule 40 PVC pipe. The 3.0 m long screened section of the well was surrounded by a 0.2 m by 0.2 m zone of #1 silica sand. The injection well was positioned prior to placement of backfill within the test bed and the soil was compacted in lifts around the well.

3.2.5 Instrumentation

3.2.5.1 FLDTST1

Four pore pressure transducers (PPTs) were installed in test bed FLDTST1. The PPTs were calibrated in C-CORE's laboratory prior to being taken into the field. Summaries of transducer calibrations and other instrumentation data are included in Appendix 1. The PPTs were buried in the soil during backfilling of the test bed at the locations and elevations shown in Table 3.1.

Table 3.1. Location of Instrumentation – FLDTST1

Instrument Designation	Serial Number	Location		
		Northing (m)	Easting (m)	Elevation (m)
PPT - 1	3901	1.03	0.00	97.65
PPT - 2	L338671	0.06	-0.95	97.71
PPT - 3	L356424	-1.00	0.00	97.67
PPT - 4	4365	0.00	1.00	97.67
LDT - 1	5421	0.00	0.57	99.05
LDT - 2	5422	0.00	1.52	99.10

PPT locations are shown in Figure 3.2. Cables for the four PPTs were routed around the perimeter of the test bed to a point near the northeast corner of the excavation where they were threaded through a length of monitoring well casing and brought vertically to the ground surface. Care was taken to ensure that no sharp particles or large cobbles were placed over the PPTs or cables and limited compaction of the next two lifts of soil was carried out directly

above the PPTs. At the ground surface, the ends of the PPT cables were coiled and wrapped in plastic to protect them from the weather until the test could be carried out.

Two linear displacement transducers (LDTs) were used to monitor ground deformations during the injection test. The LDTs were calibrated in C-CORE's laboratory prior to being taken into the field and the results of these calibrations are included in Appendix 1. The LDTs were installed at the ground surface at the locations shown in Table 3.1.

LDT locations are shown in Figure 3.2. The LDTs were fixed to a 3 m long steel channel section that was positioned parallel to the ground surface between the injection well and the east side of the test bed. The channel section was bolted at both ends to lengths of steel reinforcing rods that were driven into the ground.

3.2.5.2 FLDTST2

Thirteen pore pressure transducers were utilized for test FLDTST2. Transducers P-01 to P-10 and P-13 were buried within the test bed along a cross-section line perpendicular to the horizontal well at the mid-point of the well (Figure 3.3 and Figure 3.4). The PPTs were buried at depths from 3.0 to 0.5 m below ground surface at distances varying from 0 to 4.0 m from the injection well. Transducer P-11 was used to monitor the water level in an 11,000 litre water reservoir during the injection process, and P-12 was used to monitor the pressure in the

47

injection well at the wellhead during the experiment. A total stress cell (TSC-1) was buried in the test bed at a depth of 2.0 m below ground surface and at a distance of 1.0 m from the injection well. The face of the total stress cell was oriented to measure the horizontal stress in the test bed. The locations and depths of the instrumentation are summarized in Table 3.2 and are shown in Figure 3.3 and Figure 3.4.

Cables for the buried instrumentation were routed to the ground surface through vertical plastic tubing that was installed in the test bed. The annulus of the tubing was grouted with a bentonite slurry following completion of the test bed. When installing buried instrumentation, care was taken to ensure that no sharp particles or large cobbles were placed over the instrument or its cable and limited compaction of the next two lifts of soil was carried out directly above the PPTs. At the ground surface, the ends of the cables were coiled and wrapped in plastic to protect them from moisture prior to the test.

Linear displacement transducers were installed in rows at the ground surface along a cross-section perpendicular to the horizontal well and along a second cross-section parallel to the horizontal well (Figure 3.3 and Figure 3.4). The locations of the LDTs are summarized in Table 3.2. The LDTs were mounted on a frame constructed from two 4" x 2" x .188W x 24 ft long hollow structural steel sections that were bolted together in a T-configuration spanning the test bed. The ends of the LDT frame were supported on 0.1 by 0.1 m pressure treated wood posts that were founded on undisturbed soil.

Table 3.2. Location of Instrumentation - FLDTST2

Instrument Designation	Type	Serial Number	Location		
			Northing (m)	Easting (m)	Depth (m)
P-01	PPT	7471	1.0	0.0	3.0
P-02	PPT	C02	0.0	0.0	2.5
P-03	PPT	9099	2.0	0.0	2.5
P-04	PPT	C03	3.0	0.0	2.0
P-05	PPT	C04	0.0	0.0	1.5
P-06	PPT	4378	2.0	0.0	1.5
P-07	PPT	6805	1.0	0.0	1.0
P-08	PPT	L338671	3.0	0.0	1.0
P-09	PPT	3901	0.0	0.0	0.5
P-10	PPT	4365	2.0	0.0	0.5
P-11	PPT	4386	Water tank	Water tank	Water tank
P-12	PPT	7291	0.0	-2.0	Wellhead
P-13	PPT	9100	4.0	0.0	0.5
TSC-1	Stress cell	--	1.0	0.0	2.0
L-01	LDT	#1	-0.3	-2.0	0.0
L-02	LDT	#2	-0.3	-1.0	0.0
L-03	LDT	#3	-0.3	1.0	0.0
L-04	LDT	#4	-0.3	2.0	0.0
L-05	LDT	#6	0.0	0.0	0.0
L-06	LDT	#8	0.5	0.0	0.0
L-07	LDT	#9	1.0	0.0	0.0
L-08	LDT	#10	2.0	0.0	0.0
L-09	LDT	#18	3.0	0.0	0.0
L-10	LDT	#19	4.0	0.0	0.0

The PPTs, total stress cell and LDTs were calibrated in C-CORE's laboratory prior to being taken into the field and the results of these calibrations are included in Appendix 1. Airflow probes and thermocouples were buried within the south side of the test bed. These instruments were installed to allow pre and post test measurement of the permeability of the soil to airflow. Due to the adverse weather conditions following the test, post test air permeability testing was not carried out.
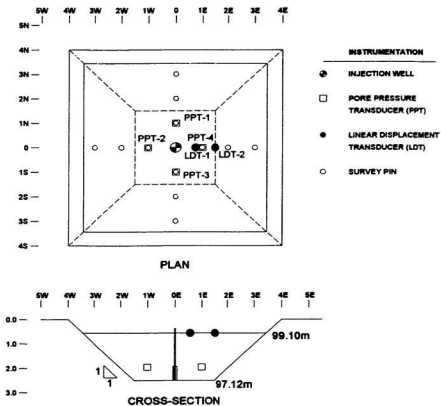
Figure 3.2. Test bed configuration - FLDTST1
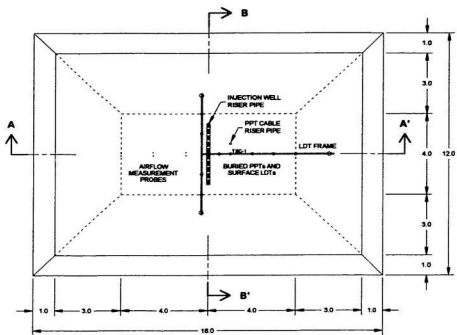
Figure 3.3. Test bed configuration (Plan) - FLDTST2

51
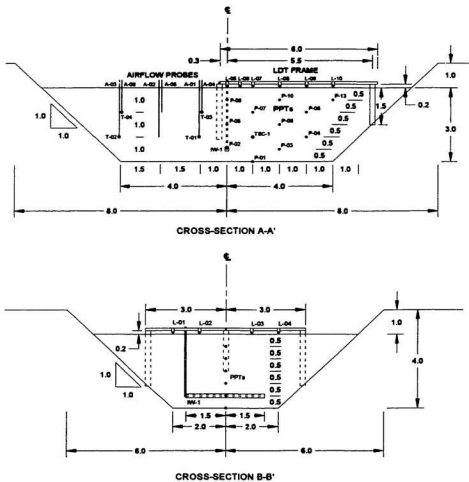
Figure 3.4. Test bed configuration (Section) - FLDTST2

3.3 Test Methodology And Experimental Results

3.3.1 FLDTST1

3.3.1.1 Initial *in situ* permeability testing

On June 24 and 26, falling head permeability tests using fresh water were carried out from the injection well to determine the approximate initial permeability of the compacted test bed soil before the injection test. Additional permeability testing was carried on June 27 following the injection test. Data from the falling head tests are included in Appendix 3.

For the initial permeability tests, the injection well casing was first filled several times with clean water over a period of approximately one-half hour prior to the test. The stick-up of the injection well casing above the ground surface was measured, the total depth of the well was confirmed, and the initial static water level was recorded. Falling head tests were then carried out by filling the well casing with fresh water and monitoring the water level response in the well over time. The average horizontal permeability of the soil prior to the injection test was found to be 5.7 x 10^{-4} cm/s using fresh water.

3.3.1.2 Equipment setup

Support equipment for the injection test was set up on June 24. The water supply for the

experiment was established using an 11,000 litre capacity polyethylene water tank positioned near the test bed and filled using potable water from a nearby fire hydrant. Although there was a source of electrical power located about 50 m from the test bed, it was more convenient to use a small 2500 W gasoline powered generator to supply electricity for the injection pump and the computer used with the data acquisition unit.

The pump used for fluid injection was a 19 mm close coupled gear pump (Figure 3.5) rated at 0.63 l/s at a pressure of up to 690 kPa (10 US gpm @ 100 psi). Specifications and a rating curve for the pump are included in Appendix 1. It was found that if the inlet pressure on the gear pump was low, the pump would cavitate and disrupt the flow of water. This was resolved by attaching a 50 mm diameter gasoline powered centrifugal pump in-line between the water tank and the inlet side of the gear pump. The centrifugal pump provided a relatively high inlet pressure for the gear pump. Connections between the water tank, the pumps, and the injection well were made using 50 mm diameter heavy duty braided plastic hose.

A flow meter and a pressure gauge were installed in the water line at the injection well. The flow meter was calibrated to measure water flows of up to 1.58 l/s (25 US gpm) and the pressure gauge was a Bourdon tube dial gauge with a range of 0 to 150 psi.

Data acquisition was carried out during the test using a Campbell Scientific CR10 measurement and control module. Six data channels were monitored during the injection test (four pore pressure transducers and two linear displacement transducers).

3.3.1.3 Use of viscosifier

Approximately 4160 litres of injection fluid was mixed using a viscosifier to increase the viscosity of the injection water. The product used was a liquid polymer emulsion called EZ-MUD[c] which contains a partially hydrolyzed polyacrylamide / polyacrylate (PHPA) copolymer. This product is generally used as a viscosifying agent in drilling applications and is non-toxic, non-fermenting and does not require a biocide to prevent reverting.

To prepare the injection fluid, 15 litres of EZ-MUD were blended with 4160 litres of water in the storage tank (i.e. 3.64 l/m³) and mixed for approximately two hours by recirculating the fluid through the pumps and back into the tank. Two - 1 litre samples were collected for viscosity measurement following the mixing process and an additional two - 1 litre samples were collected just prior to the injection test on June 27.

Viscosity measurements were made in the field using a Marsh funnel viscometer which is a simple orifice type viscometer. The Marsh funnel viscometer is normally used for routine checks of mud viscosity on drilling rigs and measures the relative viscosity of drilling mud compared to the outflow time of water. The Marsh funnel is 6 inches in diameter at the top and 12 inches long. A 10-mesh screen is fitted across one-half of the top to remove foreign materials and oversize particles from the fluid to be tested. The procedure for carrying out this test involves filling the funnel with fluid while holding a finger over the outlet tube. The finger is then removed from the outlet tube and the time required for one quart of the sample

55

to run out of the funnel is measured with a stopwatch. Funnel viscosity is reported in seconds/quart. The results of viscosity measurements are summarized in Table 3.3.

Table 3.3. Marsh funnel viscosity of injection fluid - FLDTST1

Fluid	Marsh Funnel Viscosity sec/quart
Injection water with viscosifier and no dye (20°C)	27.9
Injection fluid with viscosifier and dye (20°C)	28
Clean fresh water (20°C)	26 (+/- 0.5 sec)

3.3.1.4 Testbed pre-charging

On June 26, the storage tank containing the water/viscosifier mixture was connected directly to the injection well and the injection fluid was allowed to flow into the well by gravity. The initial fluid level in the injection well was 1.49 m below ground surface. Approximately 660 litres of fluid was allowed to flow into the well during an 18 hour time period. The fluid level in the well following the pre-charging was approximately 0.76 m below ground surface.

3.3.1.5 Dye tracer

On June 27, just prior to the injection test, 75 grams of methylene blue dye crystals was slowly mixed with approximately 3120 litres of injection fluid in the storage tank. The

purpose of the dye was to allow visual identification of the injection fluid during post-test excavation of the test bed. After mixing the methylene blue crystals with the injection fluid for 1½ hours, the injection fluid was a uniform dark blue in colour. Samples of the injection fluid containing the dye were obtained for measurement of injection fluid viscosity.

3.3.1.6 Injection Test

The injection test was carried out on the morning of June 27. The test involved pumping fluid into the injection well at a constant flow rate of approximately 0.631 l/s while monitoring pore pressures and ground surface deformations with the data acquisition system. The data acquisition system was configured to acquire data from the 4 PPTs and 2 LDTs at a rate of 1 Hz for the first 30 minutes of the experiment and 0.2 Hz for the following 4 hours. The system was activated several minutes prior to the start of injection to allow the establishment of "zero" readings.

Gross changes in ground surface elevation were monitored during injection at survey pins driven into the ground along sections extending north, south, east and west from the injection well. See Figure 3.2 for survey pin locations. A topographic survey was carried out immediately following the injection test.

Table 3.4. Injection sequence for FLDTST1

Time	Event
10:30 am	Injection test ready to begin
10:34 am	Data acquisition system on (begin collecting data)
10:37 am	Pumps on (begin pumping fluid into injection well) The flow rate immediately rises to approximately 0.631 l/s and there is an initial rapid increase in injection pressure to approximately 83 kPa as measured at the wellhead. Begin collecting surface movement data from survey pins.
10:38 am	Injection flow @ 0.631 l/s, pressure @ 69 kPa
10:38.5 am	Injection flow @ 0.631 l/s, pressure @ 62 kPa
10:39 am	Injection flow @ 0.631 l/s, pressure @ 55 kPa "Blue" fluid appears on ground surface approx. 1.4 m north of injection well in a band from 0.5 m W to 0.5 m E
10:39.5 am	Injection flow @ 0.694 l/s, pressure @ 55 kPa Fluid continues to flow out of the soil onto the surface of the test bed.
10:40 am	Stop pumping (approximately 114 litres of fluid pumped during test).
10:46 am	Disconnect flow meter and hose from injection well (elbow cut off top of well). Fluid flows out of injection well from the test bed.
10:50 am	Fluid level begins to drop in injection well. Begin measuring response with time (falling head test).
1:23 pm	Stop data acquisition
1:30 pm	Disassemble test equipment. Carry out ground surface elevation survey on same grid as was surveyed before injection test.

During the experiment, fluid was pumped into the injection well for approximately 2 minutes before the blue coloured injection fluid appeared at the ground surface 1.4 m to the north of the injection well (see Figure 3.6). The pumps were stopped after 3 minutes of injection during which time approximately 114 litres of fluid were injected into the well. The injection

sequence for the test is summarized in Table 3.4.

At the start of fluid injection, there was an initial rapid increase in wellhead pressure to approximately 83 kPa, followed by a gradual loss in pressure to approximately 55 kPa 2.5 minutes into the test. Pore pressure records and monitoring results from the displacement transducers are presented in Figure 3.7. The pore pressure transducers recorded a response similar to that observed at the wellhead. At the start of injection (at 200 s on Figure 3.7), the transducer located one metre west of the well measured pore pressures rising rapidly to a maximum of approximately 34 kPa at 270 s before falling to about 30 kPa at 370 s when the injection pump was stopped. All four pressure transducers measured a similar response during injection which indicates that the pressure response was uniform around the well.

Displacement transducers indicated an initial rapid response of approximately 1 mm during the first 40 s of fluid injection followed by a less rapid but nearly linear displacement rate during the remainder of fluid injection. LDT 5422, located 1.5 m from the injection well, measured a maximum vertical response of about 3.5 mm at the time that injection was stopped. LDT 5421, located 0.6 m from the injection well, measured a maximum response of about 2.1 mm at the time that injection was stopped. After fluid injection was stopped, both LDTs showed a gradual drop in the ground surface elevation and a permanent displacement of approximately 0.5 mm. Surface displacement measured using a surveyors level and rod, was consistent with that measured using the displacement transducers.

59

3.3.1.7 Post-injection permeability testing

Following the injection process, the injection hose was disconnected from the well and a falling head test was carried out by monitoring the drop in injection fluid level in the well over time. The initial and post-injection falling head tests were interpreted using the Hvorslev (1951) procedure incorporated into the computer program *Super Slug* which is distributed by Starpoint Software. The Hvorslev method involves the determination of the basic time lag and permeability from a plot of the change in head in the well versus time. The average horizontal permeability of the soil prior to the injection test was found to be 5.7×10^{-4} cm/s using fresh water. The average horizontal permeability from the post-injection test was 1.4×10^{-4} cm/s using injection fluid, or 6.9×10^{-3} cm/s after compensating for the difference in viscosity between the injection fluid and fresh water.

3.3.1.8 Excavation of test bed

Excavation of the test bed and mapping of dye traces began on July 4 and was completed on July 9. The procedure developed for identifying and mapping the dye traces involved first excavating a narrow trench radially outwards from the centre of the well. The side walls of the excavation were carefully examined and the northing, easting and elevation were recorded where traces of blue dye were observed in the soil.

At some locations, the blue dye tended to blend in with the brown soil and was difficult to spot, particularly at locations where only small volumes of injection fluid had penetrated. The dye traces were generally observed to be located within a region of soil with a higher moisture content than the adjacent soil. The tendency was for the dye traces to extend radially outwards and upwards in all directions from the top of the well screen. Movement of the dye through the soil appeared to be influenced by the macro structure of the soil. Dye traces were occasionally found extending horizontally between compacted lifts, or even reversing direction back towards the injection well. The dye trace locations are plotted in Figures 3.8, 3.9 and 3.10.

3.3.2 FLDTST2

3.3.2.1 Equipment setup

FLDTST2 utilized the same water supply, gear pump and flow meter as were used for FLDTST1. Although there was a source of electrical power located about 50 m from the test bed, it was more convenient to use a 5000 W gasoline powered generator to supply electricity for the injection pump and the data acquisition unit. A 25 mm diameter plastic hose was used for the water lines between the reservoir, the pump, and the injection well (Figure 3.11). The 50 mm diameter centrifugal pump used for FLDTST1 was not required for FLDTST2. Pressure at the wellhead was monitored using a dial gauge and a pore pressure transducer.

Because of the large number of instruments used for this test, the Campbell Scientific CR10 measurement and control module used during FLDTST1 was not used for FLDTST2. For FLDTST2, a mobile PC based data acquisition system was used for data acquisition and 24 channels were monitored.

3.3.2.2 Use of dye tracer for injection test

On September 11, 2700 litres of fresh water were mixed with 125 g of methylene blue dye tracer in the storage tank. The concentration of dye used for FLDTST2 was approximately twice that used for FLDTST1. After mixing for 1½ hours, the injection fluid was a uniform dark blue in colour.

3.3.2.3 Injection test

The injection test was initially carried out on the morning of September 11, 1997. The test involved pumping fluid into the injection well at a constant flow rate of approximately 0.631 l/s while monitoring pore pressures and ground surface deformations. Data was acquired from the 13 pore pressure transducers, the total stress cell and the 10 linear displacement transducers at a rate of 2 Hz. The system was activated several minutes prior to the start of pumping to allow the establishment of "zero" readings for the test. After starting the injection

pump, the injection pressure at the wellhead gauge increased to approximately 12 kPa during the first 3½ minutes of injection. The injection pressure then dropped slowly until reaching 0 kPa pressure approximately 17 minutes after starting the injection pump. The injection pump was stopped after approximately 19 minutes, during which time 719 litres of water were injected into the well. The injection sequence is summarized in Table 3.5.

The pressure responses for all PPTs are included in Appendix 3. The pressure responses due to fluid injection for PPTs P-02, P-03, P-04 and total stress cell TSC-01 are shown in Figure 3.12. Fluid injection begins at time 12.1 minutes. P-02, located within the sand pack on top of the horizontal well, showed a peak excess pressure of 30.4 kPa at a time of 15.3 minutes. P-03, located 2.0 m north of the well and at the same depth as the well screen, shows a peak excess pore pressure response of 11.9 kPa at 19.0 minutes. The total stress cell, TSC-01, located 1.0 m north of the well and 0.5 minutes above the well screen, shows a peak pressure response of 4.9 kPa at 19.1 minutes. P-04, located 3.0 m north of the well and 0.5 m above the well screen, shows the excess pore pressure gradually increasing with time and reaching a maximum of 4.8 kPa at 31.7 minutes. The injection pump was stopped at 30.8 minutes.

P-01 (PPT 7471) was damaged and showed no response during the test. P-05, P-07, P-08, P-09, P-10 and P-13 (see Figure 3.3 and Figure 3.4 for PPT locations) were working but recorded no pressure response during the injection test. The response of P-06 (PPT 4378) was erratic due to a poor electrical cable connection. There was a gradual drop of pressure recorded by P-11 during injection which corresponds to the changing fluid level in the storage

tank. P-12, which was located at the wellhead, was adversely affected when the injection pump was turned on or off, and did not produce a reliable pressure record.

Table 3.5. Injection Sequence for FLDTST2

Time	Event
12:00 pm	Injection test ready to begin
12:05 pm	Data acquisition system on (begin collecting data)
12:17.5 pm	Pumps on. The flow rate immediately rises to approximately 0.631 l/s and there is a gradual increase in injection pressure
12:19 pm	Injection flow @ 0.631 l/s, pressure @ 10.3 kPa
12:21 pm	Injection flow @ 0.631 l/s, pressure @ 12.4 kPa
12:24 pm	Injection flow @ 0.631 l/s, pressure @ 6.9 kPa
12:27 pm	Injection flow @ 0.631 l/s, pressure @ 3.4 kPa
12:35 pm	Injection flow @ 0.631 l/s, pressure @ 0 kPa
12:36 pm	Stop pumping (approximately 719 litres of fluid pumped during test).
1:10 pm	Stop data acquisition
1:15 pm	Disassemble test equipment.

The vertical displacement responses for L-01 to L-10 are shown in Appendix 3. The measured response for all LDT's was less than about 0.2 mm. The LDT records do not show any discernible vertical displacements at the ground surface due to fluid injection.

Although an initial pore pressure increase was noted during the early stage of the September 11 injection test, the injection pressure dropped off after several minutes and fluid was injected into the test bed with little or no resistance at the flow capacity of the gear pump. In

an attempt to generate a larger pore pressure response due to fluid injection, it was decided to first increase the degree of saturation of the test bed and then repeat the injection process using a more viscous injection fluid. A subsequent injection test was carried out on October 23. The second attempt at carrying out injection test FLDTST2 was aborted when a leak developed on the edge of the test bed at the interface between the compacted and natural soil.

3.3.2.4 Excavation of test bed and removal of instrumentation

Excavation of test bed FLDTST2 for removal of instrumentation and mapping of dye trace locations began on October 29 and was completed on November 3. A rubber tired backhoe and a tracked excavator were utilized for excavating the test bed. Due to the highly saturated soil and adverse weather conditions, only part of the test bed was excavated (Figure 3.13).

There were no traces of "blue" dye encountered until the excavation reached a depth of approximately 1.5 m below ground surface. At that depth, a small amount of blue staining of soil was observed around the vertical riser pipes for both the injection well and the tube for the instrumentation cables. In addition, blue staining was noted along the east side of the test bed at the interface between the compacted and non-compacted soil approximately 1 m north of the horizontal well. Because the methylene blue dye was used only for the September 11 injection process, and only 720 litres of dyed water were injected at that time, this limited extent of staining at this depth was not unexpected.

At a depth of about 2.5 m, which is the depth of the horizontal well, a planar zone of blue stained soil was observed approximately 50 mm thick. This zone extended horizontally outwards from the well for a distance of approximately 1.5 m (Figure 3.13). Because of the poor conditions for excavating the test bed, the extent of the stained region was not determined other than in the northeast quadrant of the test bed. A second smaller horizontally planar zone of stained soil was encountered approximately 200 mm below the first (Figure 3.13), which suggests that the orientation of the stained regions may have been influenced by the macro structure of the compacted soil. The proximity of the stained soil to the eastern boundary of the test bed suggests that the "leak" that occurred during the October 23 injection process may have been at least partially initiated during the September 11 injection process.

Figure 3.5. Injection pump for field tests

Figure 3.6. Appearance of injection fluid on ground surface - FLDTST1
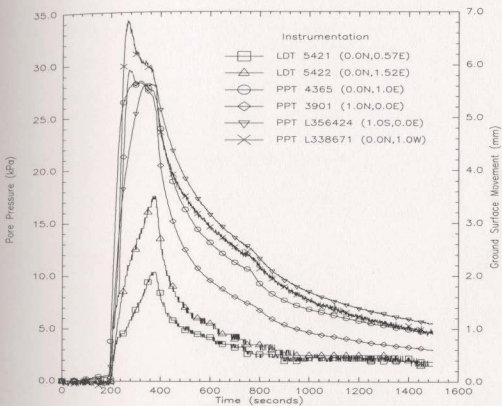
Figure 3.7. Excess pressure response and ground surface movement - FLDTST1

NORTH

Approximate location where
blue dye exited surface of
testbed. Area was disturbed
before mapping was
completed.

(-1.5,1.5)

(1.5,1.5)

Injection Well
(0,0)

WEST

EAST

(-1.5,-1.5)

(1.5,-1.5)

Start of excavation. No
mapping of dye traces
in this area.

SOUTH
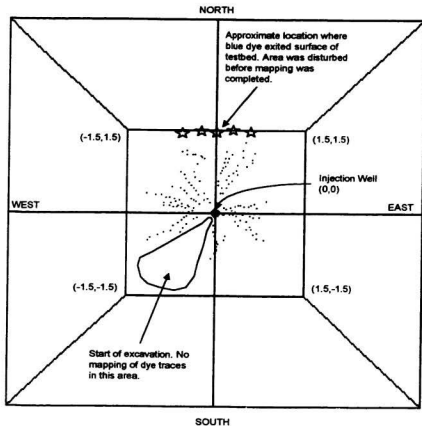
Note: Each dot represents a discrete location at which dye was observed
in the soil during the excavation of the testbed.

Figure 3.8. Dye trace locations (Plan) - FLDTST1
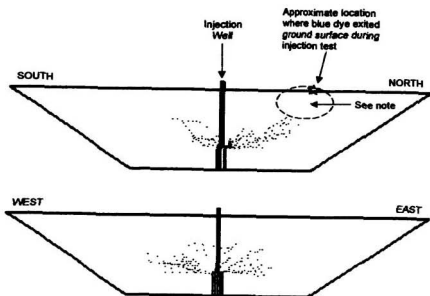
Note: Blue dye appeared at the ground surface near this location during the injection test. Following the test, the near surface soil was disturbed before dye traces could be mapped.

Figure 3.9. Dye trace locations (Section) - FLDTST1
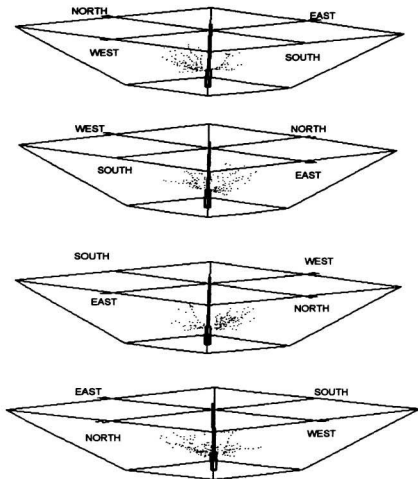
Figure 3.10. Dye trace locations (Oblique) - FLDTST1

Figure 3.11. Appearance of injection fluid on ground surface - FLDTST2
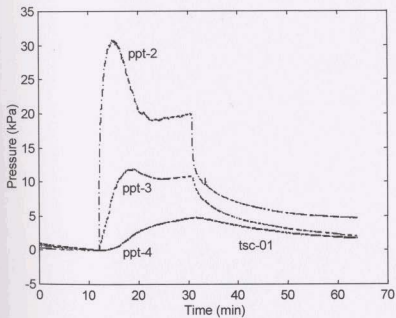
Figure 3.12. Pore pressure response - FLDTST2

NORTH

BLUE STAINING AROUND
VERTICAL RISER PIPE
TO APPROX 1m ABOVE
HORIZONTAL WELL

TEST BED
NOT EXCAVATED
IN THIS
DIRECTION

BLUE STAINING AROUND
VERTICAL RISER PIPE
TO APPROX 1m ABOVE
HORIZONTAL WELL

TEST BED
NOT EXCAVATED
IN THIS DIRECTION

PPT's

EXTENT OF PLANAR ZONE
OF BLUE STAINED SOIL
APPROX 50 mm THICK

REGION WHERE BLUE
STAINING TRAVELLED ALONG
EDGE OF TESTBED
TO 1.5 m ABOVE HORIZONTAL WELL

APPROXIMATE UPPER
EXTENT OF TESTBED
EXCAVATION

TEST BED - PLAN

EXTENT OF DYE TRACES
NOT DETERMINED
IN THIS DIRECTION

APPROX 1.5 m

APPROX 0.05 m

APPROX
0.5 m

0.2m x 0.2m SAND PACK
AROUND HORIZONTAL WELL

TEST BED - SECTION

Figure 3.13. Extent of dye traces - FLDTST2

73

CHAPTER 4 - REDUCED SCALE CENTRIFUGE EXPERIMENTS

4.1   General

This chapter presents the results of reduced scale injection tests using vertical wells installed in clay and sand testbeds. The tests were carried out in a large geotechnical centrifuge at accelerations equivalent to 25 g and 50 g. Sixteen injection tests were carried out in four specially prepared testbeds. Two of the testbeds (tests CCFS01 and CCFS02) were constructed using overconsolidated Speswhite kaolin clay. The remaining two testbeds (tests CCFS03 and CCFS04) were constructed using a mixture of silt and fine sand.

Injection tests were carried out from both shallow and deep wells equivalent to 5 m and 10 m prototype depths. Water containing a dye was injected through the wellbore and into the test soil at a constant rate. During the experiments, pore pressure was monitored at the wellhead and within the soil surrounding the well. Vertical displacement was monitored at the ground surface near the well. The testbeds were excavated following completion of the experiments and the locations of dye traces in the soil were mapped. Laboratory tests were carried out to determine the strength and deformation properties of the soil.

4.2 Reduced Scale Centrifuge Modelling

It is common practice for researchers investigating geotechnical problems to carry out physical experiments to observe the response of soil and soil structures under various loading situations. Ideally, these experiments are well instrumented and are carried out at full scale with well known soil and boundary conditions. The results obtained from such testing may provide direct insight into the processes and mechanisms involved in the experiment. The primary disadvantage to full scale testing is that the experiments are often very expensive to set up and carry out, and for many projects, there is only a limited budget to investigate problems. In addition, full scale testing is often very labour intensive and time consuming. Where a series of tests are required to examine the effect of variations in key parameters, testing at full scale is very often impractical.

Reduced scale physical models tested at one gravity are often used to investigate the response of soil and soil structures to loading. Reduced scale experiments are generally much less expensive to set up and carry out than a full scale test, and greater control may be exerted over such things as soil conditions, instrumentation, and boundary conditions. The mechanical response of soil is highly dependent on the stress level in the soil and the stress history of the soil. For reduced scale models tested at one gravity, the stresses in the soil do not replicate those in the full scale prototype, and thus the mechanical response of the soil due to loading may be quite different between the model and the prototype. This may cause difficulties with interpretation of data and extrapolation of scale model results to full scale.

Geotechnical centrifuges are used by researchers to carry out reduced scale physical model tests where gravity affects are important. They have been used for many diverse applications including dynamic response to earthquakes, diffusion of heat and chemical pollutants, soil-structure interaction, marine geotechnics, permafrost, and others. The use of a centrifuge for physical modelling of geotechnical problems allows gravity dependent parameters in a reduced scale model to be controlled such that the response of the model is representative of that in a full scale prototype.

4.2.1 Theoretical concepts

Geotechnical centrifuges have been used for many years for modelling soil stresses in relation to such problems as slope stability, deep foundations, retaining walls and footings. More recently, geotechnical centrifuges have been used to investigate other types of problems including groundwater flow and contaminant transport.

Scaling laws have been derived and validated for a number of modelling situations. Scaling laws concerning the modelling of stresses, strains, seepage processes, consolidation, particle size effects, etc. have been discussed by many authors (see for example, Schofield, 1980). A comprehensive discussion of scaling laws related to environmental geomechanics and transport processes in porous media was presented by Culligan-Hensley and Savvidou (1995). Some common centrifuge scale factors are summarised in Table 4.1.

The fundamental scaling law of centrifuge modelling is that similarity is achieved at homologous points in a prototype and a model by accelerating a 1:N scale model to N times the earth's gravity. An example from geotechnical engineering that is often used to demonstrate this basic scaling law is that of an embankment. A centrifuge model embankment is constructed using the same soil and to the same density as the prototype embankment with every linear dimension in the prototype N times larger than in the model (i.e. model is 1/N the size of the prototype). If the centrifuge is operated such that the centripetal acceleration acting on the model is N gravities, then the stresses due to gravity at corresponding points in the model and the prototype will be identical (Figure 4.1). If care is taken to ensure that any other boundary or applied stresses in the model also correspond with the prototype, then the strain fields, deformations and behaviour will be similar.

It was suggested by Palmer (1991), that modelling of brittle materials in the centrifuge may require different scaling laws than would be required for modelling materials whose behaviour is governed by a failure stress or yield stress. Brittle materials are those materials which are characterized by a fracture toughness and whose deformation is governed by the formation of cracks which propagate and multiply when the stress intensity reaches a critical value. The behaviour of the soil used in this research is quite different from the behaviour of brittle materials such as ice, glass, steel, etc. and it is unlikely that Palmer's proposed scaling laws for brittle materials are applicable. It is likely that the behaviour of the soil used in this research is governed by failure stresses and the classical centrifuge scaling laws.

77

Table 4.1. Centrifuge scaling factors.

Parameter	Scale Factor
length	$l_m = (1/N)\, l_p$
stress	$\sigma_m = \sigma_p$
soil or fluid density	$\rho_m = \rho_p$
fluid viscosity	$\mu_m = \mu_p$
acceleration	$N_m = N\, N_p$
angle of friction*	$\phi_m = \phi_p$
shear strength	$c_m = (c_c)_p$
strain	$\varepsilon_m = \varepsilon_p$
pore fluid velocity	$u_m = N\, u_p$
hydraulic conductivity	$k_m = N\, k_p$
force	$F_m = (1/N^2)\, F_p$
mass	$M_m = (1/N^3)\, M_p$
energy	$E_m = (1/N^3)\, E_p$
time for inertial events	$t_m = (1/N)\, t_p$
time for diffusion events	$t_m = (1/N^2)\, t_p$

Notes: a) Subscript m denotes model, p denotes prototype.
b) Using same soil in model as in prototype.

A centrifuge may be used to model fluid flow problems in soil. In a centrifuge with an acceleration of $N \cdot g$, the increase in self weight of the pore fluid results in the local seepage velocity at any point in the model being N times greater than in the corresponding point in the prototype. Because the model has been scaled by a factor of N, the seepage paths are N times shorter in the model than in the prototype and there is an N times decrease in the distance that the pore fluid must travel. The result is that diffusion controlled flow events in the centrifuge, such as consolidation under changing effective stress conditions, occur N^2 times faster than in a full-scale prototype. Diffusive flow events which may require long prototype times can therefore be replicated in a centrifuge in short model times.

A basic assumption for the validity of Darcy's Law is that fluid flow through the soil is laminar. Because seepage velocity in the centrifuge is N times greater than at one gravity, it is possible that flow may exceed the laminar range and become turbulent. The transition from laminar to turbulent flow is determined using the Reynolds number [Eqn. 4.1],

$$Re = \rho v D / \mu \qquad \text{[Eqn. 4.1]}$$

where ρ is the fluid density, v is the fluid velocity, D is some particle size representative of the average soil pore diameter (typically D_{50} or D_{10} can be used), and μ is the viscosity of the pore fluid. Bear (1979) indicates that the upper limit for laminar flow is a Reynold's number of between 1 and 10. For the range of conditions used in this research and at a centrifuge acceleration to 50 g, the Reynolds number varied from 0.001 to 0.2 in the Speswhite kaolin tests and from 0.02 to 1.5 in the silty sand tests. For this range of Reynolds numbers, pore fluid flow is within the laminar region and Darcy's Law is valid.

Soil shearing for environmental applications is a new area of research. There is no previous experience modelling the process in a geotechnical centrifuge and no previous work has been carried out to determine scaling relationships for the process. Based on classical centrifuge scaling laws, linear dimensions of the centrifuge injection models are scaled from the prototype by $L_m = (1/N) L_p$. Stresses and fluid pressures in the model are equivalent to stresses and fluid pressures at analogous locations in the prototype. Soil properties, i.e. density, angle of friction and shear strength are equivalent at the model and prototype scales.

79

Injection and pore fluid properties, including density and viscosity, are also equivalent at the model and prototype scales.

The scaling relationship that applies to the injection velocity may be derived by examining the governing equations for processes similar to an injection test. At low injection rates and prior to the development of discontinuities around the well, the injection mechanism is quite similar to a pumping test in a partially penetrating well (see Figure 4.2a), where the flow rate is determined using Eqn. 4.2.

$$Q = \frac{\pi k \left(H^2 - h_w^2 \right)}{\ln\left(\frac{R}{r_w} \right)} \qquad \text{[Eqn. 4.2]}$$

A similar relation [Eqn. 4.3] simulates the case of an injection test where flow is occurring through the pore space of shear induced discontinuities. In this case, the injection process is more similar to a pumping test in a well through a very thin artesian zone (see Figure 4.2b).

$$Q = \frac{2\pi k D \left(H - h_w \right)}{\ln\left(\frac{R}{r_w} \right)} \qquad \text{[Eqn. 4.3]}$$

Using the scaling relations provided in Table 4.1 for hydraulic conductivity and length, the flow rate during an injection test [Eqns. 4.2 and 4.3] scales as shown in Eqn 4.4. The surface area of the injection interval is scaled from the prototype to the model using the relation shown in Eqn. 4.5 and the injection fluid velocity is scaled using Eqn. 4.6.

$$Q_m = (1/N) \, Q_p \qquad\qquad \text{[Eqn. 4.4]}$$

$$A_m = (1/N^2) \, A_p \qquad\qquad \text{[Eqn. 4.5]}$$

$$v_m = N \, v_p \qquad\qquad \text{[Eqn. 4.6]}$$

4.2.2 C-CORE Centrifuge Centre

The C-CORE Centrifuge Centre is a research facility located between the Captain Robert A. Bartlett building and the S. J. Carew building on the campus of Memorial University of Newfoundland. The Centre includes a two story building containing laboratories and workshops on the main floor with offices on the second floor. A containment structure, housing an Acutronic 680-2 centrifuge, is located at the rear of the building.

The Acutronic 680-2 centrifuge has a radius of 5.5 m from the centre of rotation to the surface of the swinging platform and is capable of testing models to 200g. The centroid of the test package is typically at a working radius of 5m. At the maximum centrifuge rotational speed of 189 rpm, the acceleration of the test package is approximately 200g. The maximum payload capacity is 100g x 2.2 tonnes = 220 g-tonnes at the 5 m working radius. The maximum payload size is 1.1 m high by 1.4 m long and 1.1 m wide.

The centrifuge arm consists of two parallel steel tubes held apart by a central drive box and spacers. The swinging platform is suspended on pivots from the ends of the load carrying beams and is covered by an aerodynamic shroud to reduce drag. When the centrifuge is at rest, the swinging platform is horizontal, allowing test packages to be placed on the platform in an upright position. As the centrifuge is accelerated, the platform swings outward. The platform and the payload are balanced by a counterweight massing 20,200 kg. The position of the counterweight is adjusted by driving a series of gear wheels along screw threads on the outside of the parallel steel tubes using an electric motor.
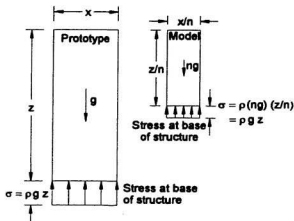
Figure 4.1. Stress comparison at similar points in prototype and centrifuge model

a) An injection test at low flow rates and before the development of discontinuities may be represented as a pumping test in a partially penetrating well

b) Following the development of discontinuities, the injection process may be represented as a pumping test in an artesian well
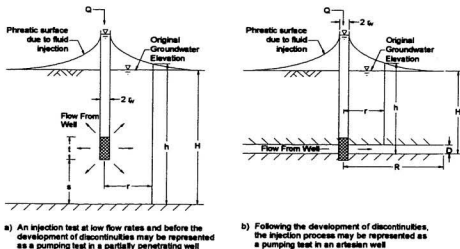
Figure 4.2. Simplified representation of injection test as a well pumping test

83

4.3   Injection Test Setup

4.3.1   Clay testbeds

Tests CCFS01 and CCFS02 were carried out in testbeds constructed using fine Speswhite kaolin clay processed by English China Clays, Lovering Pochrin & Co. Ltd. of Cornwall, England. The clay was purchased through the US distributor, Hamill & Gilepsie. Speswhite kaolin is a high quality clay of uniform properties which has been used extensively by C-CORE and at other centrifuge facilities. Properties of Speswhite kaolin are documented by numerous researchers including Al-Tabbaa (1987), Rossato et al (1992), Lin (1995), and others. Typical geotechnical properties of Speswhite kaolin clay are summarised in Table 4.2.

For the soil shearing tests, it was desirable to construct a soil model with K>1 and with a pronounced peak strength followed by post peak strain softening. Heavily overconsolidated clay soils often have these characteristics (see for example Brooker and Ireland, 1965; Ladd, 1971). The principle effective stress ratio, K, for overconsolidated Speswhite kaolin may be determined using Eqns 4.7 and 4.8 (Wroth, 1975).

For OCR>5,
$$m\left[\frac{3(1-K_{nc})}{(1+2K_{nc})} - \frac{3(1-K)}{(1+2K)}\right] = \ln\left[\frac{OCR(1+2K_{nc})}{1+2K}\right] \qquad \text{[Eqn. 4.7]}$$

and for OCR<5,
$$K = OCR \cdot K_{nc} - \frac{v'}{1-v'} \cdot (OCR - 1) \qquad \text{[Eqn. 4.8]}$$

The parameter m is an experimentally derived index property for a soil (m=1.81 for Speswhite kaolin), K_{nc} is the normally consolidated value of K (0.64 for Speswhite kaolin), and v' is the effective Poisson's ratio (v'=0.325).

Table 4.2. Typical geotechnical properties of Speswhite kaolin

Parameter		Value[a]	Reported by
Specific Gravity,	G_s	2.61 2.64	Poorooshasb, 1991 Phillips, 1989
Atterberg Limits,	w_l w_p I_p	69% 38% 31%	Poorooshasb, 1991
Saturated density,	ρ_{sat}	1700 kg/m³ at w=50%	
Angle of friction,	ϕ'	23°	
Plastic slope in V-p' space,	λ	0.26	
Elastic slope in V-p' space,	κ	0.05	
Slope of critical state line in q-p' space,	M	1.02	
V on critical state line, V on 1-dimensional consolidation line, V on isotropic consolidation line,	V_{cs} V_{1-D} V_{iso}	3.44 at p'=1 kPa 3.58 at p'=1 kPa 3.77 at p'=1 kPa	

Coefficient of consolidation
    for normal consolidation,
    for swelling,
	c_v
	c_s
		0.5 mm²/s
		1.0 mm²/s	

Clay fraction (<2 μm)		81-82 %	Phillips, 1989 Rossato et al, 1992

Coefficient of permeability
    kaolin consolidated at 100 kPa,
    k as a function of voids ratio
	k_v
	k_v
	k_h
		1.5 x 10⁻⁹ m/s
		$k_v = 0.5e^{3.29}$ x 10⁻⁹ m/s
		$k_h = 1.43e^{3.29}$ x 10⁻⁹ m/s
			Paulin et al, 1993
			Al-Tabbaa, 1987
			Al-Tabbaa, 1987

Note: [a] See also the results of geotechnical testing provided in Appendix 2.

The mechanical capacity of the frame used to consolidate the large 904 mm diameter

85

centrifuge models was approximately 750 kPa. Consolidating the clay to $\sigma'_v = 750$ kPa and then testing in the centrifuge at 50 g resulted in a design OCR and K distribution with depth similar to that shown in Figure 4.3.

4.3.1.1 Testbed preparation

The design thickness of the consolidated clay testbeds was 375 mm. Each clay cake was cylindrical in shape and was formed in a 904 mm diameter by 500 mm deep circular strongbox. A steel plate was placed at the bottom of the strongbox to allow extrusion of the clay from the strongbox following the tests. An 85 mm thick layer of coarse sand was placed below the kaolin as a base drain during the consolidation process. The sand was covered with a filter cloth and saturated with water prior to placing the kaolin in the strongbox.

The kaolin clay was placed in the strongbox as a slurry which was mixed at approximately 120% water content using de-ionized water. The mixing time was about 4 hours for CCP501 and about 14 hours for CCP502. Because the initial height of the clay slurry exceeded the height of the 500 mm high strongbox, a 415 mm high cylindrical extension was bolted to the top of the strongbox during placement and consolidation of the slurry. The inside walls of the strongbox and the strongbox extension were coated with a film of grease to reduce sidewall friction during consolidation.

4.3.1.2 Clay consolidation

After placement of the slurry in the strongbox, the upper surface of the clay was levelled and covered with filter fabric followed by a 50 mm thick layer of coarse drainage sand. The consolidometer piston was placed over the clay and the slurry was allowed to consolidate under the self-weight of the sand and piston (<5 kPa) for approximately 48 hours with drainage allowed from the top and bottom of the clay.

The strongbox was then moved into a large consolidation frame where an initial vertical pressure of 25 kPa was applied to the slurry using a hydraulic ram. The clay was allowed to consolidate under the applied pressure with free drainage from the top and bottom of the clay. A small back pressure of approximately 5 kPa was maintained at the bottom drain on the strongbox to ensure that the base of the soil remained saturated. Vertical displacement of the piston was monitored over time. After 90% consolidation was achieved at 25 kPa, the vertical stress was increased to 50, 100, 200, 400, and 750 kPa, allowing time for approximately 90% consolidation to be achieved at each stress increment prior to increasing the stress to the next level.

After achieving approximately 90% consolidation at 750 kPa, the stress was stepped down to 400, 200 and 100 kPa, allowing sufficient time at each stress level for approximately 90% of the swelling to be completed. Consolidation curves for the Speswhite kaolin are included in Appendix 2. After swelling to a vertical stress of 100 kPa, the drainage valve at the base

of the strongbox was closed and the vertical load was removed from the clay.

After consolidation, the strongbox was removed from the consolidometer, and the piston, upper sand layer and filter fabric were removed from the surface of the clay. The surface of the clay was trimmed level using a blade resting on horizontal guides placed across the top of the strongbox. The final trimmed surface of the soil for both clay tests was 55 mm below the top flange of the strongbox. A thin coating of grease was applied to the trimmed surface of the clay to reduce water loss due to evaporation.

4.3.2 Silty sand testbed

Tests CCFS03 and CCFS04 were carried out in testbeds constructed using a 70% sand and 30% silt mixture. The sand used was Type 00 silica sand obtained from Shaw Resources of Shubenacadie, Nova Scotia. The silt used was Sil-Co-Sil Silt obtained from US Silica Company, Berkeley Springs, West Virginia. Both the sand and the silt were obtained from the suppliers in 40 kg bags. The soil for the model was prepared in small 10 kg batches by combining 7 kg of dry sand with 3 kg of dry silt in a container and mixing to a homogeneous state using an electric mixer. The small batches were then mixed together in a large bin to form the material source for the testbeds. Geotechnical properties of the silty sand mixture are summarised in Table 4.3.

Table 4.3. Geotechnical properties of silty sand mixture

Parameter	Value		Reported by
Specific Gravity, G_s	Su-Co-Sil Silt	2.67	Parsons, 1995; Lin, 1995
	Type 00 Sand	1.61	
Particle Size:			See Appendix 2.
D_{10}		0.01 mm	
D_{30}		0.10 mm	
D_{50}		0.18 mm	
D_{60}		0.23 mm	
D_{90}		0.40 mm	
Coefficient of uniformity, C_u		23	
Coefficient of curvature, C_c		4.3	
Mohr-Coulomb parameters, c'		0 kPa	
ϕ'		48.2°	
ϕ'_{cv}		41.8°	
Permeability (triaxial)			
k_1	$\rho_d=1920$ kg/m³ and $\sigma'_c=-100$ kPa,	3.8 × 10⁻⁷ m/s	
k_2	$\rho_d=1894$ kg/m³ and $\sigma'_c=-125$ kPa,	1.4 × 10⁻⁷ m/s	

The design thickness of the silty sand testbeds was 300 mm. The testbeds were constructed in a 904 mm diameter by 500 mm deep circular strongbox. A 160 mm thick layer of coarse drainage sand was compacted in place at the base of the strongbox using a hand tamper. The purpose of the coarse sand layer was to allow improved water flow to the base of the silty sand during the saturation process. The drain sand was covered with a filter fabric prior to placing the silty sand in the strongbox.

The silty sand was placed and compacted in 25 mm thick horizontal lifts to a target dry density of 1950 kg/m³. The design location of the top of each compacted lift of soil was marked on the inside perimeter of the strongbox. The sand required for each 25 mm lift was pre-weighed, and evenly spread out within the strongbox. The soil was then compacted

uniformly over the surface of the strongbox using a hand tamper until the surface of the sand was level and corresponded with the appropriate markings on the inside of the strongbox. The as-constructed dry density was 1964 kg/m³ for CCFS03 and 1932 kg/m³ for CCFS04.

Following construction of the testbed, the silty sand was saturated from the bottom up while the sample was maintained under a vacuum of between -40 to -50 kPa using a configuration similar to that shown in Figure 4.4. In order to shorten the time required to saturate the sample, a surcharge of approximately 12 kPa was applied to the top of the soil and a hydraulic gradient of approximately 4.33 m/m was applied across the sample. Under these conditions, it took approximately 5 days for one pore volume of water to be added to the soil.

4.3.3   Installation of injection wells and pore pressure transducers

Four injection wells and as many as eight miniature Druck pore pressure transducers (PPTs) were installed in each of the testbeds. Although the locations of PPTs varied between tests, all testbeds used the same injection well configuration. A typical test layout showing injection well and buried PPT locations for CCFS01 is shown in Figure 4.5a. A photograph showing well locations during preparation of test CCFS04 is provided in Figure 4.5b.

4.3.3.1 Clay testbeds

The injection wells and PPTs were installed in the clay testbeds after the consolidation process was completed and the strongbox was removed from the consolidometer. The procedure used for installing the wells in the clay testbeds involved drilling a vertical hole at the desired location to a depth equal to the buried length of the well. The wells were then pushed into the pre-drilled holes to the desired depth. A tight fit was ensured along the soil/well interface by using a drill bit of the same diameter as the well and by filling the wells with water after to promote swelling of the clay against the injection wells.

The procedure for installing the PPTs in the clay soil involved drilling small diameter vertical holes at the desired locations and to depths equal to the design tip elevations for the PPTs. The PPTs were then placed in the pre-drilled holes, making sure that the tip of the transducer was at the bottom of the hole. The holes were then backfilled by placing small beads of a moist kaolin-bentonite clay mixture in the hole and firmly tamping them to the bottom of the hole using a thin rod. A summary of PPT locations is provided in Table 4.4.

4.3.3.2 Silty sand testbeds

The injection wells and PPTs were installed in the silty sand testbeds during placement and compaction of sand in the strongbox. During installation of the sand, the injection wells were

rigidly clamped to a cross-member that was fastened across the top of the strongbox. The
sand was then compacted around the well using the hand tamper. Care was taken not to bump
the well during compaction and to use approximately the same compactive effort around the
wells as was used elsewhere in the strongbox.

Table 4.4. Summary of pore pressure transducer locations

PPT	Radial distance from well mm (m)*	Depth below ground surface mm (m)*	PPT	Radial distance from well mm (m)*	Depth below ground surface mm (m)*
CCFS01			CCFS03		
A1	100 (5.0)	-85 (-4.3)	I1	25 (1.3)	-200 (-10.0)
A2	50 (2.5)	-165 (-8.3)	I2	50 (2.5)	-175 (-8.8)
B1	100 (5.0)	-145 (-7.3)	J1	25 (1.3)	-200 (-10.0)
B2	100 (5.0)	-250 (-12.5)	J2	50 (2.5)	-175 (-8.8)
C1	100 (5.0)	-45 (-2.3)	K1	25 (1.3)	-100 (-5.0)
C2	75 (3.8)	-110 (-5.5)	K2	50 (2.5)	-75 (-3.8)
D1	100 (5.0)	-100 (-5.0)	L1	25 (1.3)	-100 (-5.0)
Welltop	--	+110 (+5.5)	L2	50 (2.5)	-75 (-3.8)
Wellside	--	+55 (+2.8)	Welltop	--	+110 (+5.5)
			Wellside	--	+55 (+2.8)
CCFS02			CCFS04		
E1	25 (1.3)	-200 (-10.0)	M1	25 (0.6)	-200 (-5.0)
E2	50 (2.5)	-200 (-10.0)	M2	25 (1.3)	-150 (-3.8)
F1	25 (1.3)	-200 (-10.0)	N1	25 (0.6)	-200 (-5.0)
F2	50 (2.5)	-200 (-10.0)	N2	25 (1.3)	-150 (-3.8)
G1	25 (1.3)	-100 (-5.0)	O1	25 (1.3)	-100 (-5.0)
G2	50 (2.5)	-100 (-5.0)	O2	50 (2.5)	-50 (-2.5)
H1	25 (1.3)	-100 (-5.0)	P1	25 (1.3)	-100 (-5.0)
H2	50 (2.5)	-100 (-5.0)	P2	50 (2.5)	-50 (-2.5)
Welltop	--	+110 (+5.5)	MN Well	--	+55 (+1.4)
Wellside	--	+55 (+2.8)	OP Well	--	+55 (+2.8)

Note: * Prototype dimension shown in parenthesis.

The PPTs were placed in the sand at the appropriate locations and depths during construction
of the testbeds. The cables for the PPTs were routed directly towards the nearest wall of the

strongbox and were brought up along the wall of the strongbox to the final ground surface elevation. Care was taken during compaction of the soil located directly above the transducers to avoid damaging the PPTs due to impact. A summary of PPT locations is provided in Table 4.4.

4.4   Instrumentation and Mechanical Assembly

4.4.1   Injection wells

Four injection wells were constructed for use in the centrifuge experiments. Dimensions of the injection wells are shown in Figure 4.6. Two wells were sized such that there would be a distance of 200 mm between the ground surface and the top of the perforated section of the well. The remaining two wells were sized to allow 100 mm between the ground surface and the top of the well perforations. The upper riser pipe section of the injection wells was fabricated using steel tubing with outside diameter of 9.5 mm and an inside diameter of 6.2 mm. The upper end of the riser pipe was threaded to allow the attachment of a brass fitting and injection fluid supply tubing. The inside of the lower end of the riser pipe was drilled out to allow a tight fit between the riser pipe and the perforated section of tubing.

The perforated sections of the wells were each 25 mm in length and were constructed from 6.4 mm outside diameter stainless steel tubing. The perforations consisted of fourteen 2.4 mm

diameter holes drilled in four vertical rows around the perimeter of the tubing. A 9.5 mm outside diameter plug was machined to fit over the lower end of the perforated tubing. The riser pipe and the plug were fixed to the perforated tubing using an epoxy adhesive. A geotextile fabric was wrapped and sewn in place around the perforated section of the injection wells to prevent entry of soil into the well through the perforations.

4.4.2 Injection pump

The pump utilized for the injection tests was a "syringe" style pump utilizing a piston, a cylinder (fluid reservoir), and a vertical actuator as shown in Figure 4.7. The vertical actuator used to operate the pump was powered by a Compumotor Digiplan S83-93 stepper motor. This type of motor provides accurate displacement rates and can be configured to move to either displacement or load controlled limits. The vertical drive unit was remotely controlled from a personal computer located in the centrifuge control room. The cylinder was bolted to the fixed base plate of the vertical actuator. Operation of the stepper motor for the vertical drive allowed the piston to be moved into the cylinder, thereby displacing the injection fluid out of the cylinder through a port at its base. The cylinder used for CCFS01 had a bore of 19.05 mm and an effective piston stroke length of approximately 115 mm. The stroke length was increased to 165 mm for tests CCFS02, CCFS03 and CCFS04. The injection pump and vertical drive unit were held in position above the injection wells using a horizontal frame that spanned the top of the strongbox containing the soil model (see Figures 4.8 and 4.9). A

solenoid valve was placed in-line between the pump and the injection well (see Figure 4.7).

4.4.3 Measurement of surface displacement

Vertical displacement of the ground surface was monitored using six linear variable displacement transducers (LVDTs) located near the injection well. The transducers were clamped to a bracket that was supported by the horizontal frame located on the top of the strongbox (Figures 4.8 and 4.9). The positions of the six LVDTs relative to the monitoring well are summarised in Table 4.5.

Table 4.5. Monitoring locations for ground surface displacements

LVDT	Serial Number of LVDT				Location	
	CCFS01 A,B,C,D	CCFS02 E,F,G,H	CCFS03 I,J,K,L	CCFS04[a] M	Angle[b] (deg)	Radial distance from well mm (m)[c]
1	61595	3314	3315	3315	270	26.0 (1.3)
2	61593	61595	61595	61595	327	47.7 (2.4)
3	3316	61593	61593	61593	342	84.1 (4.2)
4	3315	3313	3316	3316	68	53.9 (2.7)
5	3313	3316	3313	3313	135	70.7 (3.5)
6	3314	3315	3314	3314	29	103.0 (5.2)

Note: [a] Ground surface displacements were not measured for tests CCFS04 N, O and P.
  [b] Angle is measured positive in a clockwise direction, with 0° in the direction of the center of the strongbox from the monitoring well.
  [c] Prototype dimension shown in parenthesis. Prototype dimension for well M is 1/2 of that shown.

4.4.4 Measurement of injection and pore pressure

The injection pressure was monitored at the wellhead using miniature Druck pore pressure transducers (PPTs). The wellhead/PPT configuration used for tests CCFS01, CCFS02 and CCFS03 is shown in Figure 4.7. For these tests, the centrifuge was stopped after injection was completed at each well, and the wellhead was repositioned on the next well prior to restarting the centrifuge. Pressure transducers "Welltop" and "Wellside" were located 110 mm and 55 mm, respectively, above the surface of the soil.

Test CCFS04 was set up to allow the four injection tests to be carried out without stopping the centrifuge. Individual solenoid valves were used to isolate the wells from each other. A PPT was located on the well side of each solenoid, 55 mm above the ground surface. These PPTs were used to monitor the injection pressure at the four well locations.

As many as eight miniature Druck PPTs were buried in the soil and used to monitor changes in pore pressure during the centrifuge experiments. The procedure used to bury the PPTs in the soil was described in Section 4.3.3. The locations of the buried PPTs are summarized in Table 4.4.
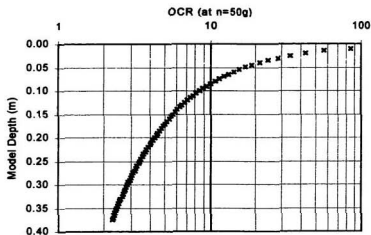
a) Design OCR with depth in centrifuge at 50g
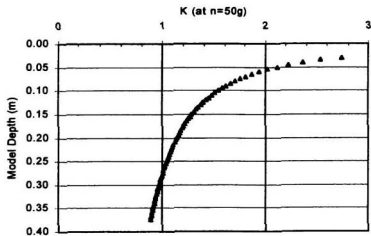
b) Design K₀ with depth in centrifuge at 50g

Figure 4.3. Variation in design OCR and K with depth
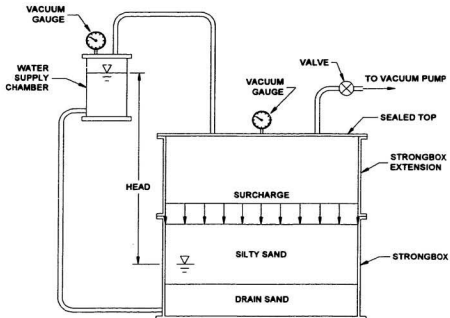
Figure 4.4. Saturation of silty sand testbed under a vacuum
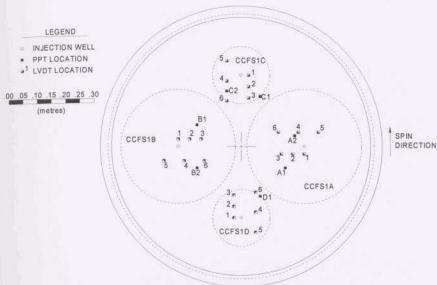
a) Schematic of well and instrumentation locations for CCFS01

b) Photo showing well locations during preparation of CCFS04

Figure 4.5. Typical location of injection wells and instrumentation
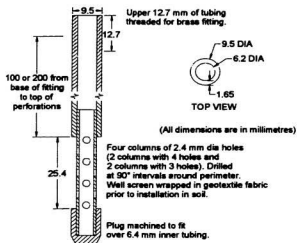
Figure 4.6. Injection well details
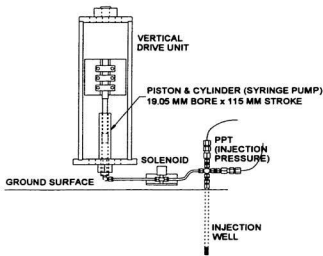
Figure 4.7. Injection pump and wellhead details
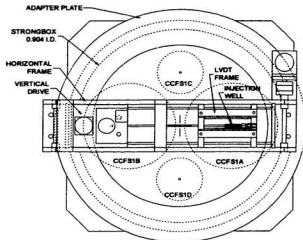
Figure 4.8. Centrifuge test assembly – Plan
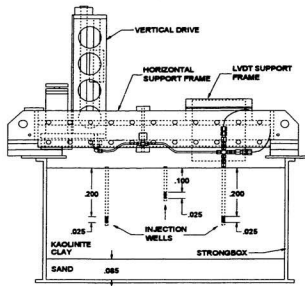
Figure 4.9. Centrifuge test assembly – Section

101

4.5   Injection Test Procedure And Post-test Laboratory Testing

4.5.1   Installation of test package on centrifuge

The test package was partially assembled on the floor of the main centrifuge laboratory (see Figures 4.10 and 4.11); and was transported to the centrifuge and placed on the platform (see Figure 4.12) using a forklift.

The operation of the instrumentation (PPTs, LVDTs, solenoids, and vertical potentiometer or string potentiometer) was checked prior to spin-up. Instrumentation details, including serial numbers, calibration constants, gains and excitation voltages, are provided in Appendix 1. Two on-board video cameras were positioned to allow real time viewing of the ground surface near the injection wells and the injection pump during flight. The operation of the vertical drive was checked and calibrated prior to spin-up to ensure that the desired piston velocity and displacements would be achieved. The vertical (or string) potentiometer was calibrated to provide a digital record of drive position with time.

The injection fluid consisted of a mixture of Methylene-blue powder and water at a concentration of 10 g of methylene-blue powder per litre of water. Prior to spin-up, the pump cylinder, the interior of the test well, and the tubing connecting the well to the injection pump were filled with injection fluid. Care was taken to minimize the amount of air remaining in the well and tubing.

4.5.2 Centrifuge spin-up and hold

Power was supplied to the instrumentation well before spin-up in order to allow time for the transducers to warm up and for the instrument readings to stabilize. Data acquisition was started just prior to spin-up. A sampling rate of 5 Hz was used during the injection tests.

After all pre-flight checks were completed, the centrifuge was spun-up to the test acceleration. Tests CCFS01, CCFS02 and CCFS03 were carried out at an acceleration of 50g at a depth of 150 mm below the ground surface of the model. In test CCFS04, wells M and N were tested at 25g at a depth of 200 mm below the ground surface, and wells O and P were tested at 50g at a depth of 100 mm below the ground surface. After reaching the test acceleration, the centrifuge was held at a constant speed while the instrument readings stabilized.

4.5.3 Injection test

During each injection test, the injection pressure was monitored at the wellhead, and pore pressure was monitored at two locations within the soil near the well. Ground surface displacements were monitored at six LVDT locations surrounding the injection well.

The solenoid located between the injection pump and the wellhead was opened prior to

beginning an injection test. Due to the mechanical configuration of the test setup, fluid pressure would sometimes build up within the tubing between the injection pump and the solenoid. When the solenoid was opened prior to the start of injection, this pressure would be applied instantaneously to the soil surrounding the well at the point of injection.

The injection tests in the clay were carried out by lowering the piston in a series of 5, 10 and 50 mm increments with wait periods of 5 minutes between each injection increment. The injection tests in the silty sand were carried out by lowering the piston in one continuous stroke. All injection tests were carried out at piston velocities varying between 0.05 mm/s and 10 mm/s, which is equivalent to injection rates of 14.3 mm³/s to 2850 mm³/s respectively. When the injection stage was completed, the solenoid valve between the pump and the wellhead was closed and the centrifuge speed was maintained for an additional 15 minutes to record the post-injection pore pressure and deformational response. Details of the injection process are summarized in Table 4.6.

Table 4.6. Injection test details

Test ID		Model Scale (1:N)	Well Depth (mm)	Pressure Response at Wellhead Due to Solenoid Activation[a] (kPa)	Test Time (sec)		Pumping Details				
					Open Solenoid	Start Pump	Total Piston Stroke (mm)	Piston Velocity (mm/s)	Injection Time[b] (s)	Injection Volume (litres)	Injection Rate (mm³/s)
CCFS01	A	50	200	from 9.0 to 26.2	74	103	115	0.10	1150	0.0328	28.5
	B	50	200	no change (25.8)	0	200	115	1.00	115	0.0328	285
	C	50	100	from 15.5 to 35.6	127ᵇ	114	115	1.00	115	0.0328	285
	D	50	100	from 14.8 to 25.3	107	124	115	1.00	115	0.0328	285
CCFS02	E	50	200	from -2.4 to 82.0	142	152	165	10.0	16.5	0.0470	2850
	F	50	200	from 26.4 to 66.9	525	552	165	0.05	3300	0.0470	14.3
	G	50	100	from -10.0 to 126.9	1574ᵃ	344	115	0.05	2300	0.0328	14.3
	H	50	100	from 6.8 to 75.7	501	514	115	0.05	2300	0.0328	14.3
CCFS03	I	50	200	from -2.2 to 34.6	285	300	160	0.10	1600	0.0456	28.5
	J	50	200	from 4.8 to 53.0	296	301	160	1.00	160	0.0456	285
	K	50	100	from -6.5 to 43.8	284	300	110	0.10	1100	0.0314	28.5
	L	50	100	from 1.5 to 51.7	244	259	110	1.00	110	0.0314	285
CCFS04	M	25	200	from -3.0 to 5.0	80	106	78	0.20	390	0.0223	57.0
	N	25	200	from 12.3 to 14.9	37	57	174	1.00	174	0.0497	285
	O	25	100	from 13.3 to 81.6	150	162	5.9	0.10	62	0.0017	28.5
	P	25	100	from -10.0 to 122.6	46	54	6.4	8.00	0.8	0.0018	2280

Note: a Pressure change was measured at the wellhead at an elevation 55 mm above the ground surface.
b Solenoid was activated after the injection pump was operating.
c Does not include wait time between injection stages.

105

4.5.4   Centrifuge spin-down and rotation of test assembly

Following the completion of each injection test for CCFS01, CCFS02, and CCFS03, the centrifuge was brought to a stop, the test assembly was disconnected from the well and the strongbox, and the assembly was rotated to the next test location. The assembly was then bolted back onto the strongbox. Any injection fluid remaining in the previous test well was removed using a vacuum line and the well was capped. The wellhead was then repositioned at the new test location and prepared in the same manner as was described in Section 4.5.1 - Installation of test package on centrifuge.

The centrifuge was stopped after completion of injection Test CCFS04 M and the gains on the PPTs were adjusted. The centrifuge was then restarted and tests N, O and P were carried out without stopping the centrifuge. Solenoid valves located near each wellhead were used to switch the injection pump from one test well to the next in flight. Following each injection test, the cylinder on the injection pump was refilled in flight by raising the piston while allowing flow into the cylinder from a reservoir bolted to the top of the strongbox wall.

Following completion of the four injection tests, the test package was removed from the centrifuge and transported to the centrifuge laboratory for disassembly.

4.5.5 Post-test sampling and laboratory testing

4.5.5.1 Clay tests

Laboratory testing was carried out to determine moisture content, density and undrained strength profiles in the testbed soil, and strength and deformation parameters from consolidated drained triaxial tests. The sampling for most tests was carried out immediately after the mechanical systems were removed from the top of the strongbox following the injection tests. Some supplementary strength tests were carried out during excavation and mapping of the clay using a torvane, a pocket penetrometer, and UU triaxial tests. The results of the laboratory testing are presented in Appendix 2 - Soil Test Results.

4.5.5.2 Silty sand tests

Laboratory testing was carried out to determine the grain size distribution of the soil, the permeability, and the strength and deformation parameters. The permeability and strength testing was carried out in a triaxial cell using samples that were constructed in the laboratory to densities similar to that used in the centrifuge experiments. The results of the laboratory testing are presented in Appendix 2 - Soil Test Results.

4.5.6 Excavation and mapping of dye traces

4.5.6.1 Clay testbeds

After the completion of the injection tests, the clay cake was extruded from the stongbox using lifting straps fastened to hooks threaded into the extrusion plate at the base of the clay (Figure 4.13). The soil surrounding the four injection wells was then excavated and the locations recorded where traces of methylene blue dye were observed in the clay.

The procedure used for excavating and mapping the dye traces evolved as experience was gained with the excavation process. Typically, the excavation and mapping process involved first cutting and removing "pie" shaped slices of soil from around the injection well. Each well was cut into 36 slices, each spanning a 10° arc around the well. The locations where dye was observed on the sides of the slices were recorded using a local polar coordinate system (angle, radius, depth) with the origin defined at the centre of each well. The orientations of the clay slices for CCFS01 are shown in Figure 4.14. The orientation of slices for CCFS02 was similar to CCFS01 except all wells were oriented with 0° at the centre of the strongbox.

The locations of the dye traces for well B and for a portion of well D (80° to 320°) were determined by physically measuring and recording the angle, radius and depth of points along the dye trace on each slice. This process was very time consuming. For the region of well D between 330° to 80° and for wells A, C, E, F, G, and H, the locations of dye traces on the soil

slices were traced onto overhead transparency film and later digitized to a computer file.

4.5.6.2 Silty sand testbeds

After the testbed was removed from the centrifuge, the base drain was opened on the strongbox and the pore water was allowed to drain from the sample. The four wells were removed from the testbed and the resulting cavities were filled with dry sand. The surface of the testbed was excavated in 5 mm thick horizontal slices using a steel scraper blade fixed to *an adjustable mount that could slide on tracks placed across the rim of the strongbox.* Following the removal of each 5 mm thick sand layer, the dye traces around each well were photographed, traced onto transparency film, and later digitized to a computer file.
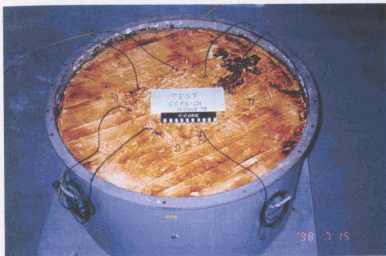
Figure 4.10. Greased surface of clay following installation of wells and PPTs
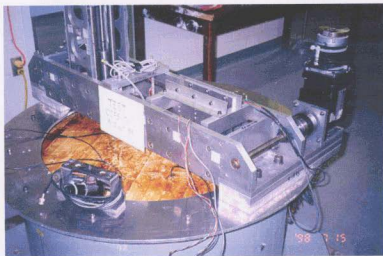
Figure 4.11. Test assembly prior to placement on centrifuge
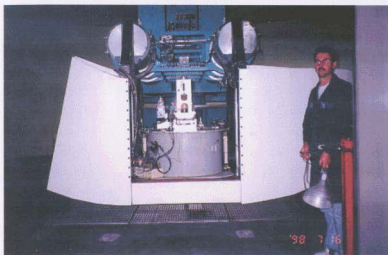
Figure 4.12. Test assembly following placement on centrifuge arm

Figure 4.13. Extrusion of clay from strongbox
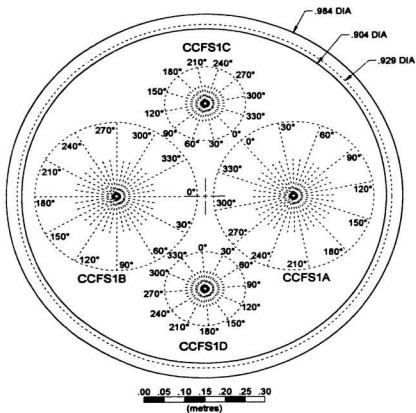
Figure 4.14. Typical location and orientation of excavated clay sections

4.6   Injection Test Results

Records of piston displacement, injection volume, pressure response and ground surface displacement for tests CCFS01, CCFS02, CCFS03 and CCFS04 are provided in Appendix 3 - Injection Test Results. An overview of the results from these tests is provided in the following sections.

4.6.1   Injection pressure

Injection pressure is plotted against time in Figure 4.15 for CCFS01 tests A, B, C and D; in Figure 4.16 for CCFS02 tests E, F, G and H; in Figure 4.17 for CCFS03 tests I, J, K and L; and in Figure 4.18 for CCFS04 tests M, N, O and P. Injection pressure is plotted against injection volume in Figure 4.19 for CCFS01 tests, Figure 4.20 for CCFS02 tests, in Figure 4.21 for CCFS03 tests; and in Figure 4.22 for CCFS04 tests. In Figures 4.15 through 4.22, the pressure shown is the injection pressure at the top of the injection interval as determined from measurements taken at the wellhead. A summary of injection pressures and pressure trends is provided in Table 4.7.

At prototype scale, the peak pressure in the clay tests varied between 292.7 and 345.9 kPa in the 10 m deep wells, and from 191.0 to 238.3 kPa in the 5 m deep wells. For the silty sand tests, the peak pressure varied between 162.2 and 179.4 kPa in the 10 m deep wells, and from

119.0 to 160.6 kPa in the 5 m deep wells. In the silty sand tests, the peak pressure response generally occurred when the solenoid was activated.

Table 4.7. Injection pressure response

Test ID		Maximum Pressure After Solenoid Opened[1] (kPa)	Peak Pressure P_p (kPa)	Injection Pressure Trend At Completion of Injection Stage
CCFS01	A	152.5	286.1	Less than peak, decreasing to steady-state at 245 kPa
	B	154.8	306.5	Less than peak, decreasing to steady-state at 245 kPa
	C[2]	111.0	191.0	Less than peak, decreasing to steady-state of 150 kPa
	D	100.7	238.3	Less than peak, decreasing to steady-state of 138 kPa
CCFS02	E[3]	208.3	345.9	Less than peak, increasing with time
	F	193.2	292.7	Less than peak, decreasing to steady-state of 263 kPa
	G[2]	75.8	203.7	Less than peak, decreasing to steady-state of 150 kPa
	H	182.2	205.9	Less than peak, decreasing to steady-state of 140 kPa
CCFS03	I[3]	162.2	162.2	Less than peak, steady-state of 129 kPa
	J[3]	179.4	179.4	Less than peak, increasing with time
	K[3]	119.0	119.0	Less than peak, steady-state at 69 kPa
	L[3]	127.0	127.0	Less than peak, increasing with time
CCFS04	M	67.6	68.7	At peak, steady-state at 68 kPa
	N	77.4	149.8	Peak not yet achieved, increasing with time
	O	119.6	119.6	Less than peak, decreasing with time
	P	160.6	160.6	Less than peak, decreasing with time

Notes: [1] In most tests, an instantaneous pressure of variable magnitude was applied to the wellhead when the solenoid was opened.
[2] Solenoid was activated after the injection pump was operating.
[3] Peak injection pressure achieved while injection pump was off.
[4] All pressures referenced to top of injection interval elevation.

4.6.2 Ground surface displacement

Ground surface displacements are plotted against time in Figures 4.23 through 4.30 for the clay test wells A through H, respectively. Very small ground surface displacements were

measured during the injection tests in the sand test wells (I through P). Ground surface displacement monitoring results from the sand tests are included in Appendix 3 - Injection Test Results. In addition, plots of ground surface displacement versus injection volume are included in Appendix 3 for all injection tests.

4.6.3 Location and extent of dye traces

Cross-sections showing the dye traces from all tests are included in Appendix 3. For the clay tests, the dye was generally found along injection induced discontinuities that originated and extended radially outwards from the injection well. A thick zone of dyed soil was sometimes observed around all or part of the well adjacent to the injection interval (see for example, Figure A3.53 in Appendix 3 which shows cross-sections 330° and 350° from test CCFS01C). In most test wells, the depth at which the discontinuities originated was near the top and/or the bottom of the 25 mm long injection interval. The discontinuities generally sloped upwards a small amount as they extended away from the well and it was common for one discontinuity to separate into two or more separate discontinuities (see for example, Figure A3.51 in Appendix 3). In wells C, E and H the dye traces extended upwards far enough to daylight at the ground surface.

Discrete discontinuities were not observed in the sand. For the sand tests, evidence of the injection fluid was generally observed as a strongly dyed region which was pear-shaped in

115

cross-section and nearly symmetrical about the injection well. The dyed region of soil was deep blue near the wellbore, becoming a lighter blue with distance from the well. It is possible that closely spaced discontinuities developed within the dyed region, however, any visual evidence of this was overpowered by the dark blue colour of the injection fluid.

Table 4.8. Extent of dye traces

Test ID		Model Scale		Prototype Scale		Shape[1]
		Max Extent From Well (mm)	Coverage Area (mm²)	Max Extent From Well (m)	Coverage Area (m²)	
CCFS01	A	123.9	10,600	6.2	26.5	E-C
	B	155.0	33,800	7.8	84.5	SE-O
	C	162.J	13,050	8.1	32.6	E-O
	D	150.5	35,100	7.5	87.8	SE-O
CCFS02	E	270.3	27,800	13.5	69.5	E-O
	F	95.8	4,200	4.8	10.5	SE-O
	G	87.4	10,500	4.4	26.2	SE-O
	H	190.6	15,900	9.5	39.8	E-O
CCFS03	I	44.7	4,593	2.2	11.5	C-C
	J	45.2	5,339	2.3	13.3	C-C
	K	39.2	3,566	2.0	8.9	C-C
	L	37.7	3,487	1.9	8.7	C-C
CCFS04	M	46.2	4,659	1.2	2.9	C-O
	N	46.0	5,771	1.2	3.6	C-C
	O	50.1	3,764	2.5	9.4	SE-C
	P	38.4	1,667	1.9	4.2	C-C

Note: [1] In plan view, the shape of the dye trace is described as follows:

C-C   Circular, centred about well
C-O   Circular, offset from centre of well
SE-C   Semi-elliptical, centred about well
SE-O   Semi-elliptical, offset from centre of well
E-C   Elliptical, centred about well
E-O   Elliptical, offset from centre of well

The lateral extent to which the blue dye was observed around the injection wells is plotted in Figures 4.31 through 4.34 for CCFS01 to CCFS04 respectively. Also shown on these figures are the locations of the injection wells, LVDT and PPT locations, and the orientation of cross-sections trimmed from the clay soil during the excavation process. The areal extent of the dye traces are summarised for all wells in Table 4.8.

Photographs of the blue dye traces within the white kaolin clay are provided in Figures 4.35 to 4.40 for CCFS01 well sections and in Figures 4.41 to 4.45 for CCFS02 well sections. Photographs of the blue dye traces within the silty sand are provided in Figures 4.46 and 4.47 for CCFS03 and in Figures 4.48 and 4.49 for CCFS04. Cross-sections are presented in Appendix 3, which show the locations of the dye traces in the soil around wells A to L. Three-dimensional representations of the dye traces, oriented to provide views of the injection well in both the 0°-180° and 90°-270° planes, are plotted in Figures 4.50 to 4.57 for CCFS01 tests, Figures 4.58 to 4.65 for CCFS02 tests, in Figures 4.66 to 4.73 for CCFS03 tests, and in Figures 4.74 to 4.81 for CCFS04 tests.
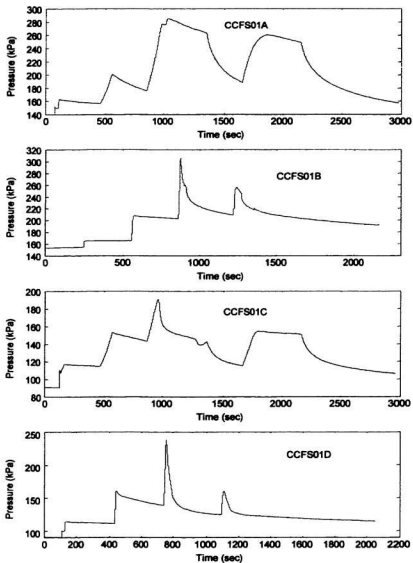
Figure 4.15. Injection pressure vs time for CCFS01 tests

118
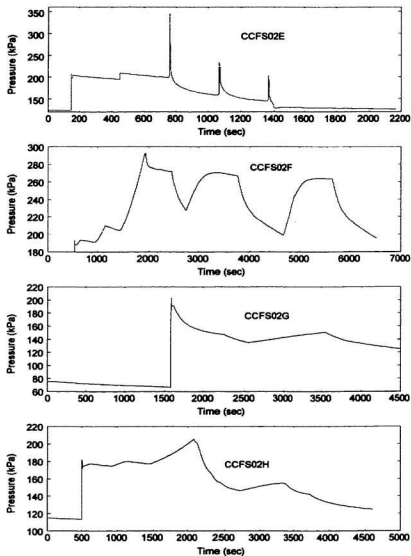
Figure 4.16. Injection pressure vs time for CCFS02 tests

119
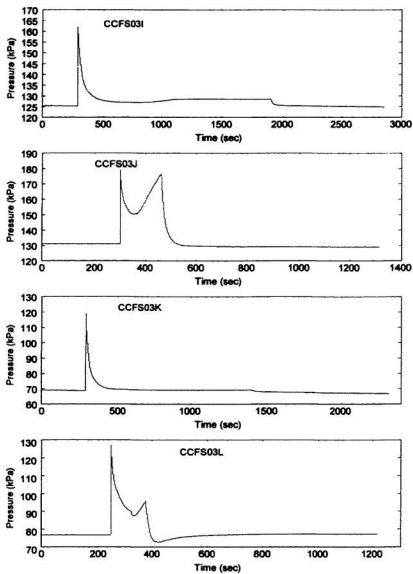
Figure 4.17. Injection pressure vs time for CCFS03 tests

120
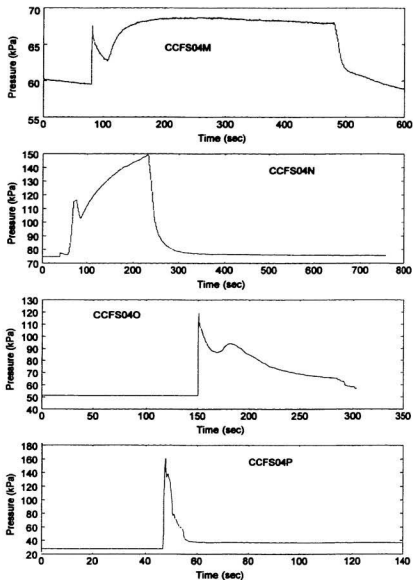
Figure 4.18. Injection pressure vs time for CCFS04 tests

121
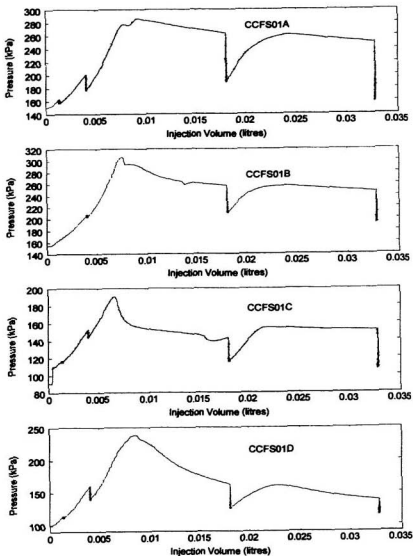
Figure 4.19. Injection pressure vs volume of fluid injected for CCFS01 tests

122
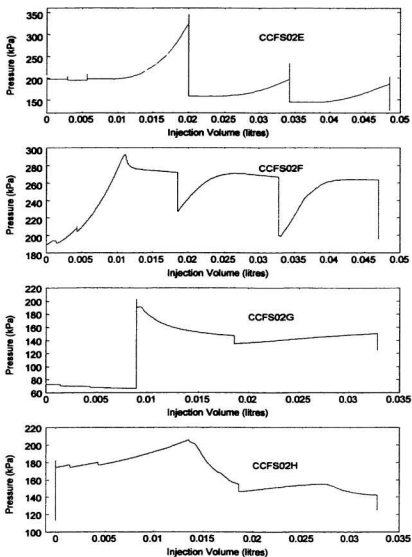
Figure 4.20. Injection pressure vs volume of fluid injected for CCFS02 tests
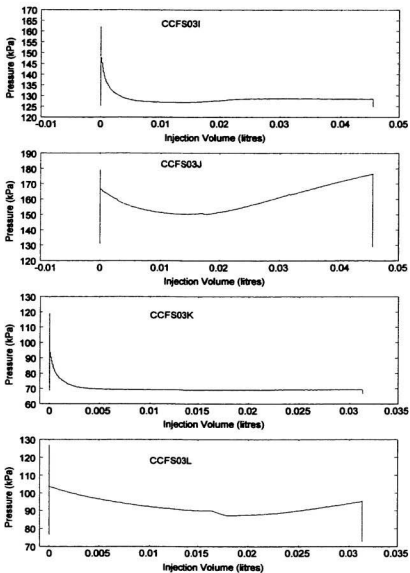
Figure 4.21. Injection pressure vs volume of fluid injected for CCFS03 tests

124
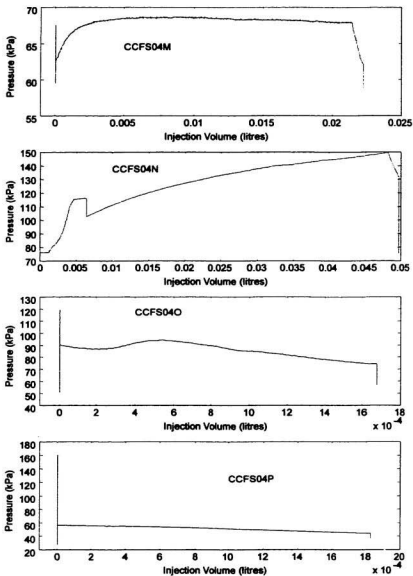
Figure 4.22. Injection pressure vs volume of fluid injected for CCFS04 tests
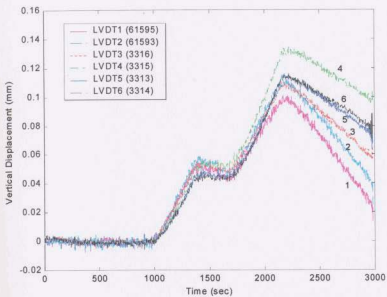
Figure 4.23. Ground surface displacement vs time for well A
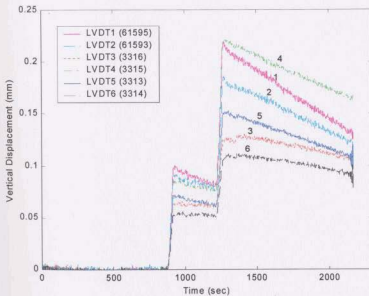
Figure 4.24. Ground surface displacement vs time for well B
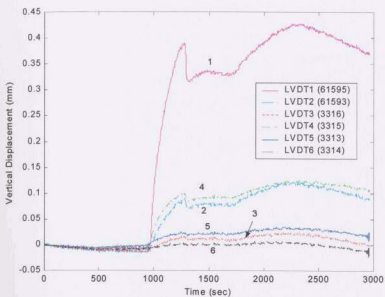
Figure 4.25. Ground surface displacement vs time for well C
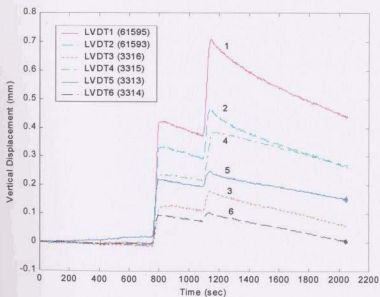
Figure 4.26. Ground surface displacement vs time for well D

127
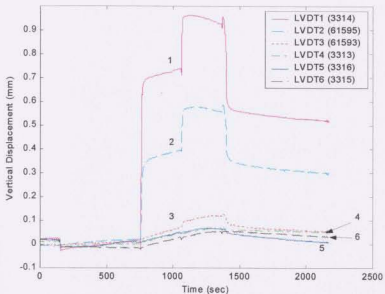
Figure 4.27. Ground surface displacement vs time for well E
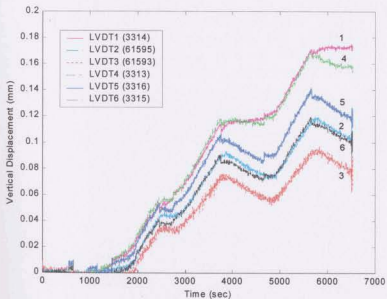
Figure 4.28. Ground surface displacement vs time for well F
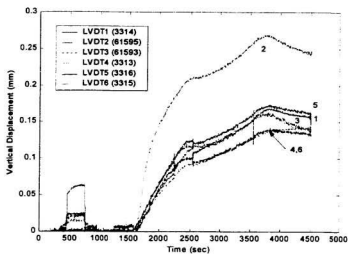
Figure 4.29. Ground surface displacement vs time for well G
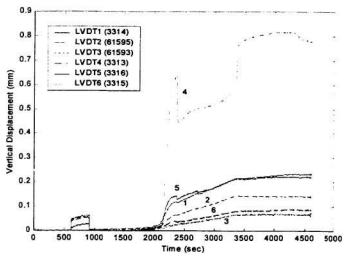
Figure 4.30. Ground surface displacement vs time for well H

129
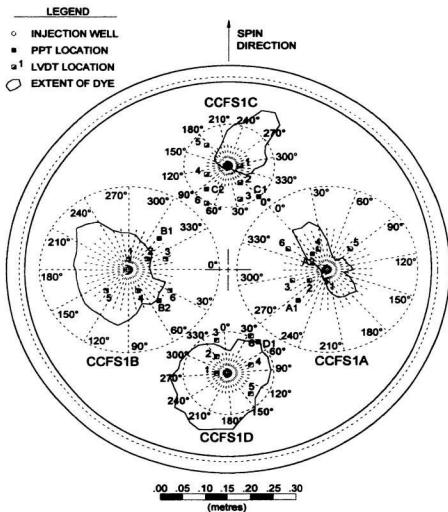
Figure 4.31. Horizontal extent of dye traces for CCFS01

LEGEND

○ INJECTION WELL
■ PPT LOCATION
◻¹ LVDT LOCATION
◯ EXTENT OF DYE

SPIN DIRECTION

CCFS2G

CCFS2E

CCFS2F

CCFS2H

.00 .05 .10 .15 .20 .25 .30
(metres)
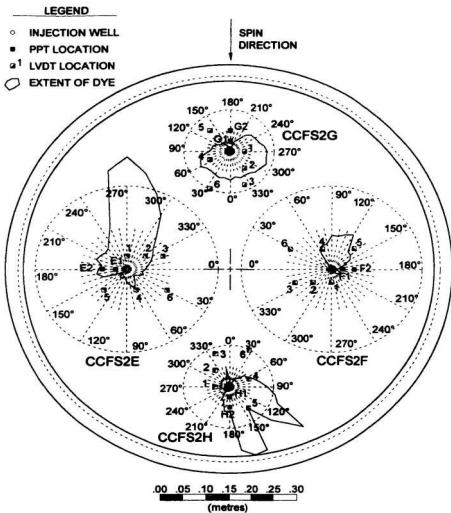
Figure 4.32. Horizontal extent of dye traces for CCFS02
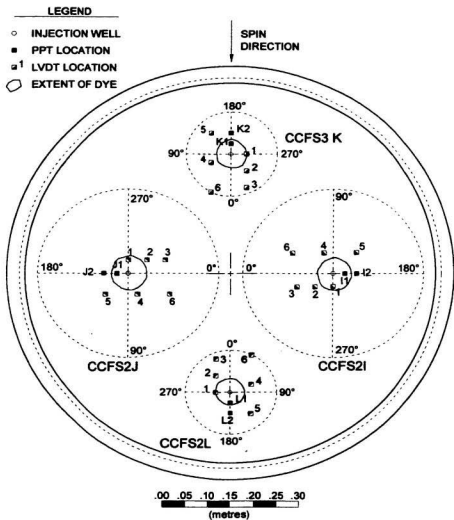
Figure 4.33. Horizontal extent of dye traces for CCFS03

132
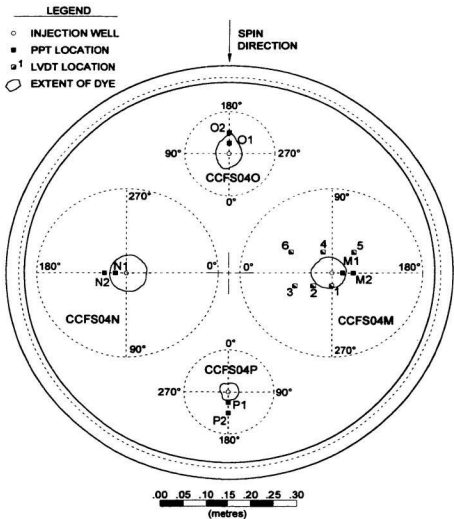
Figure 4.34. Horizontal extent of dye traces for CCFS04

133

Well A is a deep well (200 mm).
The discontinuity has initiated at
locations above and below the
injection interval.
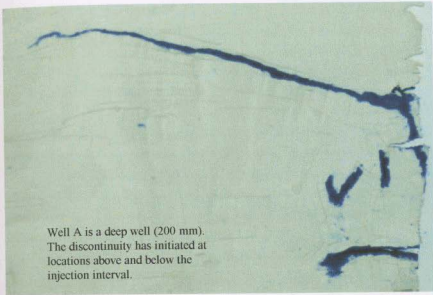
Figure 4.35. Dye trace from well A - Section 0°

Well C is a shallow well (100 mm).
Shearing appears to be dominant mechanism.
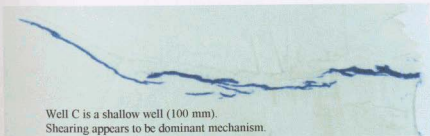
Figure 4.36. Dye trace from well C - Section 230°

Well C is a shallow well (100 mm). The dye trace is substantially thicker nearer the well.
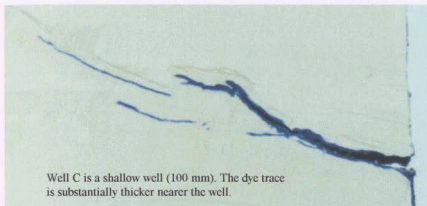
Figure 4.37. Dye trace from well C - Section 280°

Well D is a shallow well (100 mm). Note the two distinct discontinuities that have developed above and below the point of injection.
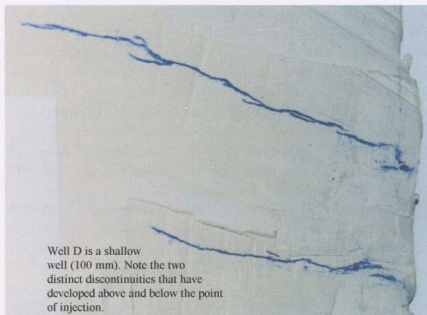
Figure 4.38. Dye trace from well D - Section 160°

Well D is a shallow well (100 mm)
Note the two nearly parallel dye traces.
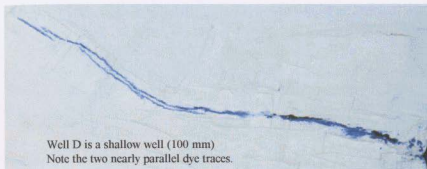
Figure 4.39. Dye trace from well D - Section 210°

Well D is a shallow well (100 mm). Note the
two nearly parallel dye traces. Also note the
heavily dyed region near the injection well
and the discontinuities beginning to form at the
top and bottom of the injection interval.
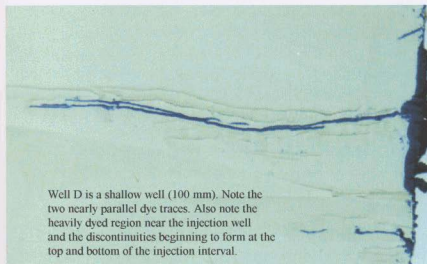
Figure 4.40. Dye trace from well D - Section 340°

Well E is a deep well (200 mm).
Note the long thin dye trace.
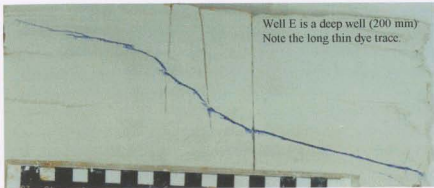
Figure 4.41. Dye trace from well E - Section 270°

Well F is a deep well (200 mm).
Note the short thick dye trace.

Figure 4.42. Dye trace from well F - Section 110°

Well G is a shallow well (100 mm)
Note the short thick dye trace.
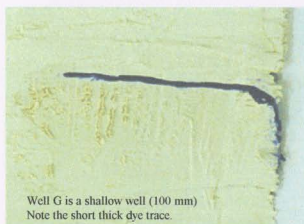
Figure 4.43. Dye trace from well G - Section 260°

Well H is a shallow well (100 mm)
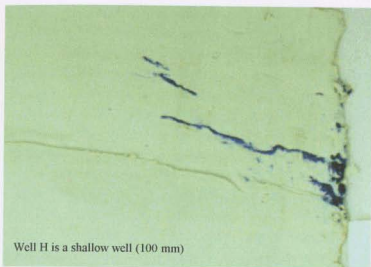
Figure 4.44. Dye trace from well H - Section 190°

Well H is a shallow well (100 mm).
Note the heavily dye region near
the point of injection.
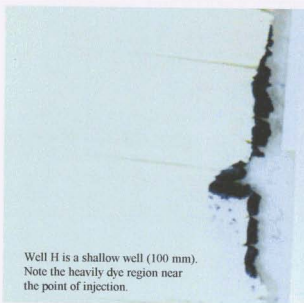
Figure 4.45. Dye trace from well H - Section 310°
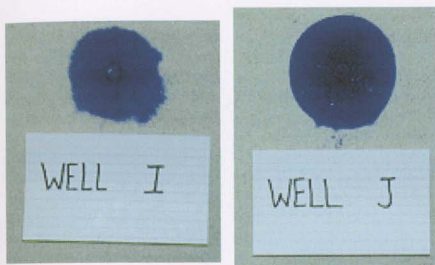
Figure 4.46. Dye traces from wells I and J at depth 200 mm
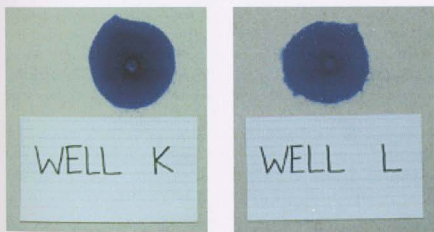
Figure 4.47. Dye traces from wells K and L at depth 100 mm
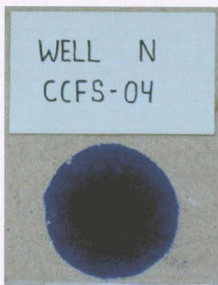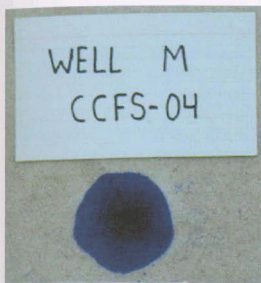
Figure 4.48. Dye trace from well M at depth 245 mm and well N at depth 205 mm
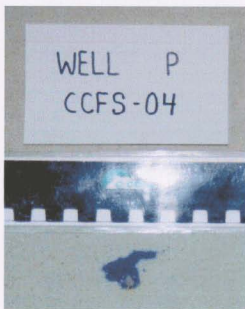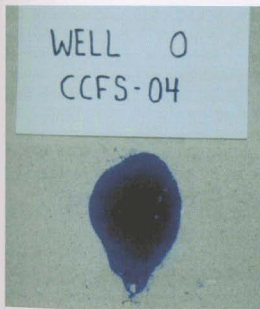
Figure 4.49. Dye trace from well O at depth 90 mm and well P at depth 35 mm

180°   0°

CCFS01
WELL A
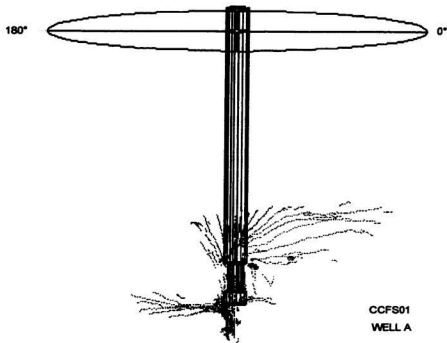
Figure 4.50. 0 to 180° view of dye traces for well A

270°   90°

CCFS01
WELL A
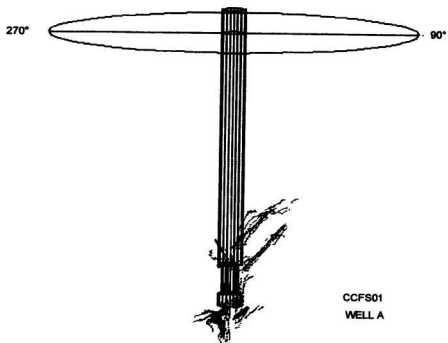
Figure 4.51. 90 to 270° view of dye traces for well A

180°   0°

CCFS01
WELL B
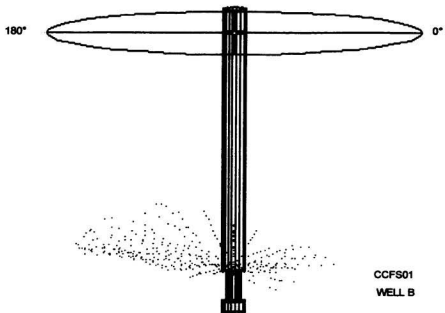
Figure 4.52. 0 to 180° view of dye traces for well B

144

270°   90°

CCFS01
WELL B
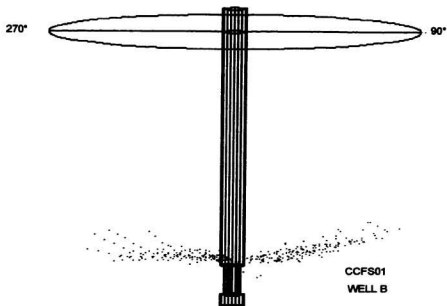
Figure 4.53. 90 to 270° view of dye traces for well B
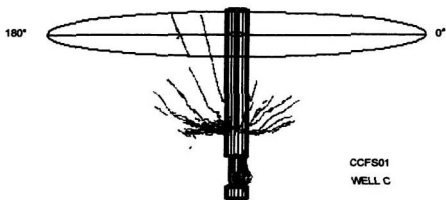
Figure 4.54. 0 to 180° view of dye traces for well C
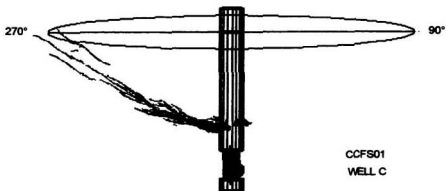
Figure 4.55. 90 to 270° view of dye traces for well C

146
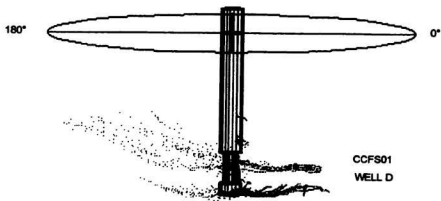
Figure 4.56. 0 to 180° view of dye traces for well D
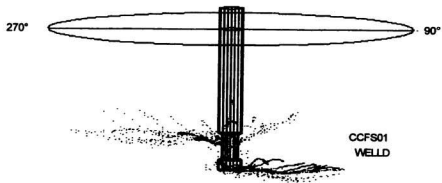
Figure 4.57. 90 to 270° view of dye traces for well D

180° ... 0°

CCFS02
WELL E
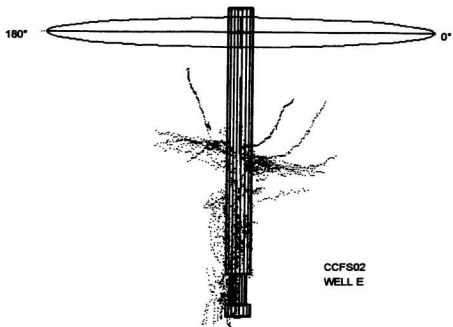
Figure 4.58. 0 to 180° view of dye traces for well E

148
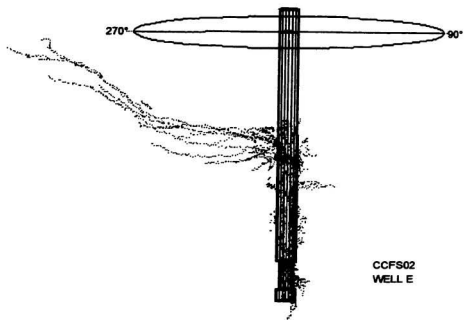
Figure 4.59. 90 to 270° view of dye traces for well E

149
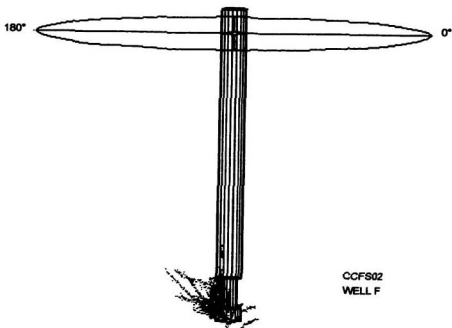
Figure 4.60. *0 to 180° view of dye traces for well F*

CCFS02
WELL F

180°   0°

270°   90°

CCFS02
WELL F
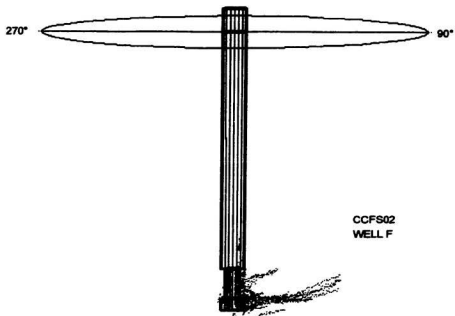
Figure 4.61. 90 to 270° view of dye traces for well F
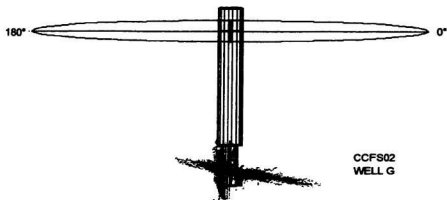
Figure 4.62. 0 to 180° view of dye traces for well G
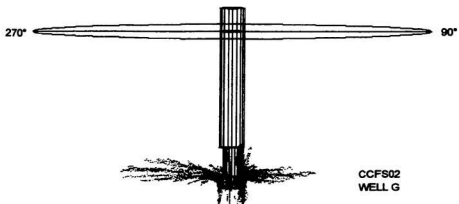
Figure 4.63. 90 to 270° view of dye traces for well G

152
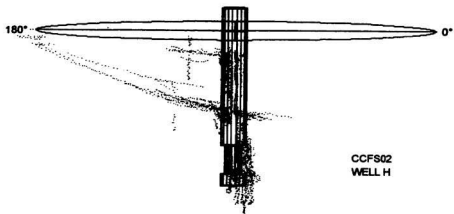
Figure 4.64. 0 to 180° view of dye traces for well H
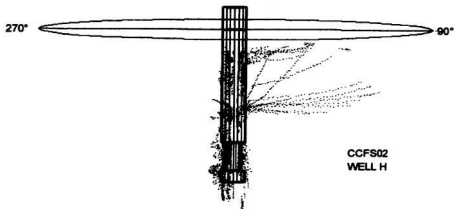
Figure 4.65. 90 to 270° view of dye traces for well H

153
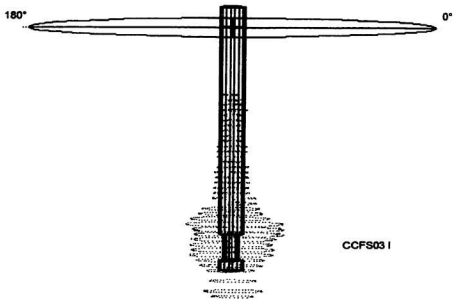
Figure 4.66. 0 to 180° view of dye traces for well I

154

CCFS03 I
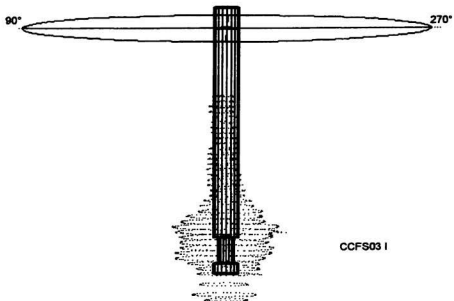
Figure 4.67. 90 to 270° view of dye traces for well I

180°   0°

CCFS03 J
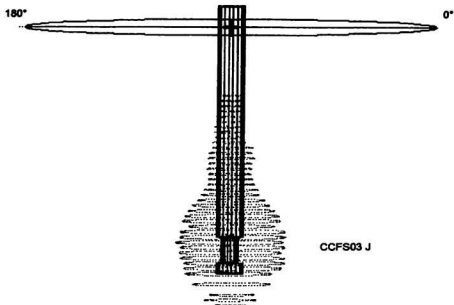
Figure 4.68. 0 to 180° view of dye traces for well J

156
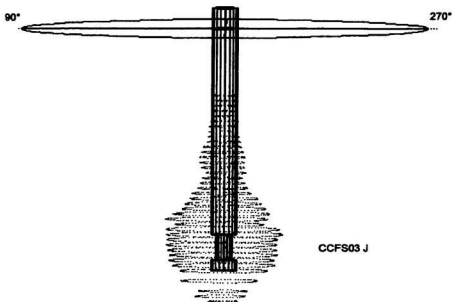
Figure 4.69. 90 to 270° view of dye traces for well J
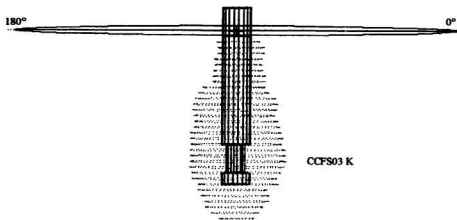
Figure 4.70. 0 to 180° view of dye traces for well K
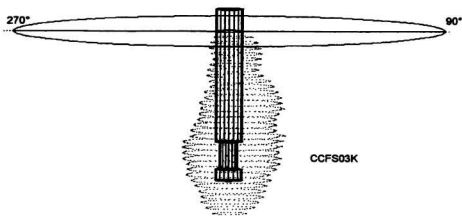
Figure 4.71. 90 to 270° view of dye traces for well K
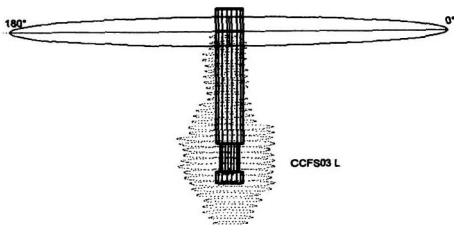
Figure 4.72. 0 to 180° view of dye traces for well L
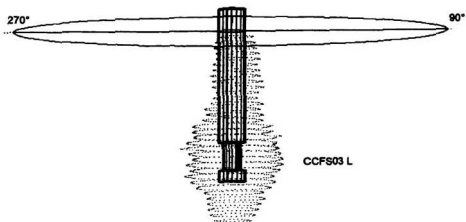
Figure 4.73. 90 to 270° view of dye traces for well L
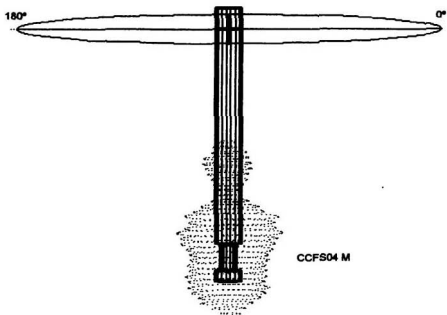
Figure 4.74. 0 to 180° view of dye traces for well M

270° ⋯⋯⋯⋯⋯ 90°

CCFS04 M
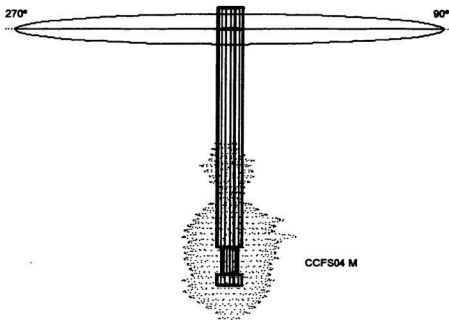
Figure 4.75. 90 to 270° view of dye traces for well M
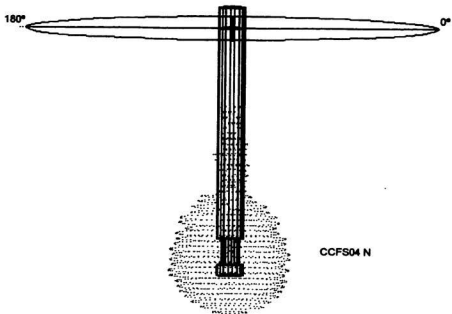
Figure 4.76. 0 to 180° view of dye traces for well N
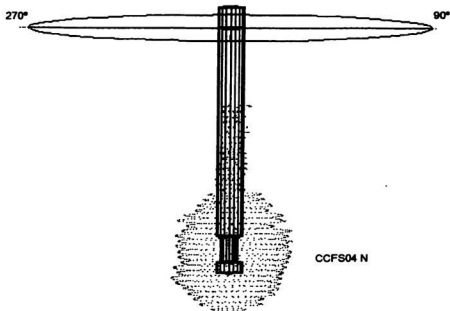
Figure 4.77. 90 to 270° view of dye traces for well N
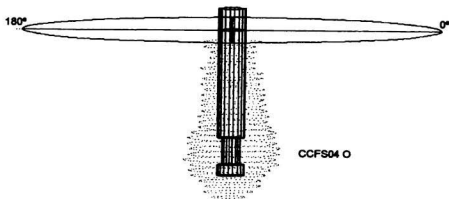
Figure 4.78. 0 to 180° view of dye traces for well O
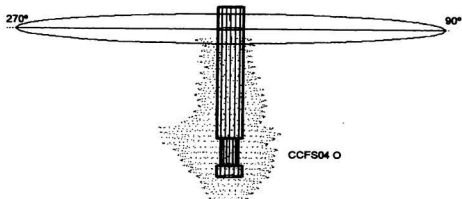
Figure 4.79. 90 to 270° view of dye traces for well O
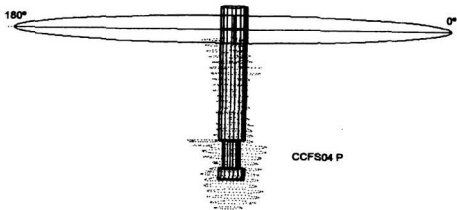
Figure 4.80. 0 to 180° view of dye traces for well P
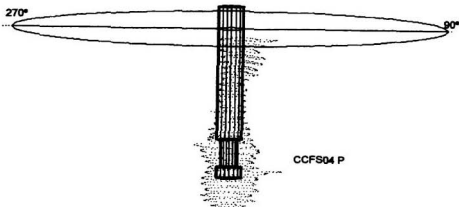
Figure 4.81. 90 to 270° view of dye traces for well P

CHAPTER 5 - NUMERICAL MODELLING OF FLUID INJECTION

5.1 Introduction

Numerical analyses were carried out to investigate the stress and deformational response of soil due to fluid injection through a wellbore, and to investigate the manner in which changes in soil or injection parameters may influence the shearing mechanism. Numerical simulations were carried out utilizing test data obtained from field and centrifuge experiments as well as using data provided by Golder Associates Ltd (1991, 1992 and 1994) from injection tests carried out in a large calibration chamber. The following sections contain descriptions of the computer program and the constitutive model used for the numerical simulations. The problem geometry, boundary conditions and test parameters are described. The results of the modelling runs are presented.

5.2 Selection of a Numerical Model

A major objective of the injection process is to utilize a soil shearing approach to enhance the movement of fluids in low permeability contaminated soil. It was anticipated that an enhanced flow regime would result in conditions more amenable to cleanup using conventional soil remediation techniques. The injection process involves pumping a fluid through a wellbore and into the soil at a flow rate that is greater than would freely occur through the pore space

of the soil. During the fluid injection process, the injection pressure rises, *in situ* stresses change, and deformations occur in response to the stress changes. Under some stress change conditions, the soil may reach a state where yielding occurs. In some soils, particularly those that are dilatant and characterized by a peak strength and a post-peak reduction in strength, the yielding process may also be accompanied by a permeability increase which may significantly influence the shearing process.

In selecting a program for the numerical simulation of the injection process, consideration was given to several commercially available codes that have either been written specifically for geotechnical applications, or have had extensive geotechnical constitutive modelling capabilities built into the code. A summary of the main features of the five programs reviewed is provided in the following sections.

5.2.1 CRISP

The CRItical State soil mechanics Program, CRISP, is a geotechnical finite element analysis program that was developed over 20 years ago by researchers at Cambridge University's Engineering Department in the United Kingdom. The program was originally written to be run from a mainframe computer, but has been updated over the years to operate on a personal computer operating in a DOS environment, and more recently with a Graphical User Interface for operating under Microsoft Windows™ 3.xx. The three primary components of the

software comprise a pre-processor, the FE analysis program and a post-processor.

Linear, non-linear and strain hardening / softening constitutive soil models are supported as well as structural models and a Coulomb frictional interface model. The models have been well established during the past 20 years, as demonstrated by more than 60 technical publications which reference the use of the program (SAGE CRISP, 1997). The program can be used to carry out drained, undrained and fully coupled consolidation analyses. Two-dimensional plane strain or axisymmetric runs can be carried out using the Windows version of the program, and three-dimensional analyses can be carried out using the DOS version.

5.2.2 SIGMA/W

SIGMA/W is a finite element analysis program for analysing geotechnical stress and deformation problems (GEO-SLOPE, 1996). The program can be operated on a personal computer using Windows™ 3.xx. The program was formulated for elastic and elastic-plastic constitutive soil models including linear-elastic, anisotropic linear-elastic, nonlinear-elastic (hyperbolic), elastic-plastic (Tresca & Mohr-Coulomb failure criterion), strain-softening (Von Mises failure criterion), Cam-clay (critical state), and modified Cam-clay (critical state) models. Analysis types include drained effective stress, undrained effective stress, and total stress analysis with pore-water pressures based on total stress changes, all carried out under plane strain or axisymmetric conditions. Volume changes (deformation due to changes in

pore-water pressure) and uncoupled consolidation may be modelled by integration with a separate finite element seepage analysis program called SEEP/W. Soil-structure interaction problems can be analysed by including structural components in the finite element mesh that have equivalent structural stiffness parameters. Contact between the soil and a structure can be modelled by any of the constitutive soil models or as a special slip surface.

5.2.3 ABAQUS

ABAQUS/Standard is a comprehensive general-purpose finite element program designed specifically for advanced analysis applications in a wide range of problem areas. The program runs effectively on computers ranging from desktop systems running Windows NT or UNIX to departmental servers and supercomputers. Analysis procedures include general linear or nonlinear analyses, and linear perturbation analyses. Models are provided for metals, cast iron, rubber, plastics, composites, resilient and crushable foam, concrete, sand, clay, and jointed rock. The material response for each of the models may be highly nonlinear. General elastic, elastic-plastic, and elastic-viscoplastic behaviours are provided. Both isotropic and anisotropic behaviour can be modelled. User-defined materials can also be created with a subroutine interface. One-, two-, and three-dimensional continuum elements are provided, as well as beams, membranes, and shells. Elements are formulated to provide accurate modelling for arbitrary magnitudes of displacements, rotations, and strains.

Boundary conditions can include prescribed kinematic conditions and prescribed foundation conditions. Loading conditions can include point forces, distributed loads, and thermal loading. Loads and boundary conditions for pore fluid pressure, electric potential, and other scalar fields are also available. Initial conditions for temperature, velocity, stress, and numerous other fields can be specified. General capabilities are included for modelling interactions between bodies, including surface-to-surface contact, with or without friction.

Fully coupled thermal-stress interfaces are provided, where heat and traction may both be transmitted and where the thermal resistance of the interface may depend on the pressure between contacting surfaces or the mechanical separation of the surfaces. Acoustic interface elements are included to couple structural and acoustic medium models for dynamic and vibration analysis. Coupled pore fluid flow-stress and coupled thermal-electrical interactions are also available. Partially saturated flow problems involving phreatic surfaces and capillary effects can be addressed. Elements and contact pairs may be removed throughout an analysis to simulate applications including geotechnical problems such as tunnel or dam construction, welding simulations, and tool removal for springback calculations.

5.2.4 PISA

The Program for Incremental Stress Analysis, PISA, is a finite element computer program for geotechnical deformation analysis. The program incorporates advanced modelling features

that allow simulation of various geotechnical structures including dams, embankments, tunnels, excavations, retaining structures, and others. A number of constitutive models are available including linear and non-linear elastic, frictional and non-frictional plastic, critical state, and creep models. Undrained and drained deformation with user specific phreatic surfaces can be modelled. The program includes a graphical user interface that is operated from a personal computer using a Windows™ operating system.

5.2.5   FLAC

Fast Lagrangian Analysis of Continua, FLAC, version 3.3, is a two-dimensional explicit finite difference algorithm written for engineering mechanics computation. A description of the theoretical basis of the program, program features, and the program command structure are presented by Itasca Consulting Group (1996). The program is used to model the behaviour of structures built of soil, rock, or other materials that may undergo plastic flow when their yield limits are reached.

Materials are represented by zones (elements) which are assembled to form a grid that is adjusted by the user to fit the shape of the object to be modelled. Each zone of the grid behaves according to prescribed linear or non-linear stress/strain relations in response to applied forces or boundary constraints. The material can yield and flow, and the grid can deform and move with the material that is represented. The program is formulated to allow

171

problems with two-dimensional plane strain or axisymmetric geometries to be analysed as well as a plane stress option for elastic and Mohr-Coulomb analysis. In the axisymmetric case, cylindrical coordinates are used where x=0 is the axis of symmetry, the positive x-direction corresponds to the radial coordinate, the y-direction corresponds to the axial coordinate, and the tangential direction (z-direction) to the circumferential coordinate. The tangential stress, σ_z is calculated for all symmetry conditions and is taken into account in plastic yield calculations for both plane strain and axisymmetric analyses.

FLAC incorporates the facility to model groundwater flow and pore pressure dissipation, with full coupling between a deformable porous solid and a viscous fluid flowing within the pore space. The pore fluid is considered to be deformable and obeys either the isotropic or anisotropic forms of Darcy's law. Non-steady flow is modelled with steady flow treated as an asymptotic case. Fixed pore pressure and constant-flow boundary conditions may be used, and injection or extraction wells may be modelled. The flow model can be run independently from the mechanical calculation, and both confined and unconfined flow can be simulated.

FLAC incorporates a built-in programming language within the code called FISH, that can be used to customize operation of the program by defining new variables and functions. For example, FISH routines may be used to plot or print new variables, implement special grids, specify distributions of properties to be applied to a model, and automate parametric studies.

FLAC models the development of shear bands within the grid by using a realistic procedure

for simulating the release and dissipation of the kinetic energy that forms due to the evolution of the shear bands (see for example; Cundall, 1989; Cundall, 1990; and Cundall, 1991). Although the physics of band development is modelled correctly, band development is grid dependent and FLAC will not accurately model the thickness or the spacing of shear bands.

5.2.6 Selection of model

Various technical and non-technical issues were considered in selecting a computer program for modelling the fluid injection process. It was considered to be a more efficient use of time to utilize existing software than to develop a numerical model coded specifically for this project. The program should be written for geotechnical applications and should be well established within the geotechnical community. As the interaction and relationship between the injection fluid, groundwater, and the soil skeleton are considered to be of extreme importance to the shearing process, stress and deformation calculations should be carried out using a program that incorporates full coupling between groundwater flow and mechanical response of the soil. The program must also be able to accommodate the injection of fluid into the soil through a well (i.e. fluid source). The program should have an elastic-plastic constitutive model that can simulate strain weakening behaviour and should have the capability to model permeability changes due to shearing. Consideration was also given as to how well the program can model progressive failure and the development of shear bands.

It was considered important that the program be well documented, user friendly, and have comprehensive pre-and post-processing capabilities. The software used must be readily available and the associated purchase/rental costs must be within the project budget. The ability to run the program on a personal computer using a Windows™ based operating system was also considered to be essential.

After reviewing the features and capabilities of the five programs described above, a decision was made to use FLAC for the numerical modelling component of this research. Some of the features which made FLAC the first choice were: the ability to model large displacements; the availability of a suitable strain softening model; full coupling between groundwater flow and mechanical behaviour; the versatility of the programmable macro language FISH including the capability of introducing functions to control permeability and porosity based on strain; and the programs compactness and ease of operation.

5.3   Strain Softening Constitutive Model

The Strain-Softening/Hardening model incorporated into FLAC is based on an implementation of the Mohr-Coulomb model with non-associated shear and associated tension flow rules. The difference between the strain-softening/hardening model and the Mohr-Coulomb model is that the cohesion, friction, dilation and tensile strength may increase or decrease after the soil begins to yield plastically. The Mohr-Coulomb model is an elastic-

perfectly plastic model where the cohesion, friction, dilation and tensile strength are assumed to remain constant as yielding occurs. With the strain softening model, the cohesion, friction and dilation are defined as piecewise-linear functions of a hardening parameter measuring the plastic shear strain. A piecewise-linear softening law for the tensile strength is prescribed in terms of a similar parameter measuring the plastic tensile strain. The total plastic shear and tensile strains are measured by incrementing the hardening parameters at each time step and causing the soil properties to conform to the user-defined functions.

The principal stresses σ_1, σ_2, and σ_3 are used for calculations. FLAC includes the tangential stress σ_z as one of the principal stresses. The principal stresses and principal directions are evaluated from the stress tensor components and ordered so that $\sigma_1 \leq \sigma_2 \leq \sigma_3$ where compressive stresses are negative. The corresponding principal strain increments Δe_1, Δe_2, Δe_3 are decomposed as $\Delta e_i = \Delta e_i^e + \Delta e_i^p$ where the superscript e and p refer to elastic and plastic parts, respectively, and the plastic components are non-zero only during plastic flow. The incremental expression of Hooke's law in terms of principal stress and strain has the form shown in Eqns. 5.1 to 5.3, where $\alpha_1 = B + 4G/3$ and $\alpha_2 = B - 2G/3$.

$$\Delta\sigma_1 = \alpha_1 \, \Delta e_1^e + \alpha_2 \, (\Delta e_2^e + \Delta e_3^e) \qquad \text{[Eqn. 5.1]}$$

$$\Delta\sigma_2 = \alpha_1 \, \Delta e_2^e + \alpha_2 \, (\Delta e_1^e + \Delta e_3^e) \qquad \text{[Eqn. 5.2]}$$

$$\Delta\sigma_3 = \alpha_1 \, \Delta e_3^e + \alpha_2 \, (\Delta e_1^e + \Delta e_2^e) \qquad \text{[Eqn. 5.3]}$$

The failure criterion is represented in the (σ_1, σ_3) plane as shown in Figure 5.1. The failure

175

176

envelope is defined from point A to point B by the Mohr-Coulomb yield function [Eqn. 5.4],

$$F^s = \sigma_1 - \sigma_3 N_\phi + 2c(N_\phi)^{1/2}$$ [Eqn. 5.4]

and from B to C by a tension yield function of the form shown in Eqn. 5.5.

$$F^t = \sigma^t - \sigma_3$$ [Eqn. 5.5]

where φ is the friction angle, c is the cohesion, σ^t is the tensile strength and N_ϕ is as shown in Eqn. 5.6.

$$N_\phi = (1 + \sin \phi) / (1 - \sin \phi)$$ [Eqn. 5.6]

Only the major and minor principal stresses are active in the shear yield formulation, the intermediate principal stress has no effect. For a soil with friction angle, φ≠0, the tensile strength of the soil cannot exceed the value σ^t_max, given by σ^t_max = c / tan φ. The shear potential function g^s corresponds to a non-associated flow rule and has the form shown in Eqn. 5.7,

$$g^s = \sigma_1 - \sigma_3 N_\psi$$ [Eqn. 5.7]

where ψ is the dilation angle and N_ψ is as defined in Eqn. 5.8.

$$N_\psi = (1 + \sin \psi) / (1 - \sin \psi)$$ [Eqn. 5.8]

The associated flow rule for tensile failure is derived from the potential function g^t, with $g^t = -\sigma_3$. The flow rules for this model are given a unique definition in the vicinity of an edge of the composite yield function in three-dimensional stress space by application of an edge function. Vermeer and deBorst (1984) defined an incremental form of shear hardening parameter e^{ps}, [see Eqn. 5.9], which is utilized by FLAC to measure plastic shear strain:

$$\Delta e^{ps} = \{ \tfrac{1}{2} (\Delta e_1^{\,m} - \Delta e_m^{\,ps})^2 + \tfrac{1}{2}(\Delta e_m^{\,ps})^2 + \tfrac{1}{2}(\Delta e_3^{\,m} - \Delta e_m^{\,ps})^2 \}^{\frac{1}{2}} \qquad \text{[Eqn. 5.9]}$$

where $\Delta e_m^{\,ps} = (e_1^{\,m} + e_3^{\,m})$ and $e_j^{\,m}$, j=1,3 are the principal plastic shear strain increments. The tensile hardening parameter e^{pt} measures the accumulated tensile plastic strain; its increment is defined as $\Delta e^{pt} = e_3^{\,m}$, where $\Delta e_3^{\,m}$ is the increment of tensile plastic strain in the direction of the major principal stress (tensile stresses are positive).
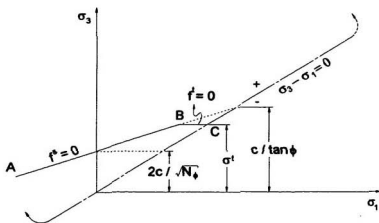
Figure 5.1. Failure criterion for Mohr-Coulomb model (after Itasca, 1996)

5.4   Problem Geometry and Boundary Conditions

All but one of the numerical runs were carried out using a vertical injection well installed at depth within an axisymmetric model. Numerical simulation of field test FLDTST2 was carried out using a horizontal injection well and plane strain conditions. All simulations involved injecting water through a well and into the soil at a constant rate of flow. The soil was initially fully saturated with the water table at the ground surface. Full coupling was incorporated between groundwater flow and the mechanical response of the system. A discussion of the technique used for groundwater flow/stress coupling is provided by Itasca (1996). The strain-softening/hardening plasticity constitutive model described in Section 5.3 was used for the analysis.

5.4.1   Chamber tests

Data from a laboratory study of hydraulic fracture propagation in oil sands was made available by Golder Associates Ltd (1991, 1992 and 1994) for analysis and interpretation. The Golder Associates test data is directly applicable to the soil shearing process, and is analysed and interpreted as part of this thesis.

During the three phases of the Golder Associates hydraulic fracturing test program, eighteen injection tests were carried out in homogeneous sand within a large triaxial calibration

179

chamber. The design and setup of the calibration chamber was described previously by Kosar and Been (1989) and Been and Kosar (1991). The test chamber can accommodate a soil sample with a diameter of 1.4 m and a height of up to 1 m. Principal stresses of up to 1000 kPa may be applied independently through a circumferential (σ_h) and upper (σ_v) cavity. The pore fluid pressure is applied to the sample through drainage ports in the base of the chamber and in the top loading plate. A system of air-over-water cells and pressure regulators is used to impose a variety of stress conditions on the sample. In a manner very similar to that used in a conventional triaxial test cell, horizontal stresses are transmitted to the sample through a latex membrane, and vertical stresses are applied through a steel loading plate. A schematic drawing of the chamber is shown in Figure 5.2. Test parameters and experimental results from the chamber testing program are included in Appendix 4.

Numerical simulations of the chamber tests were carried out using the finite difference grid shown in Figure 5.3, the boundary conditions shown in Table 5.1 and the FLAC parameters from Table 5.2.

Table 5.1. Test parameters from Phase 2 & 3 Chamber tests[d]

Test ID	Height of Injection Interval (mm)	Perm.[a] k (m/s)	K	σ_v (kPa)	σ_h (kPa)	u (kPa)	Q (ml/s)	t (s)	Volume (ml)
2FRAC2[b] a b c d e	50	3.71(10)^-8	2	400	600	200	0.28 0.40 1.00 0.25 0.40	3036 2125 850 3400 500	850 850 850 850 200
2FRAC3[b] a b c d e f	50	4.86(10)^-8	2	400	600	200	1.0 3.0 10.0 30.0 3.0 30.0	850 283.3 85.0 28.3 283.3 28.3	850 850 850 850 850 200
2FRAC4	50	4.24(10)^-8	2	400	600	200	30	8.3	250
2FRAC5	50	5.48(10)^-8	2	400	600	200	200	1.3	260
3FRAC1	50	5.21(10)^-8	1	500	600	100	41	22	900
3FRAC2	50	4.42(10)^-8	2	400	600	200	41	22	900
3FRAC3	50	5.48(10)^-8	2	400	600	200	200	4.5	900
3FRAC4	50	4.15(10)^-8	2	500	800	200	200	4.5	900
3FRAC5[c]	6.4	3.71(10)^-8	2	400	600	200	200	4.5	900
3FRAC6[c]	6.4	3.27(10)^-8	2	400	600	200	200	1.5	300

Note: [a] Hydraulic conductivity of Lane Mountain Sand was determined from flow tests carried out at a design soil density of 2031 kg/m³, and using liquid invert sugar as pore fluid and injection fluid (specific gravity of liquid sugar is 1.36 and viscosity is 1.49 Pa-s at 20° C.). Hydraulic conductivity assumed to be homogeneous and isotropic throughout soil.

[b] Multiple injection tests carried out in a single sample with pore pressure dissipation between subtests.

[c] The finite difference grid constructed for this test is based on an injection well 6.4 mm in height and 33.5 mm in diameter. The actual laboratory test configuration utilized an 84.3 mm diameter by 6.4 mm high pointed notch built into the injection well.

[d] Reference: (Golder Associates Ltd., 1994).

181

Table 5.2. Parameters used in FLAC analysis of injection tests

Parameter		Symbol and Units	Data Set			
			Chamber Lane Mn. Sand	Centrifuge Kaolin	Centrifuge Silty Sand	Field Test Argenta Till
FLAC Control Parameters	configuration		axisymmetric	axisymmetric	axisymmetric	axi & pl strain
	grid size		50 x 50	60 x 60	60 x 60	40 x 40
	groundwater		off	on	on	on
	mechanical		on	on	on	on
	maximum unbalanced force	N	20	20	20	20
Gravity*		g, m/s²	off	9.81 x 50	9.81x50, 9.81x25	9.81
Pore/Injection fluid properties	density	ρ_f, kg/m³	1360	1000	1000	1000
	bulk modulus	B_f, Pa	3.33 x 10⁹	2 x 10⁹	2 x 10⁹	2 x 10⁹
	tension limit	σ_m, Pa	0	0	0	0
Soil properties	porosity	n, –	0.48	0.52	0.27	0.33
	dry density	ρ_d, kg/m³	1378	1277	1950	1800
	shear modulus	G, Pa	1.64 x 10⁷	1.28 x 10⁸	1.54 x 10⁷	2.3 x 10⁹
	bulk modulus	B, Pa	2.74 x 10⁷	2.78 x 10⁸	3.33 x 10⁷	5.0 x 10⁹
	specific gravity	G_s, –	2.65	2.64	2.65	2.67
	horizontal to vertical effective stress ratio	K, –	1.25 or 2.0	1.2, 1.6	1.5	1.5
Soil properties as function of plastic strain	friction angle	ϕ', degrees	0.38 : 0.01,30	0.24 : 0.05,20	0.49 : 0.03,41	0.35 : 0.04,31
	cohesion	c', Pa	0.0 : 0.03,0	0.6000 : 0.05,0	0.0 : 0.04,0	0.0 : 0.04,0
	dilation angle	ψ', degrees	0.30 : 0.01,5	0.5 : 0.05,0	0.30 : 0.03,10	0.10 : 0.04,0
	tensile strength	σ', Pa	0.0 : 0.03,0	0.0 : 0.05,0	0.0 : 0.03,0	0.0 : 0.04,0

Note: * Numerical simulations of centrifuge tests were carried out at model scale.

182

5.4.2 Centrifuge and field tests

Numerical simulations of the centrifuge tests and field tests were carried out using the finite difference grid and boundary conditions shown in Figure 5.4 and the properties summarised in Table 5.2 and Table 5.3. The centrifuge test simulations were carried out at model scale using a gravitational acceleration of 50 g, except for CCFS04 M and N which were carried out at an acceleration of 25 g. Descriptions of the soil properties, equipment, test setup, test procedures, and results from these tests were described previously in Chapters 2 and 3, and in Appendices 1 through 3 of this thesis.

Table 5.3. Summary of test conditions for field and centrifuge tests[a]

Test ID		Well Type	Gravity g	Injection Interval			FLAC Permeability[b]		Q (l/s)	t (s)	Vol. (l)
				Depth (m)	Height (m)	Area (m²)	k_1 (m²/kg)	k_2 (m²/kg)			
FLDTST1		Vertical	1	1.5	0.5	0.236	1.2×10^{-12}	1.2×10^{-11}	0.631	180	114
FLDTST2		Horiz.	1	2.3	0.2	2.4	1.2×10^{-12}	1.2×10^{-11}	0.631	1140	719
CF501	A	Vertical	50	0.2	0.025	7.48×10^{-3}	8.5×10^{-13}	3.2×10^{-12}	2.9×10^{-4}	1150	0.033
	B	"	50	0.2	0.025	7.48×10^{-3}	8.5×10^{-13}	3.2×10^{-12}	2.9×10^{-4}	115	0.033
	C	"	50	0.2	0.025	7.48×10^{-3}	8.5×10^{-13}	3.2×10^{-12}	2.9×10^{-4}	1150	0.033
	D	"	50	0.1	0.025	7.48×10^{-3}	8.5×10^{-13}	3.2×10^{-12}	2.9×10^{-4}	115	0.033
CF502	E	Vertical	50	0.2	0.025	7.48×10^{-3}	8.5×10^{-13}	3.2×10^{-12}	2.9×10^{-4}	16.5	0.047
	F	"	50	0.2	0.025	7.48×10^{-3}	8.5×10^{-13}	3.2×10^{-12}	1.4×10^{-4}	3300	0.047
	G	"	50	0.2	0.025	7.48×10^{-3}	8.5×10^{-13}	3.2×10^{-12}	1.4×10^{-4}	2300	0.033
	H	"	50	0.1	0.025	7.48×10^{-3}	8.5×10^{-13}	3.2×10^{-12}	1.4×10^{-4}	2300	0.033
CF503	I	Vertical	50	0.2	0.025	7.48×10^{-3}	3.1×10^{-13}	7.7×10^{-12}	2.9×10^{-4}	1600	0.046
	J	"	50	0.2	0.025	7.48×10^{-3}	3.1×10^{-13}	7.7×10^{-12}	2.9×10^{-4}	160	0.046
	K	"	50	0.2	0.025	7.48×10^{-3}	3.1×10^{-13}	7.7×10^{-12}	2.9×10^{-4}	1100	0.031
	L	"	50	0.1	0.025	7.48×10^{-3}	3.1×10^{-13}	7.7×10^{-12}	2.9×10^{-4}	110	0.031
CF504	M	Vertical	25	0.2	0.025	7.48×10^{-3}	3.1×10^{-13}	7.7×10^{-12}	5.7×10^{-2}	390	0.022
	N	"	25	0.2	0.025	7.48×10^{-3}	3.1×10^{-13}	7.7×10^{-12}	2.9×10^{-4}	174	0.050
	O						Numerical simulations not carried out for tests O and P				
	P										

Note: [a] All properties and dimensions are shown at test scale.
[b] FLAC permeability defined as $k/(\rho_w g)$ where k_1 is horizontal direction and k_2 is vertical.
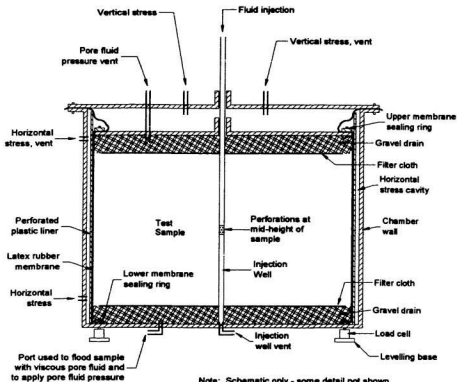
184

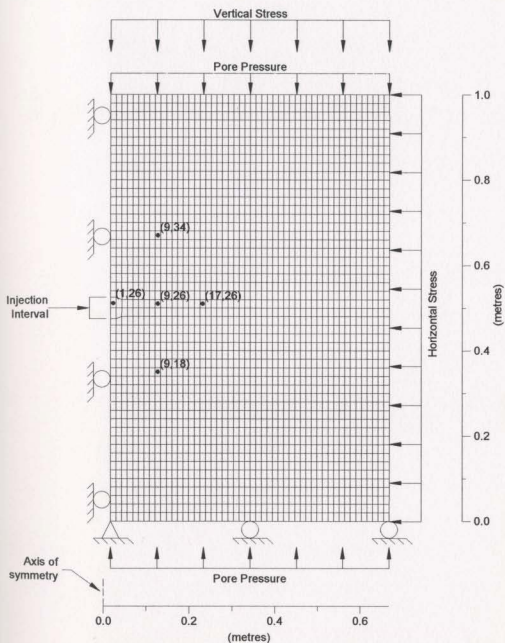Figure 5.2. Schematic of calibration chamber (after Kosar and Been, 1989)

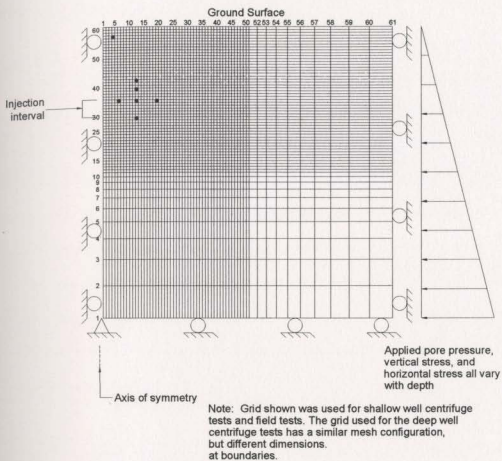**Figure 5.3.** FLAC grid and boundary conditions for analysis of chamber tests

186

Figure 5.4. FLAC grid and boundary conditions used for centrifuge and field tests

5.5   Analysis Procedure

The applied boundary stresses in the chamber tests are large compared with the stresses due to self-weight, and the numerical modelling was carried out with gravity turned off. Following the application of boundary stresses and pore pressures, calculation steps were carried out until an equilibrium state was achieved. After reaching an equilibrium state under the applied boundary conditions, fluid was injected at a constant rate until the required volume of fluid had been injected (see Table 5.1). Pore pressure, horizontal stress, and vertical stress were monitored throughout the simulation at discrete locations near the injection zone (see filled circles on Figure 5.3 and history locations in Table 5.4). The stress and displacement fields for the model were generally saved after initial equilibrium was achieved and at the end of the injection stage.

Numerical simulations of the centrifuge and field experiments were carried out using procedures similar to those used for the chamber simulations. The centrifuge simulations were run using model scale dimensions and parameters. Both the field test runs and centrifuge test runs were carried out considering the *in situ* stresses due to self-weight of the soil. For the centrifuge test simulations, the acceleration due to gravity was set at either 50×9.81 m/s² (tests CCFS01, CCFS02 and CCFS03), or 25×9.81 m/s² (tests CCFS04 M and N). Pore pressure, horizontal stress, and vertical stress were monitored throughout the simulation at discrete locations near the injection zone (see Table 5.4 and also filled circles on Figure 5.4).

188

Table 5.4. Summary of history locations for numerical runs

Numerical Simulation	Grid Zone Location		Physical Location[a]	
	Column (i)	Row (j)	x (m)	y (m)
Phase 2 and Phase 3 Chamber Tests (krun0, krun1, krun2, krun3, 2frac2, 2frac2, 2frac4, 2frac5, 3frac1, 3frac2, 3frac3, 3frac4, 3frac5, 3frac6)	1	26	0.023	0.010
	9	26	0.128	0.010
	17	26	0.232	0.010
	9	18	0.128	-0.150
	9	34	0.128	0.170
Shallow Centrifuge Tests[b] (CCFS01C, CCFS01D, CCFS02G, CCFS02H, CCFS03K, CCFS03L, CCFS04M, CCFS04N)	1	35	0.007	0.010
	12	35	0.051	0.010
	24	35	0.099	0.010
	37	35	0.151	0.010
	24	41	0.099	0.034
	24	48	0.099	0.060
	24	23	0.099	-0.038
	8	57	0.035	0.098
Deep Centrifuge Tests[b] (CCFS01A, CCFS01B, CCFS02E, CCFS02F, CCFS03I, CCFS03J)	1	30	0.007	0.010
	12	30	0.051	0.010
	24	30	0.099	0.010
	37	30	0.151	0.010
	24	36	0.099	0.034
	24	43	0.099	0.060
	24	18	0.099	-0.038
	8	57	0.035	0.129
Field Test With Vertical Well (FLDTST1)	1	25	0.125	0.20
	5	25	0.525	0.20
	10	25	1.025	0.20
	15	25	1.525	0.20
	5	29	0.525	0.60
	10	29	1.025	0.60
	10	22	1.025	-0.10
Field Test With Horizontal Well (FLDTST2)	1	35	0.145	0.046
	12	35	1.135	0.046
	24	35	2.215	0.046
	37	35	3.385	0.046
	24	23	2.215	-1.058
	24	41	2.215	0.598
	24	48	2.215	1.242

Note: [a] Physical location is referenced by x (horizontal) and y (vertical) distance from the center (0,0) of the screened interval of the injection well.
[b] History locations for centrifuge tests are at model scale.

189

5.6   Results of Chamber Test Simulations

Results of the numerical simulations are presented in Appendix 5. The results for each numerical run are presented in a set of 10 figures that includes plots of:

- the extent of the yield zone at the end of injection

- plastic shear strain at the end of injection

- the change in horizontal effective stress from the initial equilibrium condition due to fluid injection

- the change in vertical effective stress from the initial equilibrium condition due to fluid injection

- the change in tangential effective stress from the equilibrium condition due to fluid injection

- the change in pore pressure from the initial equilibrium condition due to fluid injection

- the ratio of horizontal to vertical effective stress at the end of injection

- region of permeability enhancement due to shearing

- history plot showing the development of pore pressure during the injection period, and

- history plot showing σ_y' (horizontal) vs σ_x' (vertical) stress paths of soil elements during the injection period.

In FLAC, positive stresses indicate tension and negative stresses indicate compression. Positive pore pressures are presented with a positive sign. All figures plotted as output from FLAC use this sign convention. Where changes in stress are plotted, a positive stress change indicates that the magnitude of the compressive stress has decreased, and a negative stress change indicates that the magnitude of the compressive stress has increased. A positive change in pore pressure indicates an increase in pore pressure, a negative change indicates a reduction in pore pressure. Figures which were not derived from FLAC (i.e. the stress path plots in this appendix) use a sign convention where compressive stresses and are positive and tensile stresses are negative.

5.6.1 Permeability change due to shearing

Numerical runs were carried out to investigate how variations in the magnitude of the permeability change due to shearing will effect the overall shearing process. Four simulations were carried out in which fluid was injected into the soil at a rate of 30 ml/s for 8.3 sec. A FISH function was incorporated within FLAC to increase the permeability of zones where accumulated plastic shear strain exceeded a prescribed value. If the plastic strain in a grid zone exceeded 1%, the horizontal and vertical permeability of the soil in that zone was increased by a factor of 1, 10, 100 or 1000 (see Table 5.5). In the strain softening model used for the chamber tests, 1% plastic strain was also prescribed as the plastic shear strain where the soil became fully softened.

Table 5.5. Model parameters for study of shear induced permeability changes

Numerical Run ID	Initial Zone Permeability (m³/s-kg)	Permeability Increase at 1% Plastic Strain	Permeability Within Enhanced Zones (m³/s-kg)	Location of Simulation Results
KRUN0	4.32×10^{12}	x1	4.32×10^{12}	Figure A5.1 to A5.10
KRUN1	4.32×10^{12}	x10	4.32×10^{11}	Figure A5.11 to A5.20
KRUN2	4.32×10^{12}	x100	4.32×10^{10}	Figure A5.21 to A5.30
KRUN3	4.32×10^{12}	x1000	4.32×10^{9}	Figure A5.31 to A5.40

There was an obvious change in the size and shape of the yield zone with changes in the amount of permeability increase. For the case where no permeability enhancement occurs (KRUN0), the yield zone forms a semi-circular region around the point of injection (Figure A5.1). As the amount of permeability enhancement increases, the yield zone (Figures A5.11, A5.21, and A5.31) forms an increasingly narrow band that extends horizontally outwards from the point of injection. A similar trend is seen based on the contours of plastic strain (Figures A5.2, A5.12, A5.22, and A5.32).

The change in horizontal effective stress between the start and end of fluid injection is shown in Figures A5.3, A5.13, A5.23, and A5.33. Similarly, the vertical effective stress change is shown in Figures A5.4, A5.14, A5.24, and A5.34, and the tangential effective stress change is shown in Figures A5.5, A5.15, A5.25, and A5.35.

With permeability enhancement, very large pore pressures build up close to the point of injection. The zone of large pore pressure increase is confined to a narrow region of soil

near the injection interval. At the point of injection, there is a reduction in horizontal, vertical and tangential effective stress due to the large pore pressure. A small distance to the side of the well, there is a very large zone of horizontal effective stress increase, while above and below the injection interval there is a zone of horizontal effective stress decrease. There is a region of large vertical stress increase above, below, and to the sides of the injection interval, and a smaller zone of vertical stress decrease to the side of the injection well at about one-half of the distance between the well and the chamber wall.

As the amount of permeability enhancement that occurs is increased, a shear band develops that extends horizontally outwards from the injection point. With greater permeability enhancement, there is an increased capacity for fluid to move within the yielded zone. As a result, the magnitude of the pore pressure increase is substantially reduced and the zone of pore pressure increase extends horizontally outwards a greater distance from the point of injection. Restrained dilation causes a zone of decreased pore pressure to be created near the tip of the shear band. The effective stress is substantially reduced within the shear band due to the high pore pressures. Above and below the shear band, there is an increase in the horizontal and vertical effective stress. Near the tip of the shear band there is a zone of increased horizontal effective stress.

The maximum pore pressure developed at the point of injection was normalized using the minimum principal effective stress (P_p/σ_3') and plotted against degree of permeability enhancement (k/k_o) in Figure 5.5. With a permeability enhancement of one, the pore pressure

developed is very high, but drops rapidly and levels off at just over 4 after a permeability enhancement of 100. The range in P_i/σ_3' from the chamber test experimental results was 2.75 to 6.15 with an average value of 3.88. This suggests that it may be appropriate to use a permeability enhancement of approximately 100 for the numerical modelling of the chamber test results. This is supported by the work of Mori and Tamura (1986) who reported permeability enhancements of more than two orders of magnitude during shearing of grouted sand samples.

5.6.2 Injection test 2FRAC2

During chamber test 2FRAC2, five sub-injection tests were carried out at relatively low injection rates of 0.28, 0.40, 1.0, 0.25, and 0.40 ml/s. A volume of 850 ml was injected during sub-tests (a), (b), (c), and (d), and 200 ml was injected during (e). Time was allowed following each sub-injection test for excess pore pressures to dissipate and the soil stresses to stabilize. In the model, this was accomplished by turning off the injection source and allowing drainage to occur at the upper and lower boundaries while stepping forwards through time for 1000 s. Results from the 2FRAC2 simulation are presented in Appendix 5 as Figures A5.41 to A5.50 for sub-test a (0.28 ml/s), Figures A5.51 to A5.60 for sub-test b (0.40 ml/s), Figures A5.61 to A5.70 for sub-test c (1.0 ml/s), Figures A5.71 to A5.80 for sub-test d (0.25 ml/s), and Figures A5.81 to A5.90 for sub-test e (0.40 ml/s).

Only a very small yield zone developed adjacent the point of injection during sub-injection test (a) at 0.28 ml/s (Figure A5.41). At the injection well, the magnitude of the plastic strain was less than 0.5% (Figure A5.42). A small circular region of increased pore pressure developed around the injection well (Figure A5.46) with the 50 kPa contour at 0.12 m from the well. This resulted in a small decrease in the effective stresses (vertical, horizontal, and tangential) near the well (Figures A5.43 to A5.46). A zone of elevated stress ratio developed within a circular bulb to the side of the injection point (Figure A5.47). No zone of permeability enhancement was observed (Figure A5.48).

There was only a small increase in the size of the yield zone during sub-injection test (b) at 0.40 ml/s (Figure A5.51). The magnitude of the plastic strain is still less than 0.5% (Figure A5.52). The size of the zone of excess pore pressure has expanded slightly with the 50 kPa contour located about 0.17 m from the well (Figure A5.56). This has resulted in a slightly larger zone of reduced effective stress near the well. The zone of reduced horizontal stress is larger along the sides of the well than above or below the point of injection (Figure A5.53). The zone of increased vertical stress is largest above and below the point of injection (Figure A5.54). The zone of reduced tangential stress remains approximately semi-circular in shape (Figure A5.55). The zone of increased stress ratio (Figure A5.57) is approximately the same shape as during test (a), however, it is slightly larger. Again, no zone of permeability enhancement was observed (Figure A5.58).

There is a significant increase in the size of the yield zone during sub-injection test (c) at 1.0

ml/s (Figure A5.61). This is also indicated by a zone of plastic strain that has developed at the well and which extends horizontally outwards (Figure A5.62). The zone of increased pore pressure has grown much larger (Figure A5.66) with the 50 kPa contour now approximately 0.28 m from the well. The shape of the horizontal effective stress field is significantly influenced by the yield zone that has developed, and there is a zone of reduced horizontal effective stress above and below the point of injection as well as a lobe extending horizontally outwards from the well (Figure A5.63). The vertical effective stress is slightly increased above and below the injection point, and there is a large bulb of decreased vertical effective stress to the side of the injection well (Figure A5.64). The tangential effective stress is reduced over a much larger area with the greatest reduction concentrated near the yield zone. The zone of maximum stress ratio (Figure A5.67) has moved approximately 150 mm to the side of the point of injection. Permeability has increased in several zones near the point of injection (Figure A5.68).

There is no additional growth of the yield zone with the reduced injection rate of 0.25 ml/s for sub-injection test (d) (see Figure A5.71 and A5.72). The region of pore pressure increase has become smaller (Figure A5.76) with the 50 kPa contour now located 0.12 m from the well. With the decrease in the size of the excess pore pressure bulb, the horizontal, vertical and tangential effective stresses have increased (Figures A5.73, A5.74 and A5.75). The zone of maximum stress ratio (Figure A5.77) has reduced in size from test (c). The size of the zone of permeability enhancement remains unchanged (Figure A5.78).

With the injection rate increased to 0.40 ml/s for sub-injection test (e), there is again no growth in the yield zone (Figures A5.81 and A5.82). The region of pore pressure increase has expanded with the 50 kPa contour now 0.16 m from the injection well (Figure A5.86). With the increased pore pressure, the effective stresses have again decreased (Figures A 5.83, A5.84 and A5.85). The maximum stress ratio (Figure A5.87) has grown a small amount, however, the area of permeability enhancement (Figure A5.88) remains the same size.

5.6.3   Injection test 2FRAC3

During chamber test 2FRAC3, six sub-injection tests were carried out at moderately high injection rates of 1, 3, 10, 30, 3, and 30 ml/s. A volume of 850 ml was injected during sub-tests (a), (b), (c), (d), and (e); and 200 ml was injected during (f). Following each sub-injection test, 1000 s was allowed for excess pore pressures to dissipate and the soil stresses to stabilize. Results from the 2FRAC3 simulation are presented in Appendix 5 as Figures A5.91 to A5.100 for sub-test (a) at 1 ml/s, Figures A5.101 to A5.110 for sub-test (b) 3 ml/s, Figures A5.111 to A5.120 for sub-test (c) at 10 ml/s, Figures A5.121 to A5.130 for sub-test (d) at 30 ml/s, Figures A5.131 to A5.140 for sub-test (e) at 3 ml/s, and Figures A5.141 to 5.150 for sub-test (f) at 30 ml/s.

A small amount of yielding occurs near the injection well during sub-test (a) at 1.0 ml/s (Figure A5.91 and A5.92). A zone of increased pore pressure develops (Figure A5.96) with

197

the 50 kPa contour at 0.21 m from the well. The horizontal effective stress is reduced above and below the injection point, and directly to the side of the well (Figure A5.93). The vertical effective stress is reduced within a bulb of soil located to the side of the well (Figure A5.94). The tangential effective stress is reduced in a semi-circular zone surrounding the well (Figure A5.95). The zone of maximum stress ratio is located approximately 100 mm to the side of the well (Figure A5.97). No permeability enhancement has occurred (Figure A5.97).

There is a substantial increase in the size of the yield zone at the end of sub-test (b) at 3 ml/s (Figure A5.101 and Figure A5.102). The zone of increased pore pressure has grown substantially (Figure A5.106) and the 50 kPa contour is 0.32 m from the well. The zone of reduced horizontal effective stress to the side of the well has extended further outwards from the well and the magnitude of the maximum stress reduction has increased (Figure A5.103). The vertical effective stress has increased a small amount above and below the point of injection, however the bulb of decreased vertical effective stress to the side of the well has grown (Figure A5.104). The tangential effective stress is reduced over a substantial area with the greatest reduction occurring near the yield zone (Figure A5.105). The region of elevated stress ratio is "tooth like" in appearance and surrounds the yield zone on three sides (Figure A5.107). The region of enhanced permeability extends 0.14 m from the well (Figure A5.108).

At the end of sub-test (c) at 10 ml/s, the size of the yield zone has again grown significantly (Figure A5.111 and A5.112). The size of the excess pore pressure region has increased with the 50 kPa contour at 0.38 m from the well (Figure A5.116). The leading edge of the pore

pressure front is becoming flatter which may indicate that the boundaries of the chamber are having a greater influence on the process. The zone of decreased effective stress (horizontal, vertical, and tangential) is primarily within a thin band that has developed and extends horizontally outwards from the well (Figure A5.113, A5.114 and A5.115). There is still a zone of decreased effective stress (horizontal and tangential) above and below the injection interval, however, the size of the region of increased vertical effective stress has increased within this zone. The zone of elevated stress ratio has grown but still remains tooth like in appearance (Figure A5.117). The region of enhanced permeability now extends horizontally outwards from the well for 0.29 m (Figure A5.118).

At the end of sub-test (d) at 30 ml/s, the yield zone has again increased in size and extends approximately 75% of the width of the chamber (Figure A5.121 and Figure A5.122). The excess pore pressure front has grown and the 50 kPa contour is now 0.44 m from the well (Figure A5.126). The pore pressure front has become flatter in shape with a more pointed leading edge. The effective stress distribution (Figures A5.123, A5.124 and A5.125) is similar in appearance to sub-test (c), however, areas of reduced vertical effective stress have developed above and below the tip of the yield zone. The zone of elevated stress ratio is approximately the same shape but has grown in size (Figure A5.127). The region of enhanced permeability extends horizontally outwards from the well for 0.41 m (Figure A5.128).

At the end of sub-test (e) at a reduced injection rate of 3 ml/s, the yield zone has increased in size by a small amount and is actively yielding near the tip (Figure A5.131 and Figure

199

A5.132). The zone of pore pressure increase has grown and the 50 kPa contour is now 0.51 m from the well (Figure A5.136). The magnitude of the pore pressure increase within the yield zone has decreased from sub-test (d). There are now regions of increased effective stress (horizontal, vertical and tangential) above and below the body of the yield zone (Figure A5.133, A5.134 and Figure A5.135), and decreased effective stress within the yield zone. The zone of decreased vertical effective stress at, above and below the tip of the yield zone has grown and extended to the chamber wall. There are only small changes in the shape of the stress ratio distribution (Figure A5.137). The region of enhanced permeability is approximately the same size as for sub-test (d) (Figure A5.138).

The size of the yield zone remains the same at the end of sub-test (f) at 30 ml/s (Figure A5.141 and A5.142) as it was at the end of sub-test (e). The excess pore pressure front has decreased in size a small amount and is 0.47 m to the 50 kPa contour (Figure A5.146), although the magnitude of the pore pressure increase within the yield zone has increased. The shape of the effective stress distributions (Figure A5.143, A5.144, and A5.145) are similar to sub-test (e), however, the vertical effective stress increase is greater above and below the body of the yield zone for (f). Again, the stress ratio distribution (Figure A5.147), and the region of enhanced permeability (Figure A5.148) are approximately the same as for sub-tests (d) and (e).

5.6.4   Injection test 2FRAC4

A fluid volume of 250 ml was injected at 30 ml/s during test 2FRAC4. Results from the 2FRAC4 simulation are presented in Appendix 5 as Figures A5.151 to A5.160.

A horizontal disc-shaped yield zone has developed as indicated by Figures A5.151 and A5.152. There is an elliptical shaped region of increased pore pressure with the 50 kPa contour located about 0.25 m from the well (Figure A5.156). There are small regions located near the tip of the yield zone, above the well, and below the well, where the pore pressure has decreased by about 50 kPa. The maximum excess pore pressure within the yield zone is approximately 550 kPa at the point of injection. The effective stress (horizontal, vertical, and tangential) is decreased near the yield zone where the pore pressure increase is largest, and there is an increase in effective stress above and below the yield zone (Figure A5.153, A5.154 and A5.155). The stress ratio distribution is tooth like in appearance and surrounds the yield zone (Figure A5.157). A zone of enhanced permeability has developed that extends 0.22 m from the well (Figure A5.158).

5.6.5   Injection test 2FRAC5

A fluid volume of 260 ml was injected at 200 ml/s during test 2FRAC5. Results from the 2FRAC5 simulation are presented in Appendix 5 as Figures A5.161 to A5.170.

A horizontal disc-shaped yield zone has developed as indicated by Figures A5.161 and A5.162. A region of increased pore pressure of similar shape has developed with the 50 kPa contour located about 0.23 m from the well (Figure A5.166). There is a region around most of the perimeter of the yield zone where the pore pressure has decreased by as much as 150 kPa. The maximum excess pore pressure within the yield zone is greater than 1000 kPa at the point of injection. The effective stress (horizontal, vertical, and tangential) has decreased within the yield zone where the pore pressure increase is largest, and there is a large increase in effective stress above and below the yield zone (Figure A5.163, A5.164 and A5.165). The stress ratio is greatest around the perimeter of the yield zone where much of the active yielding is taking place (Figure A5.167). A zone of enhanced permeability has developed that extends 0.22 m from the well (Figure A5.167).

5.6.6   Injection test 3FRACI

A fluid volume of 900 ml was injected at 41 ml/s during test 3FRACI. Results from the 3FRACI simulation are presented in Appendix 5 as Figures A5.171 to A5.180.

At the end of test 3FRACI, the yield zone extends approximately 0.31 m horizontally outwards from the injection well (Figure A5.171 and A5.172). There are approximately 6 or 7 grid zones, extending vertically downwards from near the bottom of the injection well, that have yielded during the simulation. The shape of this region of the yield

zone is unusual in that it has not been observed in any of the other simulations. It is believed to be a result of the mesh configuration rather than the behaviour of the soil. A large bulb of increased pore pressure surrounds the yield zone (Figure A5.176), with the 50 kPa contour located 0.320 m from the well. The horizontal effective stress is reduced within the yield zone and increased above and below the yield zone and outside the tip (Figure A5.173). The vertical effective stress and tangential effective stress are reduced within the yield zone and increased above and below the point of injection (Figures A5.174 and A5.175). The stress ratio is greatest in those zones that are actively yielding (Figure A5.177). The region of enhanced permeability now extends about 0.28 m from the well (Figure A5.178).

5.6.7   Injection test 3FRAC2

A fluid volume of 900 ml was injected at 41 ml/s during test 3FRAC2. Results from the 3FRAC2 simulation are presented in Appendix 5 as Figures A5.181 to A5.190.

At the end of test 3FRAC1, the yield zone extends approximately 0.42 m horizontally outwards from the injection well (Figure A5.181 and Figure A5.182). A large bulb of increased pore pressure surrounds the yield zone (Figure A5.186), with the 50 kPa contour located 0.38 m from the well. A region of reduced pore pressure is located adjacent the tip of the yield zone. The horizontal effective stress is reduced within the yield zone and increased above and below the yield zone (Figure A5.183). The vertical effective stress and

tangential effective stress are reduced within the yield zone and increased above and below the point of injection (Figures A5.184 and A5.185). The stress ratio is greatest in those zones that are actively yielding (Figure A5.187). The region of enhanced permeability now extends about 0.37 m from the well (Figure A5.188).

5.6.8   Injection test 3FRAC3

A fluid volume of 900 ml was injected at 200 ml/s during test 3FRAC3. Results from the 3FRAC3 simulation are presented in Appendix 5 as Figures A5.191 to A5.200.

At the end of test 3FRAC3, the yield zone extends approximately 0.40 m horizontally outwards from the injection well (Figure A5.191 and A5.192). A bulb of increased pore pressure surrounds the yield zone (Figure A5.196), with the 50 kPa contour located 0.35 m from the well. Regions of reduced pressure are located above and below the point of injection and adjacent the tip of the yield zone. The effective stresses (horizontal, vertical and tangential) are reduced within the yield zone and increased above and below the yield zone (Figures A5.193, A5.194 and A5.195). The shape of the stress ratio distribution is similar to that observed in previous simulations (Figure A5.197). The region of enhanced permeability now extends about 0.35 m from the well (Figure A5.198).

5.6.9 Injection test 3FRAC4

A fluid volume of 900 ml was injected at 200 ml/s during test 3FRAC4. The test was similar to 3FRAC3 but with greater horizontal and vertical effective stresses. Results from the 3FRAC4 simulation are presented in Appendix 5 as Figures A5.201 to A5.210.

At the end of test 3FRAC4, the yield zone extends approximately 0.36 m horizontally outwards from the injection well (Figure A5.201 and A5.202). A bulb of increased pore pressure surrounds the yield zone (Figure A5.206), with the 50 kPa contour located 0.35 m from the well. Regions of reduced pressure are located above and below the point of injection and adjacent the tip of the yield zone. The effective stresses (horizontal, vertical and tangential) are reduced within the yield zone and increased above and below the yield zone (Figures A5.203, A5.204 and A5.205). The stress ratio distribution is similar in appearance to that observed in previous simulations (Figure A5.207). The region of enhanced permeability now extends about 0.35 m from the well (Figure A5.208).

5.6.10 Injection test 3FRAC5

A fluid volume of 900 ml was injected at 200 ml/s during test 3FRAC5. The chamber test incorporated a 6.4 mm high by 84.2 mm diameter V-notch on the injection well. The grid used for the simulation did not include a notch but had fluid injected over a 15 mm interval.

Results from the 3FRAC5 simulation are presented in Appendix 5 as Figures A5.211 to A5.220.

At the end of injection, the yield zone was very extensive, reaching the model boundaries on the top, bottom and sides (Figure A5.211). The plastic shear strain was very large at the injection point and extended a substantial distance from the well (Figure A5.212). The mesh configuration has obviously influenced the yield zone development. The zone of pore pressure increase is relatively small (Figure A5.216). The region of permeability enhancement extends approximately 0.47 m horizontally from the well (Figure A5.218).

5.6.11 Injection test 3FRAC6

A fluid volume of 300 ml was injected at 200 ml/s during test 3FRAC6. The test was similar to 3FRAC5 except that fluid was injected for 1.5 s rather than 4.5 sec. The chamber test incorporated a 6.4 mm high by 84.2 mm diameter V-notch on the injection well. The grid used for the simulation did not include a notch but had fluid injected over a 15 mm interval. Results from the 3FRAC6 simulation are presented in Appendix 5 as Figures A5.221 to A5.230.

A large yield zone has developed (Figure A5.221) around the well with very large plastic strains at the well (Figure A5.222). Very large increases in the effective stress occur (Figure

206

A5.223, A5.224, A5.225) just outside a relatively small region of pore pressure increase (Figure A5.226). The stress ratio is greatest approximately 0.35 m from the well over a 0.2 m high region (Figure A5.227). The zone of permeability enhancement extends 0.3 m horizontally from the well (Figure A5.228).
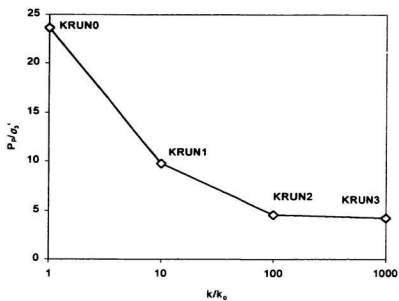
Figure 5.5. Injection pressure variation due to permeability enhancement

5.7 Results of Field Experiment Simulations

The results of field experiment simulations are presented using the same format and sign convention as was described in section 5.6 and used for the chamber test simulations. Results from the field test simulations are presented in Appendix 5.

5.7.1 Field test FLDTST1

A fluid volume of 114 litres was injected at 0.631 l/s during test FLDTST1, from a vertical well with a 0.5 m high screen located at a depth of 1.5 m. In the field test, fluid appeared at the ground surface after injecting for 120 sec. The results of the numerical simulation are presented at an injection time of 50 s in Figures A5.231 to A5.240 in Appendix 5.

The yield zone extends from approximately 3 m depth to the ground surface and extends approximately 1.4 m from the well over much of this region (Figure A5.231). At the ground surface the yield zone extends approximately 3.2 m outwards from the injection well. The plastic shear strain contours show a shear band developing near the top of the injection interval and extending horizontally outwards for about 1 m before rising vertically to the ground surface (Figure A5.232). The orientation of the yield zone is likely influenced to some degree by the configuration of the mesh used in the analysis. There are zones of increased effective stress (Figure A5.233, A5.234, A5.235) located immediately above and below the

region of elevated pore pressure near the point of injection (Figure A5.236). The region of maximum stress ratio (Figure A5.237) is located slightly outside the region where the shear band has developed, and rises outward and upward to intersect the ground surface approximately 1.5 m from the well. The zone of permeability enhancement is very similar in shape (Figure A5.238) to the region of large plastic strains shown in Figure A5.232).

5.7.2 Field test FLDTST2

A fluid volume of 719 litres was injected at 0.631 l/s during test FLDTST2, from a horizontal well with a 3 m long screen located at a depth of 2.3 m. The results of the numerical simulation are presented at an injection time of 100 s in Figures A5.241 to A5.250 in Appendix 5.

After 100 s of injection, a thin nearly horizontal yield zone has formed extending approximately 1.3 m from the injection well (Figure A5.241 and A5.242). The effective stress (Figure A5.243, A5.244, A5.245) has decreased within a long narrow zone of pore pressure increase (Figure A5.246) and the effective stress has increased above and below the region of increased pore pressure. The stress ratio is greatest in a thin region around the perimeter of the yield zone (Figure A5.247). The region of enhanced permeability extends approximately 1.1 m horizontally from the injection well (Figure A5.248).

5.8   Results of Centrifuge Experiment Simulations

All numerical simulations for the centrifuge tests were carried out at model scale. The results of centrifuge test simulations are presented using the same format and sign convention as was described in section 5.6 and used for the chamber test simulations. Results from the centrifuge test simulations are presented in Appendix 5.

5.8.1   Centrifuge test CCFS01 A

A fluid volume of 33 ml was injected into Speswhite kaolin at 0.029 ml/s from a 200 mm deep vertical injection well at 50 g. Results from CCFS01A are presented in Appendix 5 as Figures A5.251 to A5.260.

After 1150 s of injection time, a triangular shaped yield zone has formed that extends approximately 0.075 m outwards and approximately 0.035 m upwards from the top of the injection interval (Figures A5.251 and A5.252). A shear band has formed near the upper surface of the yield zone. The effective stress (Figure A5.253, A5.254, and A5.255) is reduced in the region of soil where yielding has occurred and which has an increased pore pressure (Figure A5.256). The stress ratio (Figure A5.257) is greatest near the outer perimeter of the yield zone. The zone of permeability enhancement extends approximately 0.06 m from the well (Figure A5.258).

5.8.2 Centrifuge test CCFS01 B

A fluid volume of 33 ml was injected into Speswhite kaolin at 0.29 ml/s from a 200 mm deep vertical injection well at 50 g. Results from CCFS01B are presented in Appendix 5 as Figures A5.261 to A5.270.

After 115 s of injection time, a yield zone has formed that is nearly centred around the well and which extends approximately 0.09 m outwards at the top of the injection interval (Figures A5.261 and A5.262). Two distinct shear bands have formed which originate just above and below the top and bottom of the injection interval. The effective stress (Figure A5.263, A5.264, and A5.265) is reduced in the region of increased pore pressure (Figure A5.266) where yielding has occurred. Outside of the zone of increased pore pressure, there is a zone of reduced pore pressure where the effective stress has increased. The stress ratio (Figure A5.267) is greatest near the outer perimeter of the yield zone, particularly at the tip of the upper shear band. The zone of permeability enhancement extends approximately 0.08 m from the well (A5.268).

5.8.3 Centrifuge test CCFS01 C

A fluid volume of 33 ml was injected into Speswhite kaolin at 0.029 ml/s from a 100 mm deep vertical injection well at 50 g. Results from CCFS01C are presented in Appendix 5 as Figures

AS.271 to AS.280.

After 1150 s of injection time, a yield zone has formed that extends approximately 0.11 m outwards from the injection interval (Figures AS.271 and AS.272). There are no clearly defined shear bands within the yield zone, however, it appears that a band is beginning to form at the bottom of the injection interval. There has been yielding of soil at the ground surface. The effective stress (Figure AS.273, AS.274, and AS.275) is reduced in the region of soil where yielding has occurred and which has an increased pore pressure (Figure AS.276. The stress ratio (Figure AS.277) is greatest near the upper surface of the yield zone. The zone of permeability enhancement is discontinuous to approximately 0.08 m from the well (Figure AS.278).

5.8.4   Centrifuge test CCP501 D

A fluid volume of 33 ml was injected into Speswhite kaolin at 0.29 ml/s from a 100 mm deep vertical injection well at 50 g. Results from CCP501D are presented in Appendix 5 as Figures AS.281 to AS.290.

After 115 s of injection time, a yield zone has formed which extends approximately 0.10 m outwards at the top of the injection interval (Figures AS.281 and AS.282) and extends to the ground surface. Two distinct shear bands have formed which originate just above and below

the top and bottom of the injection interval. The effective stress (Figure A5.283, A5.284, and A5.285) is reduced in the region of increased pore pressure (Figure A5.286) where yielding has occurred. Outside of the zone of increased pore pressure, there is a zone of reduced pore pressure where the effective stress has increased. The stress ratio (Figure A5.287) is greatest near the outer perimeter of the yield zone, particularly at the tip of the upper shear band. The zone of permeability enhancement extends approximately 0.09 m from the well (A5.288).

5.8.5 Centrifuge test CCFS02 E

A fluid volume of 47 ml was injected into Speswhite kaolin at 2.9 ml/s from a 200 mm deep vertical injection well at 50 g. Results from CCFS01E are presented in Appendix 5 as Figures A5.291 to A5.300.

After 16.5 s of injection time, a very large yield zone has formed which is centred around the injection interval and which extends approximately 0.25 m outwards from the well (Figures A5.291 and A5.292). There is extensive plastic straining near the point of injection, however, no distinct shear bands have formed. The effective stress (Figure A5.293, A5.294, and A5.295) is reduced in the region of increased pore pressure (Figure A5.296) around the point of injection. Outside of the zone of increased pore pressure, there is a zone of reduced pore pressure where the effective stress has increased. The stress ratio (Figure A5.297) is greatest about 0.12 m horizontally outwards from the well. The zone of permeability enhancement

extends well above and below the top of the injection interval and for approximately 0.12 m outwards from the well (A5.298).

5.8.6 Centrifuge test CCFS02 F

A fluid volume of 47 ml was injected into Speswhite kaolin at 0.014 ml/s from a 200 mm deep vertical injection well at 50 g. Results from CCFS01F are presented in Appendix 5 as Figures A5.301 to A5.310.

After 3300 s of injection time, a yield zone has formed that extends approximately 0.07 m outwards and approximately 0.06 m upwards from the top of the injection interval (Figures A5.301 and A5.302). A shear band has formed near the upper surface of the yield zone. The effective stress (Figure A5.303, A5.304, and A5.305) is reduced in a tall narrow region of soil which has an increased pore pressure (Figure A5.306). The stress ratio (Figure A5.307) is greatest near the tip of the shear band and adjacent the bottom of the injection interval. The zone of permeability enhancement extends about 0.06 m from the well (Figure A5.308).

5.8.7 Centrifuge test CCFS02 G

A fluid volume of 33 ml was injected into Speswhite kaolin at 0.014 ml/s from a 100 mm deep

vertical injection well at 50 g. Results from CCFS01G are presented in Appendix 5 as Figures A5.311 to A5.320.

After 2300 s of injection time, a yield zone has formed that extends approximately 0.1 m outwards from the injection interval (Figures A5.311 and A5.312). There are no clearly defined shear bands within the yield zone, however, it appears that bands may be beginning to form at the top and bottom of the injection interval. There has been fairly extensive yielding of soil at the ground surface. The effective stress (Figure A5.313, A5.314, and A5.315) is reduced in the region of soil where yielding has occurred and which has an increased pore pressure (Figure A5.316). The stress ratio (Figure A5.317) is greatest near the upper surface of the yield zone. The zone of permeability enhancement extends approximately 0.07 m from the well (Figure A5.318).

5.8.8   Centrifuge test CCFS02 H

A valve was opened late during centrifuge test CCFS02G which resulted in a large jump in pressure at the wellhead early in the test. The test was repeated as CCFS02H under the same test conditions as CCFS02G. The simulation results for CCFS02H are, therefore, identical to those for CCFS02G, although the experimental results are somewhat different. See the results of CCFS02G presented in Figures A5.311 to A5.320 in Appendix 5.

5.8.9 Centrifuge test CCFS03 I

A fluid volume of 46 ml was injected into silty sand at 0.029 ml/s from a 200 mm deep vertical injection well at 50 g. Results from CCFS01I are presented in Appendix 5 as Figures A5.321 to A5.330.

There was no yielding after 1420 s of injection as indicated by Figures A5.321 and A5.322. There was a very small region of reduced effective stress (Figures A5.323, A5.324, A5.325) near the point of injection where the pore pressure was slightly increased (Figure A5.326). The stress ratio at the point of injection is only marginally increased (Figure A5.327). No permeability enhancement was observed (Figure A5.328).

5.8.10 Centrifuge test CCFS03 J

A fluid volume of 46 ml was injected into silty sand at 0.29 ml/s from a 200 mm deep vertical injection well at 50 g. Results from CCFS01J are presented in Appendix 5 as Figures A5.331 to A5.340.

There was no yielding after 160 s of injection as indicated by Figures A5.331 and A5.332. There were relatively large regions of reduced effective stress (Figures A5.333, A5.334, A5.335) near the point of injection where the pore pressure was increased (Figure A5.336).

The stress ratio has increased substantially right at the point of injection, however, it drops off rapidly (Figure A5.337). No permeability enhancement was observed (Figure A5.338).

5.8.11 Centrifuge test CCFS03 K

A fluid volume of 31 ml was injected into silty sand at 0.029 ml/s from a 100 mm deep vertical injection well at 50 g. Results from CCFS01K are presented in Appendix 5 as Figures A5.341 to A5.350.

There was no yielding after 457 s of injection as indicated by Figures A5.341 and A5.342. There was a small region of reduced effective stress (Figures A5.343, A5.344, A5.345) near the point of injection where the pore pressure was increased (Figure A5.346). The stress ratio has increased only marginally at the point of injection (Figure A5.347). No permeability enhancement was observed (Figure A5.348).

5.8.12 Centrifuge test CCFS03 L

A fluid volume of 31 ml was injected into silty sand at 0.29 ml/s from a 100 mm deep vertical injection well at 50 g. Results from CCFS01L are presented in Appendix 5 as Figures A5.351 to A5.360.

There was a very small (0.02 m wide) yield zone near the injection well and at the ground surface after 1100 s of injection as indicated by Figures A5.351 and A5.352. There was a relatively large region of reduced effective stress (Figures A5.353, A5.354, A5.355) within the zone where the pore pressure was increased (Figure A5.356). The stress ratio is quite large at the point of injection (Figure A5.357) where yielding has occurred. No permeability enhancement was observed (Figure A5.358).

5.8.13 Centrifuge test CCFS04 M

A fluid volume of 22 ml was injected into silty sand at 0.057 ml/s from a 200 mm deep vertical injection well at 25 g. Results from CCFS01M are presented in Appendix 5 as Figures A5.361 to A5.370.

No yielding had occurred after 273 s of injection as indicated by Figures A5.361 and A5.362. There was a very small region of reduced effective stress (Figures A5.363, A5.364, A5.365) within the zone where the pore pressure was increased (Figure A5.366). The stress ratio is slightly elevated at the point of injection (Figure A5.367). No permeability enhancement was observed (Figure A5.368).

5.8.14 Centrifuge test CCFS04 N

A fluid volume of 50 ml was injected into silty sand at 0.29 ml/s from a 200 mm deep vertical injection well at 25 g. Results from CCFS01N are presented in Appendix 5 as Figures A5.371 to A5.380.

A small yield zone has developed near the injection point after 174 s of injection as indicated by Figures A5.371 and A5.372. There is a region of reduced effective stress (Figures A5.373, A5.374, A5.375) within a relatively large zone where the pore pressure has increased (Figure A5.376). The stress ratio is quite large at the point of injection (Figure A5.377) where yielding has occurred. No permeability enhancement was observed (Figure A5.378).

5.9   Summary

Numerical simulations of chamber, field, and centrifuge injection tests were carried out using the finite difference computer program FLAC. The numerical model established for these analyses incorporated full coupling between groundwater flow and mechanical response. In the analyses, fluid was injected into the soil at a constant flow rate. Stress/strain computations due to pore pressure changes within the soil were carried out using a strain softening constitutive model.

A FISH function was used to enhance the permeability in zones where plastic shear strains exceeded a critical value. The implementation of a permeability enhancement function allowed shear bands to develop in the soil due to fluid injection. A permeability enhancement factor of 100 provided good correspondence between experimental and numerical results in terms of pressure response and yield zone development.

A breakdown of the 38 numerical simulations carried out during this study is as follows:

- 4 runs: effect of permeability enhancement on the injection process,

- 19 runs: Phase 2 and Phase 3 chamber tests carried out by Golder Associates (1992 and 1994),

- 2 runs: field tests at the Environmental Test Facility in Argentia, NF,

- 7 runs: centrifuge injection tests in Speswhite kaolin clay

- 6 runs: centrifuge injection tests in silty sand

Results of all numerical simulations are presented in a standard format in Appendix 5 that includes extent of yield zone, contours of plastic shear strain, effective stress changes due to fluid injection (horizontal, vertical and tangential), stress ratio, permeability enhancement, pore pressure histories, and stress path plots.

CHAPTER 6 - DISCUSSION

6.1 General

This chapter presents a discussion of the mechanisms involved in the fluid injection process and the parameters that influence those mechanisms. The discussion is supported by observations and results from injection tests carried out in the field, in a calibration chamber, and in a large geotechnical centrifuge; and also by the results of numerical simulations.

The discussions presented in this chapter are primarily applicable to soils where the ratio of horizontal to vertical effective stress (σ_h'/σ_v') is greater than unity (i.e. K>1). A soil with K<1 is likely to be normally or lightly overconsolidated and will usually decrease in volume (and porosity) when sheared. With a reduction in porosity, there is generally a corresponding decrease in permeability. Soils with K>1 are often heavily overconsolidated and very dense. It is these soils that are most likely to be dilatant, exhibit a strain softening behaviour, and develop bands during shear. The porosity of the soil increases along the shear band due to dilatancy and the connectivity of the pores increases due to shear displacement (Dusseault, and Rothenburg, 1988). The result is that the shear bands become preferred flow paths that are more permeable than the original unsheared soil. This work is addressed towards those soils where permeability enhancement due to shear may occur.

6.2   Mechanisms

The four basic mechanisms that play a role in the fluid injection process include: 1) flow through the pore space with no yielding, 2) cavity expansion, 3) yield due to shear, and 4) and yield due to tension. This section includes a discussion of the injection process and the conditions that are necessary for each of these mechanisms to occur.

6.2.1   Flow through pore space without yielding

Flow through the pore space without yielding may occur when the injection rate is too low to generate excess pore pressures large enough to cause yielding of the soil. Flow through the pore space without additional yielding will also occur after the yield zone has grown far enough from the point of injection such that the flow rate is insufficient to cause further extension. In both situations, the injection pressure at the well will rise to a steady-state condition under a constant injection rate while a pressure gradient develops in the surrounding soil as fluid flows through the pore space away from the well.

It is assumed that the injection process results in an increase in pore pressure without changing the total stress; that the soil behaviour is represented by the Mohr-Coulomb failure criteria [Eqn. 6.1]; and that the soil is at some initial anisotropic stress state $(\sigma_{ho}{'}, \sigma_{vi}{'})$ where the horizontal effective stress exceeds the vertical effective stress (i.e. K>1). The initial stress

state is represented by point A in Figure 6.1. The amount by which the pore pressure may be increased without causing yielding of the soil can be determined from geotechnical principles.

$$\tau = c' + \sigma' \tan \phi' \qquad \text{[Eqn. 6.1]}$$

The Mohr-Coulomb failure criterion may be rewritten in terms of the maximum and minimum principal effective stresses at failure [Eqn. 6.2].

$$\sin \varphi' = \frac{\dfrac{\sigma'_{1f} - \sigma'_{3f}}{2}}{\dfrac{\sigma'_{1f} - \sigma'_{3f}}{2} + c \cot \phi'} = \frac{\dfrac{\sigma'_{hf} - \sigma'_{vf}}{2}}{\dfrac{\sigma'_{hf} - \sigma'_{vf}}{2} + c \cot \phi'} \qquad \text{[Eqn. 6.2]}$$

Increasing the pore pressure without changing the total stress will cause the *in situ* effective stresses to be reduced along the path indicated by line AB in Figure 6.1. The magnitude of the pore pressure change (P_e) required to reach the failure condition, B, from the original stress state, A, is expressed by Eqn. 6.3 in terms of the original *in situ* stresses and the soil strength parameters.

$$P_e = \sigma'_{vi} \left[1 - \frac{(K - 1)(1 - \sin \phi')}{2 \sin \phi'} \right] + \frac{c}{\tan \phi'} \qquad \text{[Eqn. 6.3]}$$

A similar relation was presented by Morgenstern and Vaughan (1963) for determining allowable grouting pressures for foundations. In Eqn 6.3, if $P_e \geq \sigma'_{vi}$, yielding would occur in tension. Applying Eqn. 6.3 to the chamber test 2FRAC2 conditions ($u = 200$ kPa, $\sigma'_{vi} = 200$ kPa, $K = 2$, $c' = 0$, and $\phi' = 38°$), the pore pressure increase required to cause yielding is

224

140 kPa. For sub-tests 2FRAC2a and 2FRAC2b carried out at injection rates of 0.28 and 0.40 ml/s, the maximum excess pore pressure measured at the point of injection was 290 kPa and 480 kPs, respectively. Therefore, according to Eqn. 6.3, some yielding should have occurred. The maximum increase in the pore pressure at the point of injection was determined from the numerical simulations to be 269 kPa for test 2FRAC2a and 383 kPa for test 2FRAC2b, which is in good agreement with the measured values. The numerical simulations, however, indicated a very steep pore pressure gradient over a short distance from the well (see Figures A5.46 and A5.56). A few centimetres from the point of injection, the pore pressure remained well below that required to initiate yielding. The simulations indicate that only a very small volume of soil immediately adjacent the well underwent yielding during these two tests, and that much of the fluid flow occurred through the pore space outside of the yield zone.

In CCFS04M, the injection pressure at the wellhead (Figure 4.18) increased to approximately 68 kPa early in the test and remained constant for most of the injection period. The initial jump in pressure, shown in Figure 4.18, occurred when the solenoid was opened prior to the injection pump being switched on. It is believed that the flow rate for this test was sufficiently low that the majority of fluid flow took place through the pore space of the soil. Based on σ'_{vd} = 60 kPa, u = 49 kPa, c' = 0 kPa, ϕ' = 49°, and K = 1.5, the minimum excess pore pressure required to cause yielding is 55 kPa. The measured excess pressure from the centrifuge test was 28 kPa. No yielding of soil occurred during the FLAC simulation of CCFS04M (Figure A5.361), although the peak injection pressure from the simulation was nearly identical to the pressure measured during the centrifuge test.

In addition to test 2FRAC2a, 2FRAC2b, and CCFS04M, several other tests involved flow through the pore space with little or no yielding of the soil surrounding the wellbore including: CCFS03I, CCFS03J, CCFS03K, CCFS03L, CCFS04M, and CCFS04N. Results for these tests are provided in Appendix 5.

6.2.2 Cavity expansion and initial yield

At the start of the injection process, the flow resistance provided by the soil causes the injection pressure to increase. Flow begins to occur through the pore space as a hydraulic gradient develops between the well and the surrounding soil. If the rate of fluid injection is greater than that which may freely occur through the pore space of the soil, there will be a large and rapid increase in pressure as fluid begins to accumulate at the well, displacing the adjacent soil. This type of response is similar to the cavity expansion mechanism that is observed during the early stages of a pressuremeter test.

Although the injection pressure may be quite large, the low permeability soil limits the penetration of the injection fluid, and the zone of increased pore pressure due to injection is initially quite small, dropping off very rapidly over a short distance from the well. The high injection pressure causes a reduction in the horizontal, vertical and tangential effective stress in a very small zone of soil immediately adjacent the point of injection. Outside of this zone, there may be a zone of reduced pore pressure due to the effect of restrained dilation. There

is an increase in the horizontal effective stress to the sides of the well, an increase in the vertical effective stress above and below the point of injection, and an increase in the tangential stress around the well. Figure 6.2 a) is a schematic diagram illustrating the resulting stress field during a cavity expansion stage of the injection process.

The cavity expansion mechanism and associated stress changes described in the previous paragraphs were demonstrated through the numerical simulations carried out for the injection tests. Centrifuge test CCFS02G involved injecting fluid into the wellbore at a rate of 1.4×10^{-5} l/s for 2300 s. After 100 s of fluid injection, a yield zone developed within a very small region near the injection interval (see Figure 6.3). The region where the plastic shear strain is greater than 0.5% (Figure 6.4) is very small and is limited to small zones at the top and bottom of the injection interval. The change in horizontal, vertical and tangential effective stress is shown in Figures 6.5, 6.6 and 6.7, respectively, and the pore pressure change is presented in Figure 6.8. The effective stress decreased within the small region of increased pore pressure at the well. Further away from the well, there is a larger zone where the pore pressure has decreased due to restrained dilation and stress redistribution, and the effective stress has increased.

Initial yielding occurs at the top and bottom of the injection interval, and is primarily due to an increase in the vertical effective stress. The principal stress ratio (σ_h'/σ_v') is shown in Figure 6.9. The stress ratio at the top and bottom of the injection interval has dropped to 0.6 from the original in situ state of 1.6 and the soil is yielding in vertical compression.

227

Permeability enhancement has begun within the yielding zones at the top and bottom of the injection interval (Figure 6.10). In the case of CCFS02G, initial yielding occurred due to shearing. Initial yielding may be either in shear or in tension. The mode of yielding is dependent on the initial *in situ* stress, the soil strength parameters (c', φ'), and the stress path taken to the yield surface.

The results of field and centrifuge injection tests provide additional support for the occurrence of initial yield at the top and bottom of the injection interval. In FLDTST1, post-test excavation revealed that the dye trace originated at the top of the injection interval (see Figure 3.9). Of the eight centrifuge tests carried out in Speswhite kaolin: CCFS01A (Figure 4.50) and CCFS01D (Figure 4.56) had dye traces originating from both the top and bottom of the injection interval; CCFS02F (Figure 4.61) and CCFS02G (Figure 4.63) had a dye trace originating from the bottom of the injection interval; and CCFS01B (Figure 4.53) and CCFS01C (Figure 4.55) each had a dye trace originating just above the top of the injection interval. The remaining two centrifuge tests showed evidence of cavity expansion (i.e. a thick concentrated zone of dyed soil surrounding the point of injection), however, CCFS02E (Figure 4.59) and CCFS02H (Figure 4.64) each had a dye trace initiating about half-way between the top of the injection interval and the ground surface. In both of these wells, the injection fluid travelled up along the soil/well interface for a substantial distance before the dye trace began to extend horizontally outwards.

6.2.3 Shearing

6.2.3.1 Permeability enhancement

A fundamental premise of the soil shearing process is that shear bands develop as a result of fluid injection, and that a preferred flow path is created along the injection induced shear bands where the permeability is greater than within the non-sheared soil. Shearing was identified as a primary mechanism in the SAGD process for enhanced recovery of hydrocarbons from oil sands reservoirs (Chalaturnyk and Scott, 1995; Chalaturnyk, 1996; and Chalaturnyk and Scott, 1997). In their investigations of the SAGD process, permeability enhancement was considered as a result of volumetric strains that occur due to shear stress and mean effective stress changes. Due to the complexity of the thermal-mechanical-groundwater problem posed by the SAGD process, the numerical modelling carried out by these researchers did not include full coupling between groundwater flow and mechanical behaviour, and did not use a strain softening constitutive model. With these limitations in their numerical model, formation and propagation of discrete shear bands was not simulated, and the effects of permeability enhancement on the system were not included.

From the work of researchers such as Morgenstern and Tchalenko (1967), Vardoulakis (1980), Chu et al (1996), and Oda and Kazama (1998) it is known that shear bands are initiated near the peak of the stress-strain curve. It is along these shear bands that increases in permeability are expected. Mori and Tamura (1988) carried out an experimental study in

which the permeability of grouted sand specimens was monitored during shearing in a triaxial cell. The onset of permeability increase required some strain and was relatively abrupt, indicating that some level of path connectivity must be achieved before flow enhancement occurs. Shear displacement, even without volume increase, caused increases in the axial permeability of up to two orders of magnitude. The permeability was not measured in a direction parallel to the induced shear band, but should be substantially greater than in the axial direction.

Post-test excavation and mapping carried out on field, chamber and centrifuge test specimens indicated that, in most cases, a network of discontinuities was created during injection. The exceptions to this were the centrifuge tests in silty sand where the dyed injection fluid penetrated a large volume of soil surrounding the well and masked the presence of any discontinuities that may have developed (see Figures 4.46 to 4.49). The measured and calculated extent of discontinuities are compared in Figure 6.11 as the ratio of the average measured dye trace radius to the radius of the 1% plastic shear strain contour from the FLAC simulations. A ratio of 1 indicates agreement between experimental results and the results of numerical analyses.

If it is assumed that flow occurred entirely within the pore space of the soil without yielding, and the effects of anisotropic permeability, well geometry and gravity are ignored, then the zone of soil containing injection fluid would be approximately spherical in shape. The radius of this sphere may be determined from the porosity and the volume of fluid injected. The ratio

of the average measured dye trace radius to the radius of a sphere (assuming porous flow), is shown in Figure 6.11 for the centrifuge injection tests. The movement of injection fluid during the centrifuge tests in sand (tests I through N), was primarily due to porous flow without yield. These tests have a radii ratio very close to one. In the clay tests (tests A through H), dye was observed along discrete planar features which in some cases extended substantial distances from the point of injection. These tests have a radii ratio substantially greater than one. In the latter cases, the injection fluid travelled a much greater distance than may be explained due to flow through the pore space alone.

The effect of permeability enhancement within the shear bands was investigated in the numerical simulations carried out using the chamber test data. In simulations KRUN0, KRUN1, KRUN2, and KRUN3, the amount of permeability enhancement due to plastic shear strain was varied by factors of 1, 10, 100 and 1000, respectively. The results of these numerical runs indicated that with no permeability enhancement, the yield zone around the injection well grew primarily by a cavity expansion mechanism (see Figure A5.2) and no shear banding was observed. As the permeability was allowed to increase within grid zones where the plastic shear strain exceeded some critical value, distinct shear bands were generated within the soil (see Figures A5.12, A5.22 and A5.32). The thickness of a shear band was found to vary depending on the degree of permeability enhancement used. Where the magnitude of the permeability enhancement was small (i.e. x10), the shear band tended to be quite thick (Figure A5.12), and where the magnitude of the permeability enhancement was greater (i.e. x1000), the shear band was substantially thinner (Figure A5.32).

231

If no permeability enhancement is incorporated in the numerical simulations, the pore pressure calculated at the point of injection is substantially greater than was measured in the field, chamber, and centrifuge injection tests. Incorporating a permeability enhancement factor of 100 results in calculated injection pressures that are in good agreement with those measured during the experiments (Figure 6.12). The ratio between the calculated and measured peak pressure tends to vary with changing injection velocity (Figure 6.13). It is unlikely that this is due to the test conditions, as trend lines plotted in Figure 6.13 for the chamber test data and the centrifuge test data show similar slopes for the two different types of tests. This suggests that the numerical model is not capturing some aspect of the injection process. A possible explanation for this response may be that the amount of permeability enhancement increases with increasing injection velocity. The larger pressures resulting from the higher injection rates may result in physical separation between the upper and lower surface of shear band, which allows more flow with less resistance.

As was mentioned in Chapter 5, FLAC will correctly model the physics of shear band development, however, the spacing and thickness of any shear bands that develop are mesh dependent. Therefore, the amount of permeability enhancement that is required to obtain good comparison between experimentally measured injection pressures and numerically determined injection pressures is also mesh dependent.

6.2.3.2 Stress path to the yield envelope

Various researchers have presented stress paths for soil elements undergoing pore pressure increases due to fluid injection. Kosar and Been (1991), presented a stress path that represents the behaviour of Athabasca Oil Sands at a fracture face during a fluid injection and production cycle. Similarly, Chalaturnyk and Scott (1997) indicated that the major stress path to the failure surface during the steam assisted gravity drainage process is due to a combination of injection induced pore pressure increase and thermal influence (Figure 2.5).

Yielding due to shearing (Figure 6.1), will occur in an element of soil if the effective stress path due to fluid injection touches the Mohr-Coulomb (K>1) envelope to the right of point C or if the effective stress path touches the Mohr-Coulomb (K<1) envelope above point E. In Section 6.2.1, it was indicated that the pore pressure increase required to reduce the *in situ* effective stress to the yield envelope could be determined using Eqn. 6.3. This expression assumes that the pore pressure increases during fluid injection with no change in total stress. The results of numerical simulations indicate that this assumption is only correct for some situations, as the injection process usually results in some changes to the total stress regime.

Where the zone of increased pore pressure is expanding slowly due to the injection rate being only marginally greater than the rate of pore pressure dissipation, there are only small changes in total stress, and the stress path to the yield surface is nearly parallel to the K=1 line. As the injection rate increases relative to the rate of pore pressure dissipation, there are greater and

greater changes in total stress. This is illustrated in Figure 6.14 where stress paths are plotted for soil element i=17, j=26 which is located within the path of a developing shear band (see Table 5.4 and Figure 5.3). Stress paths are shown for chamber test simulations 2FRAC2c, 2FRAC3b, 2FRAC4, and 2FRAC5 which were carried out at injection rates of 0.001, 0.003, 0.030, and 0.200 l/s, respectively. This figure clearly shows that increasing the injection rate results in stress paths that deviate more and more from being parallel with the K=1 line.

The location of a soil element with respect to the point of injection and the developing shear band(s) also plays a large role in the stress changes the element may experience. Figure 6.2 shows the typical stress conditions that may exist during the evolution of a yield zone during the fluid injection process at, (a) the initial cavity expansion stage, (b) a transitional stage as the shear band is just beginning to develop, and (c) during extension of the shear band. A soil element that is within the path of the growing yield zone (i.e. element i=17, j=26 discussed in the previous paragraph) will experience a stress path that is substantially different than a soil element located within the region above or below the yield zone. Stress paths are plotted in Figure 6.15 for a typical soil element (i=9, j=34) located above the developing shear band (see Table 5.4 and Figure 5.3). The stress paths shown are for chamber test simulations 2FRAC2c, 2FRAC3b, 2FRAC4, and 2FRAC5 which were carried out at injection rates of 0.001, 0.003, 0.030, and 0.200 l/s, respectively.

6.2.4 Yield in tension

After the effective stress has been reduced to the point where shear yield occurs, i.e. point B in Figure 6.1, an additional increase in pore pressure will further reduce the horizontal and vertical effective stresses along the path indicated by BC on the yield surface. For strain softening soils, the stress path would be similar to that shown by BC'. When the soil reaches point C or C' on the yield surface, the vertical effective stress is zero and any further yielding will be in tension. The tensile yield condition may also be achieved without the occurrence of shear yielding if the stress path from the initial stress condition is similar to that indicated by line DC in Figure 6.1. When tensile yielding occurs, there is normally a rapid loss in tensile strength which may initiate a tensile parting within the soil.

The pore pressure near the tip of the shear band increases quite rapidly as the permeability increases due to accumulated plastic strain. With the increased pore pressure, there is a corresponding decrease in the effective stress. The stress path of an element of soil located near the leading edge of the shear band will move rapidly along the yield surface towards the tensile yield zone (Figure 6.14). The result is yielding in tension and tensile parting of the soil along shear bands. The development of tension zones are modelled in the FLAC simulations, however, physical parting of soil along shear bands is not modelled.

In the numerical simulations carried out for the shallow injection well tests, a large yield zone developed near the ground surface above the injection well (see for example Figure A5.271

235

from CCFS01C). Yielding within this zone was generally in tension as the soil dilated and deformed vertically during the injection process. This yield zone develops under a K<1 condition due to a combination of vertical stress increase and horizontal stress decrease.
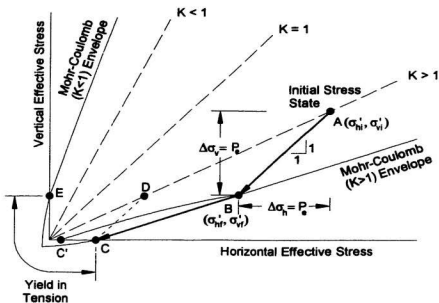
Figure 6.1. Pore pressure change required to cause shear failure
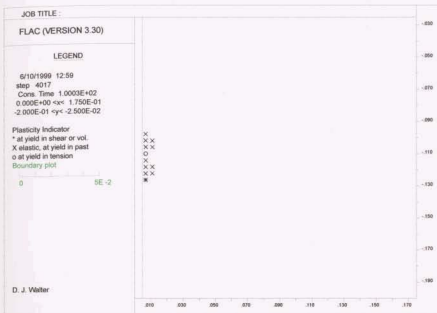
Figure 6.3 Extent of yield zone at t=100 s (CCFS02G)

Figure 6.4 Plastic strain contours at t=100s (CCFS02G)
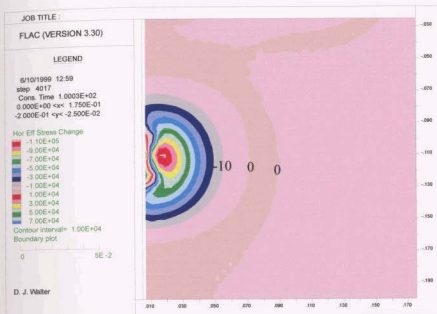
Figure 6.5 Change in horizontal effective stress at t=100 s (CCFS02G)
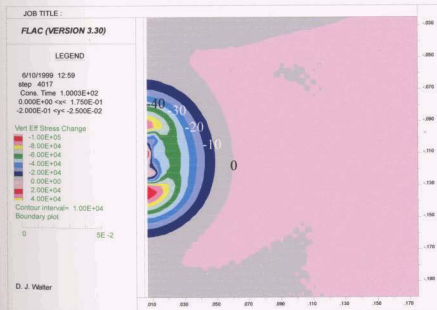
Figure 6.6 Change in vertical effective stress at t=100 s (CCFS02G)
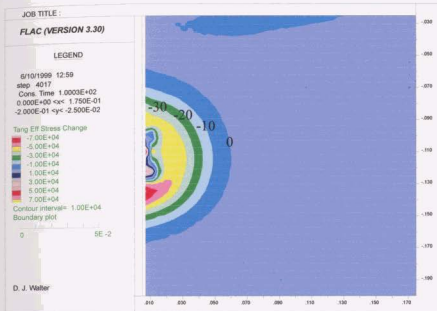
Figure 6.7 Change in tangential effective stress at t=100 s (CCFS02G)
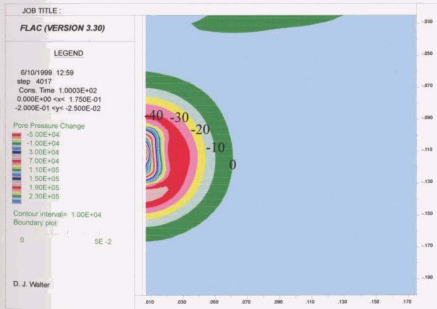
Figure 6.8 Change in pore pressure at t=100 s (CCFS02G)
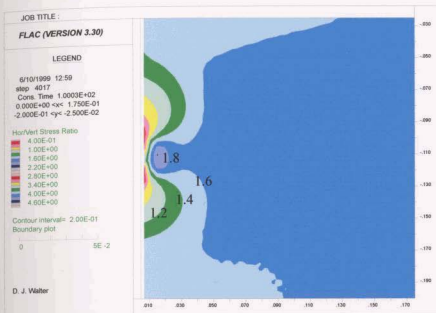
Figure 6.9 Stress ratio σ'_x/σ'_y at t=100 s (CCFS02G)

Figure 6.10 FLAC permeability at t=100 s (CCFS02G)
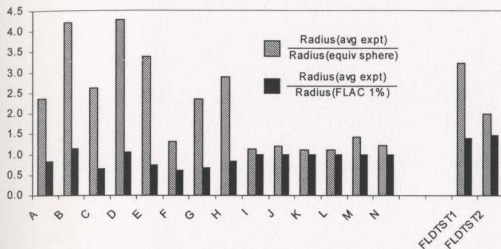
Figure 6.11. Extent of dye traces from centrifuge and field tests
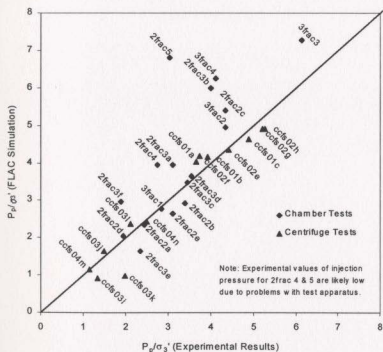
Figure 6.12. Comparison of experimental and FLAC peak injection pressures

243
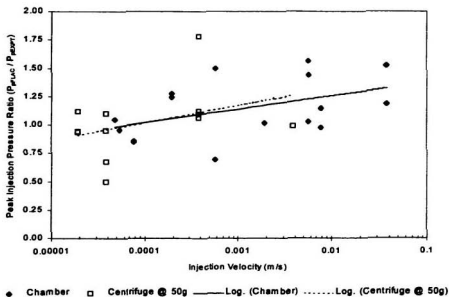
Figure 6.13. Variation of peak injection pressure ratio with injection velocity
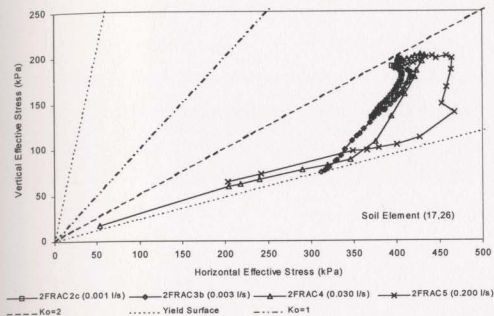
Figure 6.14. Stress path of an element within the zone of shear band development
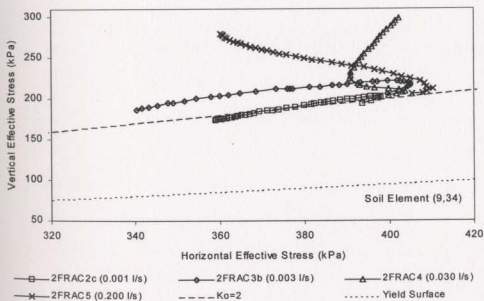
Figure 6.15. Stress path of an element above the zone of shear band development

245

6.3   Influencing Factors

The previous sections of this chapter addressed the mechanisms that occur due to fluid injection, ie. flow through the pore space without yield, cavity expansion, shearing, and tensile parting. The following paragraphs discuss how variations in key parameters, such as those shown in Figure 1.1, may influence the injection process.

6.3.1   Fluid injection parameters

6.3.1.1 Injection zone details

There are several geometrical parameters that may be varied including the injection depth, the surface area of the zone through which the fluid is injected into the soil, the use of a pre-formed slot, and the use of horizontal versus vertical wellbores.

Changing the depth of the injection zone may have a marked influence on the injection process due to changes in the magnitude of the overburden stress, σ_v, and the principal stress ratio, K. The effect of changing these parameters is discussed later in Section 6.3.2.1 - Soil stress state.

Either the well diameter or the length of the injection interval may be varied to change the

246

surface area through which fluid is injected into the soil from the wellbore. Experimental results indicate that the injection pressure has some dependence on the injection velocity. For injection tests carried out at identical volumetric flow rates in small diameter and large diameter wells of the same injection interval, the injection velocity and the initial injection pressure will be greater in the small diameter well and lower in the large diameter well. It is expected that after initial yielding has occurred and shear bands begin to develop at the wellbore, the flow of injection fluids from both wells would become concentrated in the areas of enhanced permeability. Thus with approximately equal rates of fluid flow within the shear band, the final size and shape of the yield zones should be very similar for both wells.

Alternatively, where fluid is injected in two vertical wells of the same diameter but with different injection intervals, the initial injection pressure will be greater in the shorter injection interval due to the higher injection velocity. After the injection process has been carried out for some time, the size and shape of the yield zones in the wells with long and short injection intervals may be quite different due to differences in the stress fields that develop around the wells. The centrifuge tests carried out in clay with an injection interval of 1.25 m (prototype scale) had a tendency for shear bands to initiate above the top and below the bottom of the injection interval, and extend horizontally outwards from the well (see cross-sections of dye traces from CCFS01A, CCFS01D and CCFS02F in Appendix 3). The numerical simulations carried out for these tests also indicate that yield zones will originate above and below the injection interval (see Figure A5.252 for CCFS01A, Figure A5.282 for CCFS01D and Figure A5.302 for CCFS02F), with the yield zones developing into distinct shear bands with

247

continued fluid injection. Due to the large fluid pressure within the shear bands, the soil on the top and bottom faces of the shear bands continues to yield, and there is potential for the shear bands to merge into a single band (Figure A5.282). This would occur more readily when the injection interval is relatively short and the separation distance between the shear bands is minimal.

Chamber tests 3FRAC5 and 3FRAC6 were carried out at a high injection rate and incorporated a pre-formed slot on the injection wells at the point of injection. The numerical simulations of these two tests used a slightly longer injection depth interval than was used in the experiments and the well was modelled without considering the geometry of the slot. When the results of the numerical simulations are compared with the test data, it is seen that the experimentally measured peak injection pressures (681 kPa for 3FRAC5 and 758 kPa for 3FRAC6) are substantially lower than those determined numerically (4250 kPa for 3FRAC5 and 3902 kPa for 3FRAC6) where an extensive cavity expansion mechanism was observed. The pre-formed slot appears to allow a yield zone to develop at the face of the injection well without first going through the cavity expansion stage that was observed in previous tests. For example, after a very brief injection period the stress regime around a well with no pre-formed slot may resemble that shown in Figure 6.2 a), while after the same brief injection period, the stress regime around a well with a pre-formed slot may be more similar to Figure 6.2 b) in which a zone of enhanced permeability has already formed. The injection pressure required to extend the yield zone beyond the pre-formed slot is less than would be required to initiate yielding at a well with no slot.

As discussed in Chapter 2, the use of horizontal wells can offer several advantages over vertical wells. These advantages relate primarily to the use of horizontal wells where existing infrastructure prevents the use of vertical wells; and also the ability of a horizontal well to intersect a greater volume of contaminated soil and intersect more fractures than would be possible with a single vertical well. As for the geotechnical response of the soil during injection testing in horizontal versus vertical wells, one data point is available for a horizontal well injection test from which we can make some generalizations. The setup, procedures and results for injection test FLDTST2 were described previously in Chapter 3. Numerical simulation of FLDTST2 was carried out in a manner very similar to that used for the vertical well tests, the primary difference being that the test was analysed as a plane strain problem rather than an axisymmetric problem. Simulation results for FLDTST2 are presented in Chapter 5 and Appendix 5 (see Figures A5.241 to A5.250). The numerical simulation generated injection pressures and a pattern of yield zone development that was very similar to that observed during the field test. It appears that initial yielding occurred to the side of the horizontal well rather than on the top and bottom as was observed in the vertical well simulations. This may be related to the mesh size used for the simulation, as injection was carried out over a vertical range of two grid zones. Once the shear band had formed, extension occurred under a stress regime very similar to that shown in Figure 6.2 c). Based on the limited data, it appears that the development and propagation of a yield zone from a horizontal well occurs in a manner very similar to that of vertical wells.

249

6.3.1.2 Hydraulic conductivity and injection velocity

A permeability enhancement technique such as fluid injection would not be considered for a site unless the hydraulic conductivity of the soil were sufficiently low to make conventional remediation techniques ineffective. The hydraulic conductivity of the soil plays a significant role in the injection process and its magnitude is dependent on a number of factors including the grain size distribution of the soil, the void ratio, degree of saturation, fabric (particle orientation), and pore fluid properties (i.e. density, viscosity, etc.).

The peak pressure response during injection will vary with changes in the injection velocity. An example of this was the eight injection tests carried out in Speswhite kaolin at depths of 5 m and 10 m at prototype scale. The peak injection pressure in excess of the total vertical stress was made dimensionless by dividing by the atmospheric pressure, $(P_p - \sigma_v)/\sigma_{atm}$, and was plotted against the injection velocity in Figure 6.16. For the conditions under which the clay tests were carried out, there is an approximate linear relationship (on a semi-log scale) between the peak injection pressure and the injection velocity.

The velocity at which fluid must be injected into a wellbore, to generate sufficient pore pressures to cause yielding of the soil, is very much dependent on the hydraulic conductivity of the soil. If the soil is of moderate to high permeability, it is unlikely that fluid injected into the wellbore at a low velocity would generate sufficient pore pressures to cause yielding of the soil. The same soil tested at a much higher injection velocity, however, may develop

250

excess pore pressures sufficient to cause yielding of the soil. Injection tests for CCFS03 (I, J, K, and L) were carried out at the same well depths and injection rates as tests for CCFS01 (A, B, C, D). CCFS03 tests were carried out in a test bed constructed from a medium permeability silty sand, whereas CCFS01 tests were carried out in low permeability Speswhite kaolin clay. Significant yielding, accompanied by the formation of extensive planar discontinuities, was observed in all four clay tests. In the silty sand tests, no discontinuities were observed during post-test excavation, and if some yielding did occur, it was confined to a small zone of soil adjacent the wellbore.

In Figure 6.17, the results of all injection tests are plotted in dimensionless format in terms of the pressure response $(P_p - \sigma_v)/\sigma_{vm}$ versus the injection ratio. The injection ratio is the ratio of the injection velocity to initial hydraulic conductivity (v/k). All tests were carried out at injection ratios between 10^2 and 10^7. The pressure response ranged from a minimum of nearly -1 to a maximum of approximately +8. The pressure response tended to increase with increasing injection ratio.

Centrifuge tests CCFS03 I & J and CCFS04M in silty sand, were carried out at injection ratios of between 100 and 1300 and had pressure responses less than the total vertical stress in the soil (i.e. plots in the negative region on the y-axis of Figure 6.17). No discontinuities were observed during post-injection excavation of these three tests and the numerical simulations indicated that no yielding had occurred (Figures A5.321, A5.331 and A5.361). Test CCFS03K, also in silty sand, had a pressure response slightly greater than the total

251

vertical stress, however, the injection ratio was very low (127). No discontinuities were observed following the test and no yielding occurred in the numerical simulation.

A small amount of yielding occurred in the numerical simulations for tests CCFS03L, CCFS04N and FLDTST2. These tests had pressure responses just greater than the total overburden stress with an injection ratio of between 1269 and 2191. Discontinuities were not observed in CCFS03L or CCFS04N, however, it is possible that they may have formed near the well but were not visible due to the large penetration of dye into the soil during the injection test. During excavation of FLDTST2, dye traces were observed extending approximately 1.5 m horizontally outwards from the injection well (see Figure 3.13).

Tests CCFS01 (A, B, C, D) and CCFS02 (E, F, G, H) carried out in Speswhite kaolin clay, had pressure responses ranging from approximately 1.1 at an injection ratio of 200, to 1.7 at an injection ratio of 40000. In these clay tests, there is a very moderate increase in pressure with increasing injection rate. Because the injection volume varied between tests, the areal extent of the dye traces cannot be compared directly. It was observed, however, that the plan area of the discontinuities (Table 4.8) increased with increasing injection rate.

Larger injection pressures were observed in the chamber tests carried out in sand, than in the centrifuge or field tests (Figure 6.17). It is possible that the larger pressure response may be due to differences in boundary conditions between the chamber tests and the field/centrifuge tests. The field and centrifuge tests were carried out with an unconstrained upper surface,

whereas the chamber tests utilized an upper loading plate to apply vertical loads.

The results of numerical simulations indicate that the size of the yield zone and the pore pressure response are dependent on the injection velocity. Test 2FRAC2a did not yield during the numerical simulation, yet a pressure response of nearly +1 was observed. Pressure responses of between 1 and 2 were observed in tests 2FRAC2b and 2FRAC3a, and the numerical simulations indicated only minimal yield zone development. Numerical simulations indicated moderate yield zone development in 2FRAC2c and 2FRAC3b and pressure response of approximately 4 to 4½. With increasing injection rates, there is an corresponding increase in pressure response (3FRAC1, 3FRAC2, 3FRAC3 and 3FRAC4). Tests 2FRAC4 and 2FRAC5 are believed to have had problems with the injection mechanism which resulted in lower than expected pressures measured at the well. This is evidenced by the large pressure differences measured at the wellhead and the point of injection for the two tests (Figures A4.5 and A4.7). Also, test 3FRAC3, which was carried out under the same boundary and injection conditions as 2FRAC5, resulted in a peak injection pressure of 1230 kPa, which is significantly higher than measured during 2FRAC5. Tests 3FRAC5 and 3FRAC6 also show a pressures response that is substantially lower than similar tests such as 3FRAC4, however, 3FRAC5 and 3FRAC6 had a preformed notch at the injection well which reduced the injection pressures.

253

6.3.1.3 Injection fluid

Injection fluid properties, including fluid density, viscosity, and use of a proppant in the injection fluid may be varied to influence the results of the injection process.

In the field, chamber and centrifuge tests, dye traces tended to rise to the ground surface as they propagated away from the point of injection. Dusseault and Rothenburg (1988) suggested that hydraulically propagated fractures rise towards the ground surface due to the difference in density between the injection fluid and the soil. It is likely that the propagation of shear bands towards the ground surface is influenced by the differences in injection fluid and soil density, however, the *in situ* stress field, soil structure, and spatial variability of properties are also likely to have an influence. The effects of fluid density, soil density and the *in situ* stress field were modelled in the numerical simulations. In the chamber test simulations, which were carried out without the influence of gravity, shear bands developed horizontally away from the injection well. The numerical simulations carried out for the field tests and centrifuge tests utilized gravity in the analysis and showed a greater tendency to propagate towards the ground surface. It is likely that the use of high density injection fluid would result in a reduced tendency for the shear bands to rise to the ground surface during extension. The direction in which shear bands propagated in all of the numerical simulations was influenced by the configuration of the meshes used, which were rectangular with horizontal and vertical zone boundaries.

Varying the viscosity or the density of the injection fluid will have an effect similar to that of varying the hydraulic conductivity. The hydraulic conductivity is related to the viscosity and density of the pore fluid as shown in Eqn 6.4

$$k = K_a \, \rho \, g \, / \, \mu \qquad \text{[Eqn. 6.4]}$$

where K_a is the absolute permeability, ρ is the density of the pore fluid, g is the acceleration due to gravity, and μ is the viscosity of the pore fluid. Increasing the viscosity or decreasing the density of the injection fluid will decrease the amount of leakoff that occurs from a shear band, with an effect similar to that of carrying out the injection test in a lower permeability soil. Decreasing the viscosity or increasing the fluid density would increase the amount of leakoff, and result in a faster rate of expansion of the excess pore pressure front.

The field, chamber and centrifuge injection tests discussed in this thesis were carried out without using a proppant in the injection fluid. Where a proppant such as sand is used, the fluid viscosity must normally be increased in order to keep the sand particles suspended in the injection fluid. The friction between the injection fluid and the soil is very large, which results in large injection pressures. There are also greater head losses in the pump, tubing, and injection well than would occur without the proppant. The use of a proppant and a viscosifier decreases the amount of leakoff that occurs, thus the zone of pore pressure increase in advance of the yield zone will be small. During injection, the solid particles within the injection fluid are unlikely to move through the pore space of the soil, and the partings created

255

are due to the soil being "wedged apart" by the injection fluid. The widths of tensile partings are generally greater where a proppant is used as compared to tensile partings created without a proppant (Gidley et al, 1989).

6.3.2 Soil and stress parameters

6.3.2.1 Soil stress state

Yield mechanisms due to fluid injection were discussed in detail in section 6.2, including a discussion of stress paths. The effective stress change required to move from the *in situ* stress condition to the yield surface is highly influenced by the initial *in situ* stress which varies with soil density, depth, pore pressure, and principal stress ratio (K). The principal stress ratio is influenced by such factors as OCR, weathering, dessication, and changes in groundwater levels. The injection process is primarily applicable for soils where the principal stress ratio is greater than one. It is in these soils that an increase in pore pressure may result in permeability enhancement due to effective stress reduction and yielding. As can be seen in Figure 6.1, the distance between the *in situ* stress state and the yield surface is greatest when K=1. As K increases, shorter stress paths to the yield surface become possible.

6.3.2.2 Soil strength and deformation parameters

Tension does not develop in a cohesionless soil and the primary mechanism is shearing. The pore pressure increase required to move along a stress path from the *in situ* condition to the yield surface will be greater in a soil with a high frictional strength as compared to a soil with a low frictional strength. The change in pore pressure required to reach the yield surface of a cohesionless soil is plotted for a range of P_e/σ_3' in Figure 6.18, for a range of principal stress ratios and friction angles. For cohesionless soil with a known friction angle and principal stress ratio, Figure 6.18 may be used to determine the excess pore pressure required to cause yielding.

In a cohesive soil, it is possible to develop tension in the soil if the minimum principal effective stress falls to zero. Whether yielding occurs in tension or in shear is largely a function of the cohesive strength of the soil and the initial minimum principal effective stress (i.e. the depth at which fluid injection is taking place). For example, the excess pore pressure required to cause yielding is plotted in Figure 6.19 for soil depths of up to 12.5 m and for a range in cohesive strengths from 0 to 8 kPa. (Also assume for this example that $\gamma'=8$ kN/m³, K=1.5, and $\phi'=24°$.) Tensile yielding is more likely to occur at shallow depth where P_e/σ_3' is greater than one. At greater depths where P_e/σ_3' is less than one, yielding is more likely to be due to shearing. A soil with greater cohesion requires a greater excess pore pressure to reach the yield surface.

Plotted on Figure 6.19 are the peak excess pressure responses measured at the buried PPT locations in CCFS01 and CCFS02. The Speswhite kaolin soil used for these tests had $\gamma'=8$ kN/m^3, $\phi'=24°$, and $c'=6$ kPa.. The stress ratio may be approximated as K=1.5. A number of the PPTs (A1, B1, C1, C2, F2) were not positioned near the path of the developing yield zone and showed a pressure response substantially smaller than that required to cause yielding. A more substantial pressure increase was measured at PPTs D1, E1, E2, G2, H1 and H2, although the pressure response was again not large enough to cause yield. PPTs A2, B2, F1 and G1 measured pressure responses large enough to result in yielding of the soil. PPT A2 was located 0.5 m (prototype scale) below a shear band, and showed a response in the tensile yield region. PPT B2, which is located 3.0 m (prototype scale) below a shear band, shows a response that is in the shear yield region. PPTs F1 and G1, which are both located 1.3 m (prototype scale) from the point of injection, show pressure responses in the tensile yield region. It is likely that yielding at A2 and F1 was initially due to shear and became tensile with continued pore pressure increase. G1 is located in a position where the initial yielding may have either been in shear or tension, and depends very much on the local soil conditions and the stress response due to injection.

Deformations that occur due to fluid injection were handled computationally by FLAC using the strain softening constitutive model which was described in detail in Chapter 5. To determine deformations using the strain softening model requires three parameters including the shear modulus, G, the bulk modulus, B, and a dilation angle, ψ. The shear modulus and bulk modulus are used to determine the elastic response of the soil during fluid injection.

258

Plastic response is determined using the dilation angle which is entered in FLAC as a piecewise-linear function of a hardening parameter measuring the plastic shear strain. The ground surface displacements measured during the field and centrifuge injection tests were generally smaller than the displacements determined numerically (Table 6.1). This is primarily due to the thickness of the shear bands determined numerically being greater than that observed in the injection tests. The plastic deformations are thus accumulated over a thicker zone of soil, resulting in larger total deformations. In addition, the pattern of yield zone development was not known in advance of the testing, and thus, the displacement transducers may not have been placed in the positions that would record the greatest displacements.

Table 6.1. Maximum vertical ground surface displacement at end of injection

Test		Measured (mm)	FLAC (mm)
FLDTST1		3.2	24
FLDTST2		0	2.5
CCFS01	A	0.1	0.2
	B	0.2	0.2
	C	0.4	0.7
	D	0.7	0.7
CCFS02	E	1.0	2.0
	F	0.2	0.3
	G	0.3	0.8
	H	0.8	0.8
CCFS03	I	0.0	0.0
	J	0.0	0.0
	K	0.0	0.0
	L	0.0	0.0

259

6.3.2.3 Macro structure

Structural composition on a macro level includes the effects of bedding, homogeneity/heterogeneity, and anisotropy. Shear bands will propagate in the manner that requires the least amount of energy. Where bedding features exist, such as may occur naturally in lacustrine deposits or may be created due to construction practices (i.e. compaction of soil in lifts), shear bands may develop and extend in preferred orientations and directions. This may be due to anisotropic strength or permeability conditions within the bedded soil, or may be due to a distinct preferred particle orientation. In stratified deposits, the hydraulic conductivity is normally higher in the direction parallel to bedding and lower perpendicular to the bedding. Where anisotropic permeability conditions exist, the zone of excess pore pressure will propagate further in the direction with the greatest permeability.

Some evidence of preferred orientation of dye traces was observed in both field tests. In FLDTST1, inclined dye traces were observed to change direction at boundaries between compacted lifts and travel horizontally along lift interface for short distances before again rising to the ground surface (Figure 3.9). In FLDTST2, post-test excavation revealed that the dye traces extended nearly horizontal while remaining near the interface between compacted lifts (Figure 3.13).

There are no perfectly homogeneous soils. There will be variability in the micro-structure, macro-structure and properties of the soil due to varying influences during the soils deposition

and subsequent history. The variability of properties and structure will have an influence on how a shear band may develop or extend within the soil. During extension, the shear band may "deflect" and travel above or below stronger or stiffer regions within the soil, or move around or into regions of different permeability. Where such deflections occur, the influence of gravity will likely result in the deflection being in an upward direction towards a lower stress regime rather than a downward deflection towards a higher stress regime.
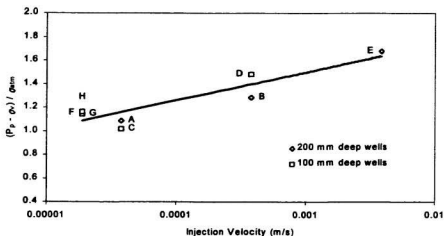
Figure 6.16. Pressure response versus injection velocity for clay tests
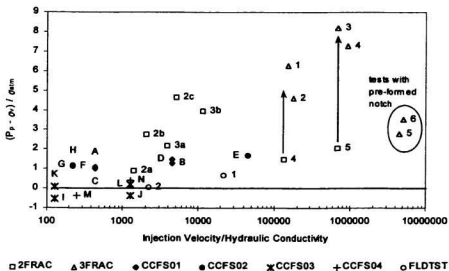
Figure 6.17. Normalized pressure response for all tests

262
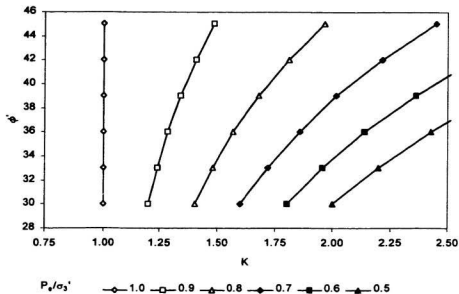
Figure 6.18. Pore pressure increase required to cause yielding of cohesionless soil
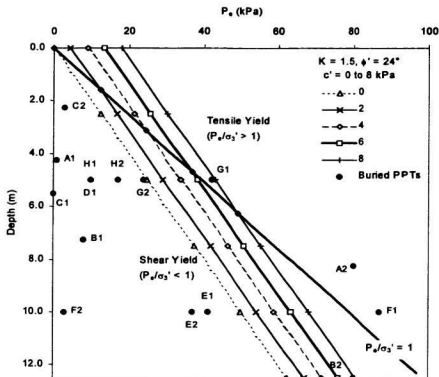
Figure 6.19. Pore pressure increase required to cause yielding of a cohesive soil

264

6.4   Summary

The results of field, laboratory, and centrifuge fluid injection tests are discussed. Where the injection velocity is low relative to the hydraulic conductivity of the soil, flow through the pore space without yielding was found to be a dominant mechanism.

If the injection ratio (v/k) is increased sufficiently, yielding of the soil will occur due to injection induced changes in the total and effective stress regime. The initial response to the higher injection ratio is a large pore pressure increase within a small region near the point of injection and increases in the horizontal, vertical and tangential effective stress outside of this region. This response is similar to that associated with a cavity expansion mechanism. These changes to the stress regime result in initial yield occurring in zones located above and below the injection interval.

Yielding of the soil may occur due to shearing or tension. The specific mechanism is dependent on the initial state of stress in the soil, the strength of the soil in terms of c' and φ', and the stress path taken to the yield surface. Yielding of the soil in advance of shear band development is more likely to occur due to shearing, particularly in soil with little or no cohesion and with K much larger than 1. After initial yielding occurs due to shear, a continued pore pressure increase will result in an element moving along a stress path on the yield surface to the $\sigma'_v = 0$ condition where yielding continues due to tension. Continued increases in pore pressure will result in the creation of tensile partings in the soil.

265

Heavily overconsolidated soils generally exhibit a strain softening behaviour when sheared, with shear bands developing shortly after the peak strength is attained. The development of shear bands increases the connectivity of voids within the pore space, resulting in a zone of increased permeability within the shear band. The zone of enhanced permeability allows the pore pressure front and the shear band to progressively advance away from the well due to fluid injection. A function was incorporated into a strain softening numerical model that would increase the permeability of zones of soil where some critical value of accumulated plastic shear strain had been exceeded. Analysis of the injection tests using this model provided good agreement between the behaviour observed and measured in the experiments and that determined numerically.

Parameters that influence the injection process fall into the two general categories: 1) fluid injection parameters, and 2) soil/stress parameters.

Fluid injection parameters may be customized to suit the injection process. Parameters that may be changed include:

- well orientation (horizontal versus vertical).

- well details (i.e. depth, well diameter, and injection interval length)

- hydraulic conductivity (the hydraulic conductivity or the pore fluid in the soil are not actually parameters that may be changed, however, increasing/decreasing the injection fluid viscosity and/or density has an effect similar to that of changing the hydraulic

conductivity)

- injection velocity (flow rate may be increased or decreased, or injection velocity may be changed by increasing the length of the injection interval)

Soil/stress parameters cannot generally be changed to suit the injection process. These parameters define the soil conditions that exist at a site and include:

- soil stress state (the *in situ* stress is a function of the soil unit weight, the depth, the groundwater conditions, and the principal stress ratio K)

- soil strength parameters (c', ϕ')

- soil deformation parameters (G, B, ψ)

- macro structure (including bedding, homogeneity and heterogeneity, and anisotropy)

CHAPTER 7 - CONCLUSIONS

7.1   General

The *in situ* treatment of contaminants located in dense low permeability soil is a particularly challenging problem. Existing *in situ* techniques for treating contaminants are generally ineffective in these soils and seldom used. The primary objective of this research has been to investigate a fluid injection technique that relies on a soil shearing mechanism to physically change the structure of dense low permeability soil, and in doing so, create an enhanced flow regime within the soil. It is anticipated that the enhanced flow regime will allow greater accessibility to contaminants located within the soil and enable conventional *in situ* treatment technologies to be used more effectively over a broader range of soil conditions.

7.2   The Fluid Injection Process

An extensive injection test program was carried out under a wide variety of soil and boundary conditions. Two field scale fluid injection tests were carried out from a vertical and a horizontal well constructed in recompacted silty sand TILL. Sixteen reduced scale centrifuge injection tests were carried out from vertical wells in overconsolidated kaolin clay and compacted silty sand. Results were also analysed and interpreted from 18 injection tests in sand carried out from a vertical well in a large triaxial calibration chamber. The chamber tests

were carried out by Golder Associates Ltd. (1991, 1992 and 1994) as part of a joint industry hydraulic fracturing investigation.

Fluid injection was carried out at a constant rate of flow and instrumentation was used to monitor injection pressures, pore pressure in the soil surrounding the well, and ground surface displacements. Major test variables included the well configuration (orientation, size, length, depth), injection parameters (rate, viscosity) and soil parameters (type, strength, permeability, *in situ* stresses). A dye tracer was used during all experiments to provide a post-test means of identifying the pathways by which injection fluid had travelled during the experiments. Testbeds were excavated following the experiments and the locations of dye traces were mapped.

Numerical simulations of the injection tests were carried out using the finite difference program FLAC. The analyses incorporated full coupling between groundwater flow and mechanical response of the soil. A strain softening constitutive model was utilized with a FISH function that simulated the effects of permeability enhancement during shear band evolution by automatically increasing the permeability of the soil in zones where the accumulated plastic shear strain exceeded a critical value.

7.3 Mechanisms

Four types of response were found to dominate the fluid injection process including: flow through pore space without yielding, cavity expansion, yield due to shearing, and yield due to tension. Conclusions related to the mechanisms occurring as a result of fluid injection in a wellbore are as follows:

- Flow through the pore space without yielding occurs when the rate at which pore pressures freely dissipating in the soil exceeds the rate at which fluid is injected into the well. This type of response is the same as would occur during a constant head permeability test in a well. Parameters that influence the injection process include rate of injection, well geometry, injection fluid properties, and soil permeability.

- When fluid is injected into a well at a rate that exceeds the rate at which pore pressures can dissipate in the soil, there is an initial rapid build-up of fluid pressure in the well and a corresponding large pore pressure increase within a small region of soil near the point of injection. High injection pressure results in increased horizontal, vertical and tangential effective stress outside the zone of elevated pore pressure in a manner very similar to that associated with a cavity expansion mechanism.

- Initial yielding generally occurs in zones located above and below the injection interval and may be in shear or tension. The specific mechanism is dependent on the

270

initial state of stress in the soil, the strength of the soil in terms of c' and φ', and the stress path taken to the yield surface.

- In dilatant strain softening soils, the onset of yield is often followed closely by an increase in permeability. It is this permeability enhancement effect that provides the greatest contribution towards shear band development. As the permeability is enhanced due to yielding, injection fluid travels more readily through the yield zones than through the adjacent non-yielded soil. Thus, an excess pore pressure front moves along the developing yield zone, resulting in additional yielding and the accumulation of plastic shear strains. It is along these zones of large accumulated plastic shear strains that shear bands develop and propagate.

- Yielding due to shearing will dominate in a soil with little or no cohesion and with K>1. Tensile yielding may dominate in soil where there is significant cohesion and the *in situ* vertical effective stress is small (i.e. shallow depths). At greater depths, the *in situ* stresses may be sufficiently large that, even with significant cohesion, yielding will occur due to shearing.

- The stress path taken by a soil element from the *in situ* stress condition to the yield surface is highly dependent on the physical location of the element with respect to the point of injection and the developing yield zone. The stress path was found to vary with injection rate. At low injection rates, an element within the zone of shear band

development will experience very small total stress changes and the stress path will be nearly parallel to the K=1 line to the yield surface. At higher injection rates, there is substantial total stress change and the element will take a more curved path to the yield surface.

- After initial yielding of an element occurs due to shear, a continued pore pressure increase results in a rapid reduction in effective stress and additional yielding in shear. When the minimum principal effective stress, σ'_3, becomes zero, yielding continues in tension. Further increases in pore pressure will result in the creation of tensile partings in the soil along shear bands.

7.4   Injection Parameters

7.4.1   Injection ratio

The injection ratio, v/k, is an important parameter in the injection process and has a substantial influence on the development of yield zones within the soil. The injection ratio is controlled by varying the flow rate, the well geometry, or the injection fluid properties. The effect of the v/k ratio in cohesionless soils (sand and silty sand) is as follows:

- Fluid injection tests carried out with an injection ratio less than about 300 did not

generate sufficient pore pressures to cause yielding of the soil. In these tests, the injection fluid moved freely through the pore space as an expanding bulb of dyed fluid.

- Tests carried out with injection ratios between about 300 and 2000 resulted in a minimal amount of yielding in a zone very close to the point of injection. After initial yielding had occurred near the well, the injection fluid tended to travel through the pore space without generating sufficient pore pressures to cause additional yielding.

- The size of the yield zone continued to increase with injection ratios greater than 2000.

The effect of varying the injection ratio in cohesive soils (clays) was:

- The amount of yielding that occurred at low injection ratios was significantly more than for the cohesionless soils. At injection ratios of between 200 and 300, the yield zones generally grew as poorly developed discontinuites that originated at the well and propagated for only short distances.

- At injection ratios of between 500 and 600, the discontinuities were larger and better defined, but rose at a moderately steep slope towards the ground surface.

273

- At injection ratios of 4000 to 5000, the discontinuities were well defined, very large, and nearly horizontal.

- At a much higher injection ratio of about 50000 the discontinuities were no longer as well defined, had become somewhat smaller in size, and again rose at a moderately steep slope towards the ground surface.

7.4.1 Yield Zone Development

In addition to the injection ratio, various other parameters will influence the development of a yield zone during fluid injection including the strength properties of the soil (c', ϕ'), the initial stress state, and the macro structure of the soil.

An expression was presented for estimating the excess pore pressure (P_e) required to initiate yield in the soil based on the initial stress condition, the Mohr-Coulomb failure envelope, and an assumption that the pore pressure increase occurs without any changes in total stress. An excess pore pressure ratio (P_e/σ'_3) greater than one indicates that yield will likely occur due to shearing, and an excess pressure ratio less than one indicates that yield will likely occur due to tension. The magnitude of the pore pressure increase required to cause the soil to yield will be small when the initial stress state is near the failure envelope (i.e. when K is large and c', ϕ' are small). The pore pressure increase required to yield the soil will increase in stronger soils

or where K is nearer to one.

7.5   Numerical Model for Fluid Injection Analysis

The numerical model adopted for analysing the injection test data, was extremely useful for providing insight into the mechanisms involved in the fluid injection process. The injection pressures and extent of yield zone development determined numerically corresponded very well with experimental results. The numerical simulations demonstrated the importance of incorporating full-coupling between mechanical calculations and groundwater flow, and the necessity of accounting for shear induced permeability changes in a strain softening soil. The development of shear bands due to fluid injection was modelled, however, the thickness and shape of the shear bands was dependent on the grid used. The development of tensile partings was not modelled and would require the introduction of a discontinuity or an interface capable of modelling physical separations between the shear band surfaces.

7.6   Recommendations for Further Research

Additional research would be useful to better understand the mechanism of permeability enhancement due to yield in strain softening soils. Efforts should be directed towards investigating the magnitude of permeability enhancement within shear bands, anisotropy of

permeability within shear bands, and permeability implications during and after transition from flow within a shear band to flow within a tensile parting.

It would be useful to carry out additional centrifuge tests in silty sand at v/k ratios ranging from 500 to at least 100000. This would allow a more direct comparison with chamber test data at similar v/k ratios. Tests should be conducted in a strongbox similar to one recently constructed by C-CORE that allows the horizontal stress at the model boundary to be controlled.

Fluid injection testing is a new application for the geotechnical centrifuge and, as such, the scaling laws governing the technique have not yet been validated. Repeating tests over a range of acceleration levels would allow a more rigorous check of the scaling relations used for the fluid injection process.

Additional field scale injection tests would be valuable in assessing the capabilities of the numerical model, particularly with respect to optimizing the injection well configuration and predicting the location and extent of yield zone development. Carrying out the field scale injection tests at a contaminated site in conjunction with a conventional remedial technique is a logical next step in the development of the soil shearing technique.

REFERENCES

Al-Tabbaa, A. 1987. Permeability and stress-strain response of Speswhite kaolin. PhD Thesis. University of Cambridge. November.

Albright, J. N. and C. F. Pearson. 1982. Acoustic emission as a tool for hydraulic fracture location: Experience at the Fenton Hill hot dry rock site. Society Petroleum Eng. Journal, August, pp. 523-30.

Andersen, K. H., C. G. Rawlings, T. A. Lunne, and H. Trond. 1994. Estimation of hydraulic fracture pressure in clay. Canadian Geotechnical Journal, Vol. 31, pp. 817-828.

Andreev, G. E. 1995. Brittle failure of rock materials: Test results and constitutive models. A. A. Balkema, Rotterdam, 446 p.

Armstrong, J. E., C. A. Mendoza, B. J. Moore, and P. E. Hardisty. 1995. A comparison of horizontal versus vertical wells for soil vapour extraction. Presented at Solutions '95, International Association of Hydrogeologists Congress XXVI. Edmonton, Alberta. June 4-10.

Barenblatt, G. I. 1962. Mathematical theory of equilibrium cracks. Advances in Applied Mechanics, 7, 55.

Bear, J. 1979. Hydraulics of Groundwater. McGraw-Hill, USA.

Been, K. and K. M. Kosar. 1991. Hydraulic fracture simulations in a calibration chamber. First International Symposium on Calibration Chamber Testing, Clarkson University, Potsdam, New York, June 27-29.

Bjerrum, L. and K. H. Andersen. 1972. In-situ measurement of lateral pressures in clay. In Proc. of the 5ᵗʰ European Conf. on Soil Mech. and Found. Eng., Madrid. Sociedad Espanola de Mecanica del Suelo y Cimentaciones, Madrid, Vol. 1, pp. 11-20.

Bjerrum, L., K. K. T. L. Nash, R. M. Kennard, and R. E. Gibson. 1972. Hydraulic fracturing in field permeability testing. Geotechnique, Vol. 22, No. 2, pp. 319-332.

Brooker, E. W. and H. O. Ireland. 1965. Earth pressures at rest related to stress history. Canadian Geotechnical Journal, Vol.2, No. 1, pp. 1-15.

Butler, R.M. 1992. Gravity drainage to horizontal wells. Journal of Canadian Petroleum Technology, 31(4).

277

Chalaturnyk, R. J. 1996. Geomechanics of the steam assisted gravity drainage process in heavy oil reservoirs. PhD thesis. University of Alberta, Edmonton, Alberta.

Chalaturnyk, R. J. and J. D. Scott. 1995. Geomechanics issues of steam assisted gravity drainage. International Heavy Oil Symposium, Calgary, Alberta, June 19-21, 1995.

Chalaturnyk, R. J. and J. D. Scott. 1997. Geomechanical response of heavy oil reservoirs to the Steam Assisted Gravity Drainage process. Proceedings of the 1997 SPE International Thermal Operations and Heavy Oil Symposium, 10-12 February, Bakersfield, California. SPE 37569.

Chan, D., X. Wang, and N. R. Morgenstern. 1997. Kinematic modelling of shear zone deformation. International Symposium on Deformation and Progressive Failure in Geomechanics, Nagoya, Japan, October 4-7.

Chhina, H. S. and J. G. Agar. 1985. Potential use of fracture technology for recovery of bitumen from oil sands. Proceedings of the Third International Conference on Heavy Crude and Oil Sands, Sponsored by: UNITAR/UNDP Information Center, Long Beach, California, July 22-30, 32 p.

Chu, J., S.-C. R. Lo, and I. K. Lee. 1996. Strain softening and shear band formation of sand in multi-axial testing. Géotechnique 46, No. 1, pp. 63-82.

Clark, J. I. 1979. Failure during construction and subsequent rehabilitation and performance of a dynamically cast-in-place concrete pile foundation. Behavior of Deep Foundations; Raymond Lundgren, Ed; ASTM STP 670, pp. 209-230.

Cleary, M. P., M. Kavvadas, and K. Y. Lam. 1983. Development of a fully three-dimensional simulator for analysis and design of hydraulic fracturing. SPE/DOE Paper 11631, SPE/DOE Low Permeability Gas Reservoirs Symposium, Denver, March 13-16.

Cornet, F. H., J. M. Hosanski, F. Bernaudat, and E. Ledoux. 1982. Shallow depth experimentation on the concept of energy extraction from deep hot dry rocks. Hydraulic Fracturing and Geothermal Energy. Nemat-Nasser, S., H. Abe and S. Hirakawa, Editors. Martinus Nijhoff Pub. The Hague, pp. 75-93.

Culligan-Hensley, P. J. and C. Savvidou. 1995. Environmental geomechanics and Transport processes: Chapter 8 in Geotechnical Centrifuge Technology, Edited by R. N. Taylor, Blackie Academic and Professional Publishers, Glasgow.

Cundall, P. A. 1989. Numerical experiments on localization in frictional material. Ingenieur-Archiv, 59, pp. 148-169.

278

Cundall, P. A. 1990. Numerical modelling of jointed and faulted rock. In Mechanics of Jointed and Faulted Rock, pp. 11-18. Rotterdam: A. A. Balkema.

Cundall, P. A. 1991. Shear band initiation and evolution in frictional materials. In Mechanics Computing in 1990s and Beyond (Proceedings of the Conference, Columbus, Ohio, May 1991), Vol. 2: Structural and Material Mechanics, pp. 1279-1289. New York: ASME.

Davis, P. M. 1983. Surface deformation associated with a dipping hydrofracture. Journal of Geophysical Research, Vol. 88, No. B7, July, pp. 5826-5834.

Dusseault, M. B. and L. Rothenburg. 1988. Shear dilatancy and permeability enhancement in oil sands. UNITAR. Proceedings 4th International Conference on Heavy Crude and Tar Sands, Edmonton, Alberta. August. Paper No. 32.

Edmunds, N. R., J. A. Kovalsky, S. D. Gittins, and E. D. Pennicioli. 1992. Review of Phase A gravity drainage test. SPE Thermal Operations Symposium, Bakersfield, SPE 21529.

Evans, K. 1983. On the development of shallow hydraulic fractures as viewed through the surface deformation field: Part 1 - principles. Journal of Petroleum Technology, February, pp. 406-410.

Frank, U. and N. Barkley. 1995. Remediation of low-permeability subsurface formations by fracturing enhancement of soil vapour extraction. Journal of Hazardous Materials, Vol. 40, pp. 191-201.

Gale, J. E. and R. MacLeod. 1995. Assessing the effectiveness of fracture stimulation for increasing well yield in Newfoundland. Prepared for Government of Newfoundland Department of Environment Water Resources Division and Environment Canada Environment Conservation Branch by Fracflow Consultants, St. John's, NF. February.

Geertsma, J. and F. de Klerk. 1969. A rapid method of predicting width and extent of hydraulically induced fractures. Journal of Petroleum Technology, Trans. AIME, 246. December, pp.1571-1581.

Geo-Slope. 1996. Evaluation Software: CAD software for geotechnical modelling. Geo-Slope Ltd., Calgary, Alberta.

Gidley, J. L., S. A. Holditch, D. E. Nierode, and R. W. Veatch. 1989. Recent advances in hydraulic fracturing. SPE Monograph, Richardson, TX, 452 p.

Golder Associates Ltd. 1991. Laboratory simulation and constitutive behaviour for hydraulic

fracture propagation in oil sands: Final Report - Phase 1. Energy, Mines and Resources Cost-Shared Energy Conversion Program and PERD under auspices of CANMET. July.

Golder Associates Ltd. 1992. Laboratory simulation and constitutive behaviour for hydraulic fracture propagation in oil sands: Final Report - Phase 2. Energy, Mines and Resources Cost-Shared Energy Conversion Program and PERD under auspices of CANMET. June.

Golder Associates Ltd. 1994. Laboratory simulation and constitutive behaviour for hydraulic fracture propagation in oil sands: Final Report - Phase 3. Energy, Mines and Resources Cost-Shared Energy Conversion Program and PERD under auspices of CANMET. July.

Griffith, A. A. 1921. The phenomena of rupture and flow in solids. Philosophical Transactions of the Royal Society, London, A221, pp. 163-198.

Hubbert, M. K. and D. G. Willis. 1957. Mechanics of hydraulic fracturing, Petroleum Transactions AIME, Vol. 210, pp. 153-168.

Hvorslev, J. 1951. Time lag and soil permeability in ground-water observations. Bulletin No. 36, Waterways Experiment Station, Corps of Engineers, U. S. Army, Vicksburg, Mississippi, April.

Ingraffea, A. R., R. J. Shaffer, and F. E. Heuze. 1985. FEEFFLAP: A finite element program for analysis of fluid-driven fracture propagation in jointed rock. Unconventional Gas Program Reports UCID-20368 and UCID-20369, March.

Irwin, G. R. 1957. Analysis of stresses and strains near the end of a crack traversing a plate. Journal of Applied Mechanics, 24, p 361.

Itasca. 1996. FLAC: Fast Lagrangian Analysis of Continua. Version 3.3. Volumes I to IV: User's Manual. Itasca Consulting Group Inc.

Ito, H. 1981. Seismic signal detection during massive hydraulic fracturing and hydraulic fracturing stress measurements in geothermal area, Japan. USGS Workshop on Hydraulic Fracturing Stress Measurements, Monterey, CA, December 3-5.

Jaworsky, G. W., J. M. Duncan, and H. B. Seed. 1981. Laboratory study of hydraulic fracturing. Journal of the Geotechnical Engineering Division, ASCE, June, pp. 713-731.

Kaback, D. D. and D. Oakley. 1996. Horizontal environmental wells in the United States: A

catalogue. Colorado Center for Environmental Management. 999 18th Street, Suite 2750, Denver, Colorado, 80202. April.

Keffer, E. B., J. J. Liskowitz, and C. D. Fitzgerald. 1996. The effect of pneumatic fracturing when applied to groundwater aquifers. In: Proceedings of the 6th West Coast Conference on Contaminated Soils and Groundwater, pp. 1-21.

Keller, C. K., G. van der Kamp, and J. A. Cherry. 1986. Fracture permeability and groundwater flow in clayey till near Saskatoon, Saskatchewan. Canadian Geotechnical Journal, Vol. 23, pp. 229-240.

Kerr, R. A. 1987. Hot dry rocks: Problems, Promise. Science. 238:1226-1228.

Koenig, L. 1960a. Economic aspects of water well stimulation. Journal American Water Works Association, Vol. 52, pp. 631-637.

Koenig, L. 1960b. Effects of stimulation on well operating costs and its performance on new and old wells. Journal American Water Works Association, Vol. 52, pp. 1499-1512.

Kosar, K. M. and K. Been. 1989. Large scale laboratory fracturing test in oil sands. Paper No. 89-40-83, 40th Annual Meeting of the Petroleum Society of CIM, Banff, Alberta, May 28-31.

Kosar, K. M. and K. Been. 1991. The effects of geomechanical behaviour on in situ recovery processes in oil sands reservoirs. Fifth International Conference on Heavy Crude and Tar Sands, United Nations Institute for Training and Research (UNITAR), Caracas, Venezuela, August 4-9.

Kulhawy, F. H. and T. M. Gurtowsky. 1976. Load transfer and hydraulic fracturing in zoned dams. Journal of the Geotechnical Division, ASCE, September, pp. 963-974.

Kwong, A. and P. K. Kaiser. 1991. Failure mechanisms of boreholes in rock with anisotropic strength and local weaknesses. Proceedings of 44th Canadian Geotechnical Conference, Calgary, Alberta, September 29 to October 2, pp. 35-1 to 35-10.

Ladd, C. C. 1971. Strength parameters and stress-strain behaviour of saturated clays. Research Report R711-23, Soils Publication 278, Department of Civil Engineering, Massachusetts Institute of Technology, 280 pp.

Leach, B., K. Kosar and P. C. Ingraham. 1994. Pneumatic and hydraulic fracturing for enhanced in situ remediation of contaminated fine grained soils. Proceedings of the Focus Conference On Eastern Regional Ground Water Issues, October 3-5, Burlington, Vermont, pp. 537-549.

Leydecker, G. 1981. Seismic locating of hydraulically induced fractures in the geothermal frac-project: Falkenberg. BGR Report No. 86549, Hannover, West Germany, March.

Lin, L. 1995. Strength characteristics of a modelling silty clay. Master's Thesis, Memorial University of Newfoundland, St. John's, NF, CA.

Looney, B. B., T. Hazen, D. Kaback, and C. Eddy. 1991. Full-scale field test of the *in situ* stripping process at the Savannah River Integrated Demonstration Test Site. WSRC-RD-91-22. Aiken, South Carolina. Westinghouse Savannah River Company. July 29.

Massarsch, K. R. and B. B. Broms. 1977. Fracturing of soil caused by pile driving in clay. 9th International Conference on Soil Mechanics and Foundation Engineering, Vol. 1/40, Tokyo, Japan, pp. 197-200.

Massarsch, R. 1978. New aspects of soil fracturing in clay. ASCE Journal of the Geotechnical Engineering Division, 104, pp. 1109-1123.

Mori, A. and M. Tamura. 1986. Effect of dilatancy on permeability in sands stabilized by chemical grout. Japanese Society of Soil Mechanics and Foundation Engineering. Soils and Foundations, Vol. 26, No. 1, March, pp. 96-104.

Mori, A. and M. Tamura. 1987. Hydrofracturing pressure of cohesive soils. Japanese Society of Soil Mechanics and Foundation Engineering. Soils and Foundations, Vol. 27, No. 1, March, pp. 14-22.

Morgenstern, N. R. and P. R. Vaughan. 1963. Some observations on allowable grouting pressures. Proceedings of the Conference on Grouts and Drilling Muds. London, England: Institute of Civil Engineering. pp. 36-42.

Morgenstern, N. R. and J. S. Tchalenko. 1967. Microscopic structures in kaolin subjected to direct shear. Géotechnique 17, No. 4, pp. 309-328.

Murdoch, L. C., G. Losonsky, I. Klich, and P. Cluxton. 1990. Hydraulic fracturing to increase fluid flow. In: F. Arendt and Others, eds. Contaminated Soil. Kluwer Academic Publishers, Netherlands, pp. 1097-1094.

Murdoch, L. C., G. Losonsky, P. Cluxton, B. Patterson, I. Klich, and B. Braswell. 1991. The feasibility of hydraulic fracturing of soil to improve remedial actions. Final report. EPA/600/2-91/012 (NTIS PB91-181818)

Murdoch, L. C. 1993. "Hydraulic Fracturing of Soil During Laboratory Experiments, Part I: Methods and Observations; Part II: Propagation; Part III: Theoretical Analysis, Geotechnique, Vol. 43, No. 2, Institution of Civil Engineers, London, pp. 255 - 287.

282

Murphy, H. 1982. Hot dry rock reservoir development and testing in the USA. Hydraulic Fracturing and Geothermal Energy. Nemat-Nasser, S., H. Abe and S. Hirakawa, Editors. Martinus Nijhoff Pub. The Hague. pp. 33-58.

Nolte, K. G. 1988. Fracture design considerations based on pressure analysis. SPEPE, February, pp. 22-30.

Oda, M. and H. Kazama. 1998. Microstructure of shear bands and its relation to the mechanisms of dilatancy and failure of dense granular soils. Géotechnique 48, No. 4, pp. 465-481.

Orowan, E. 1952. Fatigue and fracture of metals. John Wiley & Sons Inc. New York, p. 139.

Overy, R. F. and A. R. Dean. 1986. Hydraulic fracture testing of cohesive soil. 18th Annual Offshore Technology Conference, Houston, Texas, May, pp. 45-53.

Palmer, A. 1991. Centrifuge modelling of ice and brittle materials. Canadian Geotechnical Journal, 28, pp. 896-898.

Parker, B. L., R. W. Gillham, and J. A. Cherry. 1993. Diffusive disappearance of immiscible phase organic liquids in fractured geologic media. Ground Water, Vol. 32, No. 5, pp. 805-820.

Parsons, G. 1995. A laboratory investigation into the properties of modelling soils used in offshore projects at C-CORE. Engineering work-term report prepared for C-CORE and Memorial University of Newfoundland, December.

Pastor, M., J. Peraire, and O. C. Zienkiewicz. 1991. Adaptive remeshing for shear band localization problems. Arch. Applied Mechanics, 61: pp. 30-39.

Paulin, M. J., R. Phillips, and L. Lin. 1993. Centrifuge modelling relevant to the lateral loading of pipelines. Contract report for NOVA Corporation of Alberta, C-CORE Contract Number 93-C10a.

Perkins, T. K. and L. R. Kern. 1961. Widths of hydraulic fractures. Journal of Petroleum Technology, Trans., AIME, 222., September, pp. 937-949.

Phillips, R. 1989. Centrifuge lateral pile tests in clay (Exhibit A-PR-10592); Task 1 - Final Report. Prepared by the Soil Mechanics Group at Cambridge University for Lynxvale Limited. June.

Pietruszczak, S. and Z. Mroz. 1981. Finite element analysis of deformation of strain-softening materials. International Journal for Numerical Method in Engineering, 17: pp. 327-

334.

Piggott, A. R. and Elsworth, D. 1994. Formation fluid displacement induced by hydraulic fracturing. Proceedings 8th International Conference on Computer Methods and Advances in Geomechanics, Morgantown, WY, May 22-28, Vol. 2, pp. 1627-1632.

Piggott, A. R. 1995. Static and dynamic calculation of formation fluid displacement induced by hydraulic fracturing. National Water Research Institute Contribution Number 95-25.

Piggott, A. R. 1996. Contaminant mobilization impacts of hydraulic fracturing for groundwater remediation. Canadian Geotechnical Society, 49th Canadian Geotechnical Conference, September 23-25, St. John's, NF, pp. 833-840.

Poorooshasb, F. 1991. Centrifuge modelling of laterally loaded pipelines. Contract Report for NOVA Corporation of Alberta, C-CORE Contract Number 91-C14.

Rossato, G., N. L. Ninis, and R. J. Jardine. 1992. "Properties of Some Kaolin Based Model Clay Soils". ASTM GTJODJ, Vol. 15, No. 2, pp 166-179.

Ruland, W. W., J. A. Cherry, and S. Feenstra. 1990. The depth of fractures and active groundwater flow in a clayey till plain in Southwestern Ontario. Ground Water, Vol. 29, No. 3, pp. 405-418.

Rummel, F. and O. Kappelmeyer. 1982. The Falkenberg geothermal frac-project: Concepts and experimental results. Hydraulic Fracturing and Geothermal Energy. Nemat-Nasser, S., H. Abe and S. Hirakawa, Editors. Martinus Nijhoff Pub. The Hague. pp. 59-74.

Sage CRISP. 1997. Evaluation Software: SAGE CRISP Critical state soil mechanics program. A partnership project of SAGE Engineering and Cambridge University.

Schofield, A. N. 1980. Cambridge geotechnical centrifuge operations; Twentieth Rankine Lecture, Géotechnique, 30 (3), 227-268.

Schuring, J. R., P. C. Chan, and T. M. Boland. 1995. Using pneumatic fracturing for in-situ remediation of contaminated sites. Remediation. Spring, pp. 77-89.

Scott, J. D., D. Adhikary, and S. A. Proskin. 1991. Volume and permeability changes associated with steam stimulation in an oil sands reservoir. Proceedings CIM/AOSTRA 1991 Technical Conference. Paper No. 91-63.

Seed, H. B. and J. M. Duncan. 1981. The Teton Dam failure - a retrospective review. 10th

ICSMFE, Stockholm, Sweden, Vol. 4, pp. 214-238.

Sherard, J. L. 1970. Loss of water in boreholes in impervious embankment sections. Proceedings, 10ª ICOLD Congress, Montreal, Vol. VI, 1970, pp. 377-381.

Sherard, J. L. 1973. Embankment dam cracking. Embankment Dam Engineering, S. Poulos and R. Hirschfeld, Eds., John Wiley and Sons, New York, N.Y., pp. 272-353.

Sherard, J. L. 1986. Hydraulic fracturing in embankment dams. Journal of Geotechnical Engineering, Vol. 112, No. 10, October. Paper No. 20963, pp. 905-927.

Shuck, L. Z. 1974. The determination of direction and length of hydraulically induced fractures in petroleum reservoirs: A field experiment. SPE Annual Meeting, Houston, October 3-6. Paper SPE 5160.

Stewart, G. W. 1978. Hydraulic fracturing of drilled wells in crystalline rock of New Hampshire. New Hampshire Department of Resources and Economic Development, Concord, NH.

Trevits, M. A., M. E. Hanson, and V. L. Ward. 1982. Methane drainage: Identification and evaluation of the parameters controlling induced fracture geometry. SPE Unconventional Gas Recovery Symposium, Pittsburgh, May, Paper SPE 10820.

Tyler, L. D., W. C. Vollendorf, and D. D. Northrup. 1977. In-situ examination of hydraulic fractures. ERDA Symposium on Enhanced Oil Recovery and Improved Drilling Methods, Tulsa, OK, September.

U.S. EPA. 1990. Handbook of in situ treatment of hazardous waste-contaminated soils. EPA/540/2-90/002.

U.S. EPA, 1994. Manual - Alternative methods for fluid delivery and recovery. EPA/625/R-94/003, September.

U.S. EPA, 1997a. Vendor Information System for Innovative Treatment Technologies (VISITT) - Version 6.0. The Technology Innovation Office of the U.S. Environmental Protection Agency Office of Solid Waste and Emergency Response, December.

U.S. EPA, 1997b. Analysis of selected enhancements for soil vapour extraction. EPA/542/R-97/007, U.S. Environmental Protection Agency Office of Solid Waste and Emergency Response Technology Innovation Office. September.

U.S. Government Printing Office. 1976. Independent Panel to Review Cause of Teton Dam

Failure. - Report on Teton Dam Failure. Washington, D.C.

Vardoulakis, I. 1980. Shear band inclination and shear modulus of sand in biaxial tests. International Journal of Numerical and Analytical Methods in Geomechanics, 4: pp 103-119.

Vermeer, P. A., and R. de Borst. 1984. Non-associated plasticity for soils, concrete and rock. Heron, 29 (3), pp. 3-64.

Wade, A., G. W. Wallace, S. F. Siegwald, W. A. Lee, and K. C. McKinney. 1996. Performance comparison between a horizontal and a vertical air sparging well: a full-scale one-year pilot study. In: Proceedings of the 10th National Outdoor Action Conference and Exposition, Las Vegas, Nevada. National Groundwater Association. Pages 189-206. May 13-15.

Wan, R., D. Chan, and N. R. Morgenstern. 1992. Modeling discontinuous behaviour and fault formation in geomaterials. Conference on Fractured and Jointed Rock Masses, Lake Tahoe, June 3-5, pp. 328-334.

Warpinski, N. R., R. A. Schmidt, and D. A. Northrup. 1982. In situ stresses: The predominant influence on hydraulic fracture containment. Journal Petroleum Technology, March, pp. 653-64.

Wilson, D. D. 1995. Introduction to 1995 NGWA environmental horizontal well seminar. World Wide Web Home Page (http//:www.horizontalwell.com). October.

Wright, N. D. and M. Tan. 1991. Hydraulic fracture tests in heavily overconsolidated clay to determine conductor setting depths. Proceedings of the 1st International Offshore and Polar Engineering Conference, Edinburgh, UK, August, pp. 198-206.

Wroth, C. P. 1975. In-situ measurement of initial stresses and deformation characteristics. State of the art report, Session IV, ASCE GED Speciality Conference on In-Situ Measurement of Soil Properties, Raleigh, North Carolina.

Zrymiak, P. 1997. Hydraulic fracturing of a landfill to enhance environmental remediation. Proceedings of the 19th Canadian Waste Management Conference, St. John's, NF, September.

APPENDIX 1: CALIBRATION DATA AND INSTRUMENT SETTINGS

A1.1 Field Test FLDTST1

Table A1.1. Specifications for injection pump
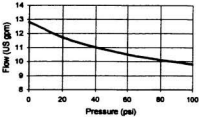
Pump Description	Rating Curve
- Sterling close coupled gear pump. - Powered by a ½ HP 115 Volt electric motor operating at 1750 rpm - The pump is machined from cast bronze and has replaceable bearings and a stainless steel shaft. - The pump has a 3/4 inch inlet and outlet and can be operated in any direction up to pressures of 100 psi. - The performance curve for this pump is shown on the adjacent figure.	

Table A1.2. Calibration data for pore pressure transducers - FLDTST1

Model	Serial Number	Excitation	Range	Calibration Constant
BHL-4269-01-1OMO-W2	L338671	4-20mA @ 24V 120 ohm resistor	0 - 600 kPa (adjusted 0 - 500 kPa)	0.066501 V/psi
BHL-4269-20-15MO	L356424	4-20mA @ 24V 120 ohm resistor	0 - 100 kPa (adjusted 0 - 100 kPa)	0.133 V/psi
Druck PPT	4365	5V	35 kPa (5 psi)	1.483 mV/V/psi
Druck PPT	3901	5V	35 kPa (5 psi)	1.293 mV/V/psi

Table A1.3. Calibration data for LDT's - FLDTST1

Instrument No	Instrument Type	Model	Type	ID. No	Excit.	Calibration Constant
LDT-01	LDT	Penny & Giles Potentiometers Ltd	HLP190	73275422	5V	-0.01001 V/mm
LDT-02	LDT	Penny & Giles Potentiometers Ltd	HLP190	73275421	5V	-0.00997 V/mm

A1.2   Field Test FLDTST2

Table A1.4. Calibration data for pore pressure transducers - FLDTST2

Instrument		Location			Serial Number	Model	Range	Exc.	Gain	Calibration Constant
Number	Type	N	E	Depth						
P-01	PPT	1.0	0.0	3.0	7471	Druck	100 psi	5V	421	0.1579 mV/V/psi
P-02	PPT	0.0	0.0	2.5	C02	Entran	100 psi	5V	1000	-0.0850 mV/V/psi
P-03	PPT	2.0	0.0	2.5	9099	Entran	100 psi	5V	510	0.1571 mV/V/psi
P-04	PPT	3.0	0.0	2.0	C03	Entran	100 psi	5V	1000	-0.0666 mV/V/psi
P-05	PPT	1.0	0.0	1.5	C04	Entran	100 psi	5V	510	-0.0925 mV/V/psi
P-06	PPT	2.0	0.0	1.5	4378	Druck	15 psi	5V	200	0.7271 mV/V/psi
P-07	PPT	1.0	0.0	1.0	6805	Druck	100 psi	5V	1000	0.1575 mV/V/psi
P-08	PPT	3.0	0.0	1.0	L338671	BHL	600 kPa	15V	1	4.4588 mV/V/psi
P-09	PPT	0.0	0.0	0.5	3901	Druck	5 psi	5V	200	1.3168 mV/V/psi
P-10	PPT	2.0	0.0	0.5	4365	Druck	5 psi	5V	200	1.4944 mV/V/psi
P-11	PPT	0.0	0.0	0.5	4386	Druck	5 psi	5V	355	1.3227 mV/V/psi
P-12	PPT				7291	Druck	100 psi	5V	355	0.1764 mV/V/psi
P-13	PPT	4.0	0.0	0.5	9100	Druck	100 psi	5V	2000	0.1562 mV/V/psi
TSC-1	Stress cell	1.0	0.0	2.0				10V	664	0.0483 mV/V/psi

Table A1.5. Calibration data for LDT's - FLDTST2

Instrument		Location			ID No.	Model	Range	Exc.	Gain	Calibration Constant
No.	Type	N	E	Depth						
L-01	LDT	-0.3	-2.0	0.0	#1	Green LP50-F	0 to 40 mm	10V	1	-0.1877 V/mm
L-02	LDT	-0.3	-1.0	0.0	#2	Green LP50-F	0 to 40 mm	10V	1	-0.2000 V/mm
L-03	LDT	-0.3	1.0	0.0	#3	Green LP50-F	0 to 40 mm	10V	1	-0.2005 V/mm
L-04	LDT	-0.3	2.0	0.0	#4	Green LP50-F	0 to 40 mm	10V	1	-0.2008 V/mm
L-05	LDT	0.0	0.0	0.0	#6	Green LP50-F	0 to 40 mm	10V	1	-0.2000 V/mm
L-06	LDT	0.5	0.0	0.0	#8	Green LP50-F	0 to 40 mm	10V	1	-0.2022 V/mm
L-07	LDT	1.0	0.0	0.0	#9	Green LP50-F	0 to 40 mm	10V	1	-0.2009 V/mm
L-08	LDT	2.0	0.0	0.0	#10	Green LP50-F	0 to 40 mm	10V	1	-0.2005 V/mm
L-09	LDT	3.0	0.0	0.0	#18	Green LP50-F	0 to 40 mm	10V	1	-0.2018 V/mm
L-10	LDT	4.0	0.0	0.0	#19	Green LP50-F	0 to 40 mm	10V	1	-0.2012 V/mm

A1.3 Centrifuge Tests

Table A1.6. Calibration constants and instrumentation settings for CCFS01

Channel		Device			Gain	Exc Volt	SE/DIFF	Calib. Constant	
SC Box	SM	Type	Number	Location				Value	Units
1	2	PPT	9099	A1	355	5	Diff	0.1579	mV/V/psi
2	3	PPT	8062	A2	664	5	Diff	0.0726	mV/V/psi
3	4	PPT	7291	B1	355	5	Diff	0.1753	mV/V/psi
4	5	PPT	8058	B2	355	5	Diff	0.072	mV/V/psi
5	6	PPT	8061	C1	664	5	Diff	0.0809	mV/V/psi
6	7	PPT	8060	C2	664	5	Diff	0.0796	mV/V/psi
7	8	PPT	9101	D1	664	5	Diff	0.1579	mV/V/psi
8	9	PPT	7483	Well top	355	5	Diff	0.1614	mV/V/psi
9	10	PPT	7471	Well side	355	5	Diff	0.1579	mV/V/psi
10	11	LVDT	61595	1	1	10	Diff	-0.6791	V/V/in
11	12	LVDT	61593	2	1	10	Diff	-0.6803	V/V/in
12	13	LVDT	3316	3	1	10	Diff	1.024	V/V/in
13	14	LVDT	3315	4	1	10	Diff	1.024	V/V/in
14	15	LVDT	3313	5	1	10	Diff	1.142	V/V/in
15	16	LVDT	3314	6	1	10	Diff	1.139	V/V/in
16	17	Cone Vert Pot			1	10	SE		

Table A1.7. Calibration constants and instrumentation settings for CCFS02

Channel		Device			Gain	Exc Volt	SE/DIFF	Calib. Constant	
SC Box	SM	Type	Number	Location				Value	Units
1	2	PPT	8061	E1	664	5	Diff	0.0831	mV/V/psi
2	3	PPT	8063	E2	664	5	Diff	0.0879	mV/V/psi
3	4	PPT	8058	F1	664	5	Diff	0.0732	mV/V/psi
4	5	PPT	9101	F2	355	5	Diff	0.1568	mV/V/psi
5	6	PPT	8059	G1	664	5	Diff	0.0802	mV/V/psi
6	7	PPT	8060	G2	664	5	Diff	0.0811	mV/V/psi
7	8	PPT	8062	H1	664	5	Diff	0.0736	mV/V/psi
8	9	PPT	9099	H2	355	5	Diff	0.1575	mV/V/psi
9	10	PPT	7471	Well top	355	5	Diff	0.1591	mV/V/psi
10	11	PPT	7291	Well side	355	5	Diff	0.1767	mV/V/psi
11	12	LVDT	3314	1	1	10	Diff	1.1390	V/V/in
12	13	LVDT	61595	2	1	10	Diff	-0.6791	V/V/in
13	14	LVDT	61593	3	1	10	Diff	-0.6803	V/V/in
14	15	LVDT	3313	4	1	10	Diff	1.1420	V/V/in
15	16	LVDT	3316	5	1	10	Diff	1.0240	V/V/in
16	17	LVDT	3315	6	1	10	Diff	1.0240	V/V/in
17	18	Cone String Pot			1	10	SE		

Table A1.8. Calibration constants and instrumentation settings for CCFS03

| Channel | | Device | | | Gain | Exc | SE/DIFF | Calib. Constant | |
SC Box	SM	Type	Number	Location		Volt		Value	Units
1	2	PPT	8062	I1	664	5	Diff	0.07358	mV/V/psi
2	3	PPT	8059	I2	664	5	Diff	0.08214	mV/V/psi
3	4	PPT	8061	J1	664	5	Diff	0.08314	mV/V/psi
4	5	PPT	8060	J2	664	5	Diff	0.0811	mV/V/psi
5	6	PPT	9101	K1	355	5	Diff	0.15676	mV/V/psi
6	7	PPT	7483	K2	355	5	Diff	0.16218	mV/V/psi
7	8	PPT	7291	L1	355	5	Diff	0.1767	mV/V/psi
8	9	PPT	7471	L2	355	5	Diff	0.15913	mV/V/psi
9	10	PPT	8063	Welltop	355	5	Diff	0.08793	mV/V/psi
10	11	PPT	9099	Wellside	355	5	Diff	0.15746	mV/V/psi
11	12	LVDT	3315	1	1	10	Diff	1.024	V/V/in
12	13	LVDT	61595	2	1	10	Diff	-0.6791	V/V/in
13	14	LVDT	61593	3	1	10	Diff	-0.6803	V/V/in
14	15	LVDT	3316	4	1	10	Diff	1.024	V/V/in
15	16	LVDT	3313	5	1	10	Diff	1.142	V/V/in
16	17	LVDT	3314	6	1	10	Diff	1.139	V/V/in
17	18	Cone String Pot			1	10	SE		

Table A1.9 Calibration constants and instrumentation settings for CCFS04

| Channel | | Device | | | Gain | Exc | SE/DIFF | Calib. Constant | |
SC Box	SM	Type	Number	Location	M,NOP	Volt		Value	Units
1	2	PPT	8062	M1	664,1000	5	Diff	0.07358	mV/V/psi
2	3	PPT	8059	M2	664,1000	5	Diff	0.08214	mV/V/psi
3	4	PPT	8061	N1	664,1000	5	Diff	0.08314	mV/V/psi
4	5	PPT	8060	N2	664,1000	5	Diff	0.0811	mV/V/psi
5	6	PPT	9101	O1	355,664	5	Diff	0.15676	mV/V/psi
6	7	PPT	7483	O2	355,664	5	Diff	0.16218	mV/V/psi
7	8	PPT	7291	P1	355,664	5	Diff	0.1767	mV/V/psi
8	9	PPT	7471	P2	355,664	5	Diff	0.15913	mV/V/psi
9	10	PPT	8063	Well M	664,1000	5	Diff	0.08793	mV/V/psi
10	11	PPT	9099	Well N	355,664	5	Diff	0.15746	mV/V/psi
11	12	PPT	8058	Well O	664,1000	5	Diff	0.072	mV/V/psi
12	13	PPT	7475	Well P	355,664	5	Diff	0.16	mV/V/psi
13	14	LVDT	3315	1	1	10	Diff	1.024	V/V/in
14	15	LVDT	61595	2	1	10	Diff	-0.6791	V/V/in
15	16	LVDT	61593	3	1	10	Diff	-0.6803	V/V/in
16	17	LVDT	3316	4	1	10	Diff	1.024	V/V/in
17	18	LVDT	3313	5	1	10	Diff	1.142	V/V/in
18	19	LVDT	3314	6	1	10	Diff	1.139	V/V/in
19	20	Cone String Pot			1	10	SE		

APPENDIX 2: SOIL TEST RESULTS

A2.1   Field Tests

Five test pits were excavated within the ETF field testing area to characterize the soil and determine a suitable location for construction of testbeds for the field injection tests. The approximate locations of the testbeds are shown on the site plan in Figure 3.1. The logs for the test pits are as follows:

Test pit TP97-1:   2.8 m deep x 2.5 m wide x 4 m long

Depth Interval	Soil Description	Notes
0.0 to 0.42 m	dark brown SAND and GRAVEL, some silt and cobbles, loose, moist, roots throughout. FILL	- cobbles up to 0.6 m dia - tough digging through large boulders
0.42 to 0.51 m	black TOPSOIL, organic	- small pockets of water throughout
0.51 to 0.61 m	dark grey-brown SAND and GRAVEL, some silt and cobbles, compact, moist	- rocks weathered and subangular
0.61 to 2.20 m	grey SAND and GRAVEL, some silt and frequent cobbles, dense, moist becoming wet.	- soil backfilled into pit and roughly levelled
2.20 to 2.80 m	dark grey SAND and GRAVEL, some silt, frequent cobbles, dense, moist.	
2.80 m	End of Test Pit	

293

Test pit TP97-2:   2.7 m deep x 3.5 m wide x 4.5 m long

Depth Interval	Soil Description	Notes
0.0 to 0.40 m	dark brown SAND and GRAVEL, some silt and cobbles, loose, moist, roots throughout. FILL	- cobbles up to 0.7 m dia - some large boulders making digging difficult
0.40 to 0.44 m	black TOPSOIL, organic	- water pockets encountered
0.44 to 0.70 m	rusty brown SAND and GRAVEL, some silt and cobbles, compact, moist	- soil backfilled into pit and roughly levelled
0.70 to 2.70 m	dark grey SAND and GRAVEL, some silt, frequent cobbles, a few boulders, dense, moist to wet.	
2.70 m	End of Test Pit	

Test pit TP97-3:   2.8 m deep x 3.5 m wide x 4 m long

Depth Interval	Soil Description	Notes
0.0 to 0.20 m	dark brown SAND and GRAVEL, some silt and cobbles, loose, moist, roots throughout. FILL	- few water pockets - soil backfilled into pit and roughly levelled
0.20 to 0.23 m	black TOPSOIL, organic	
0.23 to 0.51 m	rusty brown SAND and GRAVEL, some silt and cobbles, compact, moist, grades into next unit	
0.51 to 2.30 m	grey-brown SAND and GRAVEL, some silt, frequent small cobbles, dense, moist	
2.30 to 2.80 m	grey SAND and GRAVEL, some silt and cobbles, dense, moist to wet, small black lens at top of layer	
2.80 m	End of Test Pit	

Test pit TP97-4:   3.1 m deep x 4 m wide x 4 m long

Depth Interval	Soil Description	Notes
0.0 to 0.19 m	dark brown SAND and GRAVEL, some silt and cobbles, loose, moist, roots throughout. FILL	- rocks tend to be sub-angular to sub-rounded
0.19 to 0.45 m	rusty SAND and GRAVEL, some silt and cobbles, compact, moist, colour changes to brown with depth	- increasing difficulty in digging with depth - large boulder at 1 m depth
0.45 to 3.10 m	grey-brown SAND and GRAVEL, some silt, increasing cobbles with depth, dense, moist	- water pocket at 1.5 m - soil backfilled into pit and roughly levelled
3.10 m	End of Test Pit	

Test pit TP97-5:   2.8 m deep x 4 m wide x 4 m long

Depth Interval	Soil Description	Notes
0.0 to 0.34 m	dark brown SAND and GRAVEL, some silt and boulders, loose, moist, roots throughout. FILL	- old hydro lines near surface
0.34 to 0.44 m	rusty SAND and GRAVEL, some silt, compact, moist	- soil backfilled into pit and roughly levelled
0.44 to 0.62 m	brown SAND and GRAVEL, some silt and cobbles, compact, moist	
0.62 to 2.80 m	grey-brown SAND and GRAVEL, some silt, and cobbles, dense, moist	
2.80 m	End of Test Pit	

Table A2.1. Compaction test records for FLDTST1

Test ID	Location				Probe Depth	Density		Moisture Content
	Northing metres	Easting metres	Depth metres	Elevation metres	mm	Wet kg/m³	Dry kg/m³	%
1	0.10	-0.60	2.55	97.19	150	2324	2138	8.7
2	0.30	0.60	2.45	97.29	150	2220	1989	11.6
3	0.80	0.00	2.38	97.37	150	2280	2077	9.8
4	-1.00	0.40	2.38	97.37	150	2240	2026	10.6
5	0.80	-0.45	2.25	97.49	150	2137	1871	14.2
6	-0.20	0.80	2.25	97.49	150	2440	2259	8.0
7	-0.10	-1.20	2.14	97.60	150	2202	1900	15.9
8	-0.80	1.10	2.14	97.60	150	2276	2058	10.6
9	0.30	-1.30	1.98	97.76	150	2179	1929	13.0
10	1.20	0.30	1.98	97.76	150	2172	1891	14.8
11	-1.10	1.00	1.96	97.78	150	2149	1979	8.6
12	-1.10	-1.30	1.96	97.78	150	2197	2024	8.5
13	-1.50	0.60	1.87	97.88	150	2277	2036	11.9
14	0.35	1.65	1.87	97.88	150	2071	1889	9.6
15	-0.60	-1.60	1.70	98.04	150	2078	1877	10.7
16	-0.40	1.70	1.70	98.04	150	2278	2030	12.3
17	-0.30	0.50	1.62	98.12	150	2128	1845	15.4
18	0.90	-0.20	1.62	98.12	150	2132	1831	16.4
19	0.35	0.00	1.53	98.21	150	2126	1801	18.1
20	0.70	-1.50	1.53	98.21	150	2095	1819	15.2
21	1.25	-1.10	1.33	98.41	150	2083	1801	15.7
22	-1.30	1.00	1.33	98.41	150	2262	2000	13.1
23	1.30	0.60	1.29	98.45	150	2160	1888	14.4
24	-0.80	1.20	1.29	98.45	150	2013	1698	18.5
25	-1.20	1.20	1.21	98.53	150	2109	1866	13.0
26	1.80	0.20	1.21	98.53	150	2160	1946	11.0
27	1.00	1.10	1.03	98.71	150	2168	1906	13.7
28	-1.40	1.00	1.03	98.71	150	2107	1825	15.4
29	0.30	1.90	0.89	98.85	150	2045	1714	19.3
30	-0.70	-0.90	0.89	98.85	150	2166	1887	14.8
31	-1.10	1.50	0.77	98.97	150	2149	1851	16.1
32	-0.65	-0.55	0.77	98.97	150	2196	1885	16.5
33	-1.60	1.30	0.70	99.04	150	2073	1742	19.0
34	1.30	0.20	0.70	99.04	150	2139	1839	16.3

Table A2.2. Compaction test records for FLDTST2

Test ID	Location				Probe Depth	Density		Moisture Content
	Northing metres	Easting metres	Depth metres	Elevation metres	mm	Wet kg/m³	Dry kg/m³	%
1	2.30	-1.10		96.19	150	2122	1939	9.4
2	0.85	2.50		96.19	150	2093	1913	9.4
3	-3.55	-1.40		96.83	150	2202	2027	8.6
4	0.60	1.35		96.72	150	2045	1880	8.8
5	2.80	0.00		96.82	150	1861	1709	8.9
6	0.60	0.45		96.98	150	1944	1793	8.4
7	-1.35	0.50		96.94	150	1980	1808	9.5
8	-1.10	1.00		97.11	150	1850	1706	8.4
9	-3.25	0.25		97.35	150	1902	1741	9.2
10	-3.60	-1.50		97.43	150	1937	1804	7.4
11	-4.60	-0.20		97.66	150	1998	1841	8.5
12	-2.75	1.45		97.77	150	1972	1828	7.9
13	2.40	0.95		97.39	150	1986	1832	8.4
14	2.90	-1.07		97.56	150	1899	1761	7.9
15	2.40	-0.50		97.69	150	1825	1692	7.8
16	3.65	-1.13		97.78	150	2281	2134	6.9
17	1.20	0.40		97.86	150	2240	2074	8.0
18	2.05	0.20		97.97	150	2052	1837	11.7
19	-3.70	0.89		97.96	150	2106	1975	6.6
20	0.89	0.75		98.28	150	1808	1633	10.7
21	-3.60	-1.40		98.46	150	2031	1838	10.5
22	-2.30	-1.20		98.49	150	1924	1752	9.8
23	2.20	1.00		98.22	150	1917	1732	10.7
24	1.25	-1.30		98.29	150	1785	1626	9.8
25	2.40	-0.40		98.44	150	1999	1774	12.7
26	0.80	-1.00		98.60	150	1910	1716	11.3
27	2.70	0.20		98.82	150	2010	1884	6.7
28	-2.90	-1.10		98.72	150	2033	1802	12.8
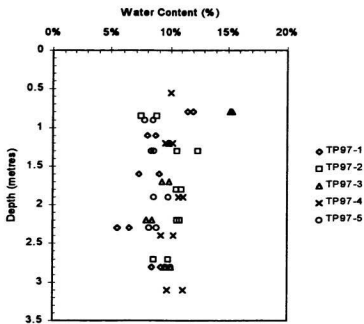
Figure A2.1. Natural moisture content of Argentia till from test pit samples
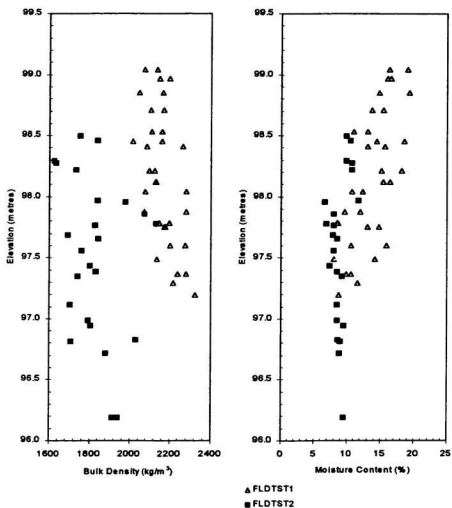
Figure A2.2. Moisture content and density distribution for FLDTST1 and FLDTST2
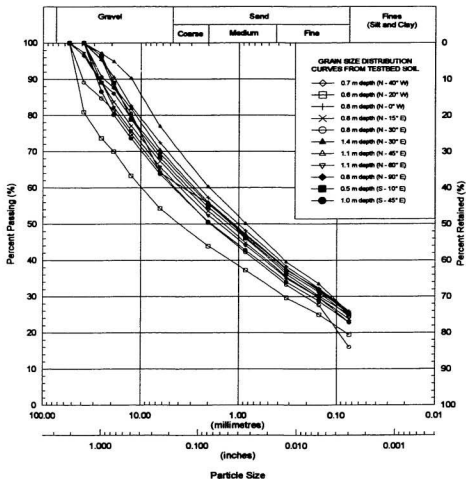
Figure A2.3. Grain size distribution for test bed soil - FLDTST1

300

A2.2 Speswhite Kaolin Tests

A2.2.1 Consolidation of clay

The vertical effective stress increments applied during consolidation of the kaolin slurry for CCFS01 and CCFS02 were 25, 50, 100, 200, 400 and 750 kPa during the loading sequence and 750, 400, 200, and 100 kPa during the unloading sequence. The vertical displacement of the consolidometer piston is plotted against time for CCFS02 in Figures A2.4 and A2.5. In Figure 2.6, the specific volume is plotted against log p' for CCFS02 (where p' = $[\sigma_v' + 2\sigma_h']$ / 3 and K is assumed to be equal to 0.64).

A2.2.1 Moisture content and density profiles

Moisture content distributions and bulk density were determined for five kaolin samples taken from CCFS01 using a 38 mm diameter thin-walled tube. The sample locations are shown in Figure A2.8. The moisture content profiles determined for the test bed are shown in Figure A2.9. The measured bulk density and moisture content of the kaolin are summarized together with the computed degree of saturation and void ratio in Table A2.3.

Table A2.3. Soil density measurements

Sample ID	Depth (metres)	w_{avg} (%)	ρ (kg/m³)	ρ_d (kg/m³)	G_s	S (%)	e_{avg}
Col 1	0 to 0.26	43.3	1763.1	1230.3	2.64	99.8	1.146
Col 2	0 to 0.28	42	1769.7	1246	2.64	99.2	1.119
Col 3	0 to 0.22	43.5	1735.3	1209.5	2.64	97	1.183
Col 4	0 to 0.22	42.4	1756.3	1233.8	2.64	98.1	1.14
Col 5	0 to 0.07	42.3	1702.8	1196.2	2.64	92.6	1.207

A2.2.2 Undrained shear strength

A2.2.2.1 Hand vane tests

The undrained shear strength of the overconsolidated kaolin from CCFS01 was determined using a Pilcon hand vane shear device. Shear vane profiles were taken at the five locations shown on Figure A2.8 at depths of 40 mm, 94 mm and 148 mm. The test depth was measured at the center of the 29 mm high by 19 mm wide vane. The undrained strengths determined from the hand vane tests are summarized in Table A2.4.

Table A2.4. Undrained strength of kaolin from vane shear tests

Test ID	Undrained Shear Strength (kPa)					
	Depth 40 mm		Depth 94 mm		Depth 148 mm	
	Peak	Residual	Peak	Residual	Peak	Residual
VS 1	38.5	12	39	12	40.5	13
VS 2	40	11	41.5	12	42.5	12
VS 3	35	10	37	10	38	12
VS 4	37	10	38.5	11	38	11
VS 5	37	12	37.5	11	46	15

A2.2.2.2 Torvane and pocket penetrometer tests

The locations in CCFS01 at which the undrained strength was determined using the Torvane and pocket penetrometer are shown in Figure A2.10. Shear strength profiles were taken immediately following the completion of the injection test. Measurements were taken at the ground surface, at a depth of 40 mm and at a depth of 160 mm. A summary of the undrained strengths determined by Torvane and pocket penetrometer is provided in Table A2.5. The torvane and pocket penetrometer tests were carried out during the excavation process, which took place several days after the injection test had been completed. The lower shear strengths obtained from the torvane and pocket penetrometer tests as compared to the vane shear tests show some softening of the clay due to moisture redistribution.

Table A2.5. Undrained strength from torvane and pocket penetrometer tests

Test ID	Torvane test (kPa)			Pocket Penetrometer (kPa)		
	Surface	40 mm	160 mm	Surface	40 mm	160 mm
TP 1	28	22	25	29	27	22
TP 2	32	--	--	29	--	--
TP 3	27	--	25	27	--	29
TP 4	30	--	--	29	--	--
TP 5	25	27	25	25	25	20
TP 6	28	--	--	29	--	--
TP 7	29	27	25	32	27	22
TP 8	29	25	23	31	18	18
TP 9	32	26	23	22	29	17
TP 10	32	27	--	27	22	--
TP 11	28	29	28	25	22	20

A2.2.2.3 Unconsolidated undrained triaxial tests

Thin-walled tube samples were taken from CCFS01 clay soil for determination of undrained shear strength by unconsolidated undrained (UU) triaxial tests. Stress strain plots for the three UU triaxial tests are provided in Figure A2.11. The undrained shear strengths determined for the three UU tests were 18 kPa, 24 kPa and 19 kPa (average 20 kPa).

A2.2.3 Triaxial testing

Thin-walled tube samples of overconsolidated Speswhite kaolin clay were taken from the CCFS01 and CCFS02 test beds for triaxial strength testing. The triaxial tests carried out on these samples were consolidated drained (CD) tests. In addition, three consolidated undrained (CU) triaxial tests and three CD triaxial tests were carried out on Speswhite kaolin clay from a smaller tub sample (300 mm diameter) that had been consolidated from a slurry to maximum preconsolidation stress of 287 kPa. The maximum preconsolidation stress for the small sample was limited by the capacity of the pneumatic cylinder used to consolidate the sample.

A2.2.3.1 Consolidated undrained triaxial tests in kaolin

Three CU triaxial tests were carried out on the kaolin clay (maximum preconsolidation stress of 287 kPa) at confining stresses of 50 kPa, 100 kPa and 150 kPa. Prior to shearing a test specimen, the targeted confining stress was applied and the sample was allowed to swell to achieve equilibrium. Shearing was carried out with no drainage at a strain rate of approximately 2.5 %/hour. Specimens were sheared to about 15% strain. The principal stress difference for the three CU tests is plotted against axial strain in Figure A2.12. The pore pressure generated during undrained shearing is plotted against axial strain in Figure A2.13. The ratio of maximum principal stress to the minimum principal stress is plotted in Figure A2.14. The effective stress paths for the three tests are plotted as $(\sigma_1' - \sigma_3')/2$ vs $(\sigma_1' + \sigma_3')/2$

in Figure A2.15.

A2.2.3.2 Consolidated drained triaxial tests on kaolin clay

Three CD triaxial tests were carried out on the kaolin clay that had been subjected to a maximum preconsolidation stress of 287 kPa. The triaxial tests were carried out at confining stresses of 50 kPa, 100 kPa and 150 kPa. Prior to shearing a test specimen, the targeted confining stress was applied and the sample was allowed to swell to achieve equilibrium. Shearing was carried out at a strain rate of approximately 0.2%/hour to ensure that minimal pore pressure generation would occur. All specimens were sheared to about 15% strain. The principal stress difference for the three CD tests is plotted against axial strain in Figure A2.16. The ratio of maximum principal stress to the minimum principal stress is plotted in Figure A2.17. The effective stress paths for the three tests are plotted as $(\sigma_1' - \sigma_3')/2$ vs $(\sigma_1' + \sigma_3')/2$ in Figure A2.18. The volumetric strain is plotted against axial strain in Figure A2.19.

Three CD triaxial tests were carried out on the CCFS01 clay at confining stresses of 50 kPa, 100 kPa and 150 kPa and three CD triaxial tests were carried out on CCFS02 clay at confining stresses of 25 kPa, 75 kPa, and 150 kPa. Prior to shearing a test specimen, the targeted confining stress was applied and the sample was allowed to swell to achieve equilibrium. Shearing was carried out at a strain rate of approximately 0.16%/hour to ensure that minimal pore pressure generation would occur. All specimens were sheared to about 15%

strain. The principal stress difference for the CD tests is plotted against axial strain in Figure A2.20. The ratio of maximum principal stress to the minimum principal stress is plotted in Figure A2.21. The effective stress paths for the tests are plotted as $(\sigma_1' - \sigma_3')/2$ vs $(\sigma_1' + \sigma_3')/2$ in Figure A2.22. The volumetric strain is plotted against axial strain in Figure A2.23.

A2.2.3.3 Shear failure envelopes

Shear failure envelopes are plotted in Figures A2.24, A2.25 and A2.26 for the CU and CD triaxial tests in kaolin clay. From the CU tests in kaolin preconsolidated to 287 kPa, the cohesion was 7.9 kPa and the peak effective friction angle was 23.5°. From the CD tests in kaolin preconsolidated to 287 kPa, the cohesion was 20.3 kPa and the peak effective friction angle was 20.3°. From the CD tests in CCFS01 clay preconsolidated to 750 kPa, the cohesion was 19.1 kPa and the peak effective friction angle was 22.1°.
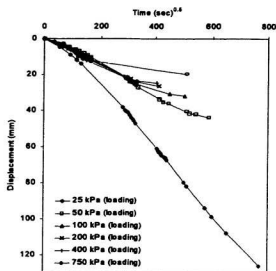
Figure A2.4. Loading curves for consolidation of clay - CCFS02
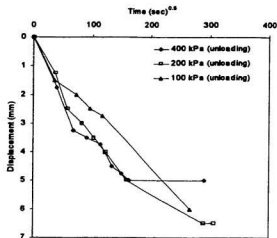
Figure A2.5. Unloading curves for consolidation of clay - CCFS02

308
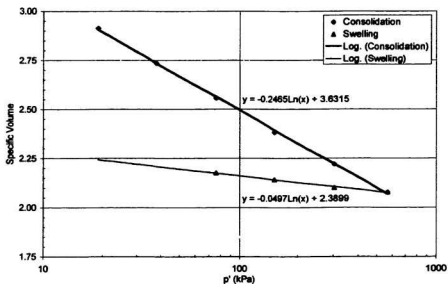
Figure A2.6. Consolidation curve for Speswhite kaolin - CCFS02

Plot annotations:
- Consolidation
- Swelling
- Log. (Consolidation)
- Log. (Swelling)

$y = -0.2465 Ln(x) + 3.6315$

$y = -0.0497 Ln(x) + 2.3899$

Axis labels: Specific Volume (y-axis), p' (kPa) (x-axis)
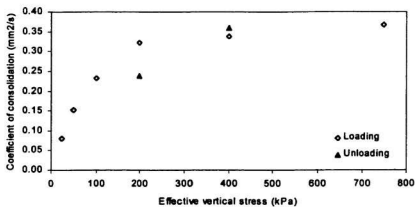
Figure A2.7. Coefficient of consolidation for Speswhite kaolin - CCFS02

Axis labels: Coefficient of consolidation (mm2/s) (y-axis), Effective vertical stress (kPa) (x-axis)

Legend:
- Loading
- Unloading
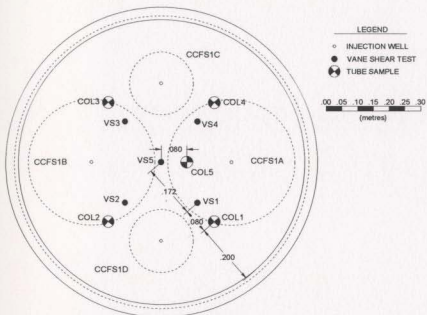
Figure A2.8. Laboratory test and strength test locations for CCFS01 clay
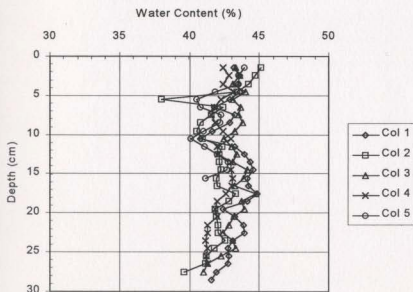
Figure A2.9. Variation of moisture content with depth (CCFS01)
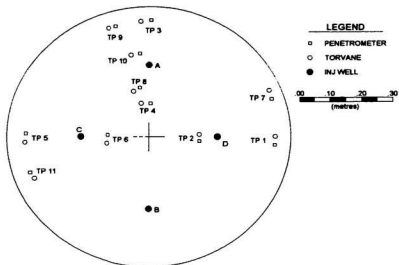
Figure A2.10. Torvane and pocket penetrometer test locations in CCFS01 clay
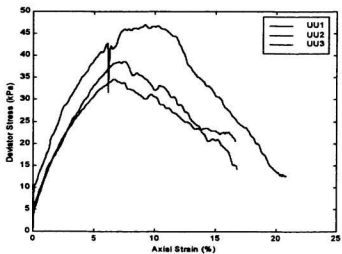
Figure A2.11. Stress versus strain plots (UU tests on CCFS01)

311
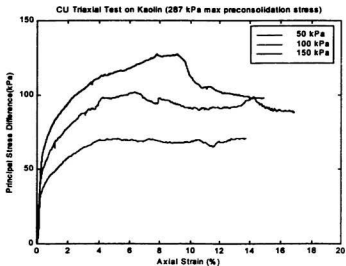
Figure A2.12. Principal effective stress difference (CU tests on kaolin)
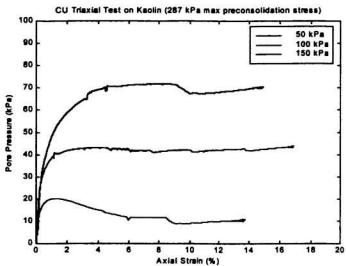
Figure A2.13. Pore pressure developed during CU triaxial tests on kaolin
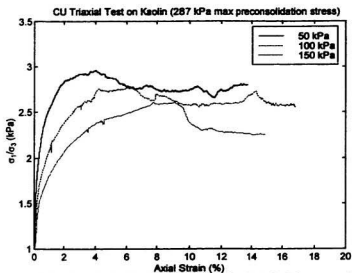
Figure A2.14. Principal effective stress ratio for CU triaxial tests on kaolin
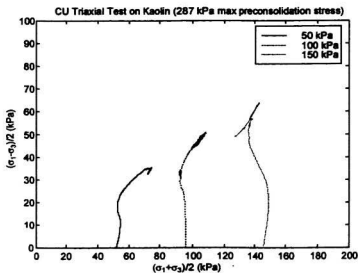
Figure A2.15. Effective stress paths for CU traixial tests on kaolin

313
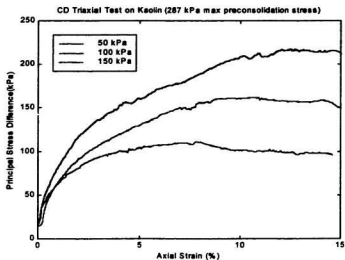
Figure A2.16. Principal effective stress difference for CD triaxial tests on kaolin
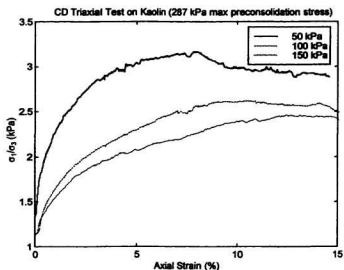
Figure A2.17. Principal effective stress ratio for CD triaxial tests on kaolin
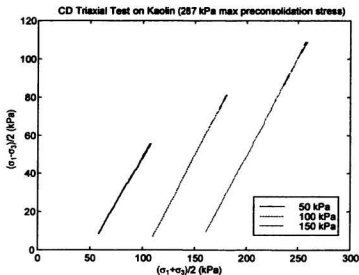
Figure A2.18. Effective stress paths for CD triaxial tests on kaolin
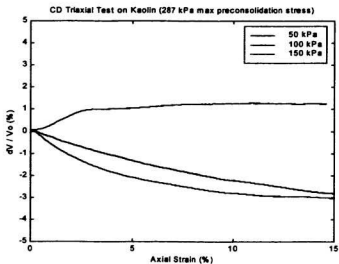
Figure A2.19. Volumetric strain for CD triaxial tests on kaolin

315
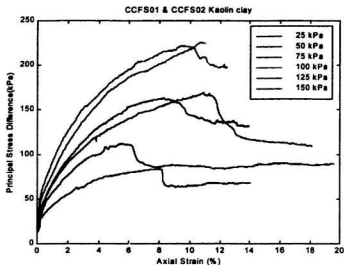
Figure A2.20. Principal eff. stress difference for CD tests (CCFS01 & CCFS02)
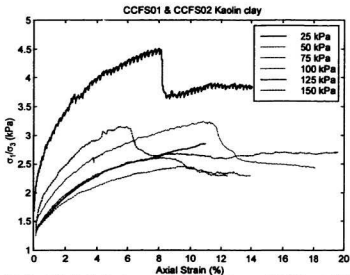
Figure A2.21. Principal effective stress ratio for CD tests (CCFS01 & CCFS02)
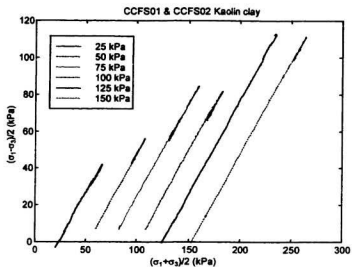
Figure A2.22. Effective stress paths for CD tests (CCFS01 & CCFS02)
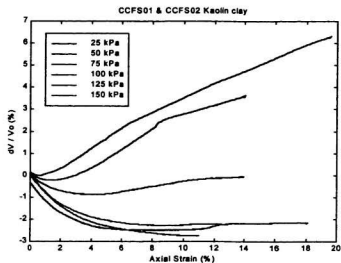
Figure A2.23. Volumetric strain for CD triaxial tests (CCFS01 & CCFS02)
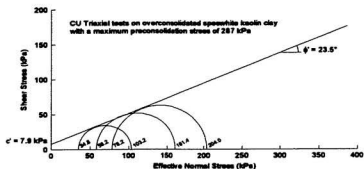
Figure A2.24. Shear failure envelope from CU triaxial tests in kaolin
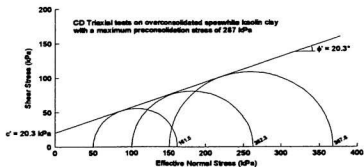
Figure A2.25. Shear failure envelope from CD triaxial tests in kaolin
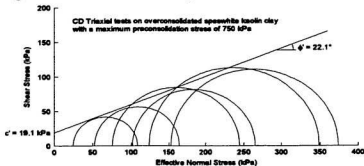
Figure A2.26. Shear failure envelope from CD tests (CCFS01 & CCFS02)

318

A2.3 Silty Sand Tests

A2.3.1 Grain size distribution

The silty sand soil used for centrifuge tests CCFS03 and CCFS04 was obtained by mixing 30% SilCoSil silt with 70% Type 00 sand (by mass). The resulting grain size distribution for the mixture is shown in Figure 2.27.

A2.3.2 Triaxial tests

Triaxial test specimens were prepared by compacting dry silty sand into a split cylindrical tube. Prior to preparing the specimen, the two halves of the 38.5 mm diameter tube were clamped together and an open ended thin latex membrane was placed inside the tube with the ends stretched over the ends of the tube. A vacuum was applied between the membrane and the inside of the tube. The tube was then set over the lower platen. A porous stone was placed on inside the tube on top of the platen. Silty sand was then placed in the tube in 10 mm thick lifts and each lift was uniformly compacted using a steel rod. The compactive effort was adjusted to achieve a target dry density of between 1900 to 2000 kg/m³. When the sample was constructed to a height of approximately 75 mm, a porous stone was placed on the upper surface and the top platen was set on top of the porous stone. The membrane was then stretched over the top and bottom platens and held in place with rubber "o" rings. The

vacuum was turned off and the split tube removed from around the sample.

The triaxial cell was filled with water and pressurized to the target cell pressure (i.e. 50, 75, or 100 kPa). To saturate the sample, the drainage line on the top of the specimen was vented to atmosphere and a water pressure of approximately 15 kPa was applied to the bottom of the sample. Approximately 4 pore volumes of water were allowed to flow into and through the specimen. The degree of saturation was checked by carrying out a "B" test. If the "B" test result was substantially less than one, the cell pressure and the back pressure were increased and the "B" test repeated. The process was repeated until a "B" value of between 0.9 and 1.0 was achieved.

Triaxial permeability tests were carried out at confining stresses of 100 and 125 kPa. The procedure used for these tests was to apply a hydraulic gradient from the bottom to the top of the sample using the back pressure reservoirs at the bottom and top of the sample. The cell pressure was maintained constant during the permeability tests. The flow of water into the bottom of the sample and out of the top of the sample was monitored. The k-test carried out at a confining stress of 100 kPa had a pressure gradient of approximately 25 kPa between the bottom and top of the specimen (see Figure 2.28). The measured permeability during the test was relatively constant at approximately 4×10^{-8} m/s (see Figure 2.29). The k-test carried out at a confining stress of 125 kPa had a pressure gradient of approximately 40 kPa between the bottom and top of the specimen (see Figure 2.30). The measured permeability during the test was approximately 1.4×10^{-8} m/s (see Figure 2.31).

Drained triaxial compression tests were carried out at confining stresses of 50, 75, and 100 kPa. Samples were sheared at a strain rate of approximately 0.4%/hour. Specimens were sheared to about 15 to 20% strain. The principal stress difference for the three CD tests is plotted against axial strain in Figure A2.32. The ratio of maximum principal stress to the minimum principal stress is plotted in Figure A2.33. The effective stress paths for the three tests are plotted as $(\sigma_1' - \sigma_3')/2$ vs $(\sigma_1' + \sigma_3')/2$ in Figure A2.34. The volumetric strain is plotted against axial strain in Figure A2.35. The peak and constant volume shear failure envelopes for the CD triaxial tests on silty sand are plotted in Figure A2.36. The peak effective friction angle was 48.2° and the constant volume friction angle was 41.8°.

A2.3.3 Hydraulic conductivity from centrifuge test

An injection test where flow is occurring freely through the pore space without yielding is similar to a constant head permeability test. Hvorslev (1951) presented a relation for determining the permeability of soil around a well from a constant head test [Eqn. A2.1]

$$k_h = \frac{q \ln\left(\dfrac{mL}{D} + \sqrt{1 + \left(\dfrac{mL}{D}\right)^2}\right)}{2\pi L H_c} \qquad \text{[Eqn. A2.1]}$$

where q is the volumetric rate of flow, L is the length of the injection interval, D is the well diameter, H_c is the constant excess head applied during the test, and m is a transformation

ratio defined as the square root of the ratio of the horizontal to vertical permeability, $m = (k_h / k_v)^{0.5}$.

The excess pressure is the total fluid pressure at the wellhead minus the pressure due to the static ground water level. Pore pressure readings from 8 buried PPTs during test M indicated that the static groundwater level was 0.039 m below the ground surface. The excess pressure at the point of injection was 28 kPa, which at 25 g is equivalent to a head of water of 0.114 m. Because the silty sand used in the test was densely compacted into the strongbox in thin horizontal lifts, it is likely that the permeability was greater in the horizontal direction than in the vertical direction and, for this analysis, it was assumed that $m = 2$. For model scale parameters: $D = 0.0093$ m, $L = 0.025$ m, and $q = 5.70 \times 10^{-8}$ m^3/s. Using these parameters in Eqn 6.4, the horizontal permeability in the centrifuge at 25 g is 7.5×10^{-6} m/s and the vertical permeability is 1.9×10^{-6} m/s. This is equivalent to $k_h = 3.0 \times 10^{-7}$ m/s and $k_v = 7.5 \times 10^{-8}$ m/s at prototype scale, which is very similar to the hydraulic conductivity determined from triaxial testing. The vertical hydraulic conductivity determined for the silty sand in a triaxial cell was 3.8×10^{-8} m/s at $\sigma_3' = 100$ kPa and 1.4×10^{-8} m/s at $\sigma_3' = 125$ kPa.
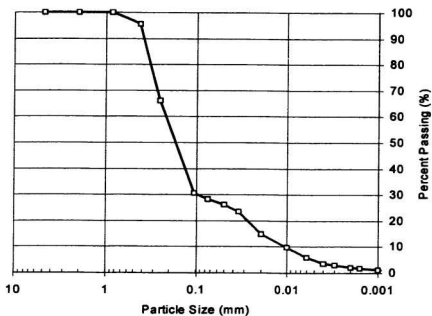
Figure A2.27. Grain size distribution for silty sand (CCFS03 &CCFS04)
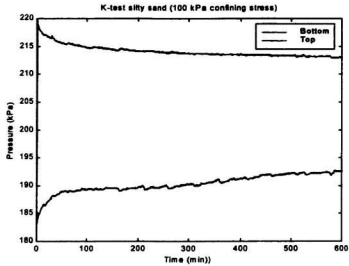
Figure A2.28. Pore pressure in silty sand during k-test ($\sigma'_3 = 100$ kPa)
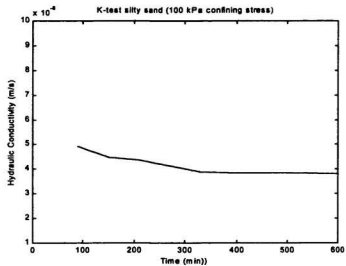
Figure A2.29. Permeability variation with time ($\sigma'_3 = 100$ kPa)
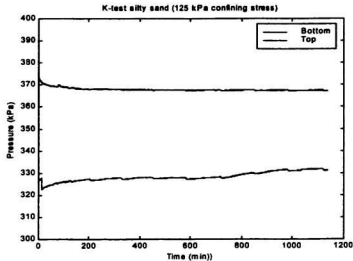
Figure A2.30. Pore pressure in silty sand during k-test $(\sigma'_3 = 125 \text{ kPa})$
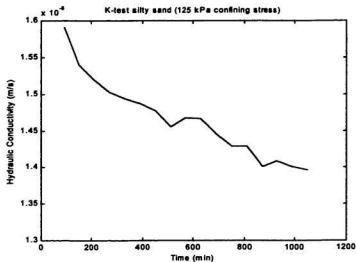
Figure A2.31. Permeability variation with time $(\sigma'_3 = 125 \text{ kPa})$

325
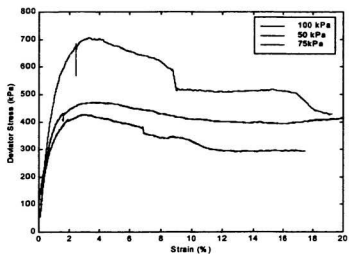
Figure A2.32. Principal effective stress difference for CD tests on silty sand
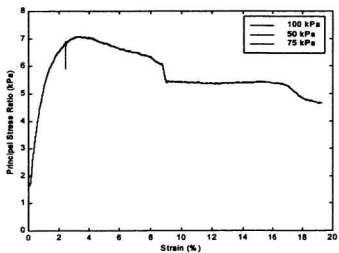
Figure A2.33. Principal effective stress ratio for CD tests on silty sand

326
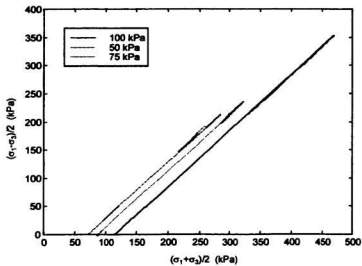
Figure A2.34. Effective stress paths for CD tests on silty sand
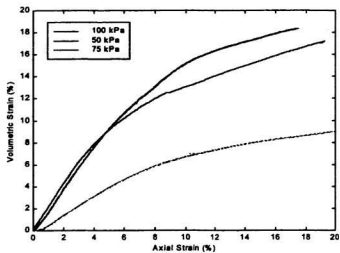
Figure A2.35. Volumetric strain for CD tests on silty sand

327
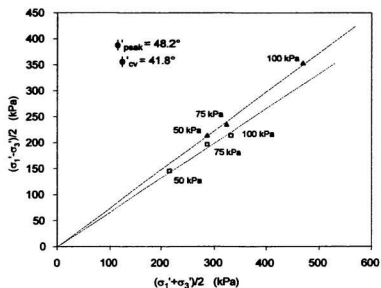
Figure A2.36. Peak and constant volume failure envelopes for silty sand

APPENDIX 3: INJECTION TEST RESULTS

A3.1. Field Tests

Hvorslev Graph

Ho is 1.905 in t = 0 sec

Time Lag is 1.32904 minutes
Hvorslev Shape Factor is 1.65598
Partial Penetration Case C

Transmissivity = 0.250515 m2/day
Hydraulic Conductivity = 0.00148691 cm/sec

Hvorslev Graph

Ho is 0.35 m at t = 208.193 sec

Time Lag is 4469.24 seconds
Hvorslev Shape Factor is 1.65598
Partial Penetration Case C

Transmissivity = 0.00446981 m2/day
Hydraulic Conductivity = 2.65302e-05 cm/sec
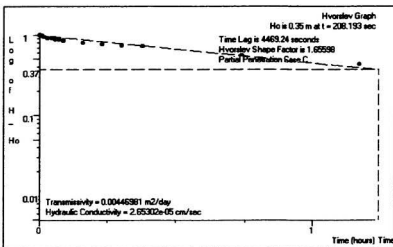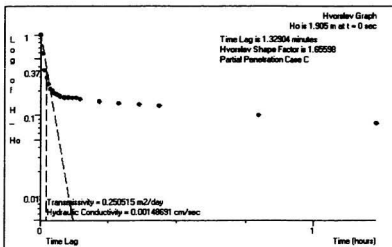
Falling head test carried out in injection well on June 24, 1997
Range in k - value using Hvorslev Method
is from 2.7 x 10-6 to 1.5 x 10-3 cm/sec
Test carried out using fresh water.

Figure A3.1. Permeability prior to injection test - FLDTST1 (June 24/97)

331

Hvorslev Graph
Ho is 1.945 m at t = 0 sec

Time Lag is 156.502 seconds
Hvorslev Shape Factor is 1.65598
Partial Penetration Case C

Transmissivity = 0.101461 m2/day
Hydraulic Conductivity = 0.000757626 cm/sec

Hvorslev Graph
Ho is 0.47 m at t = 420 sec

Time Lag is 11551 seconds
Hvorslev Shape Factor is 1.65598
Partial Penetration Case C

Transmissivity = 0.00137467 m2/day
Hydraulic Conductivity = 1.02649e-05 cm/sec
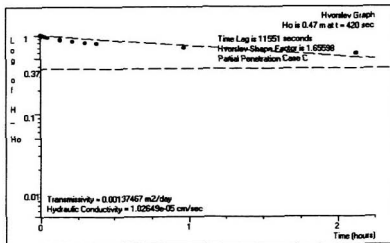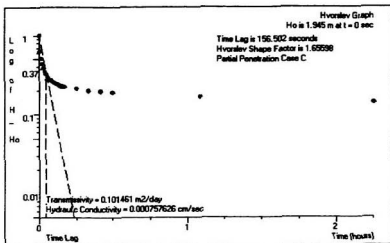
Falling head test carried out in injection well on June 26, 1997
Range in k - value using Hvorslev Method
is from 1.0 x 10⁻⁵ to 7.6 x 10⁻⁴ cm/sec
Test carried out using fresh water.

Figure A3.2. Permeability prior to injection test - FLDTST1 (June 26/97)

332
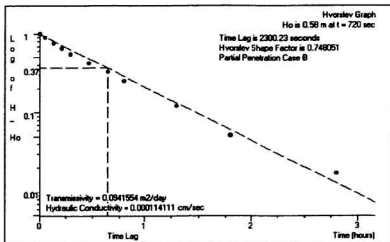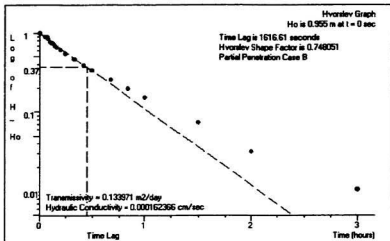
Falling head test carried out in injection well on June 27, 1997
Range in k - value using Hvorslev Method
is from 1.6 x 10⁻⁴ to 1.1 x 10⁻⁴ cm/sec
Test was carried out using injection fluid from shearing test

Figure A3.3. Permeability after injection test - FLDTST1 (June 27/97)

333
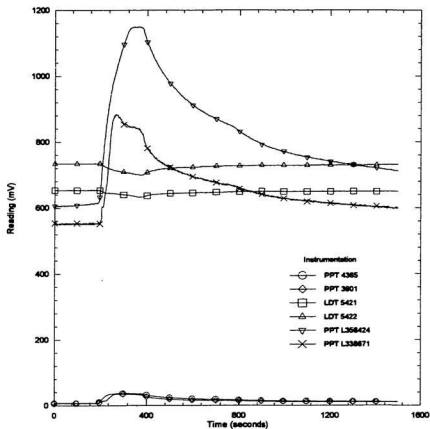
Figure A3.4. Raw PPT and LDT data from injection test - FLDTST1
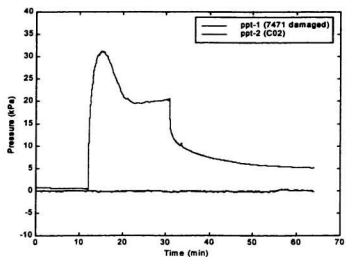
Figure A3.5. Pressure response in PPT01 and PPT02 - FLDTST2
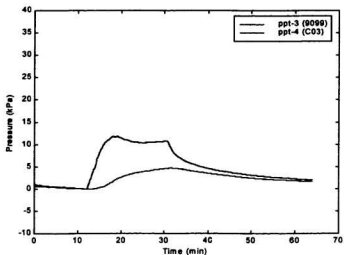
Figure A3.6. Pressure response in PPT03 and PPT04 - FLDTST2
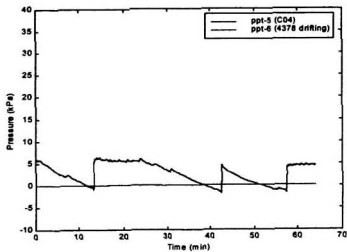
Figure A3.7. Pressure response in PPT05 and PPT06 – FLDTST2
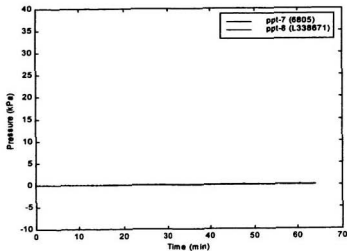
Figure A3.8. Pressure response in PPT07 and PPT08 – FLDTST2
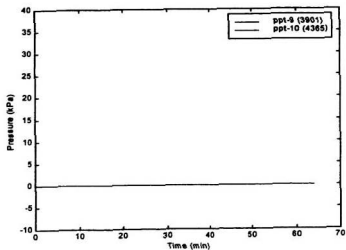
Figure A3.9. Pressure response in PPT09 and PPT10 - FLDTST2
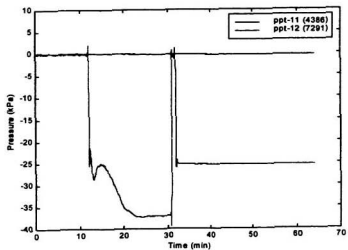
Figure A3.10. Pressure response in PPT11 and PPT12 - FLDTST2
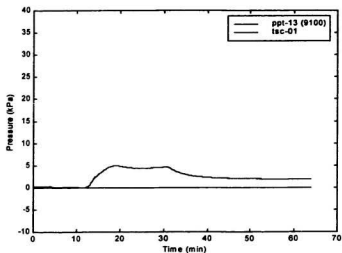
Figure A3.11. Pressure response in PPT13 and TSC01 - FLDTST2
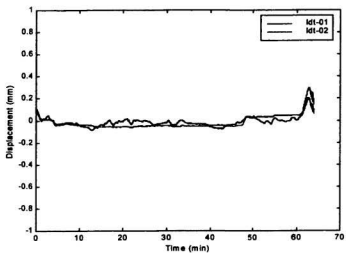
Figure A3.12. Ground surface response at LDT01 and LDT02 - FLDTST2

338
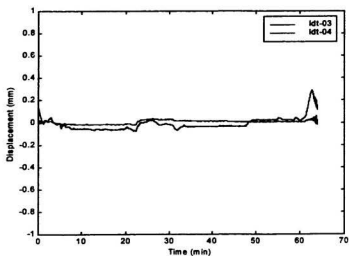
Figure A3.13. Ground surface response at LDT03 and LDT04 - FLDTST2
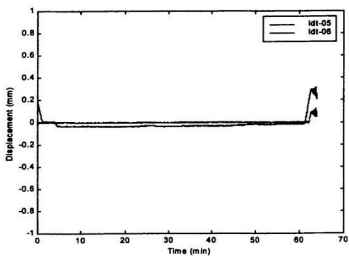
Figure A3.14. Ground surface response at LDT05 and LDT06 - FLDTST2
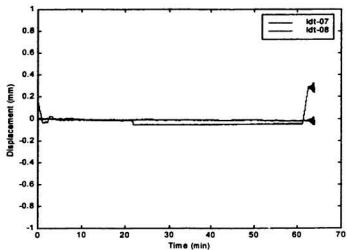
Figure A3.15. Ground surface response at LDT07 and LDT08 - FLDTST2
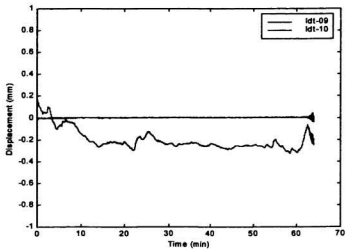
Figure A3.16. Ground surface response at LDT09 and LDT10 - FLDTST2

340

A3.2 Centrifuge Tests
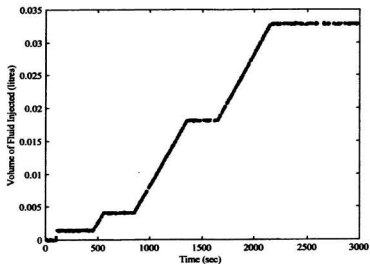
Figure A3.17. Volume of fluid injected during CCFS01A
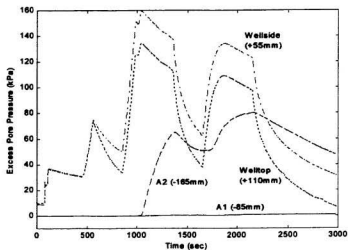
Figure A3.18. Pressure transducer response vs time for CCFS01A
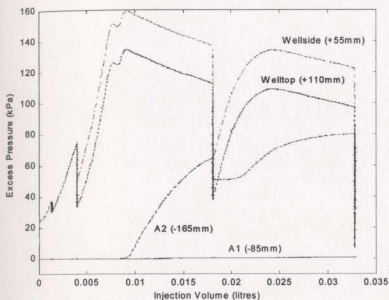
Figure A3.19. Pressure transducer response vs injection volume for CCFS01A
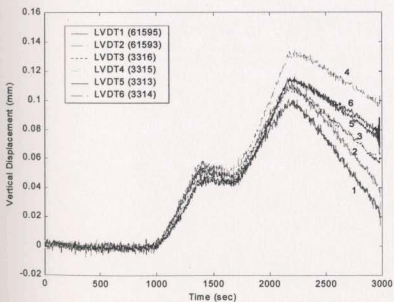
Figure A3.20. Ground surface movement vs time for CCFS01A
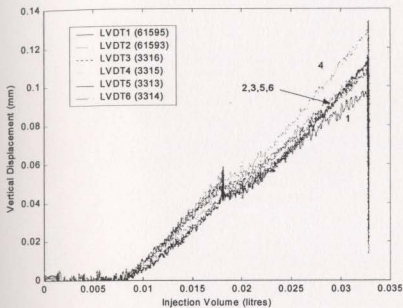
Figure A3.21. Ground surface movement vs injection volume for CCFS01A
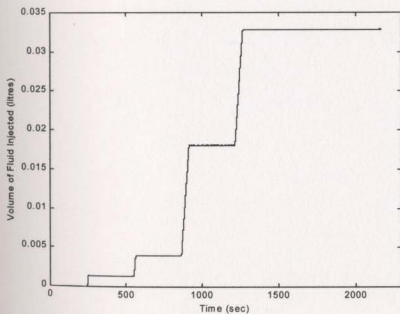
Figure A3.22. Volume of fluid injected during CCFS01B
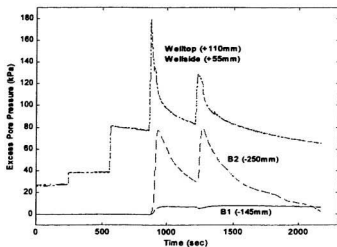
Figure A3.23. Pressure transducer response vs time for CCFS01B
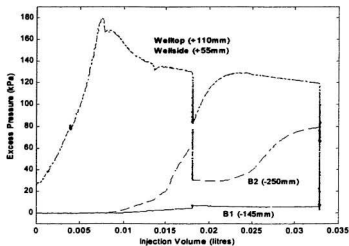
Figure A3.24. Pressure transducer response vs injection volume for CCFS01B

345
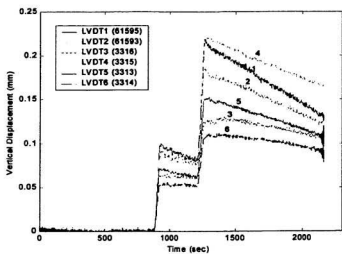
Figure A3.25. Ground surface movement vs time for CCFS01B
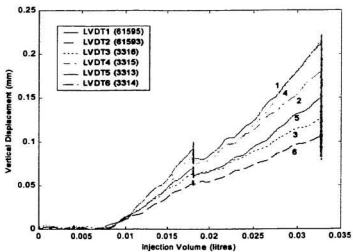
Figure A3.26. Ground surface movement vs injection volume for CCFS01B

346
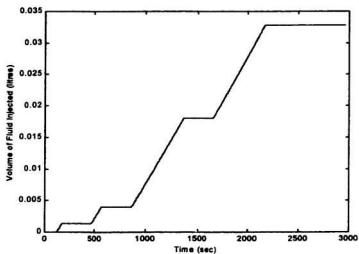
Figure A3.27. Volume of fluid injected during CCFS01C
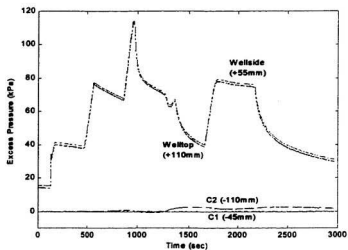
Figure A3.28. Pressure transducer response vs time for CCFS01C

347
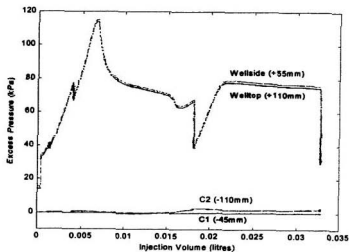
Figure A3.29. Pressure transducer response vs injection volume for CCFS01C
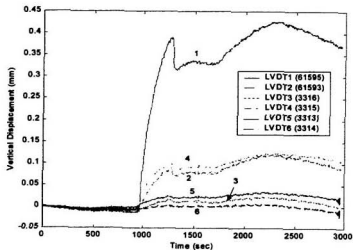
Figure A3.30. Ground surface movement vs time for CCFS01C

348
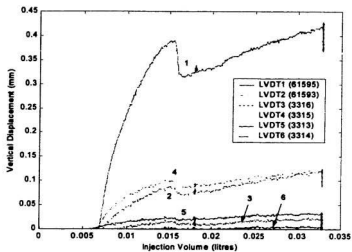
Figure A3.31. Ground surface movement vs injection volume for CCFS01C
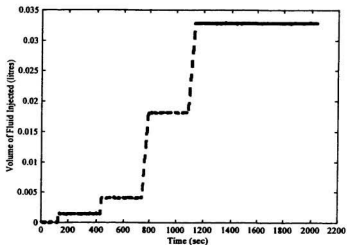
Figure A3.32. Volume of fluid injected during CCFS01D
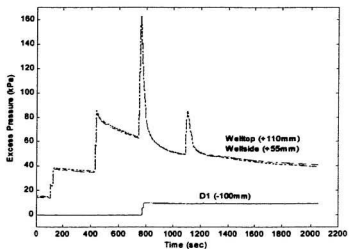
Figure A3.33. Pressure transducer response vs time for CCFS01D
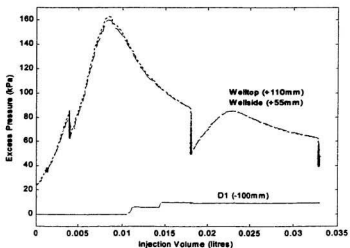
Figure A3.34. Pressure transducer response vs injection volume for CCFS01D

350
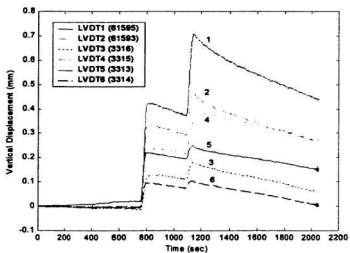
Figure A3.35. Ground surface movement vs time for CCFS01D
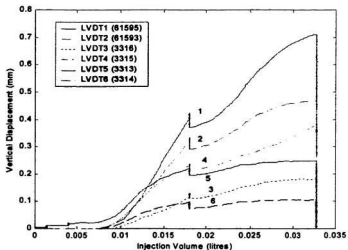
Figure A3.36. Ground surface movement vs injection volume for CCFS01D

351
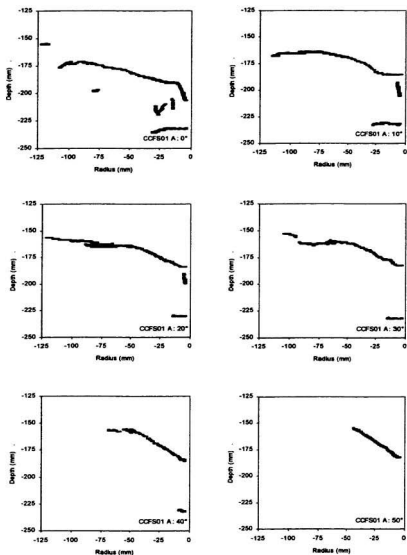
Figure A3.37. Dye trace record for CCFS01A sections 0° to 50°

352
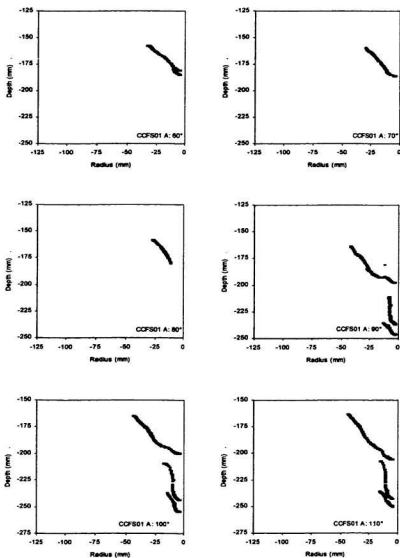
Figure A3.38. Dye trace record for CCFS01A sections 60° to 110°
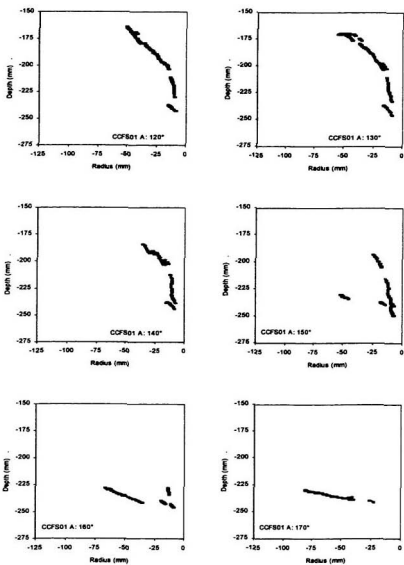
Figure A3.39. Dye trace record for CCFS01A sections 120° to 170°
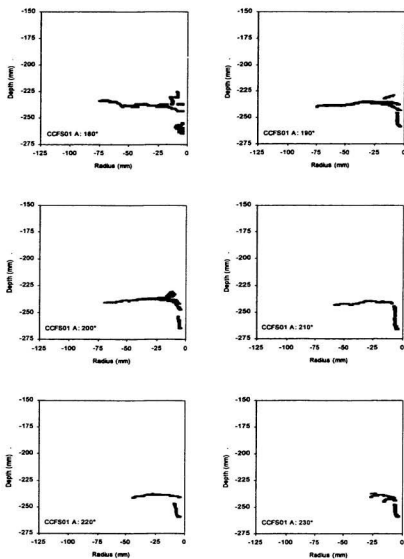
Figure A3.40. Dye trace record for CCFS01A sections 180° to 230°

355
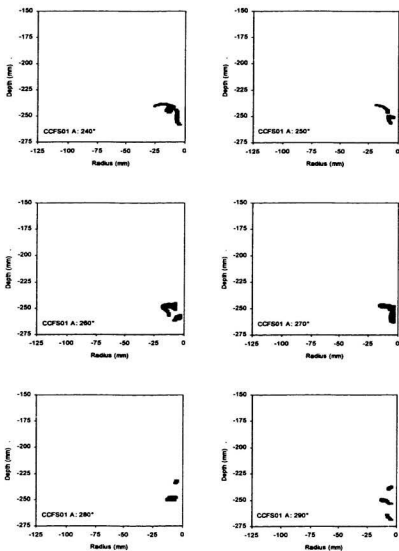
Figure A3.41. Dye trace record for CCFS01A sections 240° to 290°
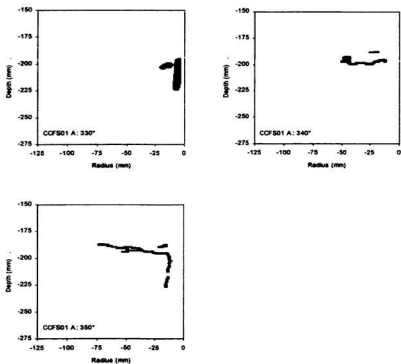
Figure A3.42. Dye trace record for CCFS01A sections 330° to 350°
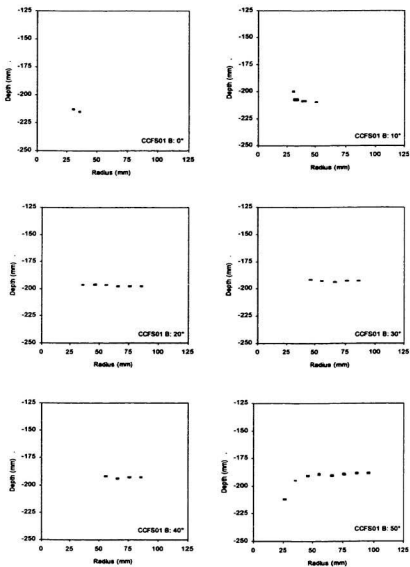
Figure A3.43. Dye trace record for CCFS01B sections 0° to 50°

Figure A3.44. Dye trace record for CCFS01B sections 60° to 110°
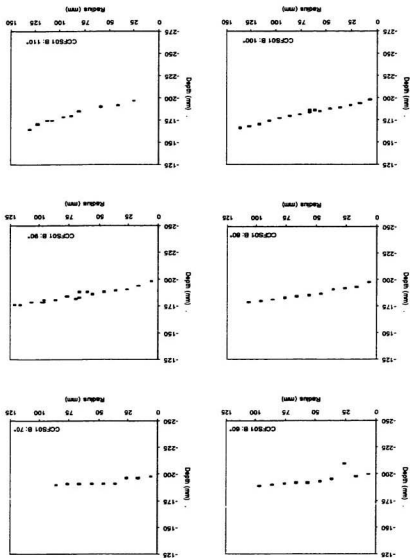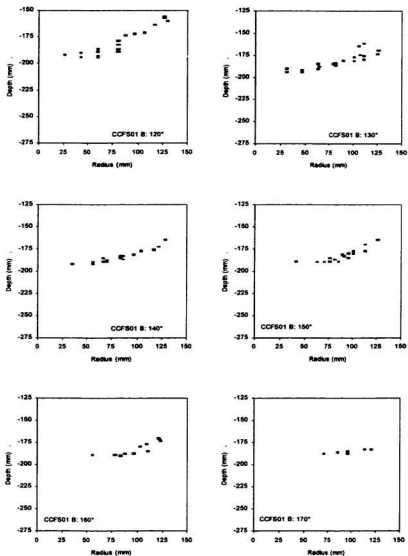
Figure A3.45. Dye trace record for CCFS01B sections 120° to 170°
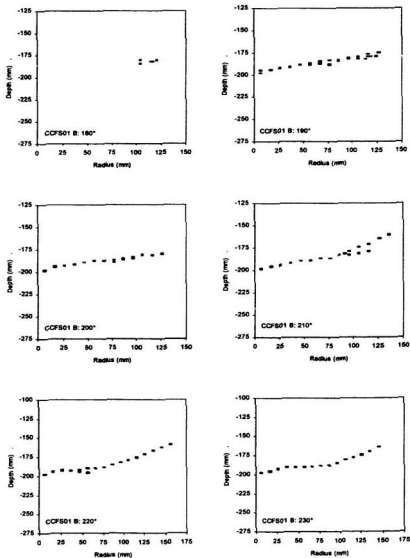
Figure A3.46. Dye trace record for CCFS01B sections 180° to 230°
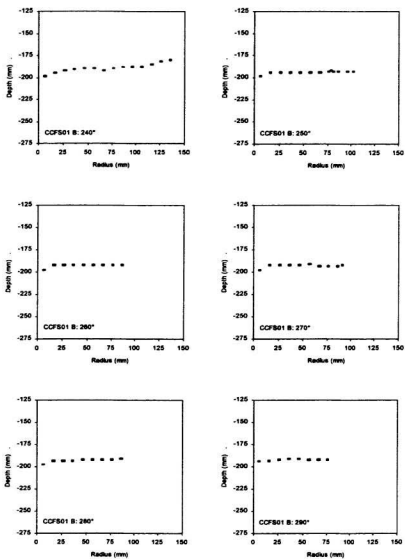
Figure A3.47. Dye trace record for CCFS01B sections 240° to 290°
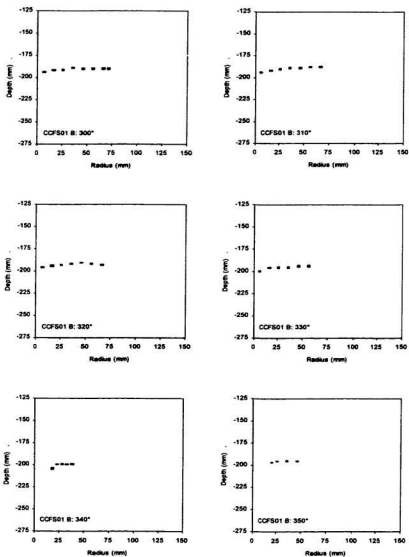
Figure A3.48. Dye trace record for CCFS01B sections 300° to 350°
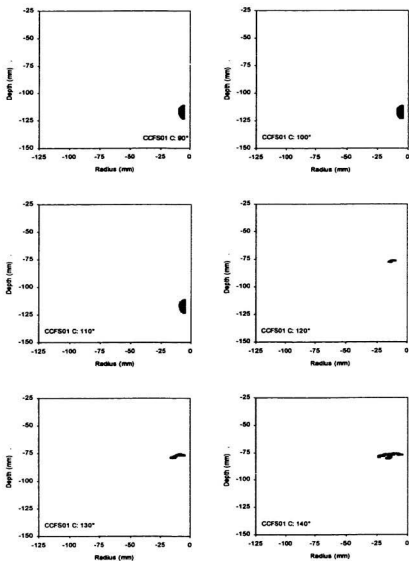
Figure A3.49. Dye trace record for CCFS01C sections 90° to 140°
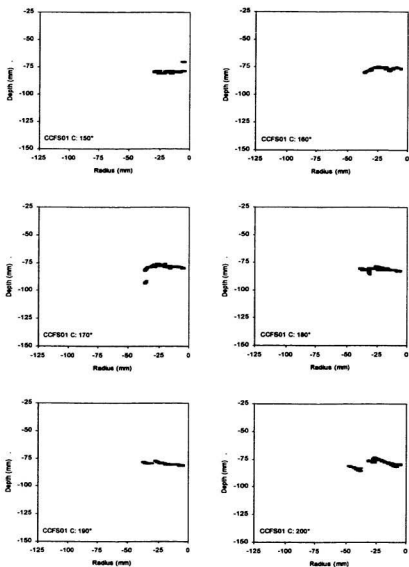
Figure A3.50. Dye trace record for CCFS01C sections 150° to 200°

365
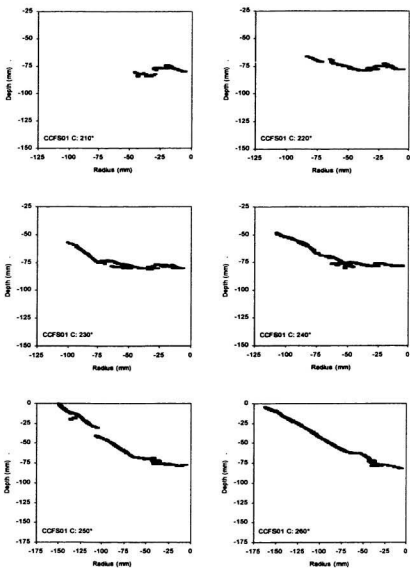
Figure A3.51. Dye trace record for CCFS01C sections 210° to 260°
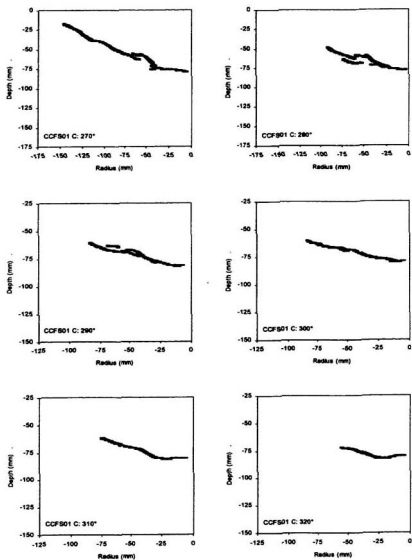
Figure A3.52. Dye trace record for CCFS01C sections 270° to 320°

367
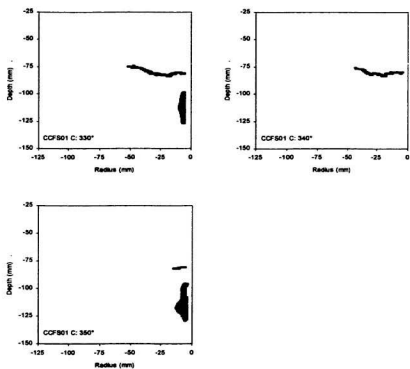
Figure A3.53. Dye trace record for CCFS01C sections 330° to 350°
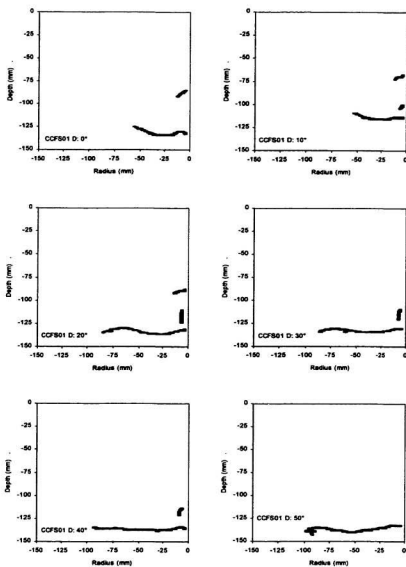
Figure A3.54. Dye trace record for CCFS01D sections 0° to 50°
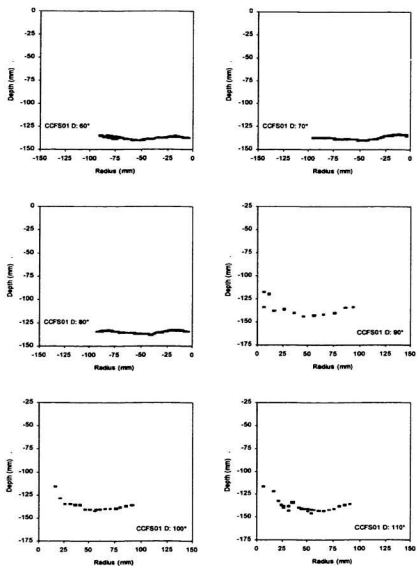
Figure A3.55. Dye trace record for CCFS01D sections 60° to 110°
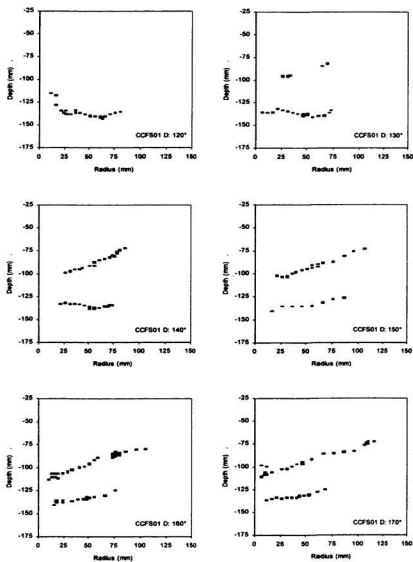
Figure A3.56. Dye trace record for CCFS01D sections 120° to 170°
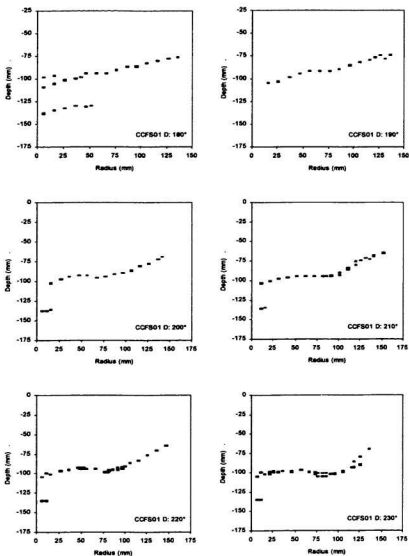
Figure A3.57. Dye trace record for CCFS01D sections 180° to 230°
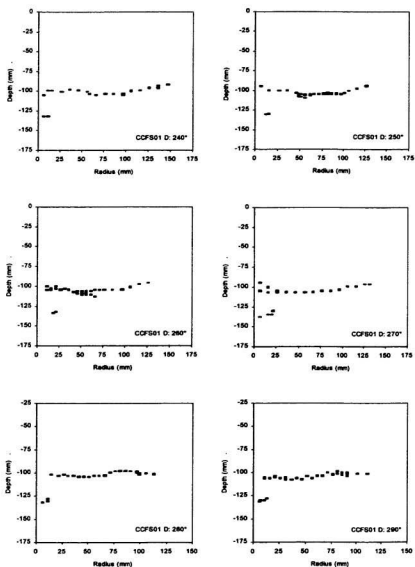
Figure A3.58. Dye trace record for CCFS01D sections 240° to 290°
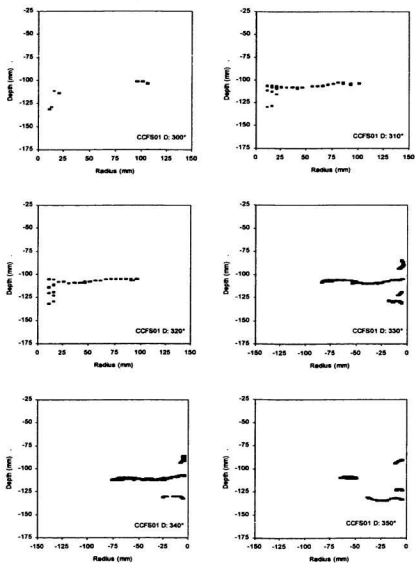
Figure A3.59. Dye trace record for CCFS01D sections 300° to 350°
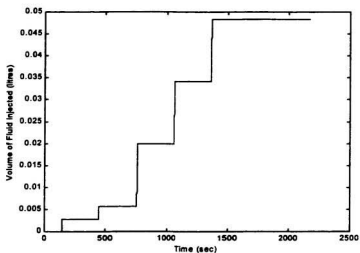
Figure A3.60. Volume of fluid injected during CCFS02E
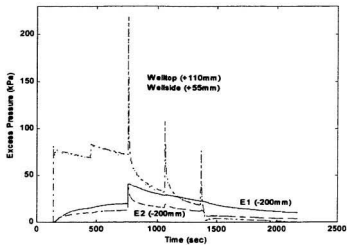
Figure A3.61. Pressure transducer response vs time for CCFS02E
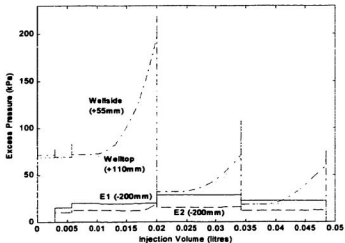
Figure A3.62. Pressure transducer response vs injection volume for CCFS02E
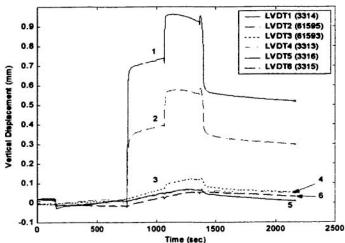
Figure A3.63. Ground surface movement vs time for CCFS02E
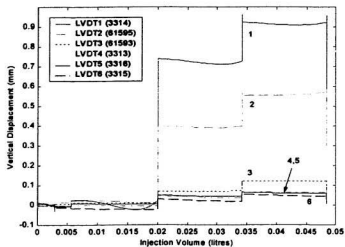
Figure A3.64. Ground surface movement vs injection volume for CCFS02E
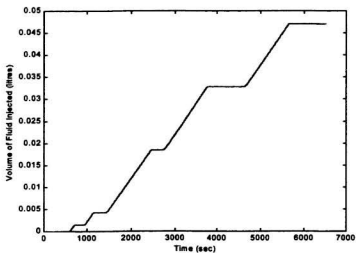
Figure A3.65. Volume of fluid injected during CCFS02F

377
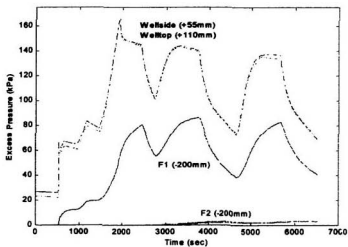
Figure A3.66. Pressure transducer response vs time for CCFS02F
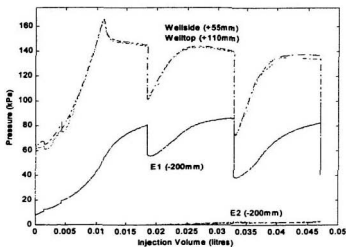
Figure A3.67. Pressure transducer response vs injection volume for CCFS02F
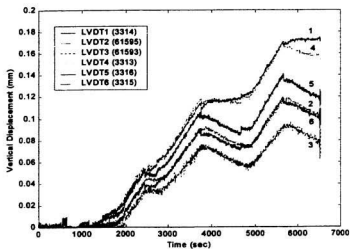
Figure A3.68. Ground surface movement vs time for CCFS02F
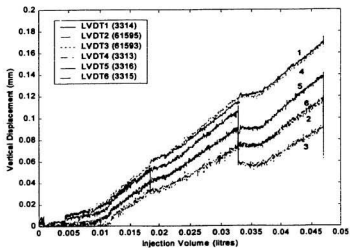
Figure A3.69. Ground surface movement vs injection volume for CCFS02F

379
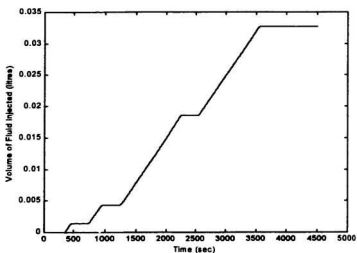
Figure A3.70. Volume of fluid injected during CCFS02G
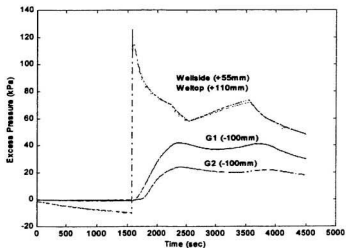
Figure A3.71. Pressure transducer response vs time for CCFS02G

380
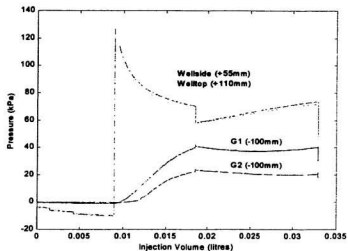
Figure A3.72. Pressure transducer response vs injection volume for CCFS02G
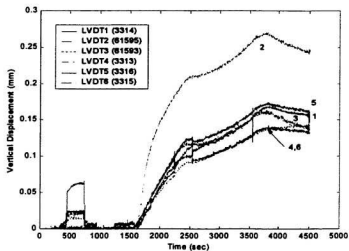
Figure A3.73. Ground surface movement vs time for CCFS02G

381
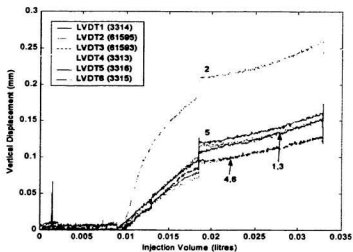
Figure A3.74. Ground surface movement vs injection volume for CCFS02G
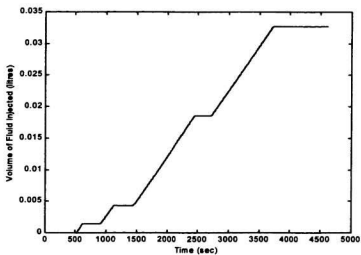
Figure A3.75. Volume of fluid injected during CCFS02H
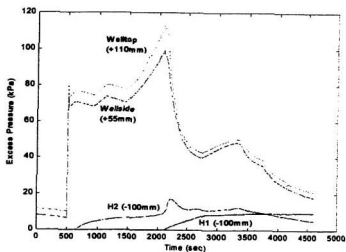
Figure A3.76. Pressure transducer response vs time for CCFS02H
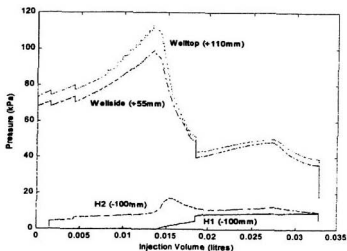
Figure A3.77. Pressure transducer response vs injection volume for CCFS02H

383
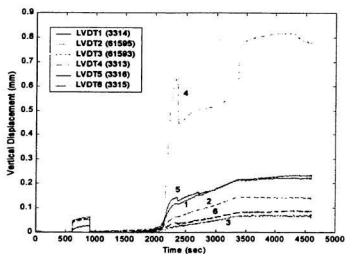
Figure A3.78. Ground surface movement vs time for CCFS02H
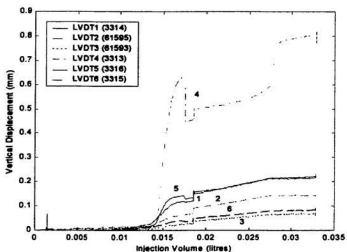
Figure A3.79. Ground surface movement vs injection volume for CCFS02H
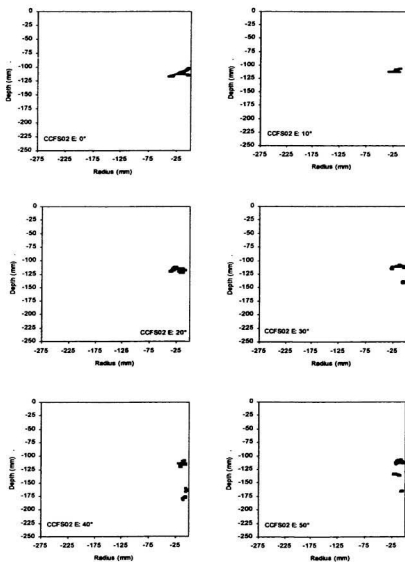
Figure A3.80. Dye trace record for CCFS02E sections 0° to 50°

385
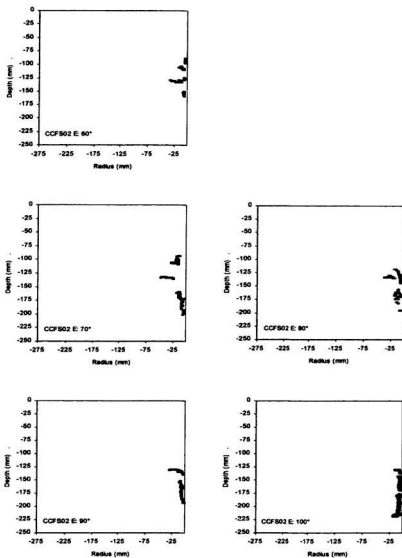
Figure A3.81. Dye trace record for CCFS02E sections 60° to 100°

386
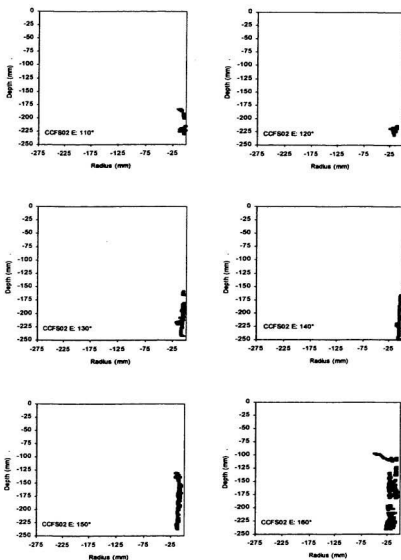
Figure A3.82. Dye trace record for CCFS02E sections 110° to 160°

387
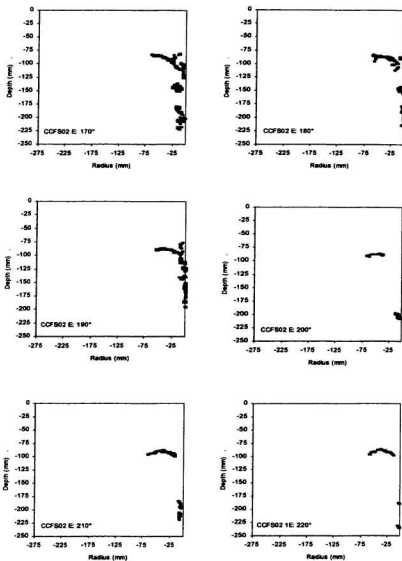
Figure A3.83. Dye trace record for CCFS02E sections 170° to 220°

388
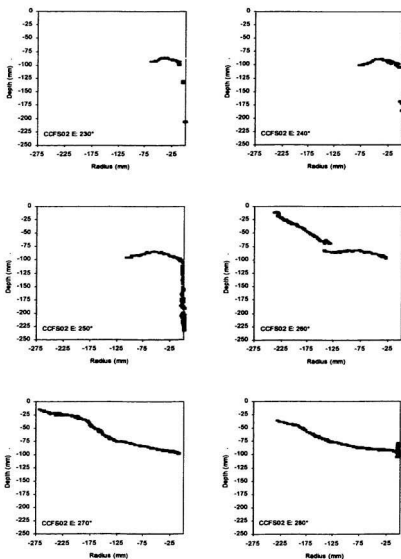
Figure A3.84. Dye trace record for CCFS02E sections 230° to 280°

389
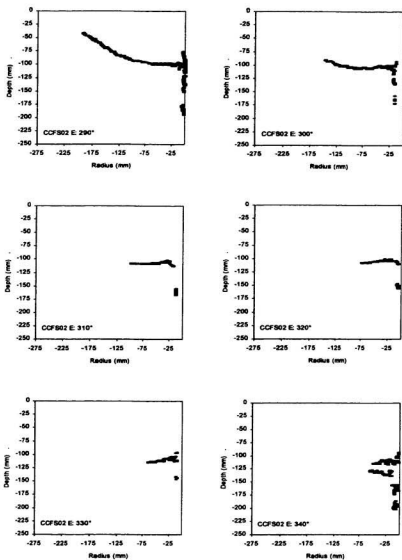
Figure A3.85. Dye trace record for CCFS02E sections 290° to 340°

390
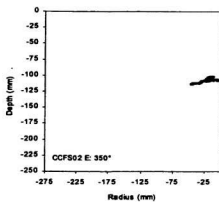
Figure A3.86. Dye trace record for CCFS02E section 350°
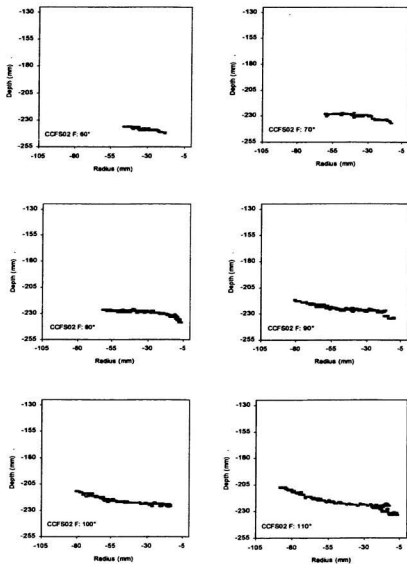
Figure A3.87. Dye trace record for CCFS02F sections 60° to 110°

392
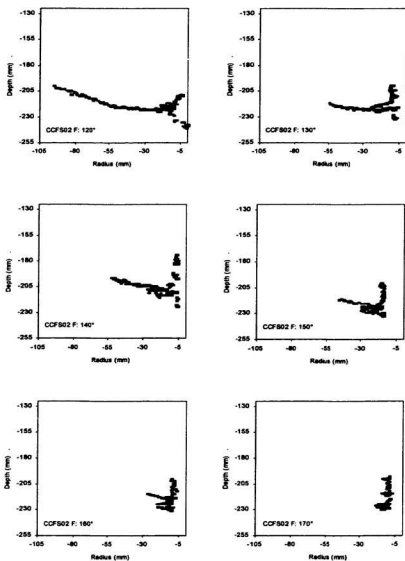
Figure A3.88. Dye trace record for CCFS02F sections 120° to 170°

393
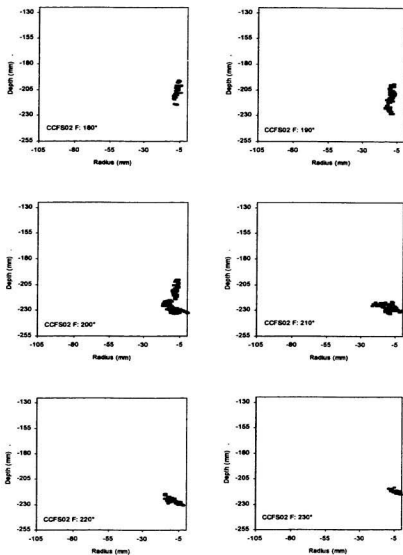
Figure A3.89. Dye trace record for CCFS02F sections 180° to 230°
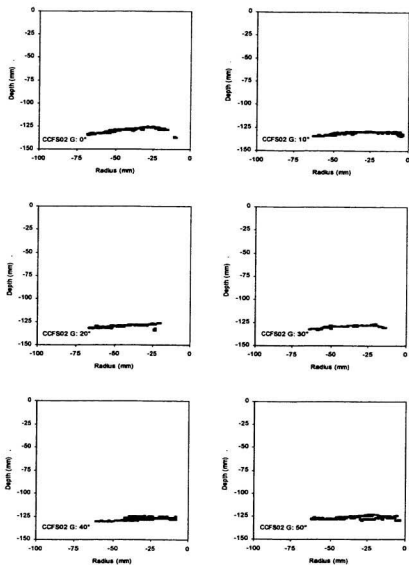
Figure A3.90. Dye trace record for CCFS02G sections 0° to 50°
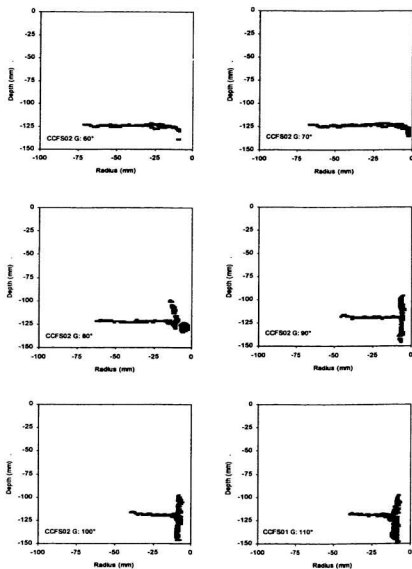
Figure A3.91. Dye trace record for CCFS02G sections 60° to 110°
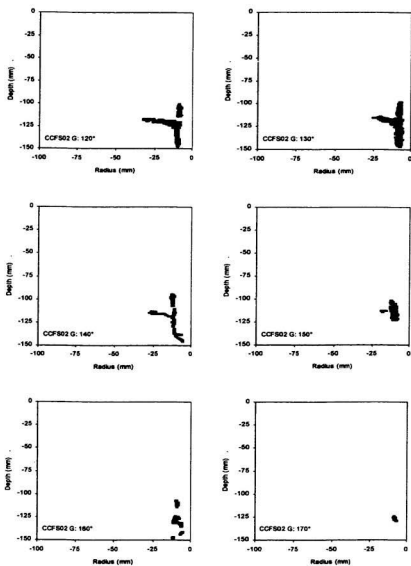
Figure A3.92. Dye trace record for CCFS02G sections 120° to 170°
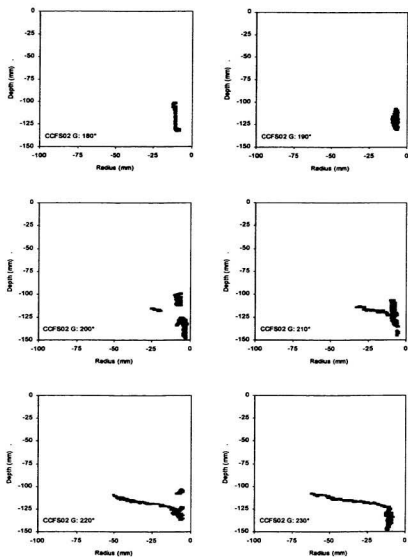
Figure A3.93. Dye trace record for CCFS02G sections 180° to 230°
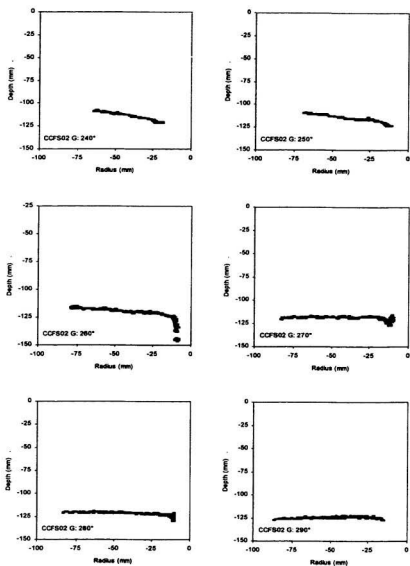
Figure A3.94. Dye trace record for CCFS02G sections 240° to 290°
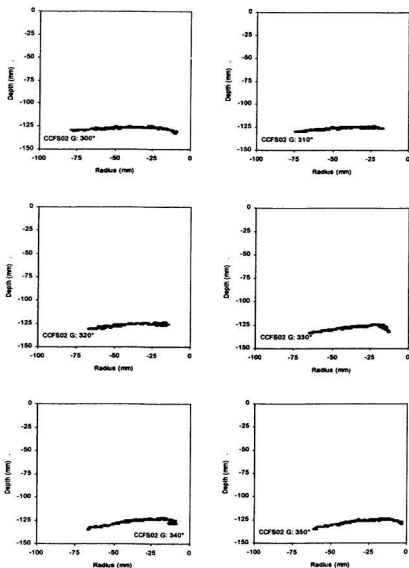
Figure A3.95. Dye trace record for CCFS02G sections 300° to 350°
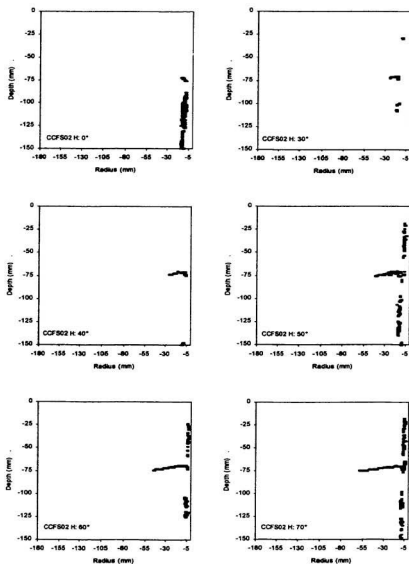
Figure A3.96. Dye trace record for CCFS02H sections 0° to 70°

401
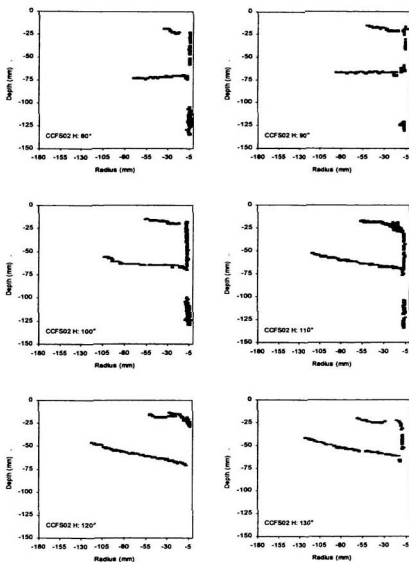
Figure A3.97. Dye trace record for CCFS02H sections 80° to 130°
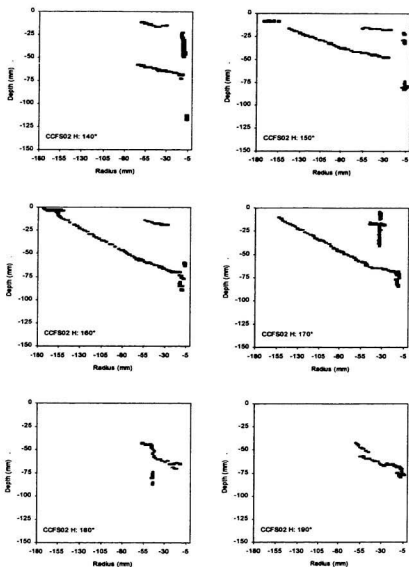
Figure A3.98. Dye trace record for CCFS02H sections 140° to 190°

403
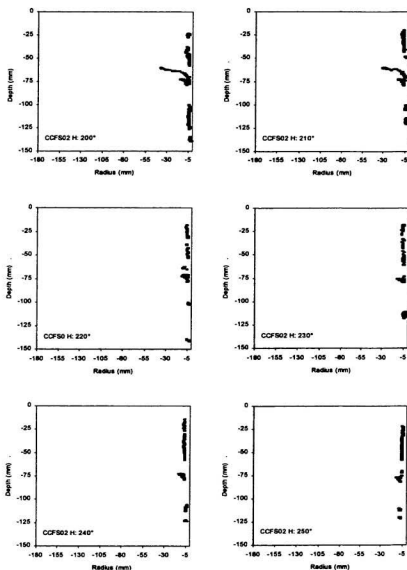
Figure A3.99. Dye trace record for CCFS02H sections 200° to 250°
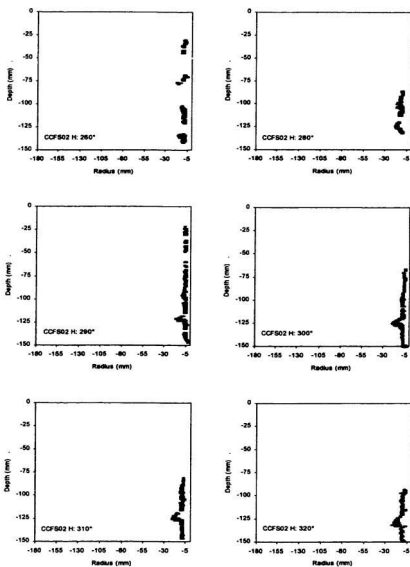
Figure A3.100. Dye trace record for CCFS02H sections 260° to 320°

405
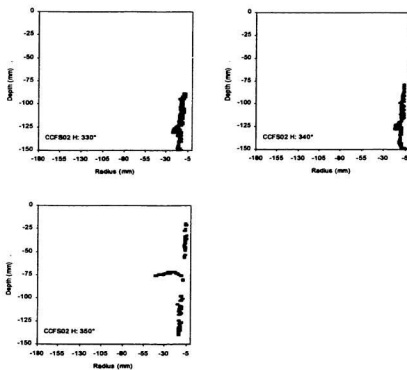
Figure A3.101. Dye trace record for CCFS02H sections 330° to 350°

406
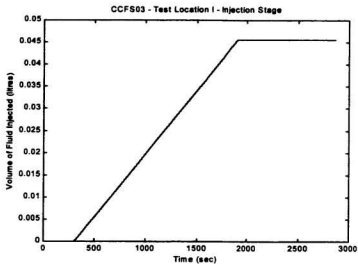
Figure A3.102. Volume of fluid injected during CCFS03I
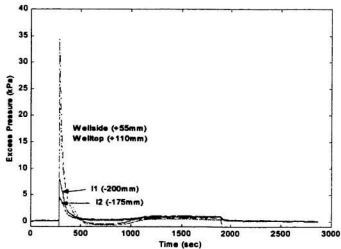
Figure A3.103. Pressure transducer response vs time for CCFS03I

407
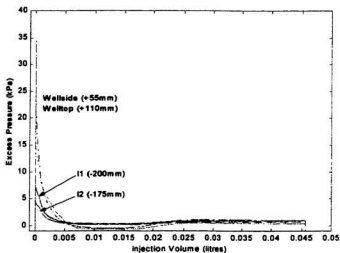
Figure A3.104. Pressure transducer response vs injection volume for CCFS03I
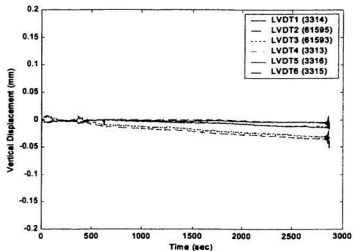
Figure A3.105. Ground surface movement vs time for CCFS03I
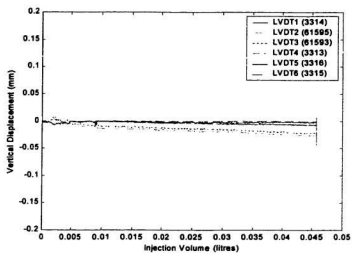
Figure A3.106. Ground surface movement vs injection volume for CCFS03I
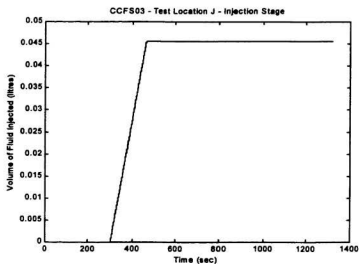
Figure A3.107. Volume of fluid injected during CCFS03J
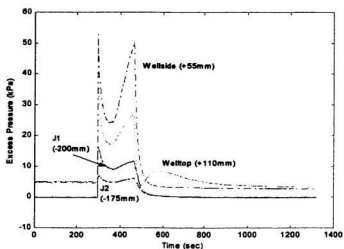
Figure A3.108. Pressure transducer response vs time for CCFS03J
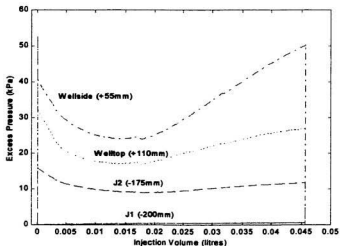
Figure A3.109. Pressure transducer response vs injection volume for CCFS03J
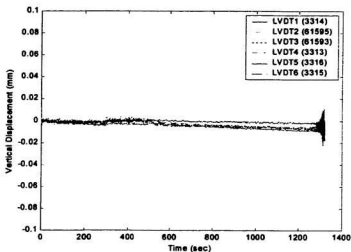
Figure A3.110. Ground surface movement vs time for CCFS03J
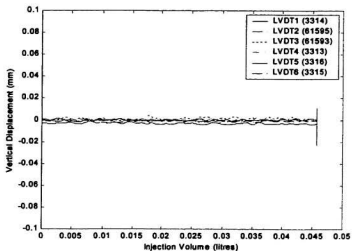
Figure A3.111. Ground surface movement vs injection volume for CCFS03J
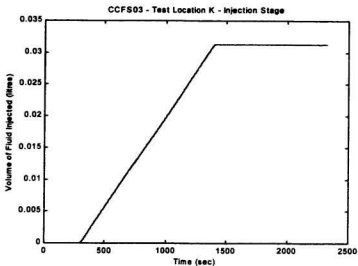
Figure A3.112. Volume of fluid injected during CCFS03K
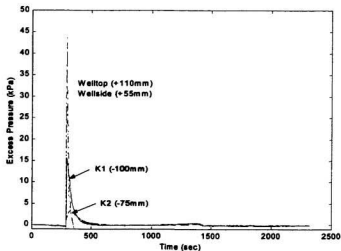
Figure A3.113. Pressure transducer response vs time for CCFS03K

412
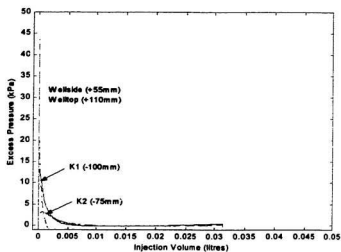
Figure A3.114. Pressure transducer response vs injection volume for CCFS03K
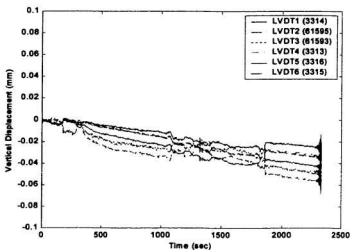
Figure A3.115. Ground surface movement vs time for CCFS03K

413
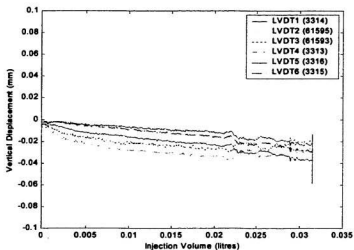
Figure A3.116. Ground surface movement vs injection volume for CCFS03K
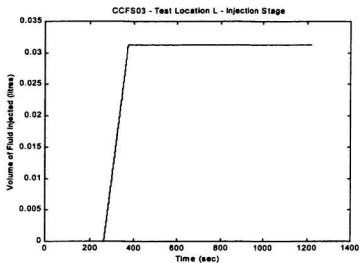
Figure A3.117. Volume of fluid injected during CCFS03L

414
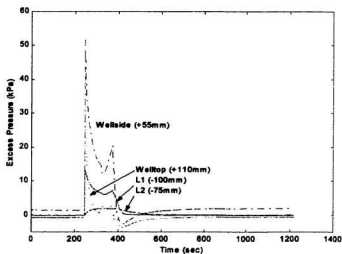
Figure A3.118. Pressure transducer response vs time for CCFS03L
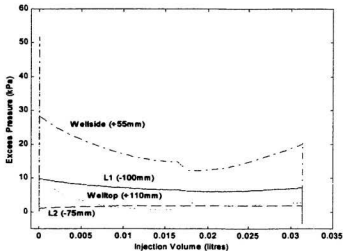
Figure A3.119. Pressure transducer response vs injection volume for CCFS03L
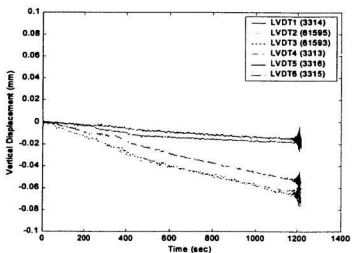
Figure A3.120. Ground surface movement vs time for CCFS03L
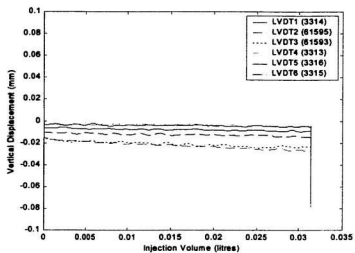
Figure A3.121. Ground surface movement vs injection volume for CCFS03L
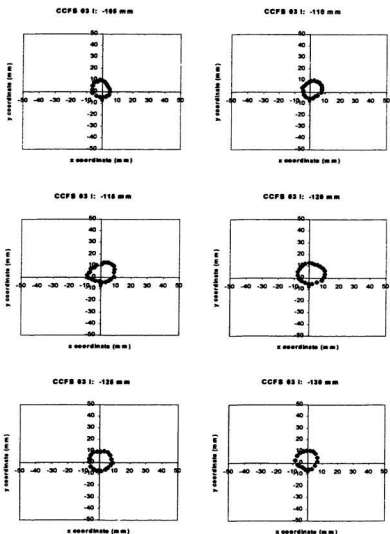
Depth is referenced from top of strongbox. Soil is uniformly blue within extents shown.

Figure A3.122. Dye trace record for CCFS03I (110-130 mm)
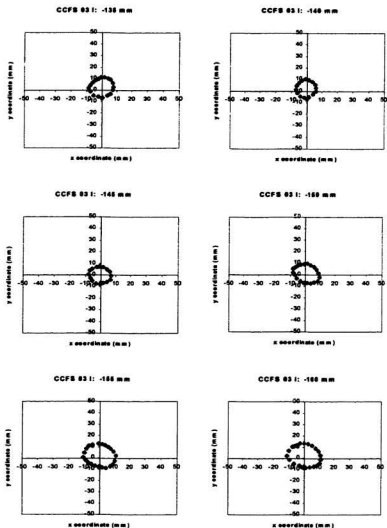
CCFS 03 I: -135 mm

CCFS 03 I: -140 mm

CCFS 03 I: -145 mm

CCFS 03 I: -150 mm

CCFS 03 I: -155 mm

CCFS 03 I: -160 mm

Depth is referenced from top of strongbox. Soil is uniformly blue within extents shown.

Figure A3.123. Dye trace record for CCFS03I (135-160 mm)

CCFS 03 I: -165 mm

CCFS 03 I: -170 mm

CCFS 03 I: -175 mm

CCFS 03 I: -180 mm

CCFS 03 I: -185 mm

CCFS 03 I: -190 mm

Depth is referenced from top of strongbox. Soil is uniformly blue within extents shown.
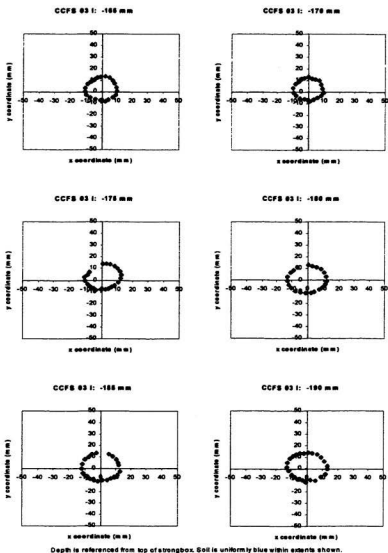
Figure A3.124. Dye trace record for CCFS03I (165-190 mm)
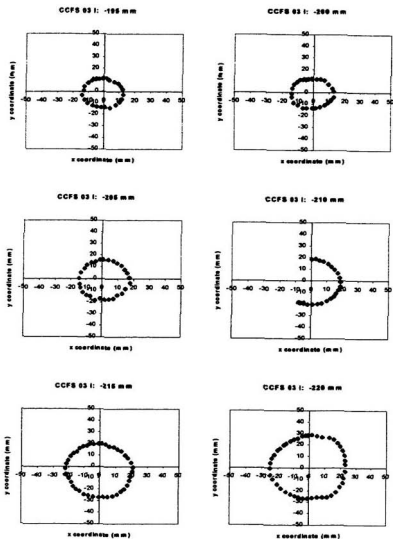
419

Figure A3.125. Dye trace record for CCFS03I (195-220 mm)
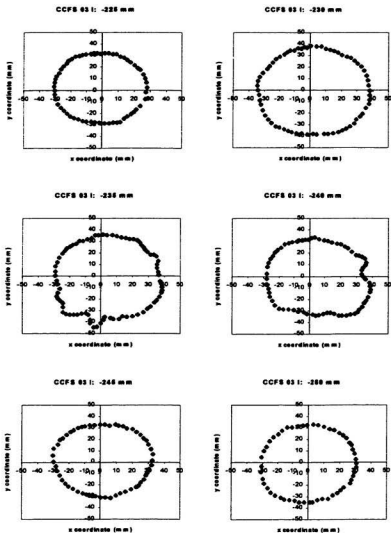
420

CCFS 03 I: -225 mm

CCFS 03 I: -230 mm

CCFS 03 I: -235 mm

CCFS 03 I: -240 mm

CCFS 03 I: -245 mm

CCFS 03 I: -250 mm

Depth is referenced from top of strongbox. Soil is uniformly blue within extents shown.

Figure A3.126. Dye trace record for CCFS03I (225-250 mm)
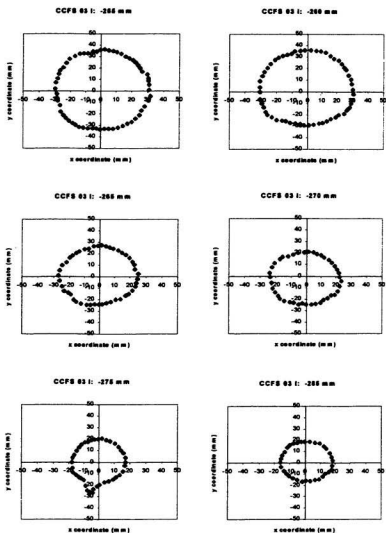
421

Figure A3.127. Dye trace record for CCFS03I (255-285 mm)
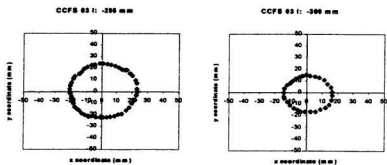
CCFS 03 I: -295 mm   CCFS 03 I: -300 mm

Depth is referenced from top of strongbox. Soil is uniformly blue within extents shown.

Figure A3.128. Dye trace record for CCFS03I (295-300 mm)
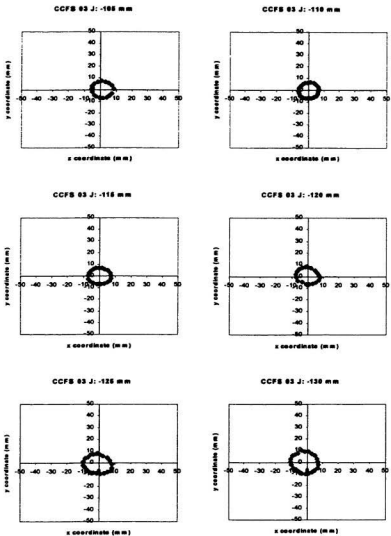
Figure A3.129. Dye trace record for CCFS03J (105-130 mm)
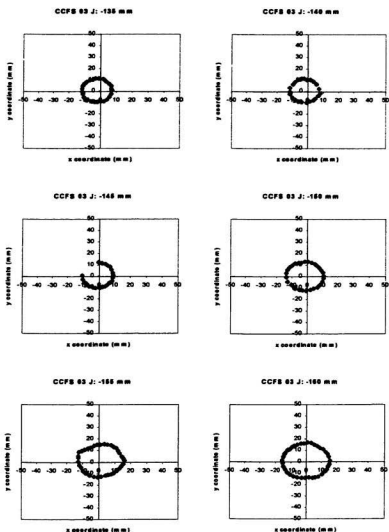
CCFS 03 J: -135 mm

CCFS 03 J: -140 mm

CCFS 03 J: -145 mm

CCFS 03 J: -150 mm

CCFS 03 J: -155 mm

CCFS 03 J: -160 mm

Depth is referenced from top of strongbox. Soil is uniformly blue within extents shown.

Figure A3.130. Dye trace record for CCFS03J (135-160 mm)
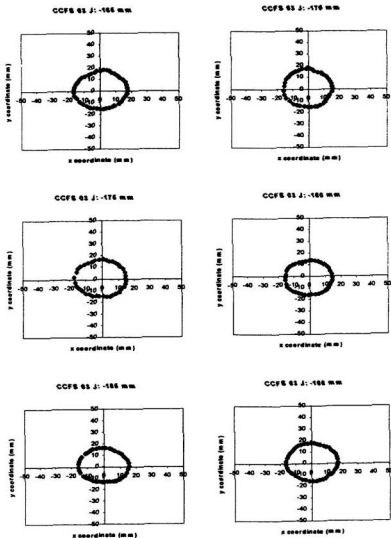
CCFS 03 J: -165 mm

CCFS 03 J: -170 mm

CCFS 03 J: -175 mm

CCFS 03 J: -180 mm

CCFS 03 J: -185 mm

CCFS 03 J: -190 mm

Depth is referenced from top of strongbox. Soil is uniformly blue within extents shown.

Figure A3.131. Dye trace record for CCFS03J (165-190 mm)
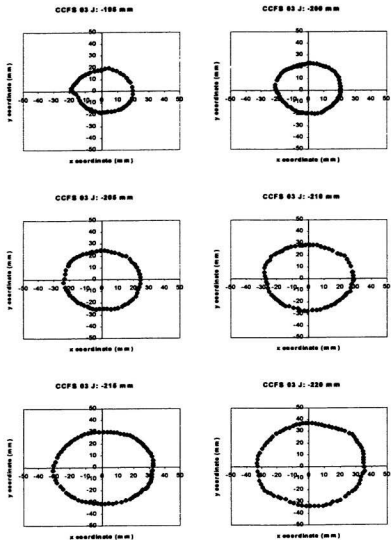
426

Depth is referenced from top of strongbox. Soil is uniformly blue within extents shown.

Figure A3.132. Dye trace record for CCFS03J (195-220 mm)
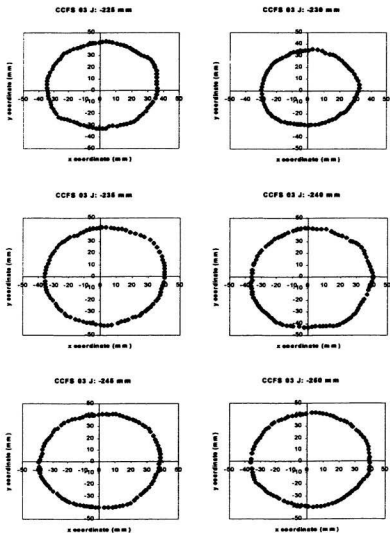
427

CCFS 03 J: -225 mm   CCFS 03 J: -230 mm

CCFS 03 J: -235 mm   CCFS 03 J: -240 mm

CCFS 03 J: -245 mm   CCFS 03 J: -250 mm

Depth is referenced from top of strongbox. Soil is uniformly blue within extents shown.

Figure A3.133. Dye trace record for CCFS03J (225-250 mm)
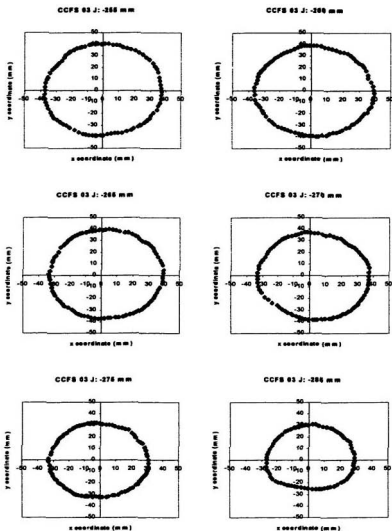
428

CCFS 63 J: -255 mm CCFS 63 J: -260 mm
CCFS 63 J: -265 mm CCFS 63 J: -270 mm
CCFS 63 J: -275 mm CCFS 63 J: -280 mm

Depth is referenced from top of strongbox. Soil is uniformly blue within extents shown.

Figure A3.134. Dye trace record for CCFS03J (255-285 mm)
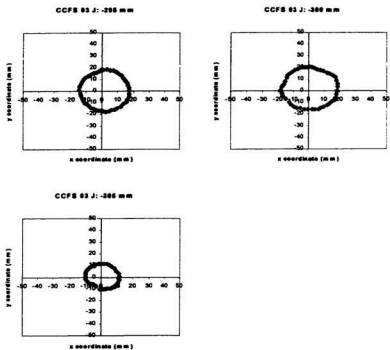
429

CCFS 03 J: -295 mm

CCFS 03 J: -300 mm

CCFS 03 J: -305 mm

Depth is referenced from top of a strongbox. Soil is uniformly blue within extents shown.

Figure A3.135. Dye trace record for CCFS03J (295-305 mm)
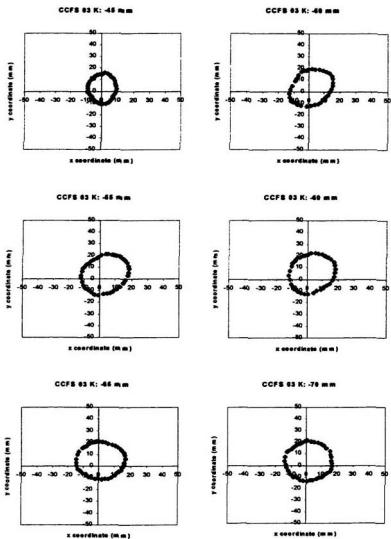
CCFS 03 K: -45 mm

CCFS 03 K: -50 mm

CCFS 03 K: -55 mm

CCFS 03 K: -60 mm

CCFS 03 K: -65 mm

CCFS 03 K: -70 mm

Depth is referenced from top of strongbox. Soil is uniformly blue within extents shown.

Figure A3.136. Dye trace record for CCFS03K (45-70 mm)
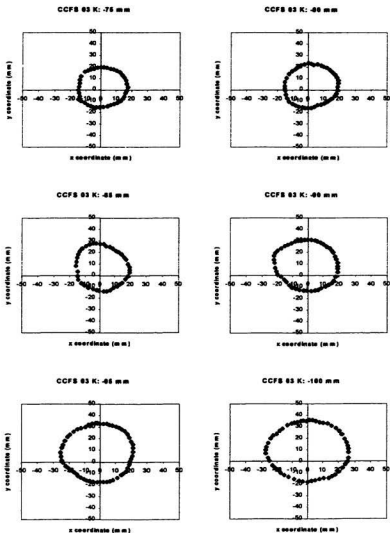
Depth is referenced from top of strongbox. Soil is uniformly blue within extents shown.

Figure A3.137. Dye trace record for CCFS03K (75-100 mm)
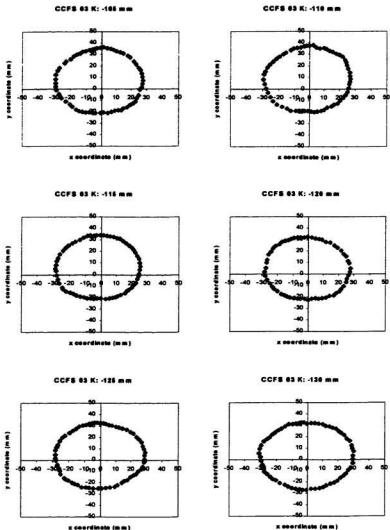
432

Depth is referenced from top of strongbox. Soil is uniformly blue within extents shown.

Figure A3.138. Dye trace record for CCFS03K (105-130 mm)
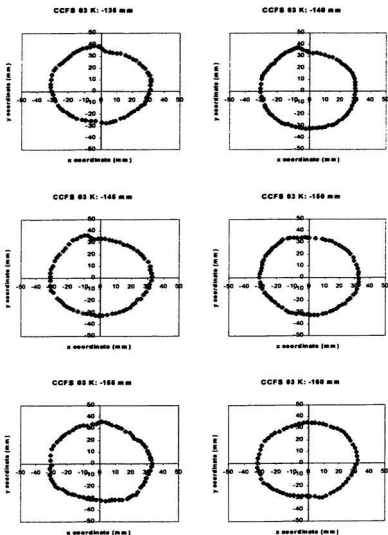
433

CCFS 03 K: -135 mm

CCFS 03 K: -140 mm

CCFS 03 K: -145 mm

CCFS 03 K: -150 mm

CCFS 03 K: -155 mm

CCFS 03 K: -160 mm

Depth is referenced from top of strongbox. Soil is uniformly blue within extents shown.

Figure A3.139. Dye trace record for CCFS03K (135-160 mm)
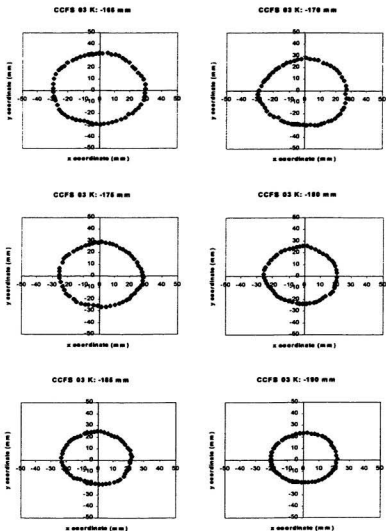
434

Depth is referenced from top of strongbox. Soil is uniformly blue within extents shown.

Figure A3.140. Dye trace record for CCFS03K (165-190 mm)
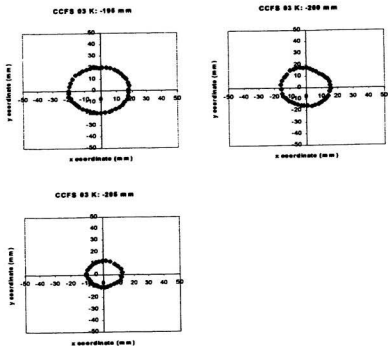
435

Depth is referenced from top of strongbox. Soil is uniformly blue within extents shown.

Figure A3.141. Dye trace record for CCFS03K (195-205 mm)
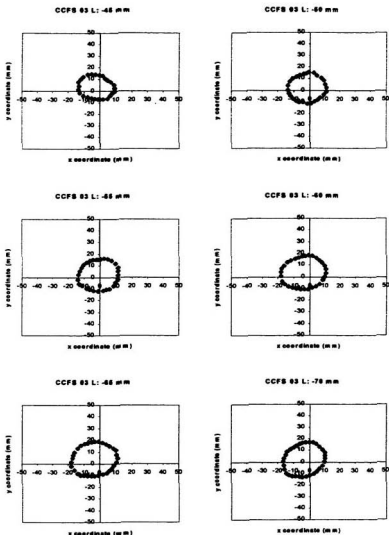
CCFS 03 L: -45 mm

CCFS 03 L: -50 mm

CCFS 03 L: -55 mm

CCFS 03 L: -60 mm

CCFS 03 L: -65 mm

CCFS 03 L: -70 mm

Depth is referenced from top of strongbox. Soil is uniformly blue within extents shown.

Figure A3.142. Dye trace record for CCFS03L (45-70 mm)
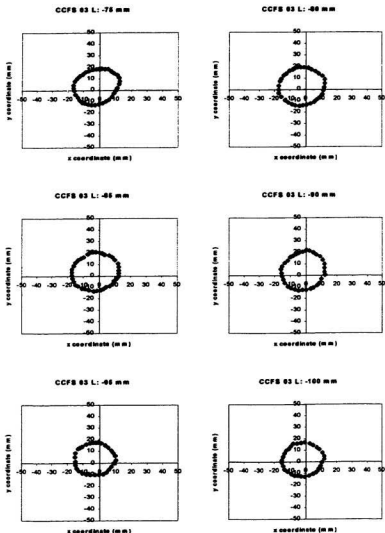
437

CCFS 03 L: -75 mm   CCFS 03 L: -80 mm

CCFS 03 L: -85 mm   CCFS 03 L: -90 mm

CCFS 03 L: -95 mm   CCFS 03 L: -100 mm

Depth is referenced from top of strongbox. Soil is uniformly blue within extents shown.

Figure A3.143. Dye trace record for CCFS03L (75-100 mm)
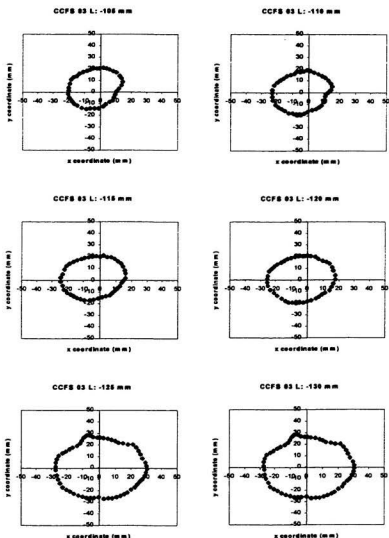
438

CCFS 03 L: -105 mm

CCFS 03 L: -110 mm

CCFS 03 L: -115 mm

CCFS 03 L: -120 mm

CCFS 03 L: -125 mm

CCFS 03 L: -130 mm

Depth is referenced from top of strongbox. Soil is uniformly blue within extents shown.

Figure A3.144. Dye trace record for CCFS03L (105-130 mm)
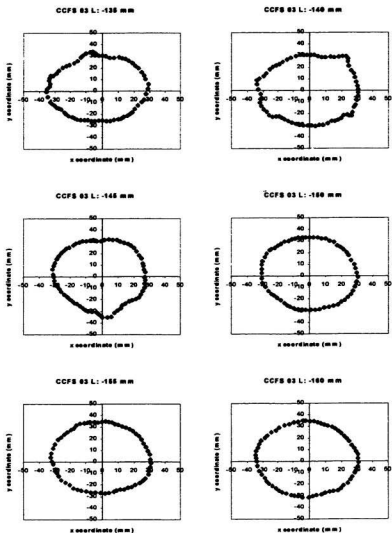
439

CCFS 03 L: -135 mm

CCFS 03 L: -140 mm

CCFS 03 L: -145 mm

CCFS 03 L: -150 mm

CCFS 03 L: -155 mm

CCFS 03 L: -160 mm

Depth is referenced from top of strongbox. Soil is uniformly blue within extents shown.

Figure A3.145. Dye trace record for CCFS03L (135-160 mm)
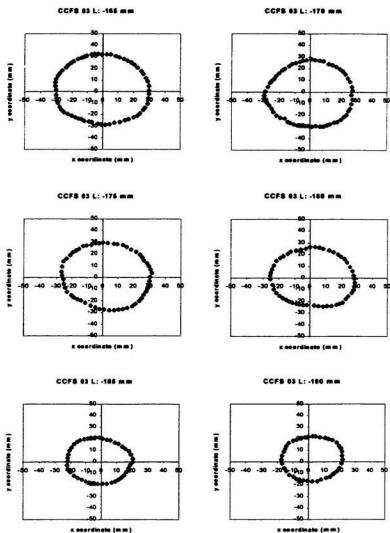
440

CCFS 03 L: -165 mm

CCFS 03 L: -170 mm

CCFS 03 L: -175 mm

CCFS 03 L: -180 mm

CCFS 03 L: -185 mm

CCFS 03 L: -190 mm

Depth is referenced from top of strongbox. Soil is uniformly blue within extents shown.

Figure A3.146. Dye trace record for CCFS03L (165-190 mm)
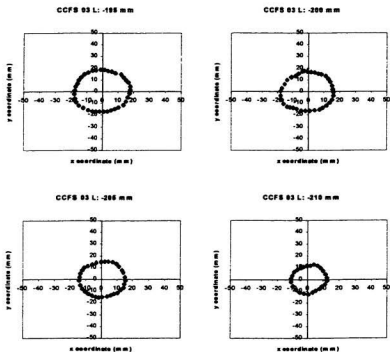
CCFS 03 L: -195 mm   CCFS 03 L: -200 mm

CCFS 03 L: -205 mm   CCFS 03 L: -210 mm

Depth is referenced from top of strongbox. Soil is uniformly blue within extents shown.

Figure A3.147. Dye trace record for CCFS03L (195-210 mm)
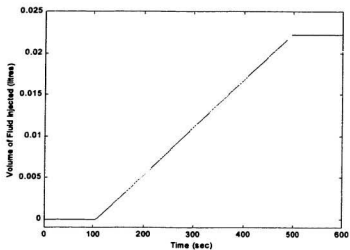
Figure A3.148. Volume of fluid injected during CCFS04M
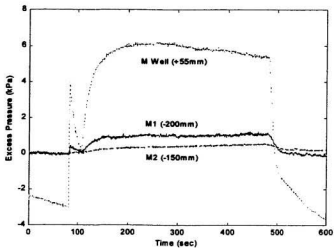
Figure A3.149. Pressure transducer response vs time for CCFS04M

443
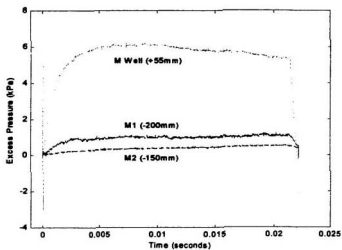
Figure A3.150. Pressure transducer response vs injection volume for CCFS04M
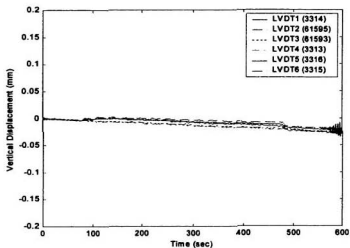
Figure A3.151. Ground surface movement vs time for CCFS04M
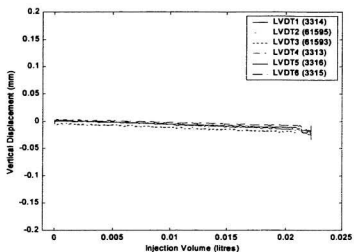
Figure A3.152. Ground surface movement vs injection volume for CCFS04M
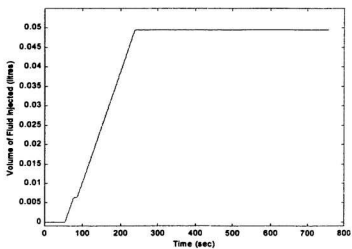
Figure A3.153. Volume of fluid injected during CCFS04N

445
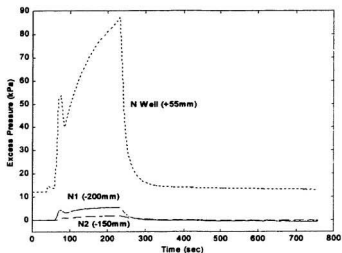
Figure A3.154. Pressure transducer response vs time for CCFS04N
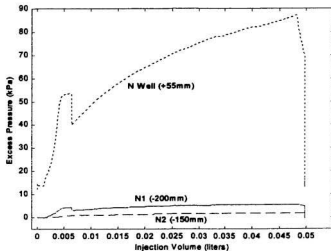
Figure A3.155. Pressure transducer response vs injection volume for CCFS04N
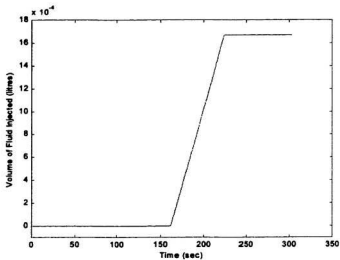
Figure A3.156. Volume of fluid injected during CCFS04O
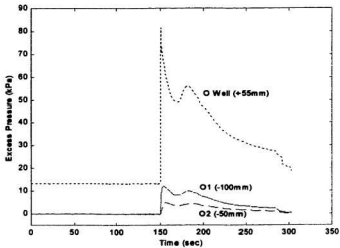
Figure A3.157. Pressure transducer response vs time for CCFS04O

447
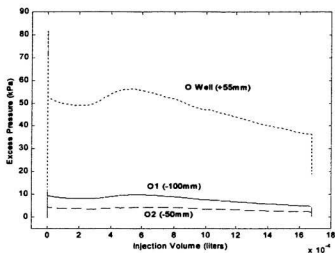
Figure A3.158. Pressure transducer response vs injection volume for CCFS04O
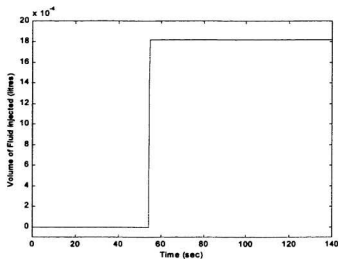
Figure A3.159. Volume of fluid injected during CCFS04P

448
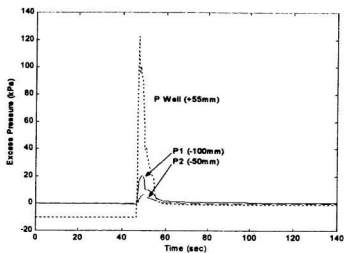
Figure A3.160. Pressure transducer response vs time for CCFS04P
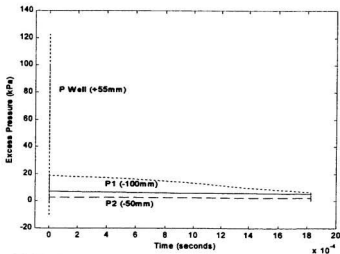
Figure A3.161. Pressure transducer response vs injection volume for CCFS04P
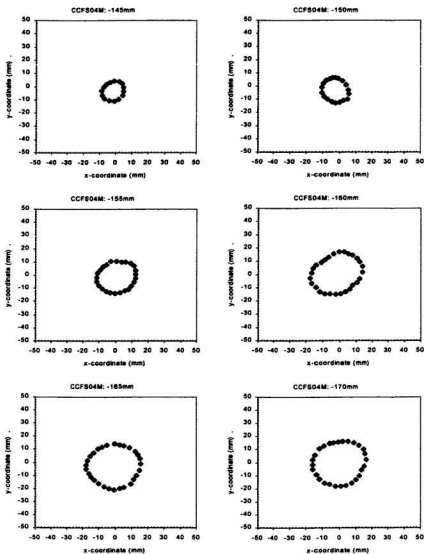
Depth is referenced from top of strongbox. Soil is uniformly blue within extents shown.

Figure A3.162. Dye trace record for CCFS04M (145-170 mm)
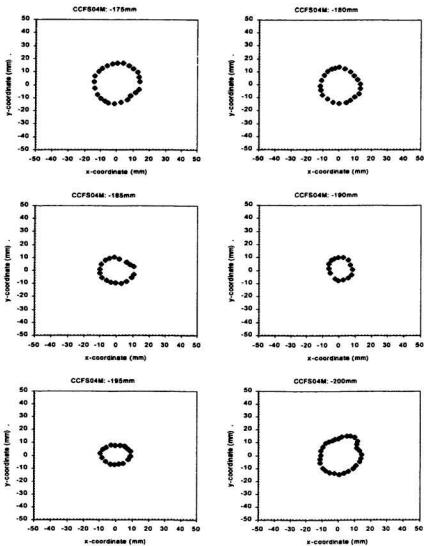
Depth is referenced from top of strongbox. Soil is uniformly blue within extents shown.

Figure A3.163. Dye trace record for CCFS04M (175-200 mm)
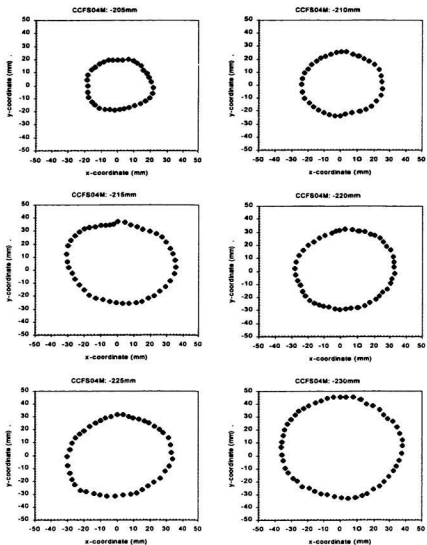
451

Depth is referenced from top of strongbox. Soil is uniformly blue within extents shown.

Figure A3.164. Dye trace record for CCFS04M (205-230 mm)
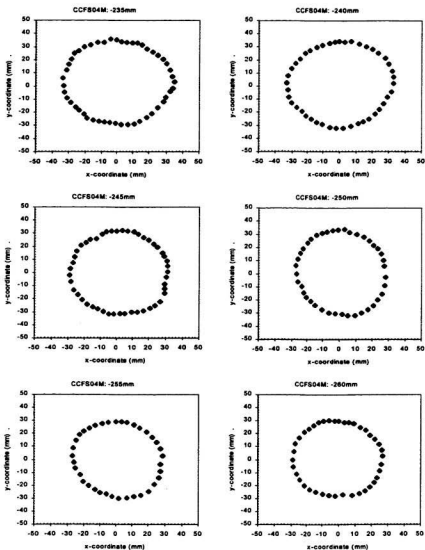
Depth is referenced from top of strongbox. Soil is uniformly blue within extents shown.

Figure A3.165. Dye trace record for CCFS04M (235-260 mm)
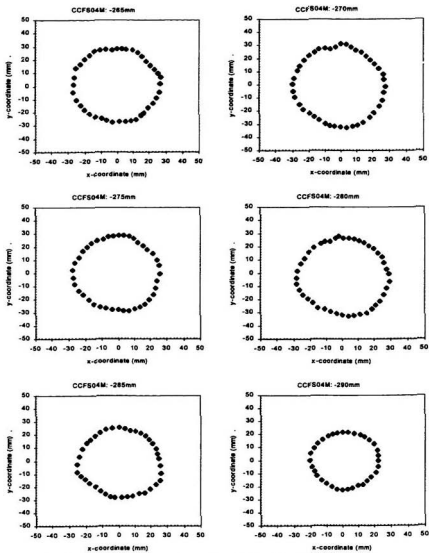
Depth is referenced from top of strongbox. Soil is uniformly blue within extents shown.

Figure A3.166. Dye trace record for CCFS04M (265-290 mm)
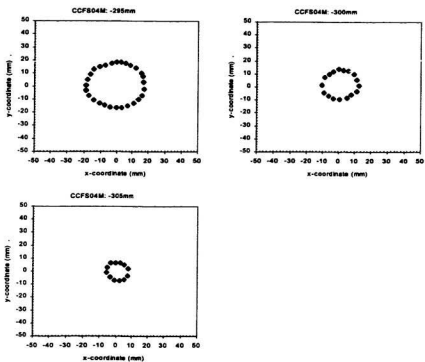
CCFS04M: -295mm

CCFS04M: -300mm

CCFS04M: -305mm

Depth is referenced from top of strongbox. Soil is uniformly blue within extents shown.

Figure A3.167. Dye trace record for CCFS04M (295-305 mm)
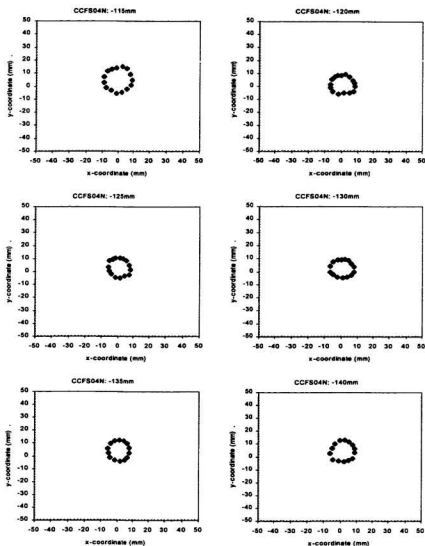
Depth is referenced from top of strongbox. Soil is uniformly blue within extents shown.

Figure A3.168. Dye trace record for CCFS04N (115-140 mm)
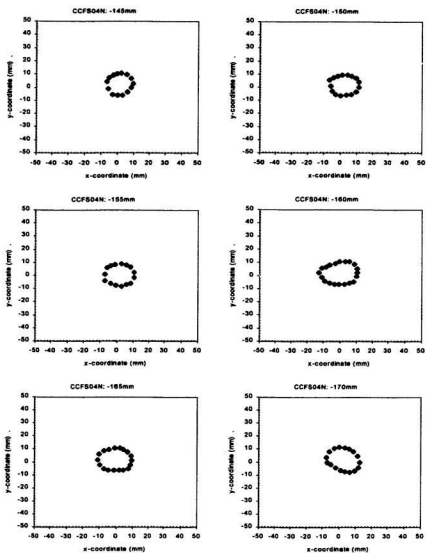
Depth is referenced from top of strongbox. Soil is uniformly blue within extents shown.

Figure A3.169. Dye trace record for CCFS04N (145-170 mm)
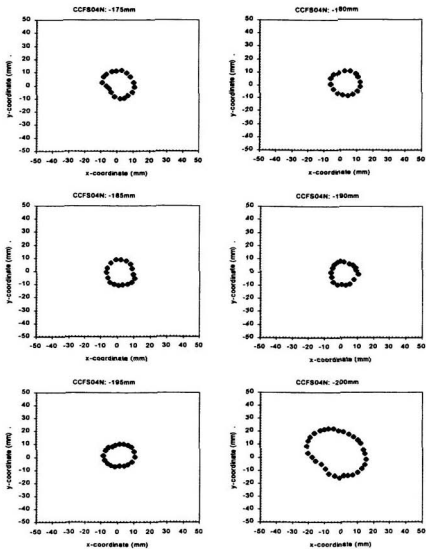
457

Depth is referenced from top of strongbox. Soil is uniformly blue within extents shown.

Figure A3.170. Dye trace record for CCFS04N (175-200 mm)
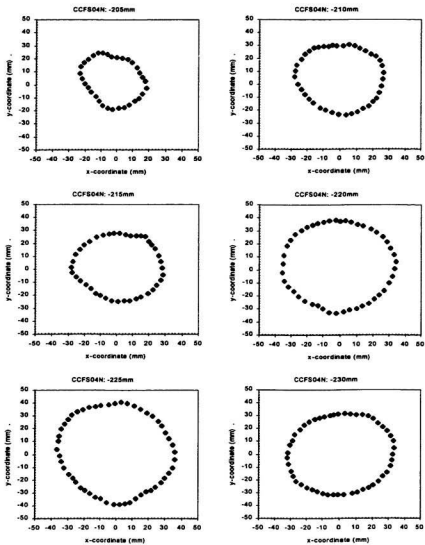
Depth is referenced from top of strongbox. Soil is uniformly blue within extents shown.

Figure A3.171. Dye trace record for CCFS04N (205-230 mm)
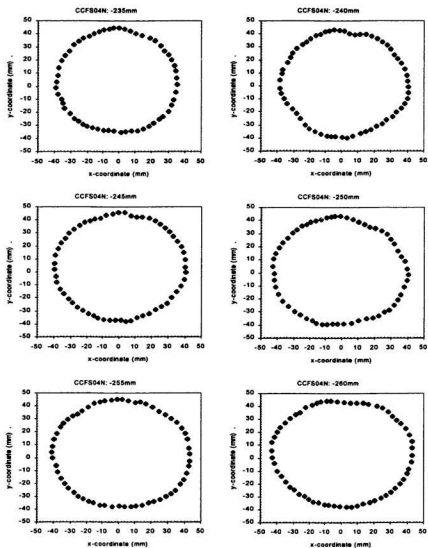
459

Depth is referenced from top of strongbox. Soil is uniformly blue within extents shown.

Figure A3.172. Dye trace record for CCFS04N (235-260 mm)
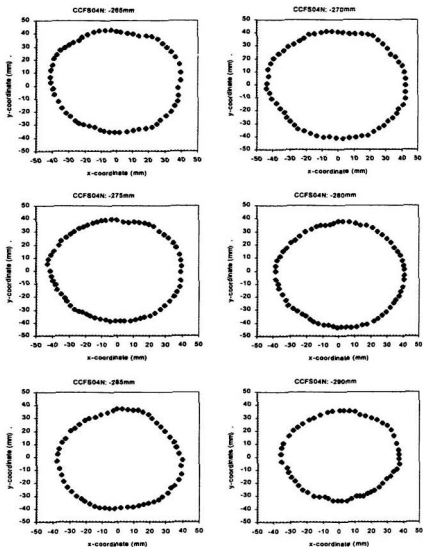
Depth is referenced from top of strongbox. Soil is uniformly blue within extents shown.

Figure A3.173. Dye trace record for CCFS04N (265-290 mm)
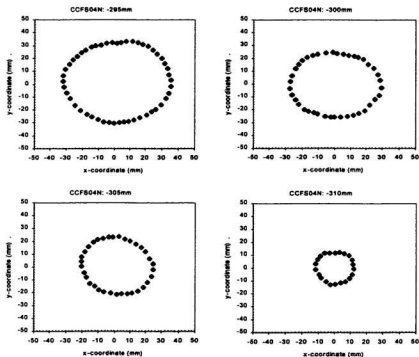
Depth is referenced from top of strongbox. Soil is uniformly blue within extents shown.

Figure A3.174. Dye trace record for CCFS04N (295-310 mm)
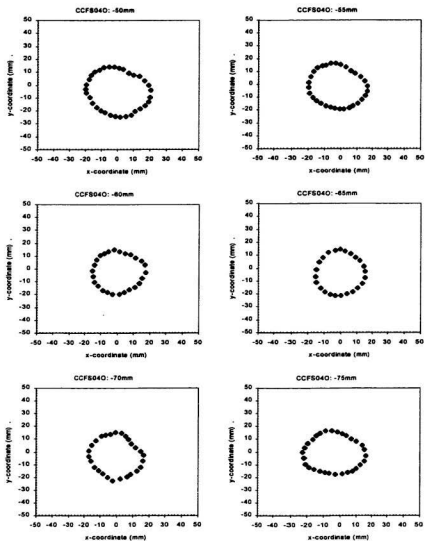
Depth is referenced from top of strongbox. Soil is uniformly blue within extents shown.

Figure A3.175. Dye trace record for CCFSO4O (50-75 mm)
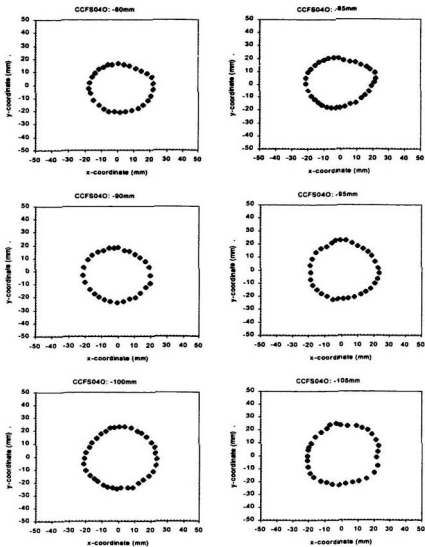
Depth is referenced from top of strongbox. Soil is uniformly blue within extents shown.

Figure A3.176. Dye trace record for CCFS04O (80-105 mm)
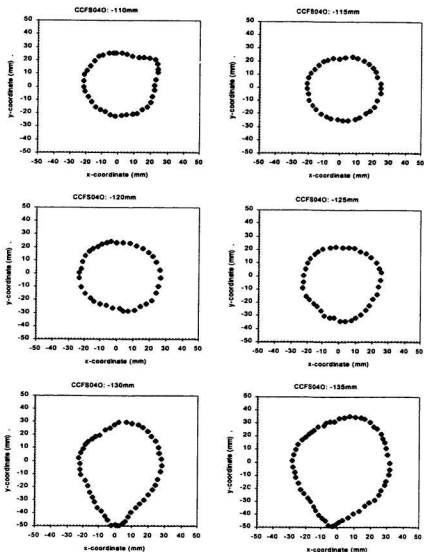
464

CCFS04O: -110mm   CCFS04O: -115mm
CCFS04O: -120mm   CCFS04O: -125mm
CCFS04O: -130mm   CCFS04O: -135mm

Depth is referenced from top of strongbox. Soil is uniformly blue within extents shown.

Figure A3.177. Dye trace record for CCFS04O (110-135 mm)
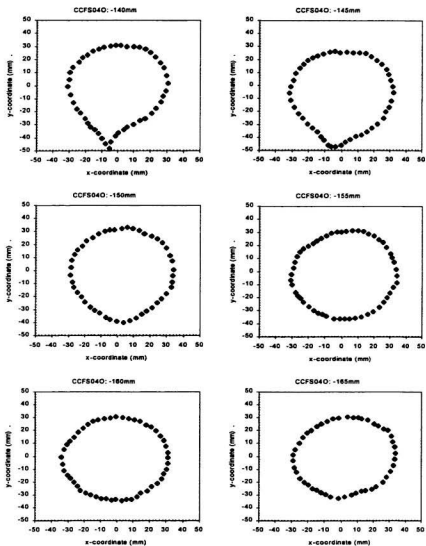
465

Depth is referenced from top of strongbox. Soil is uniformly blue within extents shown.

Figure A3.178. Dye trace record for CCFS04O (140-165 mm)
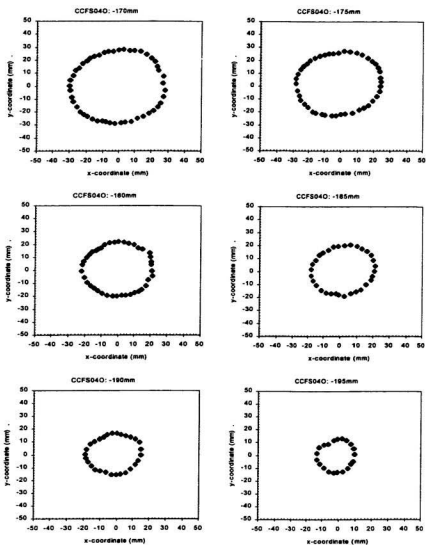
466

Depth is referenced from top of strongbox. Soil is uniformly blue within extents shown.

Figure A3.179. Dye trace record for CCFS04O (170-195 mm)
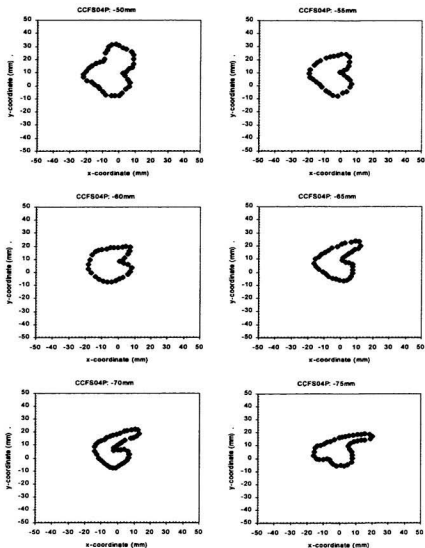
467

Depth is referenced from top of strongbox. Soil is uniformly blue within extents shown.

Figure A3.180. Dye trace record for CCFS04P (50-75 mm)
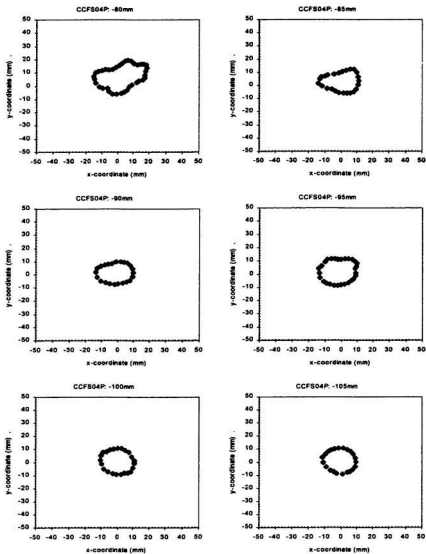
Depth is referenced from top of strongbox. Soil is uniformly blue within extents shown.

Figure A3.181. Dye trace record for CCFS04P (80-105 mm)
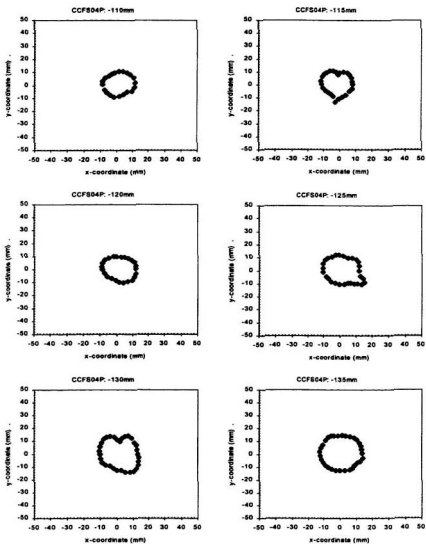
Depth is referenced from top of strongbox. Soil is uniformly blue within extents shown.

Figure A3.182. Dye trace record for CCFS04P (110-135 mm)

Depth is referenced from top of strongbox. Soil is uniformly blue within extents shown.
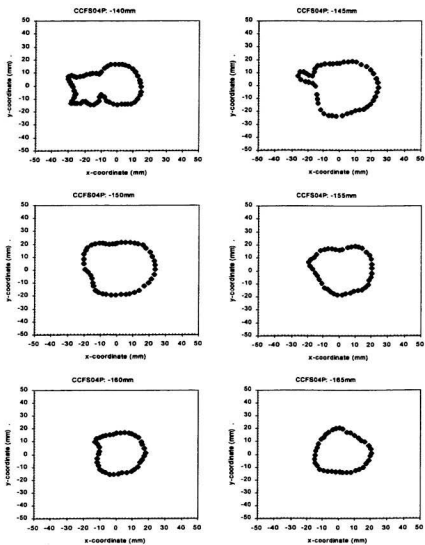
Figure A3.183. Dye trace record for CCFS04P (140-165 mm)
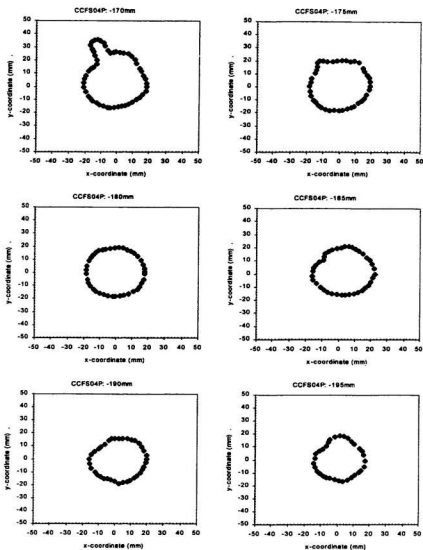
Depth is referenced from top of strongbox. Soil is uniformly blue within extents shown.

Figure A3.184. Dye trace record for CCFS04P (170-195 mm)
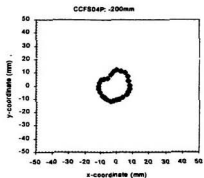
472

CCFS04P: -200mm

Depth is referenced from top of strongbox. Soil is uniformly blue within extents shown.

Figure A3.185. Dye trace record for CCFS04P (200 mm)

APPENDIX 4: CALIBRATION CHAMBER INJECTION TEST RESULTS

A4.1 Calibration Chamber Injection Test Results

A joint industry laboratory testing program was led by Golder Associates Ltd. in the early 1990's with the objective of generating experimental data that could be used to enhance the mathematical formulation of soil fracturing models. The project, which involved carrying out hydraulic fracturing experiments in sand within a large triaxial calibration chamber, was carried out in three phases (Golder Associates Ltd., 1991; Golder Associates Ltd., 1992; and Golder Associates Ltd., 1994). The data produced from this work was subsequently released to the public domain. A summary of test parameters and test results from the chamber test program is included in Table A4.1. Plots of injection pressures and soil pore pressures for the phase 2 and phase 3 injection tests are presented in Figure A4.1 through A4.20.

476

Table A4.1. Summary of chamber test results

| Test ID | Sub Test ID | Test Type | Fluid Properties | | | | | | | | K Pore (Darcy) |
| | | | Pore Fluid | | | | Injection Fluid | | | | |
			Type	T (°C)	μ (Pa-s)	σ_t	Type	T (°C)	μ (Pa-s)	σ_t	
1Frac1	-	Chamber	Glycerine	20	1.49	1.26	Glycerine	20	1.49	1.26	5.4
1Frac3	-	Chamber	Glycerine	20	1.49	1.26	Glycerine	20	1.49	1.26	5.4
1Frac4	-	Chamber	Glycerine	20	1.49	1.26	Glycerine	20	1.49	1.26	5.4
1Frac5	-	Chamber	Glycerine	20	1.49	1.26	Glycerine	20	1.49	1.26	5.4
1Frac6	-	Chamber	Invert liquid sugar	20	1.49	1.38	Glycerine	20	1.49	1.26	1.5
1Frac7	-	Chamber	Invert liquid sugar	20	1.49	1.38	Invert liquid sugar	20	1.49	1.38	4.4
1Frac8	-	Chamber	Invert liquid sugar	20	1.49	1.38	Invert liquid sugar	20	1.49	1.38	2.8
2Frac2	b	Chamber	Invert liquid sugar	20	1.49	1.38	Invert liquid sugar	20	1.49	1.38	4.2
	c	Chamber	Invert liquid sugar	20	1.49	1.38	Invert liquid sugar	20	1.49	1.38	4.2
	d	Chamber	Invert liquid sugar	20	1.49	1.38	Invert liquid sugar	20	1.49	1.38	4.2
	e	Chamber	Invert liquid sugar	20	1.49	1.38	Invert liquid sugar	20	1.49	1.38	4.2
2Frac3	-	Chamber	Invert liquid sugar	20	1.49	1.38	Invert liquid sugar	20	1.49	1.38	5.5
	b	Chamber	Invert liquid sugar	20	1.49	1.38	Invert liquid sugar	20	1.49	1.38	5.5
	c	Chamber	Invert liquid sugar	20	1.49	1.38	Invert liquid sugar	20	1.49	1.38	5.5
	d	Chamber	Invert liquid sugar	20	1.49	1.38	Invert liquid sugar	20	1.49	1.38	5.5
	e	Chamber	Invert liquid sugar	20	1.49	1.38	Invert liquid sugar	20	1.49	1.38	5.5
	f	Chamber	Invert liquid sugar	20	1.49	1.38	Invert liquid sugar	20	1.49	1.38	5.5
2Frac4	-	Chamber	Invert liquid sugar	20	1.49	1.38	Invert liquid sugar	20	1.49	1.38	4.8
2Frac5	-	Chamber	Invert liquid sugar	20	1.49	1.38	Invert liquid sugar	20	1.49	1.38	6.9
3Frac2	-	Chamber	Invert liquid sugar	20	1.49	1.38	Water	20	0.001	1.0	5.0
3Frac3	-	Chamber	Invert liquid sugar	20	1.49	1.38	Water	20	0.001	1.0	6.2
3Frac4	-	Chamber	Invert liquid sugar	20	1.49	1.38	Water	20	0.001	1.0	4.7
3Frac5	-	Chamber	Invert liquid sugar	20	1.49	1.38	Water	20	0.001	1.0	4.2
3Frac6	-	Chamber	Invert liquid sugar	20	1.49	1.38	Water	20	0.001	1.0	3.7

Reference: (Golder Associates Ltd, 1991, 1992 and 1994)

477

Table A4.1. (cont'd) Summary of chamber test results

Test ID	Sub Test ID	Soil Type	Soil Prep. Method	ρ (t/m³)	G_s	n	Sat. (%)	c' (kPa)	ϕ' (deg)	ψ (deg)
1Fmc3	-	Lane Mountain Sand	raining	1983	2.65	0.48	100	0	38	30
1Fmc4	-	Lane Mountain Sand	raining	1983	2.65	0.48	100	0	38	30
1Fmc5	-	Lane Mountain Sand	raining	1983	2.65	0.48	100	0	38	30
1Fmc6	-	Lane Mountain Sand	raining	1983	2.65	0.48	100	0	38	30
1Fmc7	-	Lane Mountain Sand	raining	2031	2.65	0.48	100	0	38	30
1Fmc9	-	Lane Mountain Sand	raining	2031	2.65	0.48	100	0	38	30
2Fmc2	a	Lane Mountain Sand	raining	2031	2.65	0.48	100	0	38	30
	b	Lane Mountain Sand	raining	2031	2.65	0.48	100	0	38	30
	c	Lane Mountain Sand	raining	2031	2.65	0.48	100	0	38	30
	d	Lane Mountain Sand	raining	2031	2.65	0.48	100	0	38	30
2Fmc3	a	Lane Mountain Sand	raining	2031	2.65	0.48	100	0	38	30
	b	Lane Mountain Sand	raining	2031	2.65	0.48	100	0	38	30
	c	Lane Mountain Sand	raining	2031	2.65	0.48	100	0	38	30
	d	Lane Mountain Sand	raining	2031	2.65	0.48	100	0	38	30
	e	Lane Mountain Sand	raining	2031	2.65	0.48	100	0	38	30
	f	Lane Mountain Sand	raining	2031	2.65	0.48	100	0	38	30
2Fmc4	-	Lane Mountain Sand	raining	2031	2.65	0.48	100	0	38	30
2Fmc5	-	Lane Mountain Sand	raining	2031	2.65	0.48	100	0	38	30
3Fmc1	-	Lane Mountain Sand	raining	2031	2.65	0.48	100	0	38	30
3Fmc2	-	Lane Mountain Sand	raining	2031	2.65	0.48	100	0	38	30
3Fmc3	-	Lane Mountain Sand	raining	2031	2.65	0.48	100	0	38	30
3Fmc4	-	Lane Mountain Sand	raining	2031	2.65	0.48	100	0	38	30
3Fmc5	-	Lane Mountain Sand	raining	2031	2.65	0.48	100	0	38	30

Table A4.1. [cont'd] Summary of chamber test results

Test ID	Sub Test ID	Injection Well Configuration						Stress Boundary Conditions					
		Orientation	Slot Dimensions (mm)	In Interval Top (m)	Bottom (m)	Well Dia (m)	Surface Area (m²)	K_o	σ_v (kPa)	σ_h (kPa)	u (kPa)	σ'_v (kPa)	σ'_h (kPa)
1Fmc1	-	Vertical	no slot	0.475	0.525	0.0335	0.0053	-	460	483	432	28	61
1Fmc3	-	Vertical	no slot	0.475	0.525	0.0335	0.0053	-	400	400	200	200	200
1Fmc5	-	Vertical	no slot	0.475	0.525	0.0335	0.0053	-	400	400	200	200	200
1Fmc5	-	Vertical	no slot	0.475	0.525	0.0335	0.0053	-	400	400	200	200	200
1Fmc6	-	Vertical	no slot	0.475	0.525	0.0335	0.0053	-	400	400	200	200	200
1Fmc7	-	Vertical	no slot	0.475	0.525	0.0335	0.0053	-	400	400	200	200	200
1Fmc8	-	Vertical	no slot	0.475	0.525	0.0335	0.0053	-	400	400	200	200	200
2Fmc2	-	Vertical	no slot	0.475	0.525	0.0335	0.0053	2.2	400	880	-	400	880
	a	Vertical	no slot	0.475	0.525	0.0335	0.0053	2.0	400	800	-	400	800
	b	Vertical	no slot	0.475	0.525	0.0335	0.0053	2.0	400	800	-	400	800
	c	Vertical	no slot	0.475	0.525	0.0335	0.0053	2.0	400	800	-	400	800
	d	Vertical	no slot	0.475	0.525	0.0335	0.0053	0.5	400	200	-	400	200
2Fmc3	a	Vertical	no slot	0.475	0.525	0.0335	0.0053	2.0	400	800	-	400	800
	b	Vertical	no slot	0.475	0.525	0.0335	0.0053	2.0	400	800	-	400	800
	c	Vertical	no slot	0.475	0.525	0.0335	0.0053	2.0	400	800	-	400	800
	d	Vertical	no slot	0.475	0.525	0.0335	0.0053	2.0	400	800	-	400	800
	e	Vertical	no slot	0.475	0.525	0.0335	0.0053	2.0	400	800	-	400	800
	f	Vertical	no slot	0.475	0.525	0.0335	0.0053	2.0	400	800	-	400	800
2Fmc4	-	Vertical	no slot	0.475	0.525	0.0335	0.0053	2.0	400	800	-	400	800
2Fmc5	-	Vertical	no slot	0.475	0.525	0.0335	0.0053	2.0	400	800	-	400	800
3Fmc1	-	Vertical	no slot	0.475	0.525	0.0335	0.0053	2.0	400	800	-	400	800
3Fmc2	-	Vertical	no slot	0.475	0.525	0.0335	0.0053	1.3	400	800	-	600	800
3Fmc3	-	Vertical	no slot	0.475	0.525	0.0335	0.0053	0.50	400	200	-	400	200
3Fmc4	-	Vertical	no slot	0.475	0.525	0.0335	0.0053	1.3	400	800	-	600	800
3Fmc4	-	Vertical	6.4 ht x 84.3 dia	0.4986	0.5032	0.0335	0.0012	2.0	500	800	-	500	800
3Fmc6	-	Vertical	6.4 ht x 84.3 dia	0.4986	0.5032	0.0335	0.0012	2.0	400	400	-	200	400

479

Table A4.1. [cont'd] Summary of chamber test results

Test ID	Sub Test ID	Injection Test Details				Pressure Peak (kPa)	dP/dt Max (kPa/s)	Fracture Configuration
		Rate (l/s)	Inj. Velocity (m/s)	Time (s)	Volume (l)			
1Fmc1		0.0956	1.82E-02	9.7	0.927	· · ·	· · ·	
1Fmc3		0.0935	1.78E-02	9.7	0.907	· · ·	· · ·	
1Fmc5		0.0050	9.50E-04	4.0	0.020	<900	175	distributed (cupped feature)
1Fmd5		0.0050	9.50E-04	3.8	0.018	240	10	distributed (conical feature - no tensile parting)
1Fmd5		0.0050	9.50E-04	· · ·	· · ·	232	9	no tensile parting
1Fmc7		0.0100	1.90E-03	4.0	0.040	425	58	distributed (limited if any tensile parting, flow through pore space)
1Fmd8		0.0100	1.90E-03	4.0	0.040	320	30	distributed (conical feature - no tensile parting)
2Fmc2	a	0.00028	5.32E-05	3038	0.850	490	· · ·	
	b	0.00040	7.60E-05	2125	0.850	870	· · ·	
	c	0.00100	1.90E-04	850	0.850	620	· · ·	
	d	0.00025	4.75E-05	3400	0.850	820	· · ·	
2Fmc3		0.00100	1.90E-04	500	0.200	620	2	compact
	a	0.00100	1.90E-04	850.0	0.850	800	· · ·	
	b	0.00300	5.70E-04	283.3	0.850	800	· · ·	
	c	0.01000	1.90E-03	85.0	0.850	690	· · ·	
	d	0.03000	1.90E-03	28.3	0.850	710	· · ·	
		0.00300	5.70E-04	283.3	0.850	470	· · ·	
2Fmc4		0.03000	5.70E-03	6.7	0.200	360	27	compact
2Fmc5		0.03000	5.70E-03	8.3	0.250	350	42	distributed (discrete surface)
3Fmc1		0.20000	3.80E-02	1.3	0.260	608	97	compact (discrete surface)
3Fmc1		0.04100	7.77E-03	22.0	0.900	1136	1922	distributed (discrete surface)
3Fmc2		0.04100	7.77E-03	22.0	0.900	867	249	distributed (discrete surface)
3Fmc3		0.20000	3.80E-02	4.5	0.900	1230	1206	distributed (discrete surface)
3Fmc4		0.20000	3.80E-02	4.5	0.900	1235	1067	distributed (discrete surface)
3Fmc5		0.20000	1.89E-01	4.5	0.900	681	509	distributed (discrete surface)
3Fmc6		0.20000	1.89E-01	1.5	0.300	758	674	distributed (discrete surface)

480
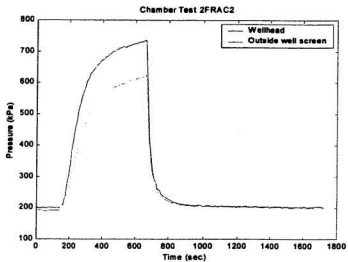
Figure A4.1. Injection pressure for 2FRAC2 (Golder Associates Ltd., 1992)
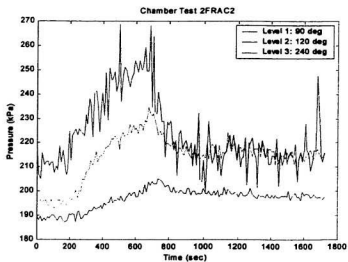
Figure A4.2. Pore pressures for 2FRAC2 (Golder Associates Ltd., 1992)

481
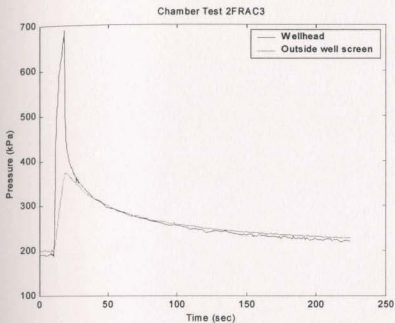
Figure A4.3. Injection pressure for 2FRAC3 (Golder Associates Ltd., 1992)
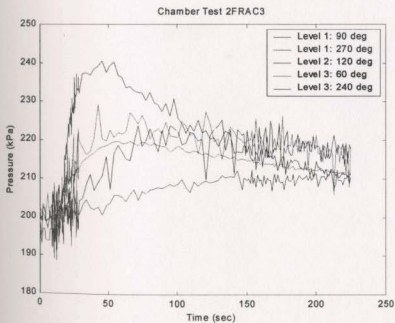
Figure A4.4. Pore pressures for 2FRAC3 (Golder Associates Ltd., 1992)

482
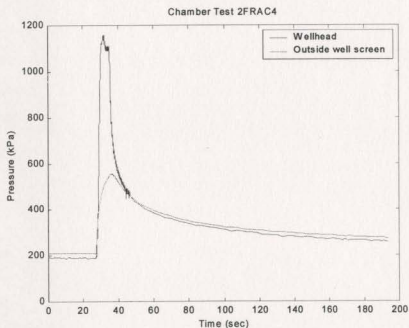
Figure A4.5. Injection pressure for 2FRAC4 (Golder Associates Ltd., 1992)
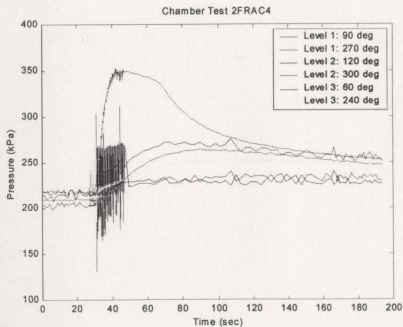
Figure A4.6. Pore pressures for 2FRAC4 (Golder Associates Ltd., 1992)
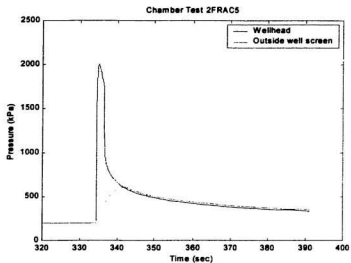
Figure A4.7. Injection pressure for 2FRAC5 (Golder Associates Ltd., 1992)
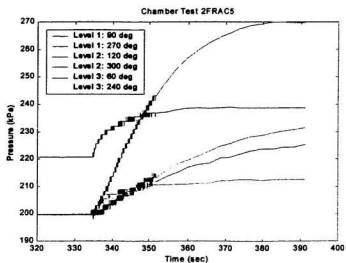
Figure A4.8. Pore pressures for 2FRAC5 (Golder Associates Ltd., 1992)

484
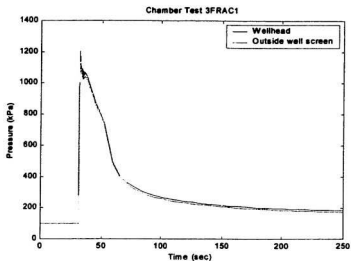
Figure A4.9. Injection pressure for 3FRAC1 (Golder Associates Ltd., 1994)
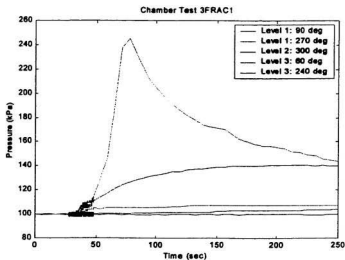
Figure A4.10. Pore pressures for 3FRAC1 (Golder Associates Ltd., 1994)
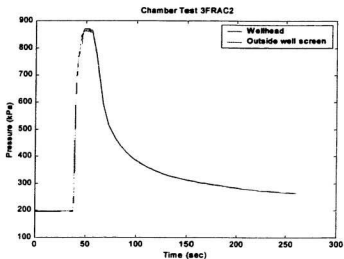
Figure A4.11. Injection pressure for 3FRAC2 (Golder Associates Ltd., 1994)
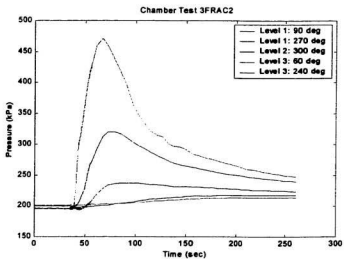
Figure A4.12. Pore pressures for 3FRAC2 (Golder Associates Ltd., 1994)

486
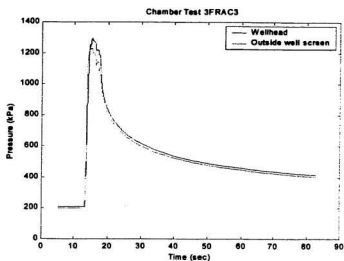
Figure A4.13. Injection pressure for 3FRAC3 (Golder Associates Ltd., 1994)
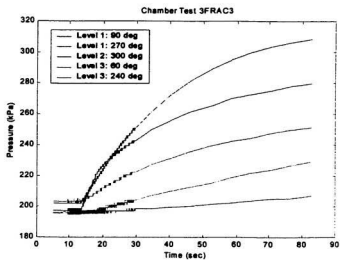
Figure A4.14. Pore pressures for 3FRAC3 (Golder Associates Ltd., 1994)
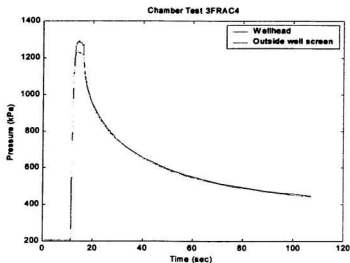
Figure A4.15. Injection pressure for 3FRAC4 (Golder Associates Ltd., 1994)
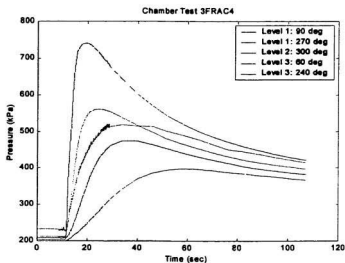
Figure A4.16. Pore pressures for 3FRAC4 (Golder Associates Ltd., 1994)
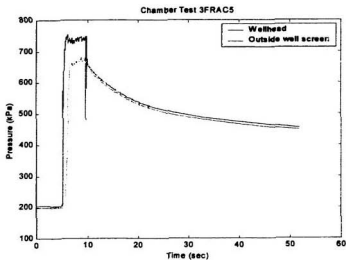
Figure A4.17. Injection pressure for 3FRAC5 (Golder Associates Ltd., 1994)
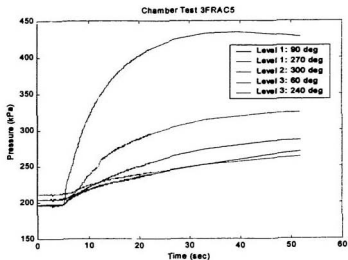
Figure A4.18. Pore pressures for 3FRAC5 (Golder Associates Ltd., 1994)

489
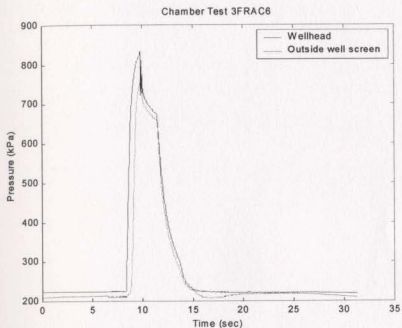
Figure A4.19. Injection pressure for 3FRAC6 (Golder Associates Ltd., 1994)
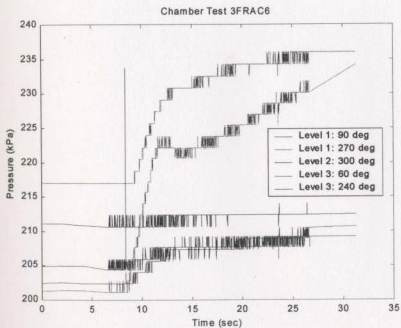
Figure A4.20. Pore pressures for 3FRAC6 (Golder Associates Ltd., 1994)

APPENDIX 5: RESULTS OF NUMERICAL SIMULATIONS

A5.1   General

The results of numerical simulations of the chamber tests are presented in Section A5.2, simulations of the field tests are presented in Section A5.3, and simulations of the centrifuge tests are presented in Section A5.4. The results of each simulation are presented in a series of 10 figures that includes plots of:

· the extent of the yield zone at the end of injection (or at some time t)

· plastic shear strain at the end injection (or at some time t)

· the change in horizontal effective stress due to fluid injection

· the change in vertical effective stress due to fluid injection

· the change in tangential effective stress due to fluid injection

· the change in pore pressure due to fluid injection

· the principal stress ratio (horizontal to vertical effective stress) at the end of injection (or at some time t)

· region of permeability enhancement due to shearing

· histories showing the development of pore pressures during the injection period, and

· histories showing stress paths of soil elements during the injection period.

In FLAC, positive stresses indicate tension and negative stresses indicate compression. Positive pore pressures are presented with a positive sign. Where changes in stress are plotted, a positive stress change indicates that the magnitude of the compressive stress has decreased, and a negative stress change indicates that the magnitude of the compressive stress has increased. A positive change in pore pressure indicates an increase in pore pressure, a negative change indicates a reduction in pore pressure. All figures plotted as output from FLAC use this convention. Figures which were not derived from FLAC (i.e. stress path plots in this appendix) use the notation where compressive stresses are positive and tensile stresses are negative.

492

A5.2 Chamber Tests
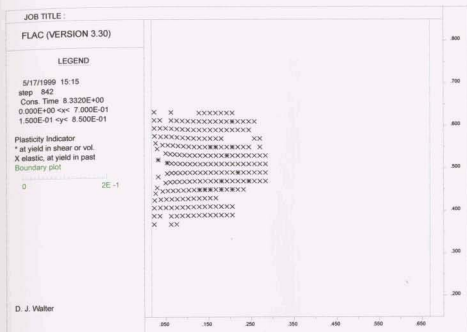
Figure A5.1. Extent of yield zone at end of injection (KRUN0: Δk=1k)
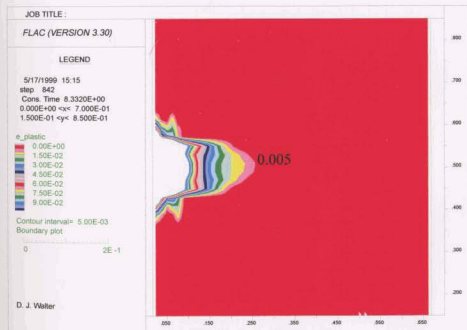
Figure A5.2. Plastic strain contours at end of injection (KRUN0: Δk=1k)
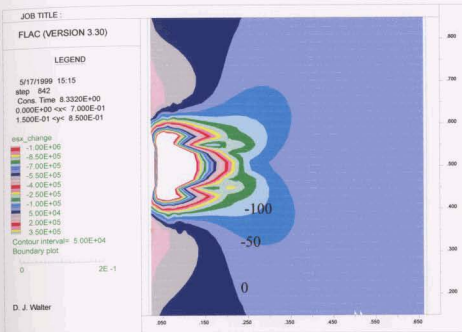
Figure A5.3. Change in horizontal effective stress (KRUN0: Δk=1k)
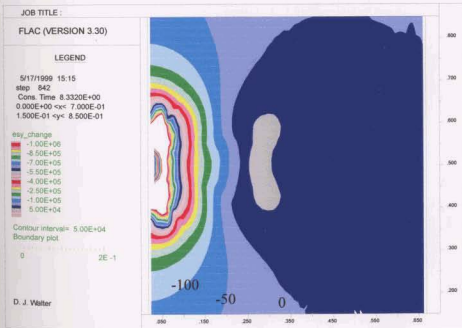
Figure A5.4. Change in vertical effective stress (KRUN0: Δk=1k)
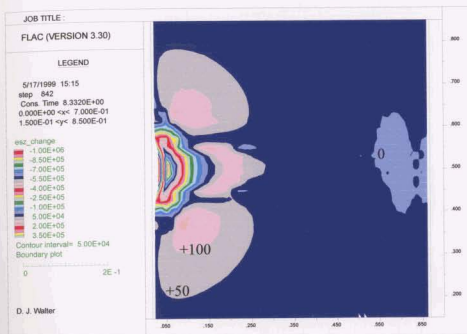
Figure A5.5. Change in tangential effective stress (KRUN0: Δk=1k)
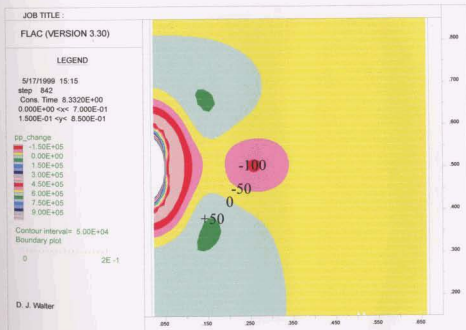
Figure A5.6. Change in pore pressure (KRUN0: Δk=1k)
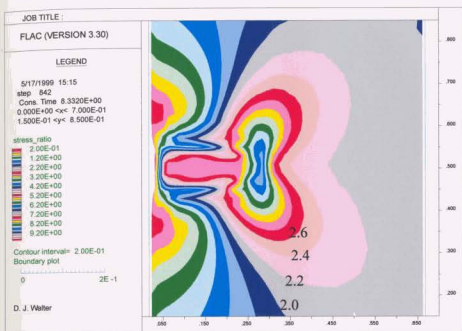
Figure A5.7. Stress ratio σ'$_x$/σ'$_y$ (KRUN0: Δk=1k)
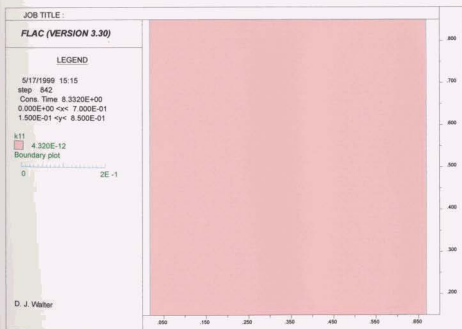
Figure A5.8. FLAC permeability (KRUN0: Δk=1k)
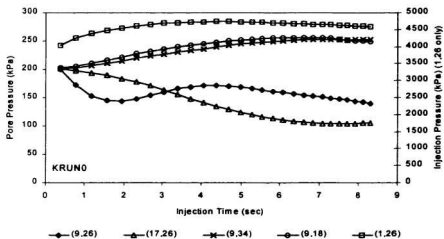
Figure A5.9. Pore pressure development during injection (KRUN0: Δk=1k)
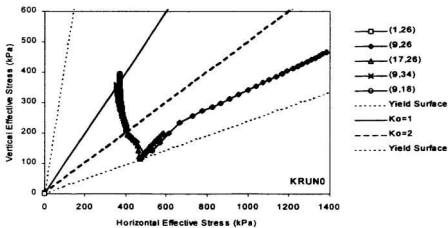
Figure A5.10. Stress paths during injection (KRUN0: Δk=1k)

498
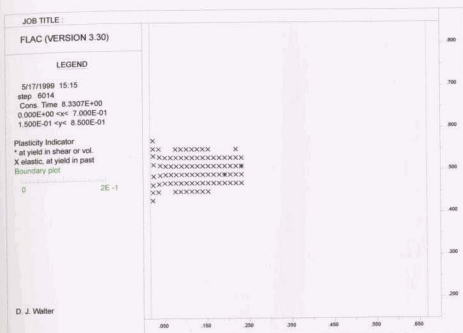
Figure A5.11. Extent of yield zone at end of injection (KRUN1: Δk=10k)
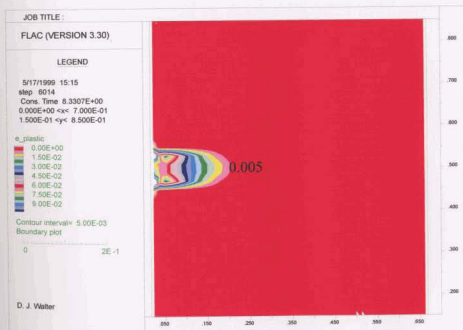
Figure A5.12. Plastic strain contours at end of injection (KRUN1: Δk=10k)
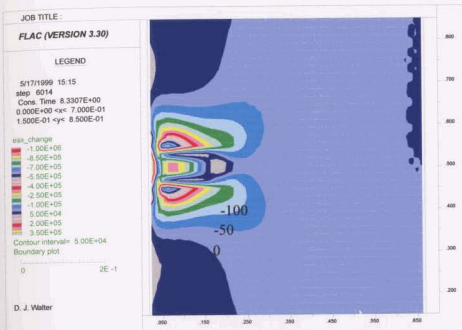
Figure A5.13. Change in horizontal effective stress (KRUN1: Δk=10k)
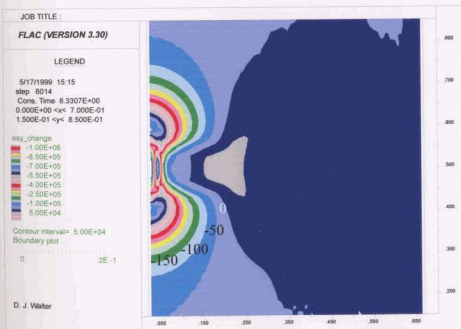
Figure A5.14. Change in vertical effective stress (KRUN1: Δk=10k)
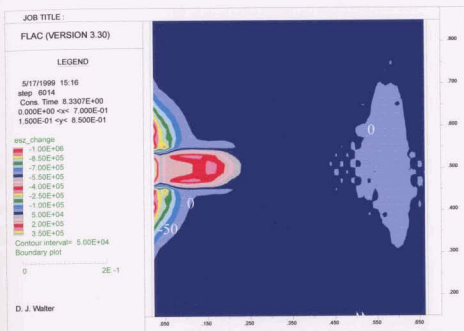
Figure A5.15. Change in tangential effective stress (KRUN1: Δk=10k)

Figure A5.16. Change in pore pressure (KRUN1: Δk=10k)
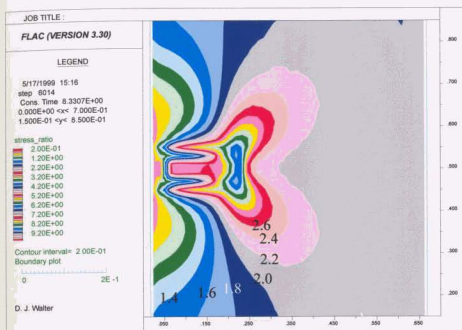
Figure A5.17. Stress ratio σ'$_x$/σ'$_y$ (KRUN1: Δk=10k)
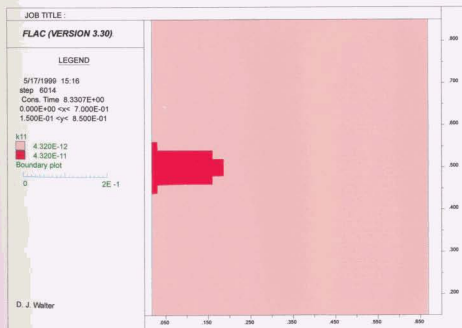
Figure A5.18. FLAC permeability (KRUN1: Δk=10k)
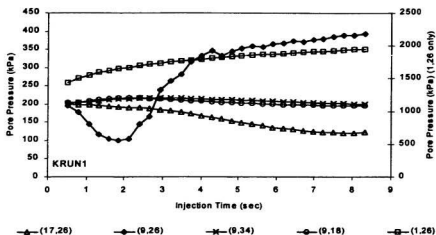
Figure A5.19. Pore pressure development during injection (KRUN1: Δk=10k)
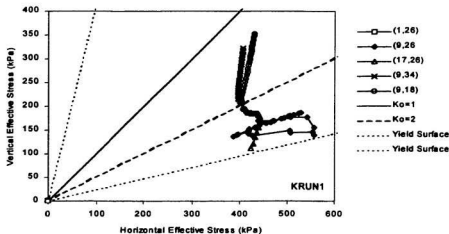
Figure A5.20. Stress paths during injection (KRUN1: Δk=10k)

503
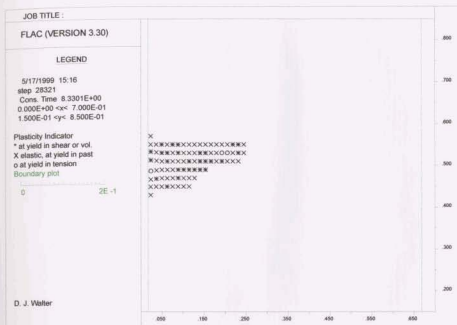
Figure A5.21. Extent of yield zone at end of injection (KRUN2: Δk=100k)
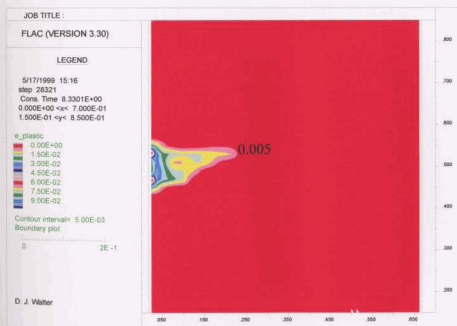
Figure A5.22. Plastic strain contours at end of injection (KRUN2: Δk=100k)
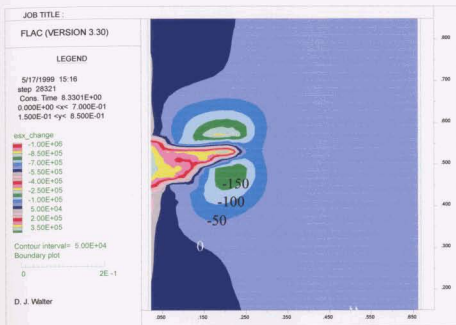
Figure A5.23. Change in horizontal effective stress (KRUN2: Δk=100k)
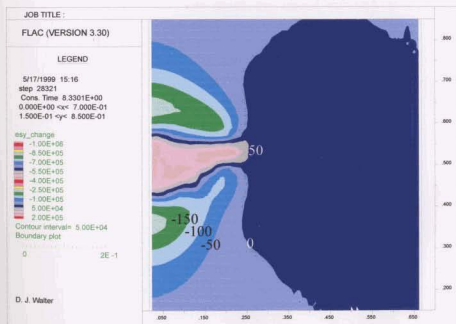
Figure A5.24. Change in vertical effective stress (KRUN2: Δk=100k)
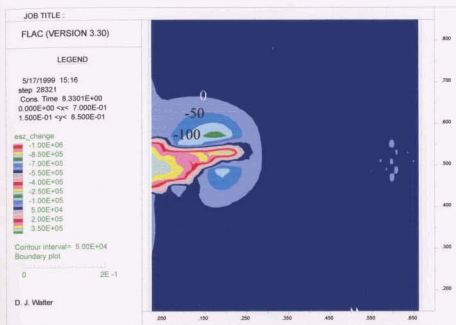
Figure A5.25. Change in tangential effective stress (KRUN2: Δk=100k)
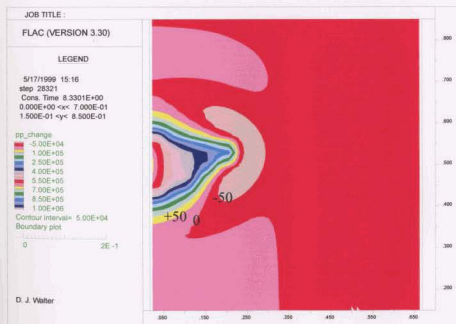
Figure A5.26. Change in pore pressure (KRUN2: Δk=100k)
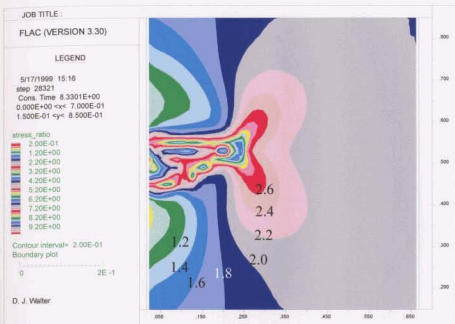
Figure A5.27. Stress ratio σ'ᵥ/σ'ₕ, (KRUN2: Δk=100k)
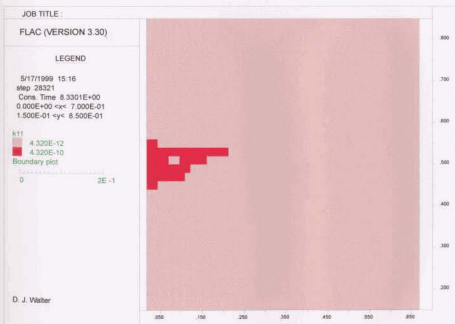
Figure A5.28. FLAC permeability (KRUN2: Δk=100k)
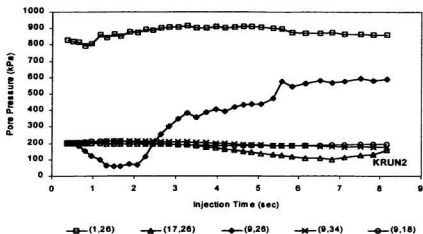
Figure A5.29. Pore pressure development during injection (KRUN2: Δk=100k)
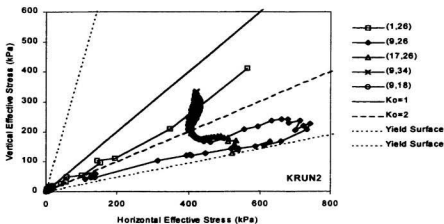
Figure A5.30. Stress paths during injection (KRUN2: Δk=100k)
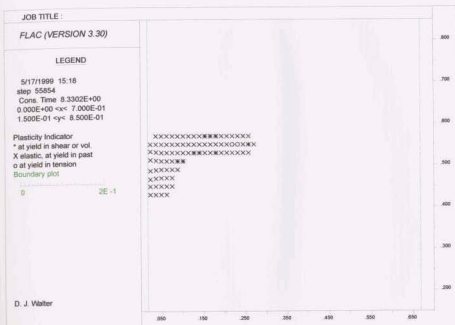
Figure A5.31. Extent of yield zone at end of injection (KRUN3: Δk=1000k)

Figure A5.32. Plastic strain contours at end of injection (KRUN3: Δk=1000k)
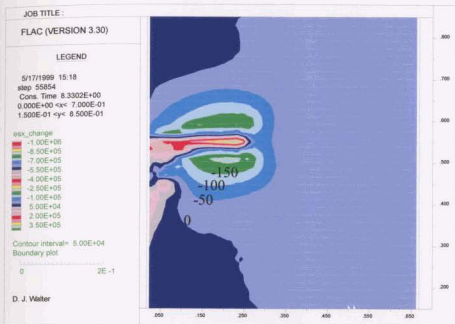
Figure A5.33. Change in horizontal effective stress (KRUN3: Δk=1000k)
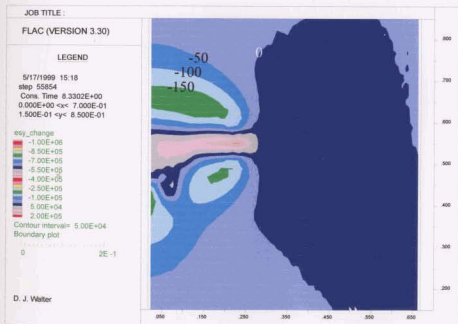
Figure A5.34. Change in vertical effective stress (KRUN3: Δk=1000k)
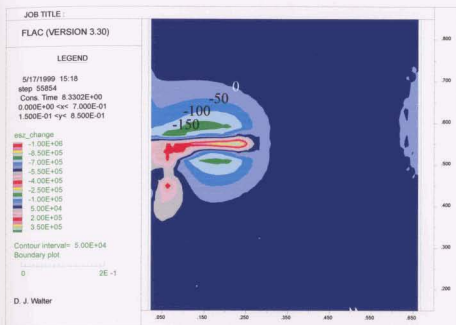
Figure A5.35. Change in tangential effective stress (KRUN3: Δk=1000k)
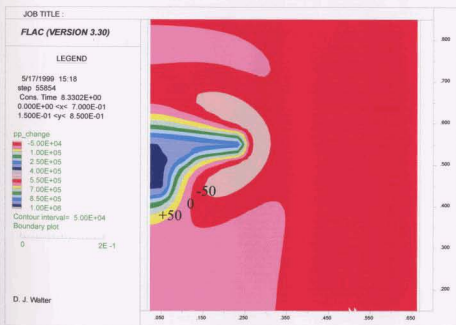
Figure A5.36. Change in pore pressure (KRUN3: Δk=1000k)
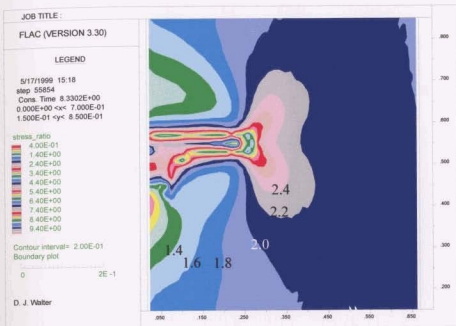
Figure A5.37. Stress ratio σ'_x/σ'_y, (KRUN3: $\Delta k=1000k$)
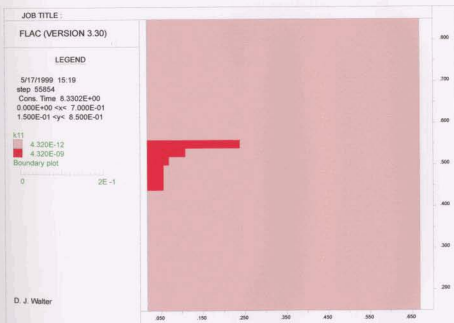
Figure A5.38. FLAC permeability (KRUN3: $\Delta k=1000k$)
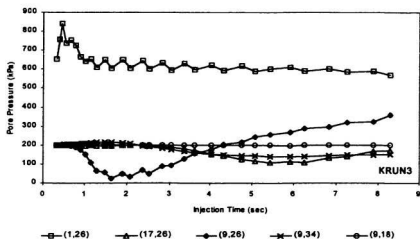
Figure A5.39. Pore pressure development during injection (KRUN3: Δk=1000k)
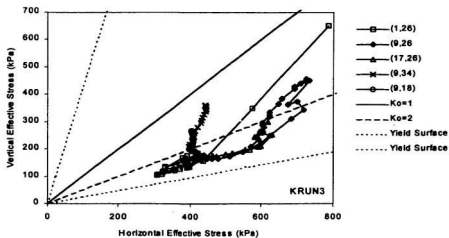
Figure A5.40. Stress paths during injection (KRUN3: Δk=1000k)

513
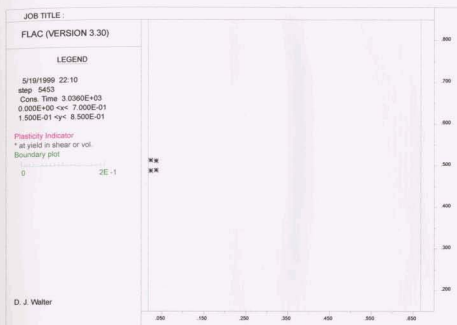
Figure A5.41. Extent of yield zone at end of injection (2FRAC2a: 0.28 ml/s)

Figure A5.42. Plastic strain contours at end of injection (2FRAC2a: 0.28 ml/s)
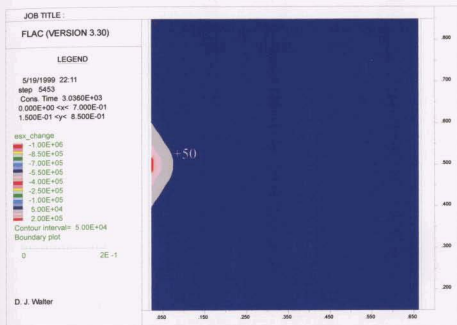
Figure A5.43. Change in horizontal effective stress (2FRAC2a: 0.28 ml/s)

Figure A5.44. Change in vertical effective stress (2FRAC2a: 0.28 ml/s)

Figure A5.45. Change in tangential effective stress (2FRAC2a: 0.28 ml/s)
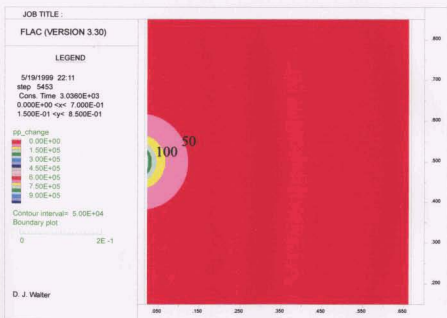
Figure A5.46. Change in pore pressure (2FRAC2a: 0.28 ml/s)
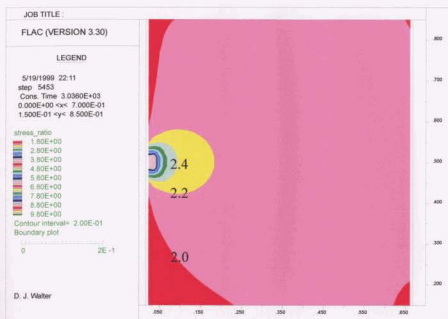
Figure A5.47. Stress ratio σ'$_x$/σ'$_y$ (2FRAC2a: 0.28 ml/s)
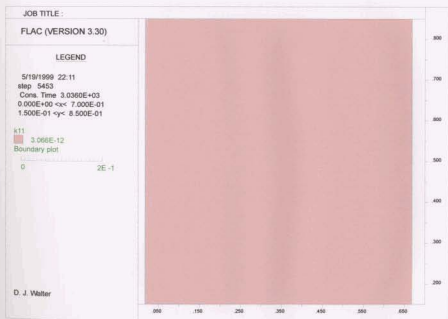
Figure A5.48. FLAC permeability (2FRAC2a: 0.28 ml/s)
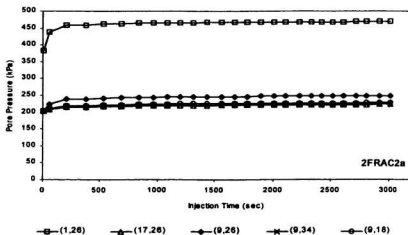
Figure A5.49. Pore pressure development during injection (2FRAC2a: 0.28 ml/s)
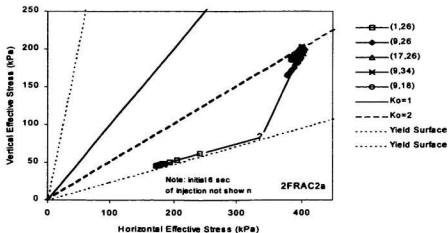
Figure A5.50. Stress paths during injection (2FRAC2a: 0.28 ml/s)
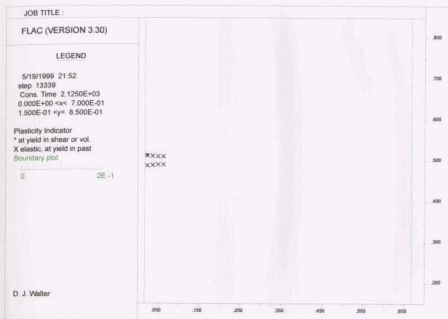
Figure A5.51. Extent of yield zone at end of injection (2FRAC2b: 0.40 ml/s)

Figure A5.52. Plastic strain contours at end of injection (2FRAC2b: 0.40 ml/s)
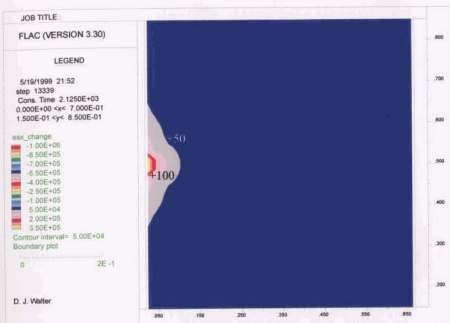
Figure A5.53. Change in horizontal effective stress (2FRAC2b: 0.40 ml/s)
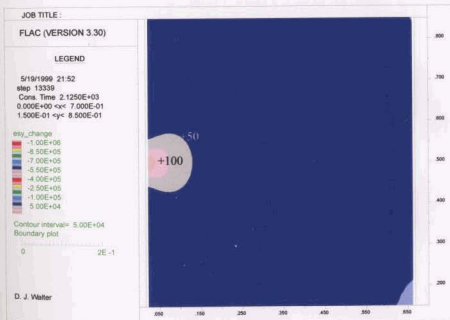
Figure A5.54. Change in vertical effective stress (2FRAC2b: 0.40 ml/s)
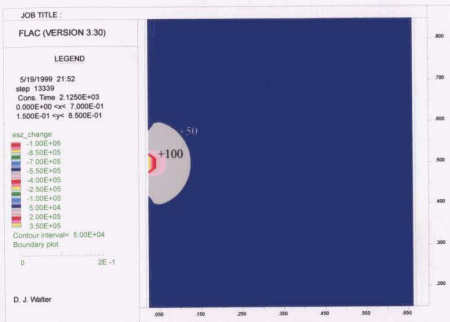
Figure A5.55. Change in tangential effective stress (2FRAC2b: 0.40 ml/s)
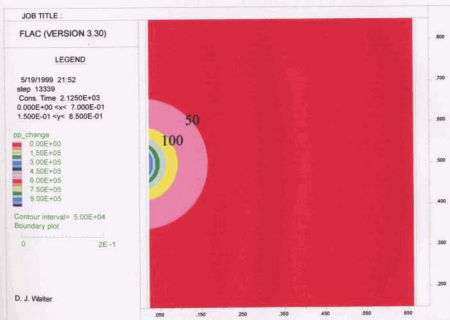
Figure A5.56. Change in pore pressure (2FRAC2b: 0.40 ml/s)

Figure A5.58. FLAC permeability (2FRAC26; 0.40 m/s)

JOB TITLE

FLAC (VERSION 3.30)

LEGEND

5/19/1999 21:53
step 13339
Cont. Time 2.1250E+03
0.000E+00 <x< 7.000E-01
1.500E-01 <y< 8.500E-01

A11 3.000E-12
Boundary plot

0   2E-1

D. J. Walter

Figure A5.57. Stress ratio σ'₁/σ'₃ (2FRAC26; 0.40 m/s)

JOB TITLE

FLAC (VERSION 3.30)

LEGEND

5/19/1999 21:52
step 13339
Cont. Time 2.1250E+03
0.000E+00 <x< 7.000E-01
1.500E-01 <y< 8.500E-01

stress_ratio
1.000E+00
2.000E+00
3.000E+00
4.000E+00
5.000E+00
6.000E+00
7.000E+00
8.000E+00
Contour interval= 2.000E-01
Boundary plot

0   2E-1

D. J. Walter

2.0

2.2

2.4
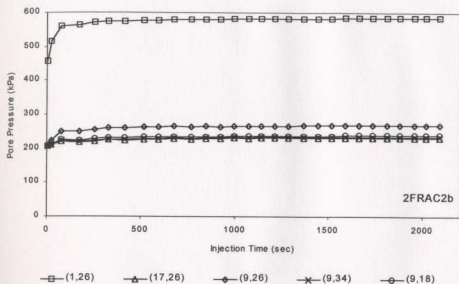
Figure A5.59. Pore pressure development during injection (2FRAC2b: 0.40 ml/s)
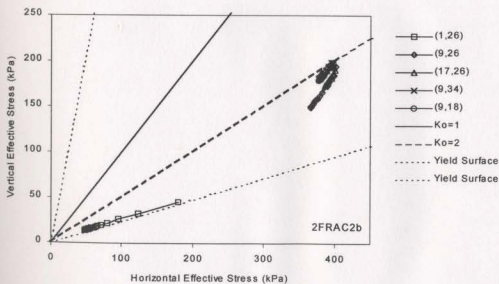
Figure A5.60. Stress paths during injection (2FRAC2b: 0.40 ml/s)
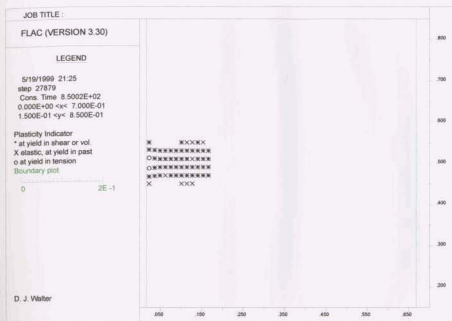
Figure A5.61. Extent of yield zone at end of injection (2FRAC2c: 1.00 ml/s)

Figure A5.62. Plastic strain contours at end of injection (2FRAC2c: 1.00 ml/s)
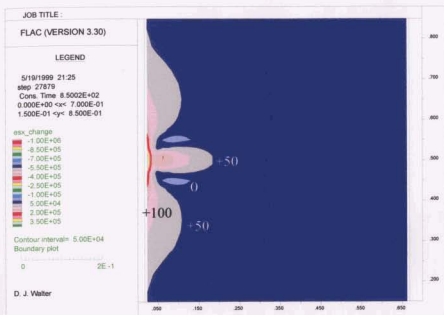
Figure A5.63. Change in horizontal effective stress (2FRAC2c: 1.00 ml/s)
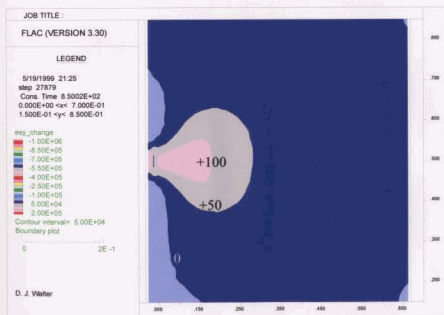
Figure A5.64. Change in vertical effective stress (2FRAC2c: 1.00 ml/s)
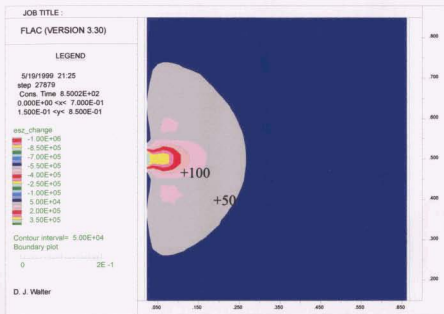
Figure A5.65. Change in tangential effective stress (2FRAC2c: 1.00 ml/s)
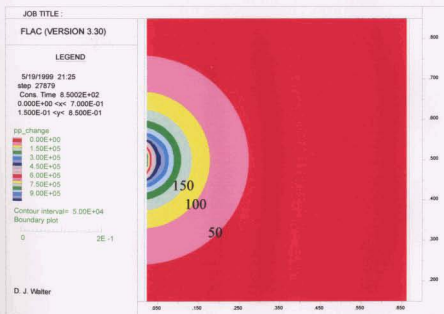
Figure A5.66. Change in pore pressure (2FRAC2c: 1.00 ml/s)
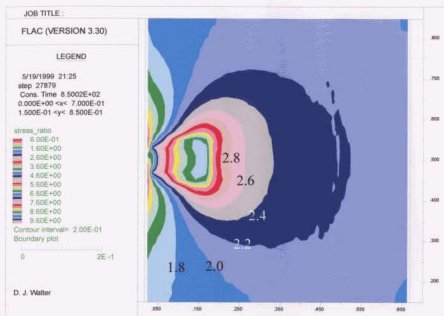
Figure A5.67. Stress ratio σ'$_x$/σ'$_y$, (2FRAC2c: 1.00 ml/s)
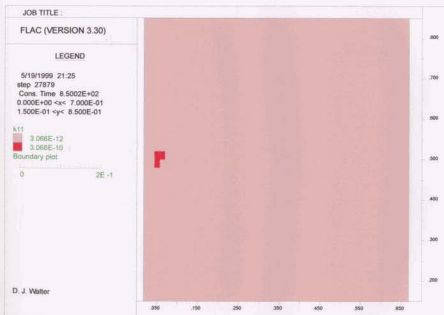
Figure A5.68. FLAC permeability (2FRAC2c: 1.00 ml/s)
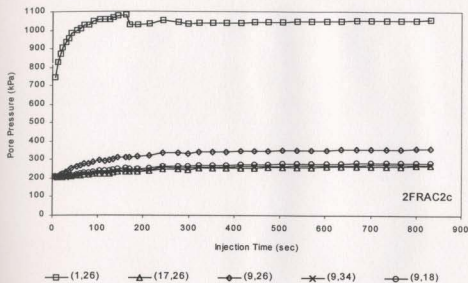
Figure A5.69. Pore pressure development during injection (2FRAC2c: 1.00 ml/s)
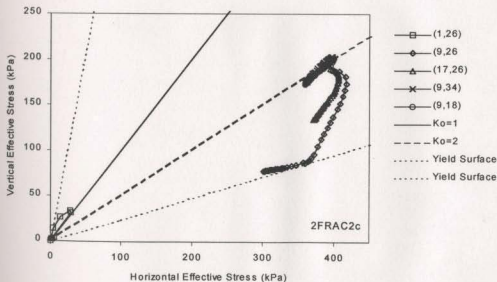
Figure A5.70. Stress paths during injection (2FRAC2c: 1.00 ml/s)
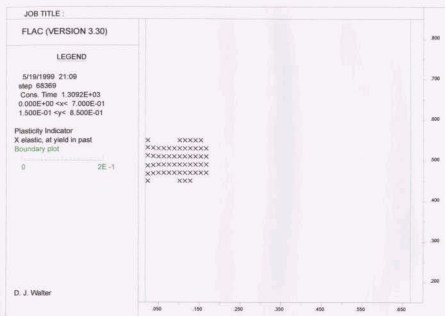
Figure A5.71. Extent of yield zone at end of injection (2FRAC2d: 0.25 ml/s)

Figure A5.72. Plastic strain contours at end of injection (2FRAC2d: 0.25 ml/s)

Figure A5.73. Change in horizontal effective stress (2FRAC2d: 0.25 ml/s)
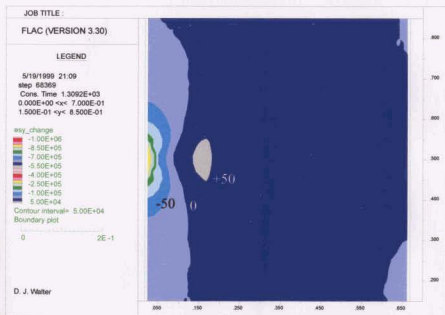
Figure A5.74. Change in vertical effective stress (2FRAC2d: 0.25 ml/s)
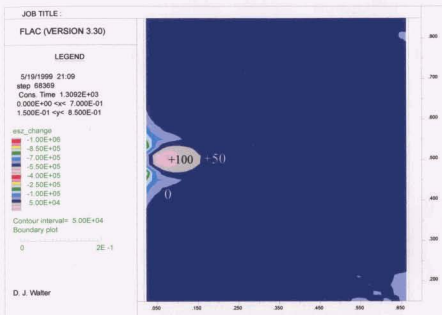
Figure A5.75. Change in tangential effective stress (2FRAC2d: 0.25 ml/s)
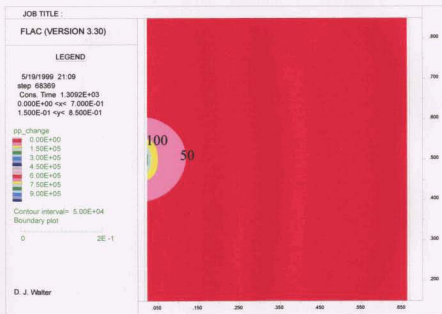
Figure A5.76. Change in pore pressure (2FRAC2d: 0.25 ml/s)
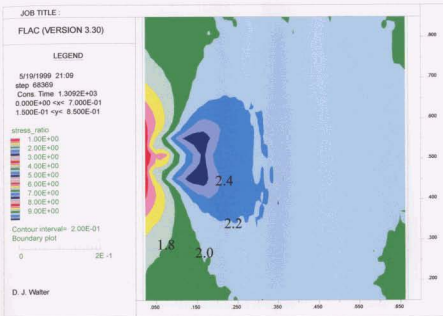
Figure A5.77. Stress ratio σ'$_x$/σ'$_y$ (2FRAC2d: 0.25 ml/s)
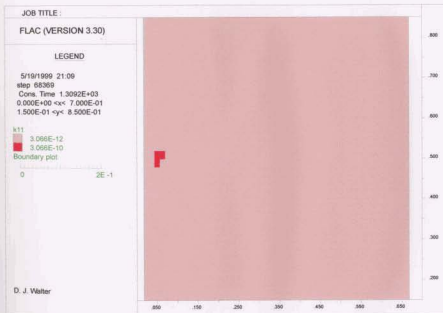
Figure A5.78. FLAC permeability (2FRAC2d: 0.25 ml/s)
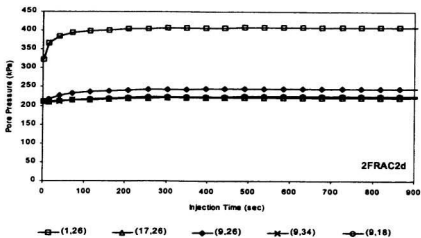
Figure A5.79. Pore pressure development during injection (2FRAC2d: 0.25 ml/s)
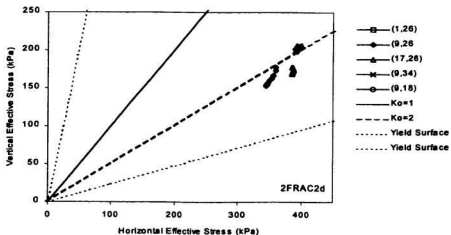
Figure A5.80. Stress paths during injection (2FRAC2d: 0.25 ml/s)

533
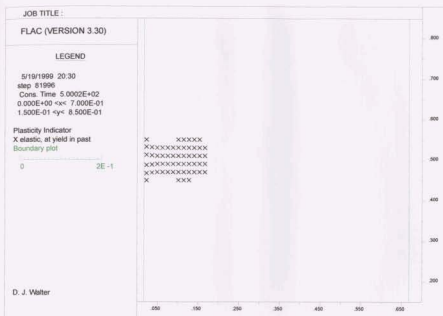
Figure A5.81. Extent of yield zone at end of injection (2FRAC2e: 0.40 ml/s)

Figure A5.82. Plastic strain contours at end of injection (2FRAC2e: 0.40 ml/s)

Figure A5.83. Change in horizontal effective stress (2FRAC2e: 0.40 ml/s)
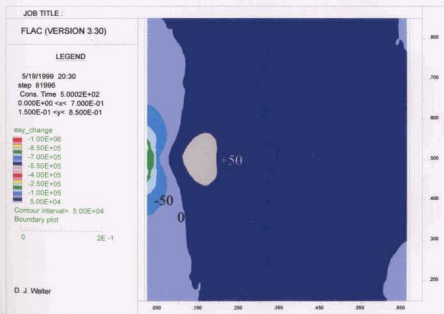
Figure A5.84. Change in vertical effective stress (2FRAC2e: 0.40 ml/s)
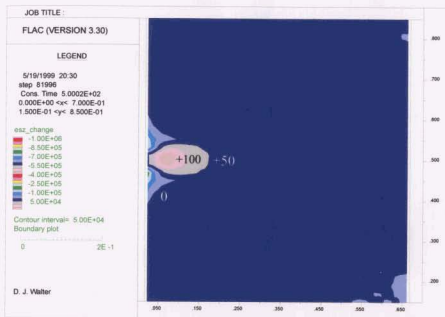
Figure A5.85. Change in tangential effective stress (2FRAC2e: 0.40 ml/s)
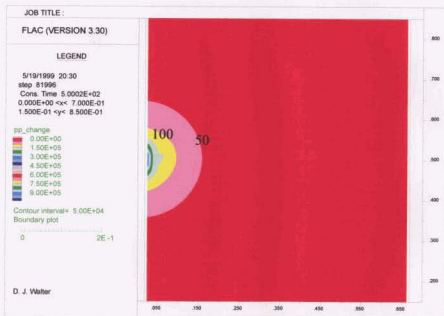
Figure A5.86. Change in pore pressure (2FRAC2e: 0.40 ml/s)
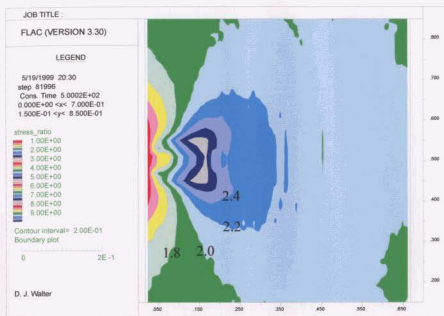
Figure A5.87. Stress ratio σ'₁/σ'₃ (2FRAC2e: 0.40 ml/s)
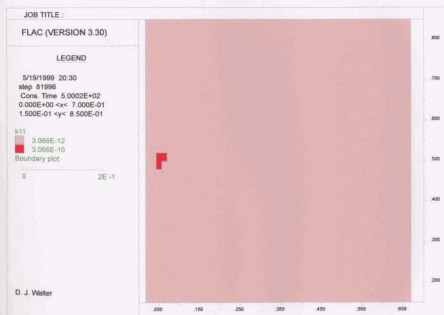
Figure A5.88. FLAC permeability (2FRAC2e: 0.40 ml/s)
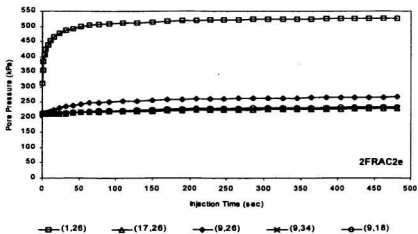
Figure A5.89. Pore pressure development during injection (2FRAC2e: 0.40 ml/s)
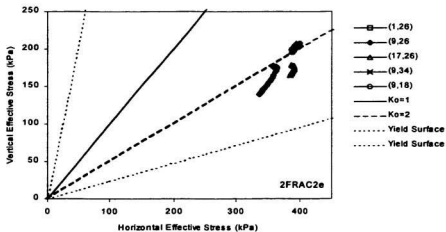
Figure A5.90. Stress paths during injection (2FRAC2e: 0.40 ml/s)

538
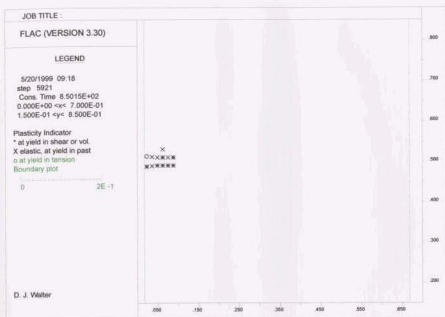
Figure A5.91. Extent of yield zone at end of injection (2FRAC3a: 1.0 ml/s)

Figure A5.92. Plastic strain contours at end of injection (2FRAC3a: 1.0 ml/s)
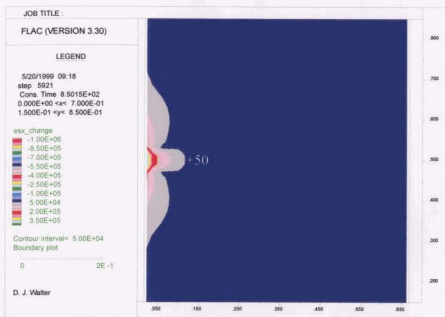
Figure A5.93. Change in horizontal effective stress (2FRAC3a: 1.0 ml/s)
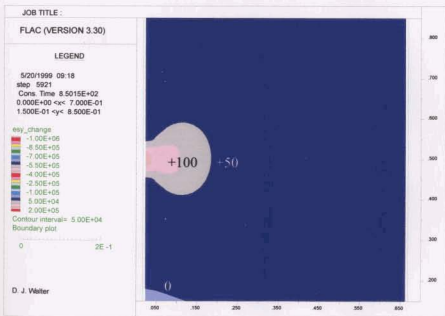
Figure A5.94. Change in vertical effective stress (2FRAC3a: 1.0 ml/s)
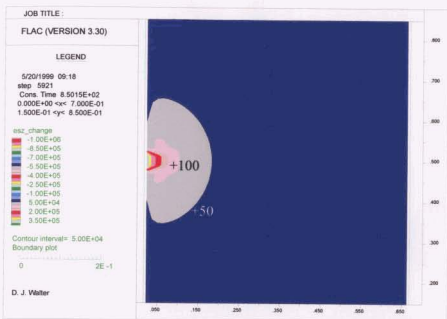
Figure A5.95. Change in tangential effective stress (2FRAC3a: 1.0 ml/s)
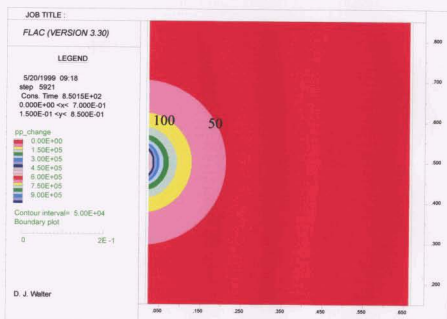
Figure A5.96. Change in pore pressure (2FRAC3a: 1.0 ml/s)
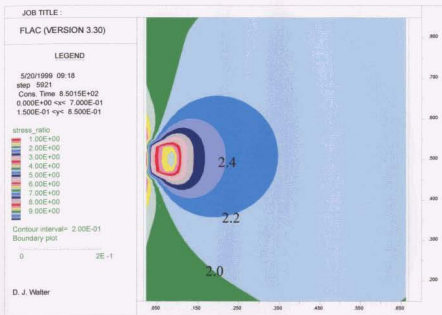
Figure A5.97. Stress ratio σ'₁/σ'₃ (2FRAC3a: 1.0 ml/s)
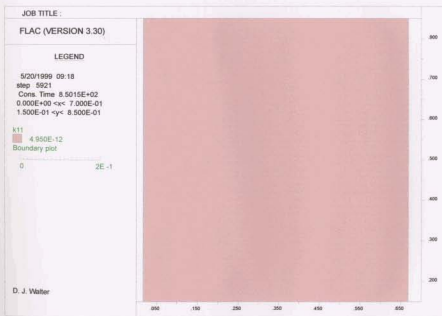
Figure A5.98. FLAC permeability (2FRAC3a: 1.0 ml/s)
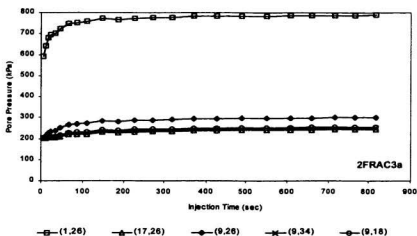
Figure A5.99. Pore pressure development during injection (2FRAC3a: 1.0 ml/s)
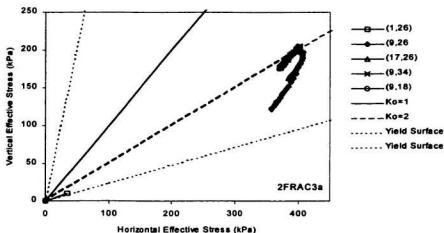
Figure A5.100. Stress paths during injection (2FRAC3a: 1.0 ml/s)
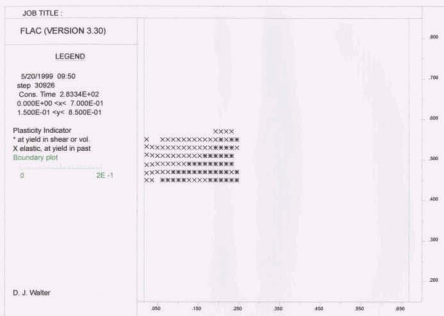
Figure A5.101. Extent of yield zone at end of injection (2FRAC3b: 3.0 ml/s)

Figure A5.102. Plastic strain contours at end of injection (2FRAC3b: 3.0 ml/s)
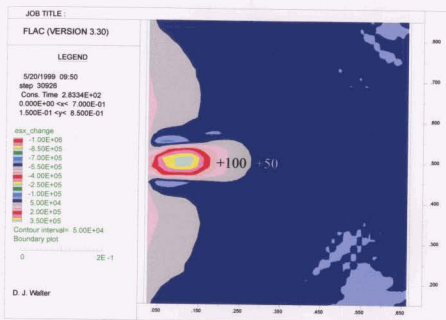
Figure A5.103. Change in horizontal effective stress (2FRAC3b: 3.0 ml/s)
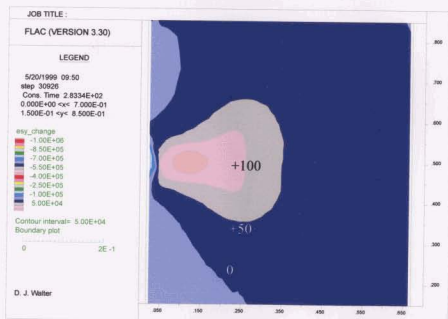
Figure A5.104. Change in vertical effective stress (2FRAC3b: 3.0 ml/s)
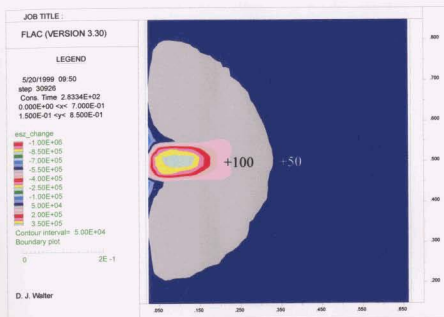
Figure A5.105. Change in tangential effective stress (2FRAC3b: 3.0 ml/s)
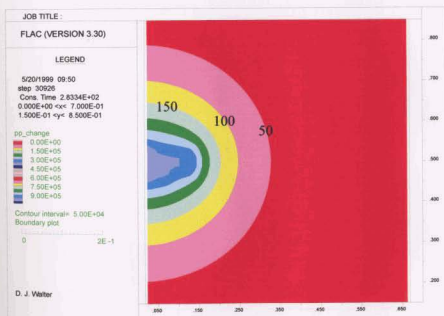
Figure A5.106. Change in pore pressure (2FRAC3b: 3.0 ml/s)
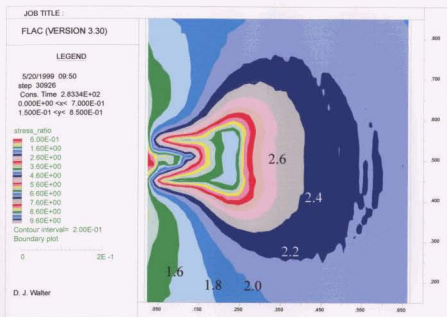
Figure A5.107. Stress ratio σ'_x/σ'_y, (2FRAC3b: 3.0 ml/s)

Figure A5.108. FLAC permeability (2FRAC3b: 3.0 ml/s)
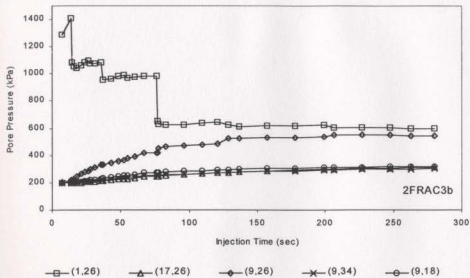
Figure A5.109. Pore pressure development during injection (2FRAC3b: 3.0 ml/s)
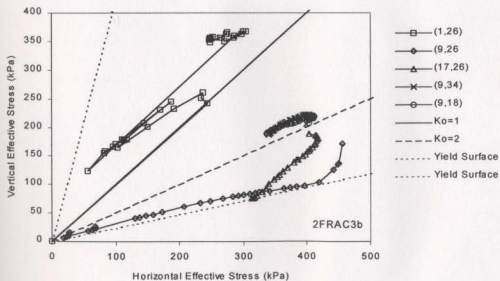
Figure A5.110. Stress paths during injection (2FRAC3b: 3.0 ml/s)
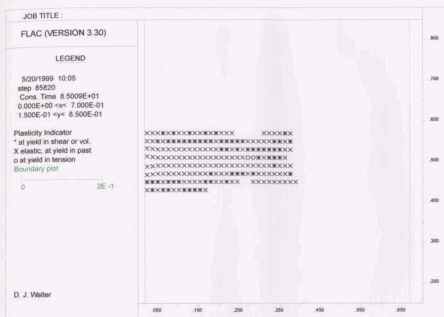
Figure A5.111. Extent of yield zone at end of injection (2FRAC3c: 10.0 ml/s)
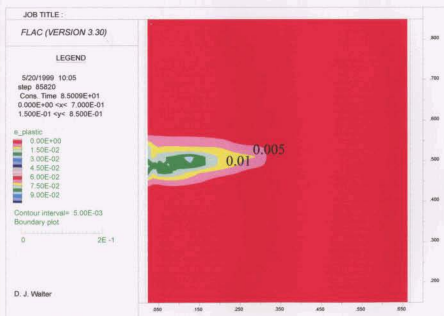
Figure A5.112. Plastic strain contours at end of injection (2FRAC3c: 10.0 ml/s)
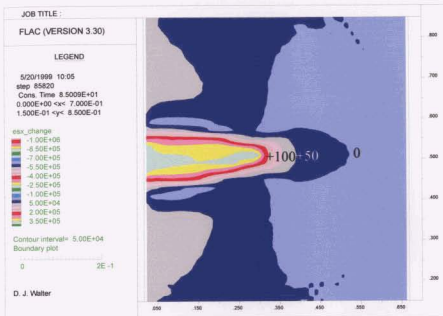
Figure A5.113. Change in horizontal effective stress (2FRAC3c: 10.0 ml/s)
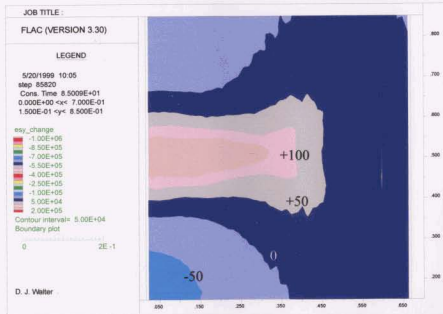
Figure A5.114. Change in vertical effective stress (2FRAC3c: 10.0 ml/s)
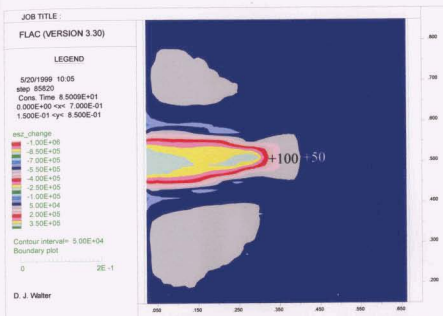
Figure A5.115. Change in tangential effective stress (2FRAC3c: 10.0 ml/s)
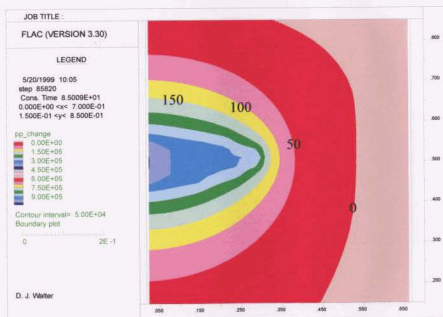
Figure A5.116. Change in pore pressure (2FRAC3c: 10.0 ml/s)
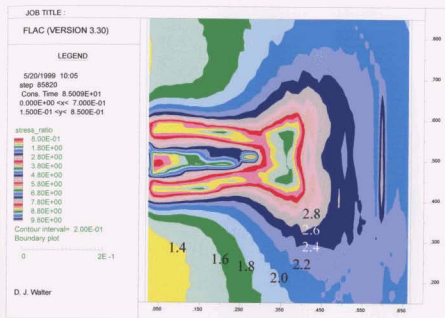
Figure A5.117. Stress ratio σ'$_x$/σ'$_y$, (2FRAC3c: 10.0 ml/s)
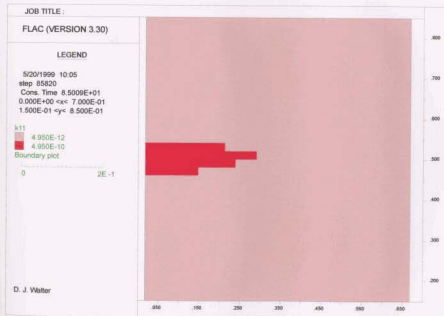
Figure A5.118. FLAC permeability (2FRAC3c: 10.0 ml/s)
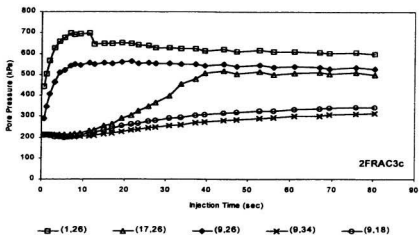
Figure A5.119. Pore pressure development during injection (2FRAC3c: 10.0 ml/s)
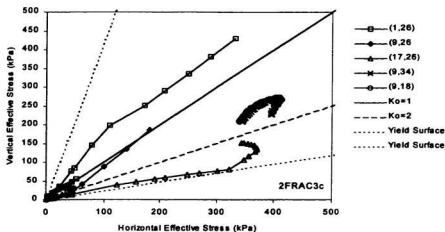
Figure A5.120. Stress paths during injection (2FRAC3c: 10.0 ml/s)

553
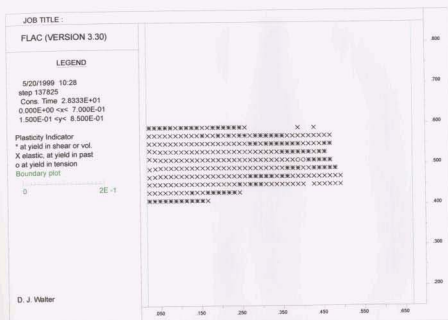
Figure A5.121. Extent of yield zone at end of injection (2FRAC3d: 30.0 ml/s)

Figure A5.122. Plastic strain contours at end of injection (2FRAC3d: 30.0 ml/s)
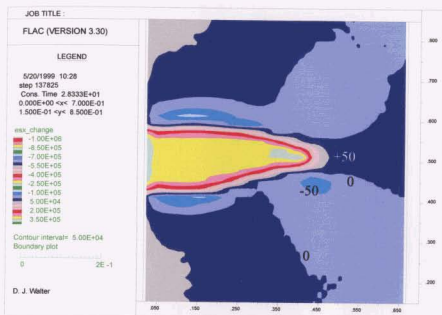
Figure A5.123. Change in horizontal effective stress (2FRAC3d: 30.0 ml/s)
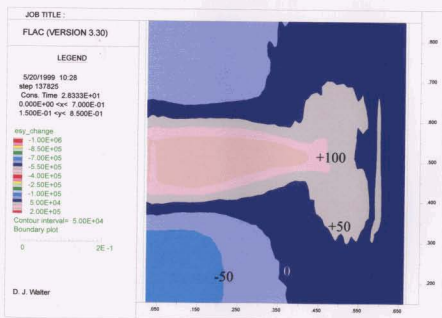
Figure A5.124. Change in vertical effective stress (2FRAC3d: 30.0 ml/s)
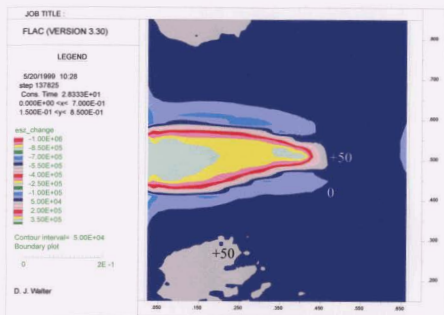
Figure A5.125. Change in tangential effective stress (2FRAC3d: 30.0 ml/s)
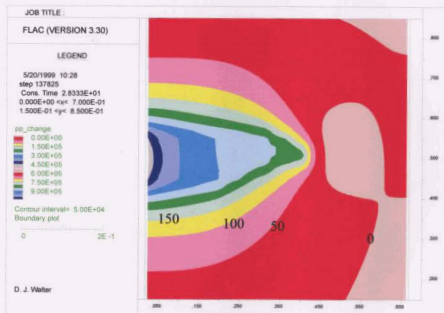
Figure A5.126. Change in pore pressure (2FRAC3d: 30.0 ml/s)
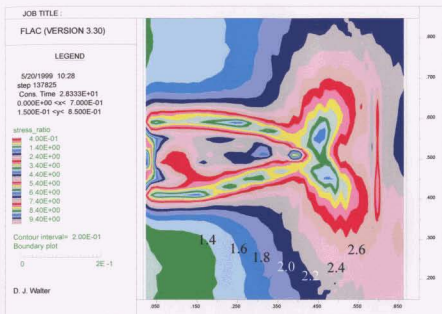
Figure A5.127. Stress ratio σ'$_x$/σ'$_y$ (2FRAC3d: 30.0 ml/s)
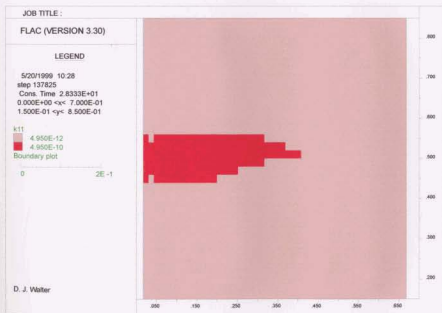
Figure A5.128. FLAC permeability (2FRAC3d: 30.0 ml/s)
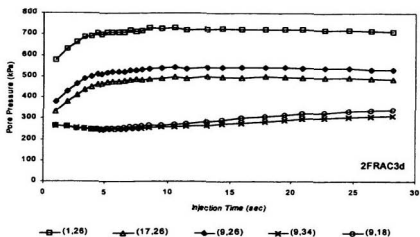
Figure A5.129. Pore pressure development during injection (2FRAC3d: 30.0 ml/s)
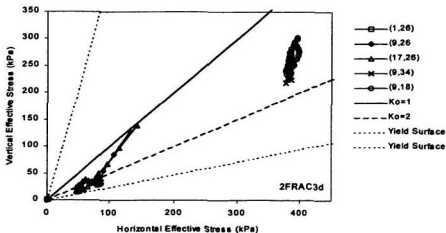
Figure A5.130. Stress paths during injection (2FRAC3d: 30.0 ml/s)

558
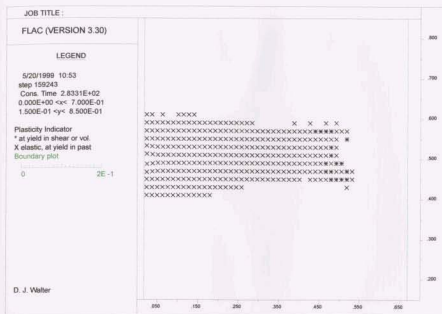
Figure A5.131. Extent of yield zone at end of injection (2FRAC3e: 3.0 ml/s)

Figure A5.132. Plastic strain contours at end of injection (2FRAC3e: 3.0 ml/s)
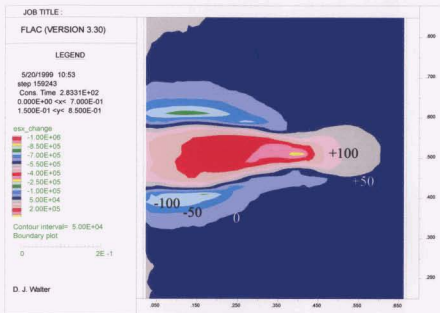
Figure A5.133. Change in horizontal effective stress (2FRAC3e: 3.0 ml/s)
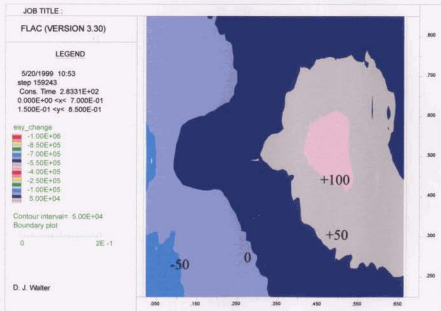
Figure A5.134. Change in vertical effective stress (2FRAC3e: 3.0 ml/s)
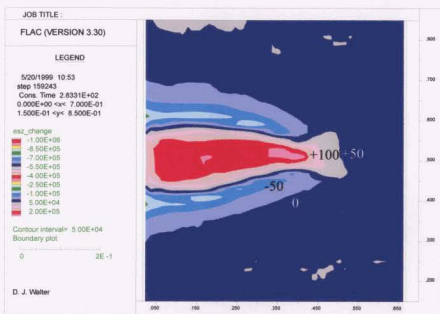
Figure A5.135. Change in tangential effective stress (2FRAC3e: 3.0 ml/s)
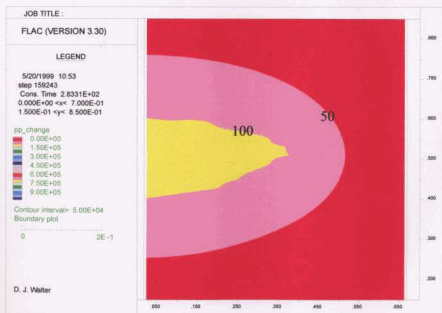
Figure A5.136. Change in pore pressure (2FRAC3e: 3.0 ml/s)
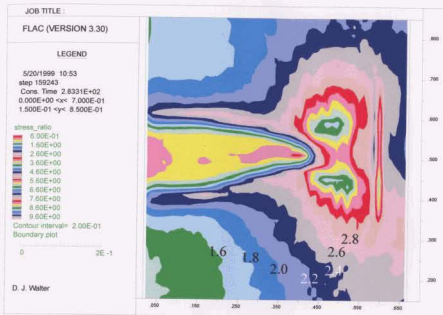
Figure A5.137. Stress ratio σ'$_x$/σ'$_y$, (2FRAC3e: 3.0 ml/s)
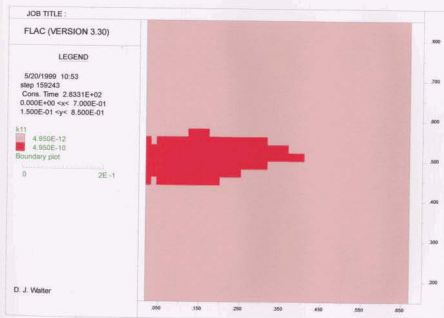
Figure A5.138. FLAC permeability (2FRAC3e: 3.0 ml/s)
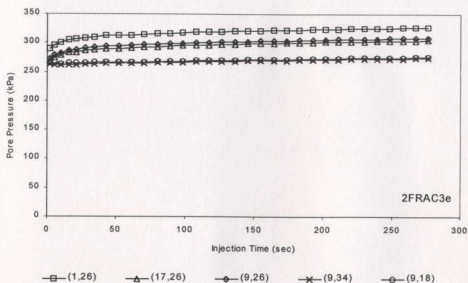
Figure A5.139. Pore pressure development during injection (2FRAC3e: 3.0 ml/s)
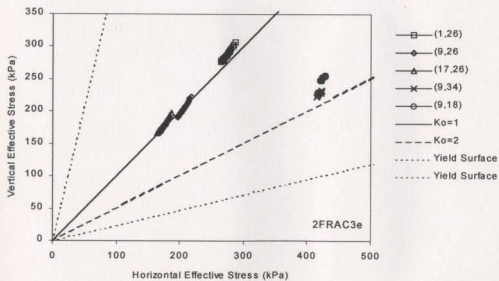
Figure A5.140. Stress paths during injection (2FRAC3e: 3.0 ml/s)
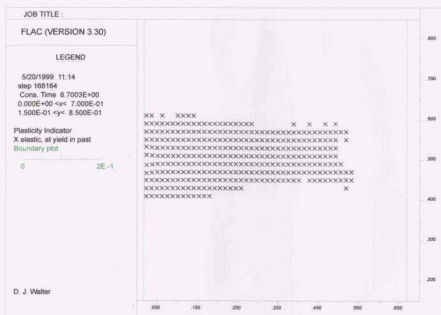
Figure A5.141. Extent of yield zone at end of injection (2FRAC3f: 30.0 ml/s)

Figure A5.142. Plastic strain contours at end of injection (2FRAC3f: 30.0 ml/s)
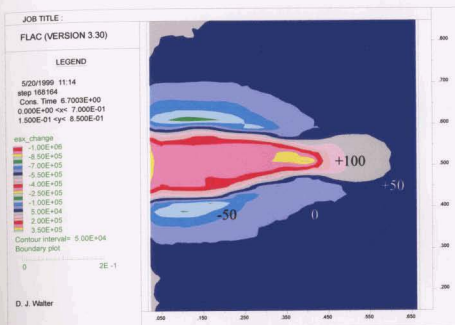
Figure A5.143. Change in horizontal effective stress (2FRAC3f: 30.0 ml/s)
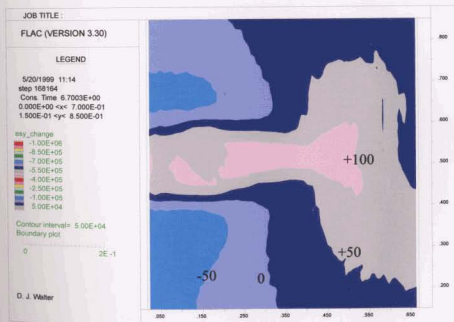
Figure A5.144. Change in vertical effective stress (2FRAC3f: 30.0 ml/s)
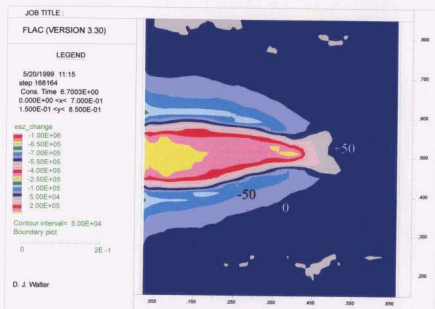
Figure A5.145. Change in tangential effective stress (2FRAC3f: 30.0 ml/s)
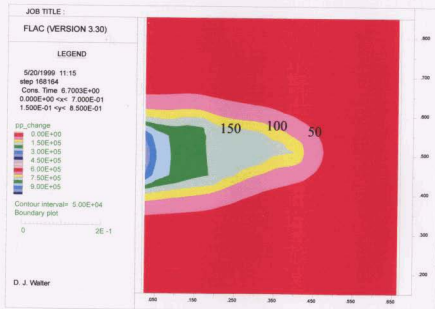
Figure A5.146. Change in pore pressure (2FRAC3f: 30.0 ml/s)
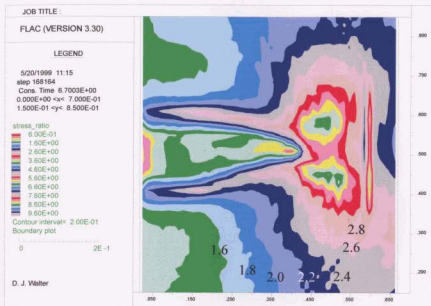
Figure A5.147. Stress ratio σ'_x/σ'_y (2FRAC3f: 30.0 ml/s)
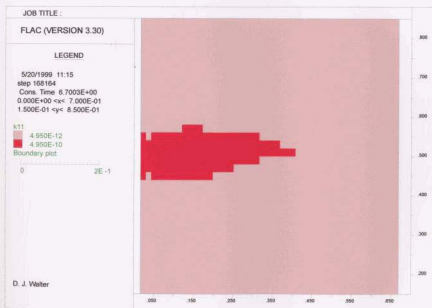
Figure A5.148. FLAC permeability (2FRAC3f: 30.0 ml/s)
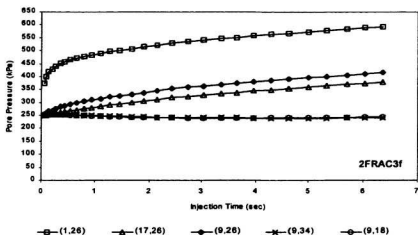
Figure A5.149. Pore pressure development during injection (2FRAC3f: 30.0 ml/s)
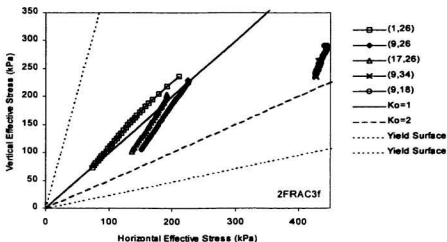
Figure A5.150. Stress paths during injection (2FRAC3f: 30.0 ml/s)
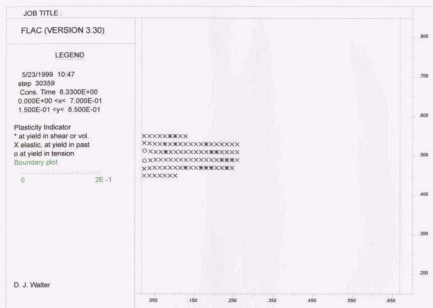
Figure A5.151. Extent of yield zone at end of injection (2FRAC4)
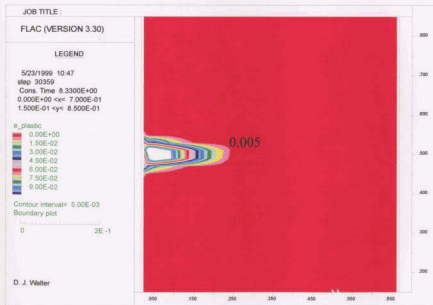
Figure A5.152. Plastic strain contours at end of injection (2FRAC4)
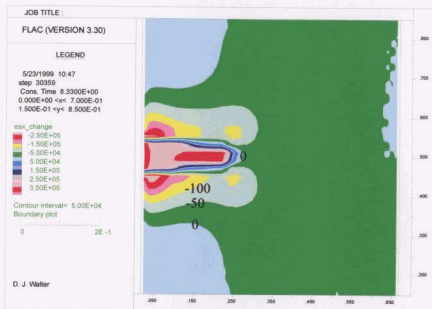
Figure A5.153. Change in horizontal effective stress (2FRAC4)
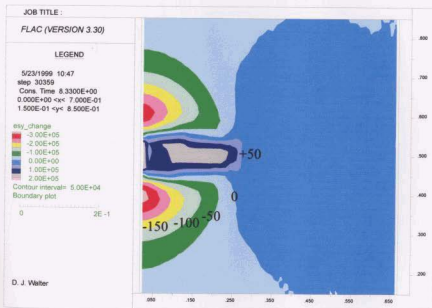
Figure A5.154. Change in vertical effective stress (2FRAC4)
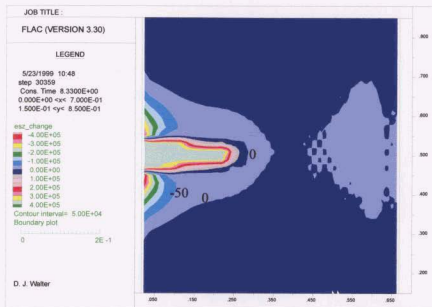
Figure A5.155. Change in tangential effective stress (2FRAC4)
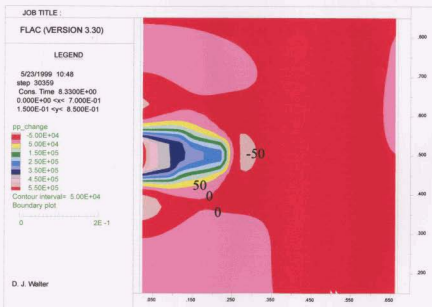
Figure A5.156. Change in pore pressure (2FRAC4)
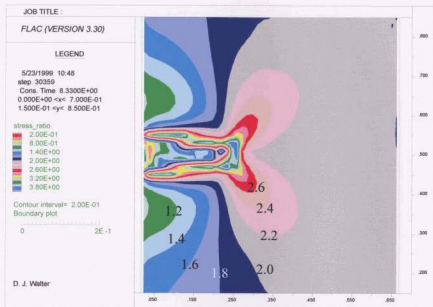
Figure A5.157. Stress ratio σ'ₓ/σ'ᵧ, (2FRAC4)
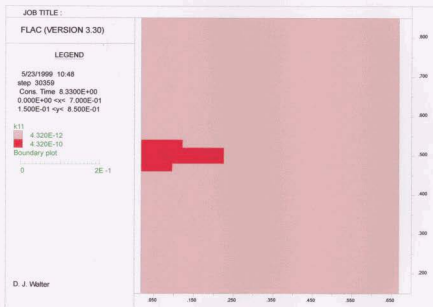
Figure A5.158. FLAC permeability (2FRAC4)
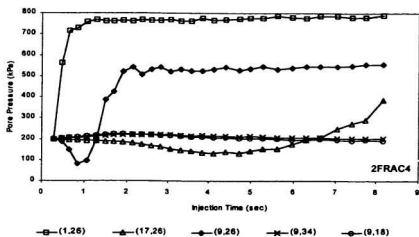
Figure A5.159. Pore pressure development during injection (2FRAC4)
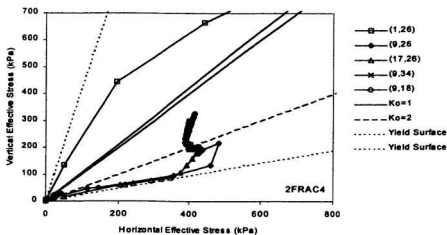
Figure A5.160. Stress paths during injection (2FRAC4)
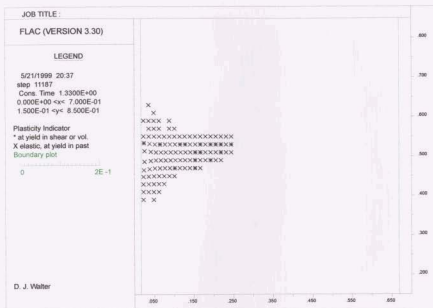
Figure A5.161. Extent of yield zone at end of injection (2FRAC5)
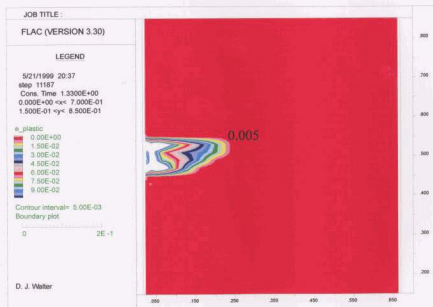
Figure A5.162. Plastic strain contours at end of injection (2FRAC5)
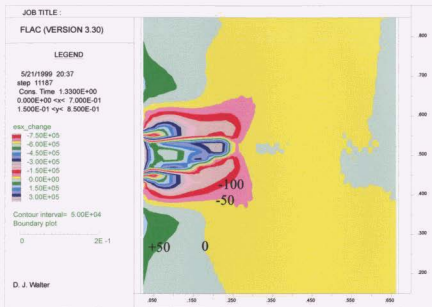
Figure A5.163. Change in horizontal effective stress (2FRAC5)
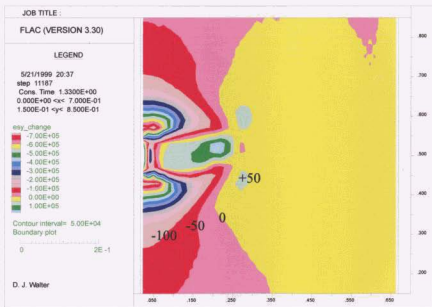
Figure A5.164. Change in vertical effective stress (2FRAC5)
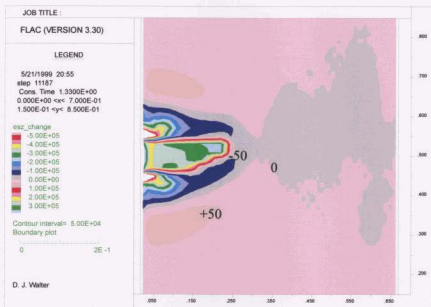
Figure A5.165. Change in tangential effective stress (2FRAC5)
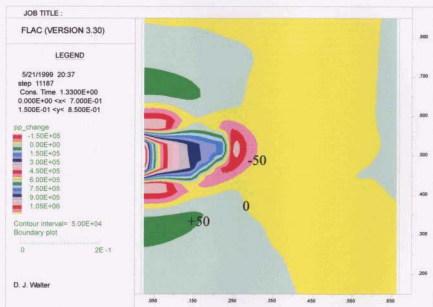
Figure A5.166. Change in pore pressure (2FRAC5)
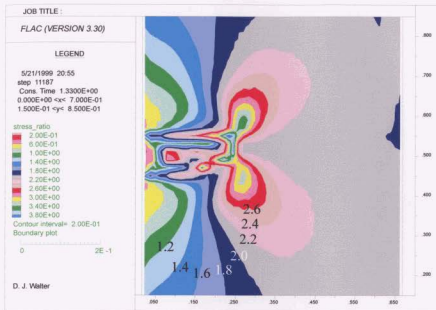
Figure A5.167. Stress ratio σ'_x/σ'_y (2FRAC5)
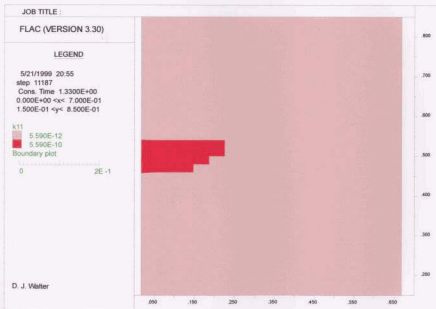
Figure A5.168. FLAC permeability (2FRAC5)
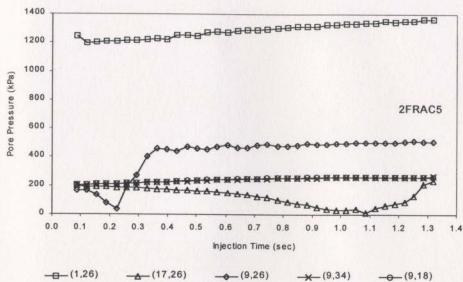
Figure A5.169. Pore pressure development during injection (2FRAC5)
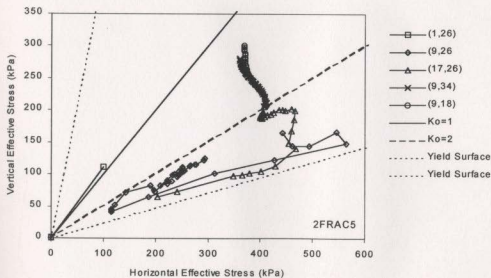
Figure A5.170. Stress paths during injection (2FRAC5)
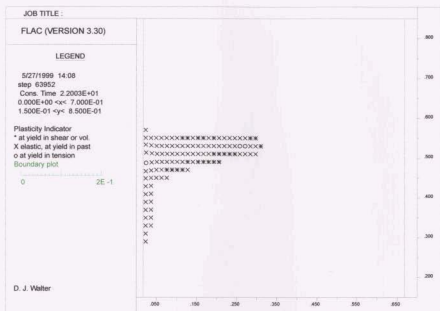
Figure A5.171. Extent of yield zone at end of injection (3FRAC1)
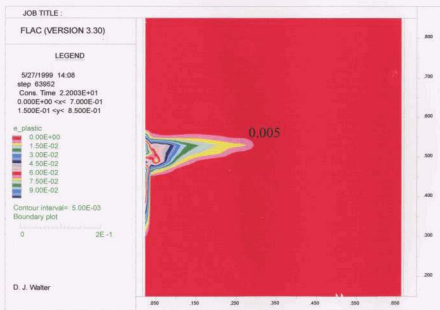
Figure A5.172. Plastic strain contours at end of injection (3FRAC1)
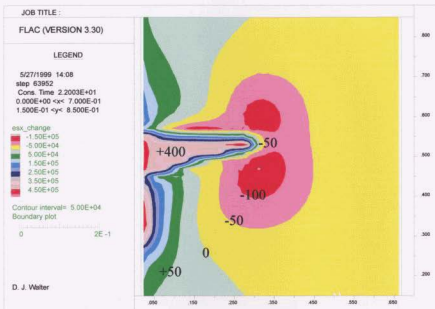
Figure A5.173. Change in horizontal effective stress (3FRAC1)
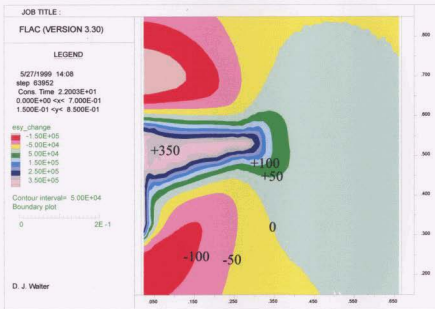
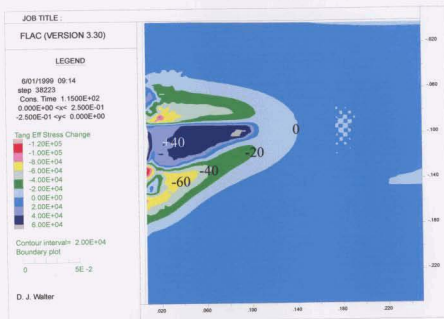**Figure A5.174.** Change in vertical effective stress (3FRAC1)
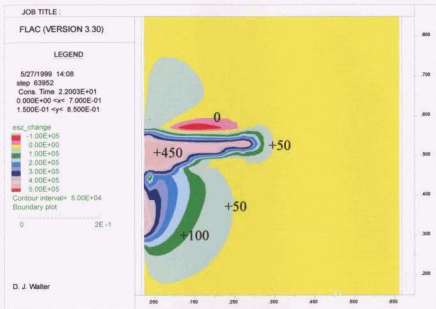
**Figure A5.175.** Change in tangential effective stress (3FRAC1)
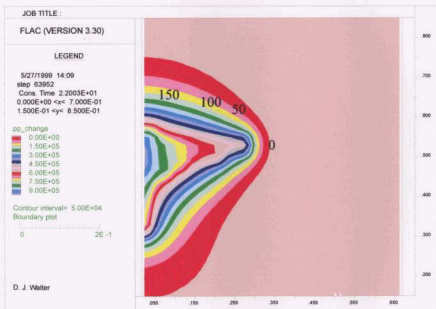
**Figure A5.176.** Change in pore pressure (3FRAC1)
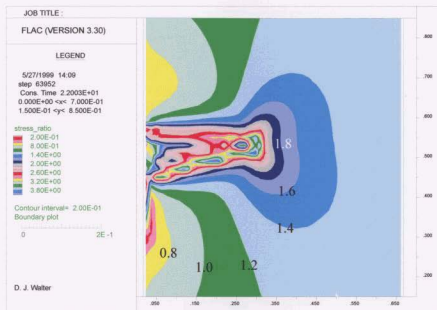
Figure A5.177. Stress ratio σ'_x/σ'_y (3FRAC1)
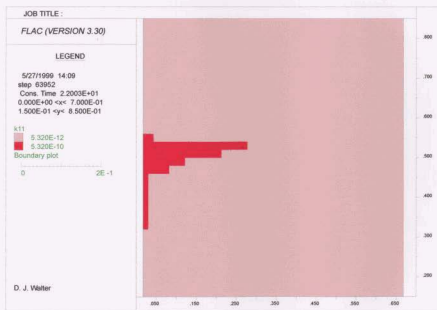
Figure A5.178. FLAC permeability (3FRAC1)
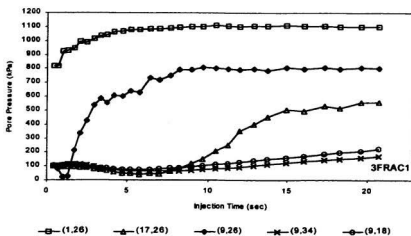
Figure A5.179. Pore pressure development during injection (3FRAC1)
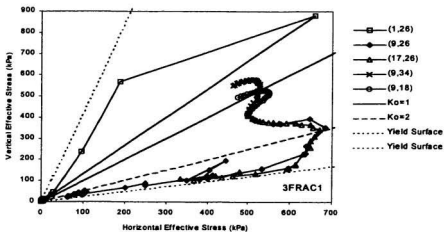
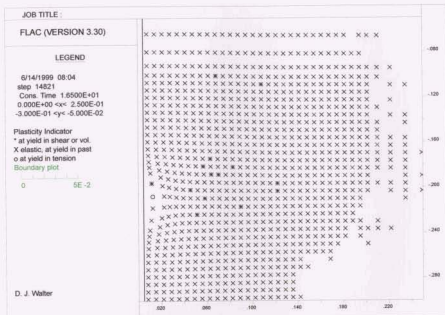**Figure A5.180.** Stress paths during injection (3FRAC1)

583
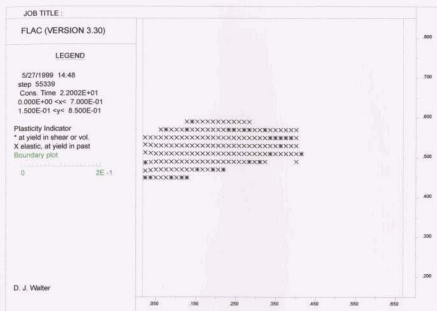
Figure A5.181. Extent of yield zone at end of injection (3FRAC2)
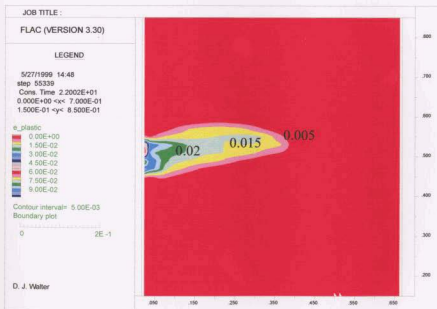
Figure A5.182. Plastic strain contours at end of injection (3FRAC2)

Figure A5.184. Change in vertical effective stress (3FRAC2)

Figure A5.183. Change in horizontal effective stress (3FRAC2)
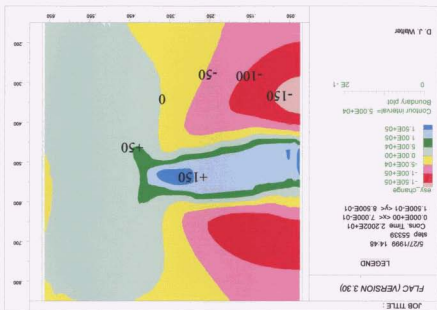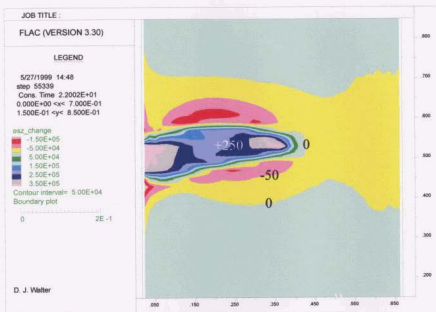
Figure A5.185. Change in tangential effective stress (3FRAC2)
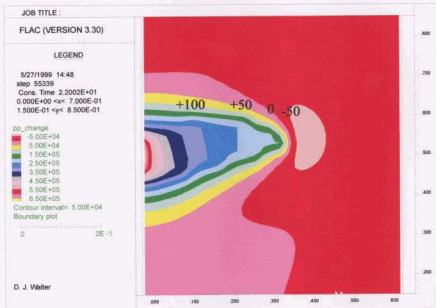
Figure A5.186. Change in pore pressure (3FRAC2)
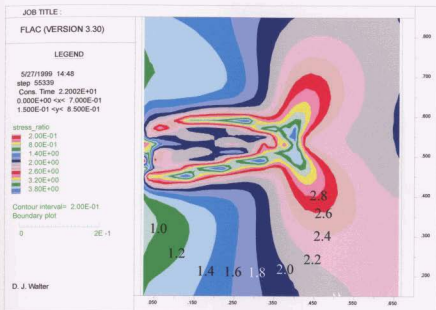
Figure A5.187. Stress ratio σ'$_x$/σ'$_y$ (3FRAC2)
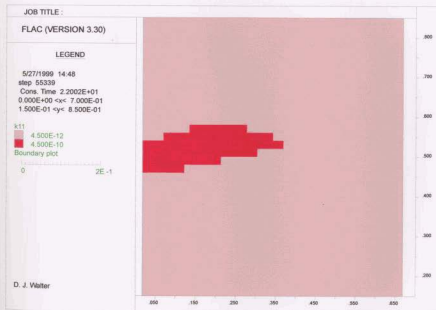
Figure A5.188. FLAC permeability (3FRAC2)
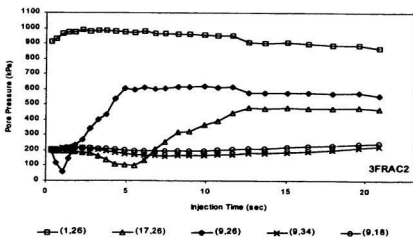
Figure A5.189. Pore pressure development during injection (3FRAC2)
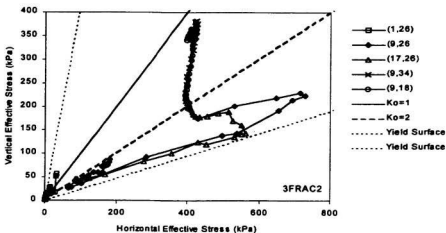
Figure A5.190. Stress paths during injection (3FRAC2)
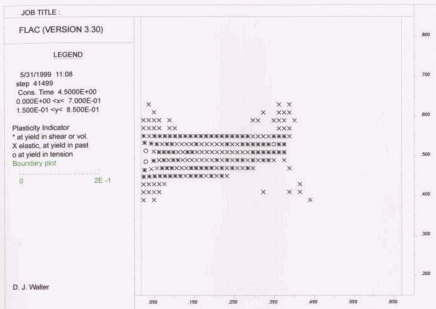
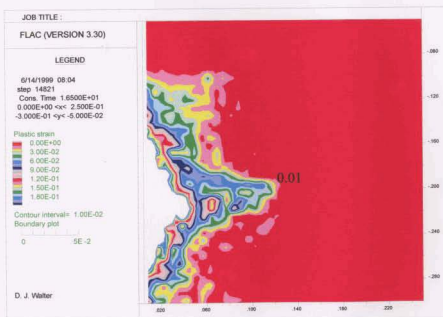**Figure A5.191.** Extent of yield zone at end of injection (3FRAC3)
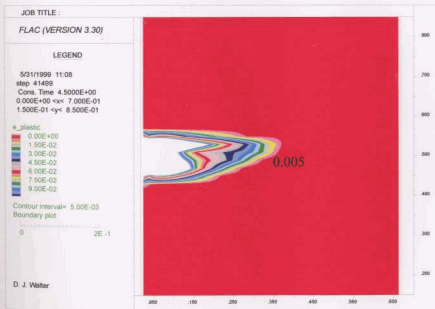
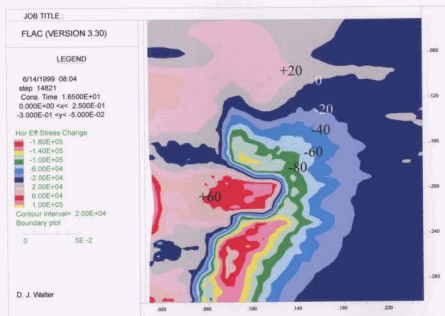**Figure A5.192.** Plastic strain contours at end of injection (3FRAC3)
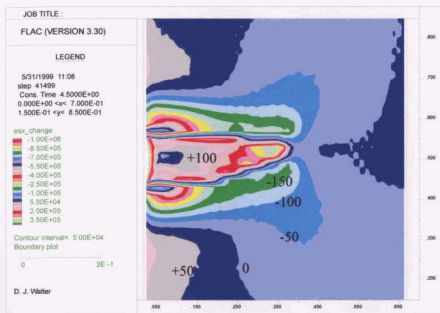
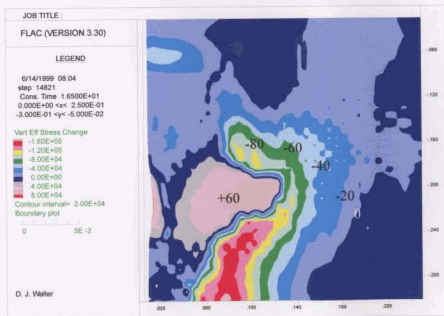**Figure A5.193.** Change in horizontal effective stress (3FRAC3)
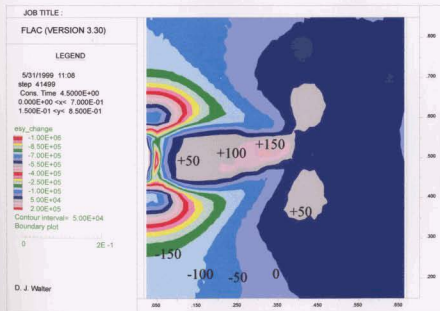
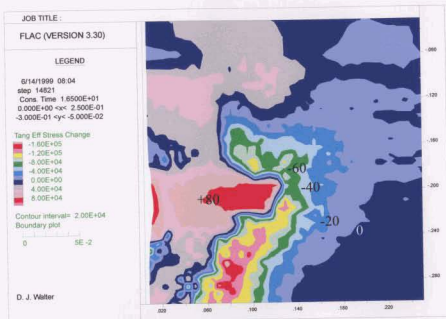**Figure A5.194.** Change in vertical effective stress (3FRAC3)
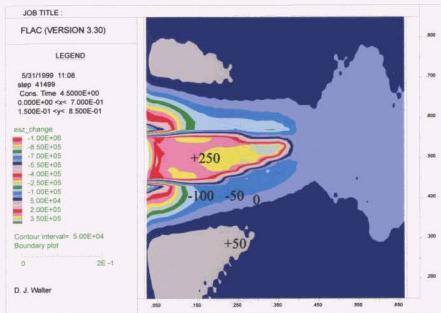
**Figure A5.195.** Change in tangential effective stress (3FRAC3)
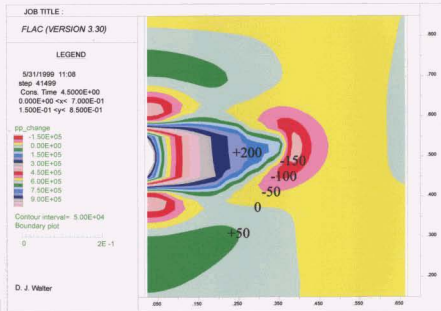
**Figure A5.196.** Change in pore pressure (3FRAC3)
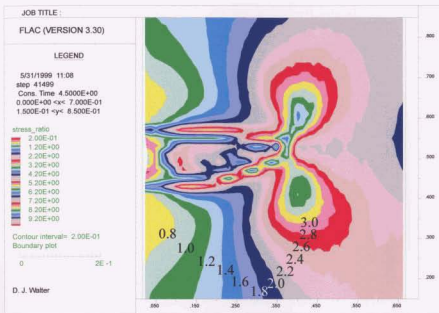
Figure A5.197. Stress ratio σ'$_x$/σ'$_y$ (3FRAC3)
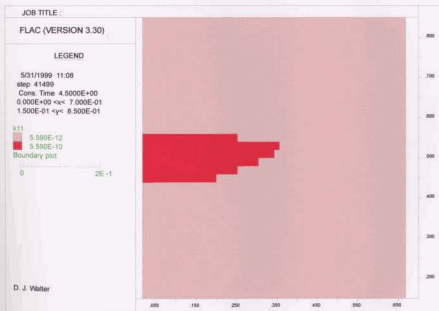
Figure A5.198. FLAC permeability (3FRAC3)
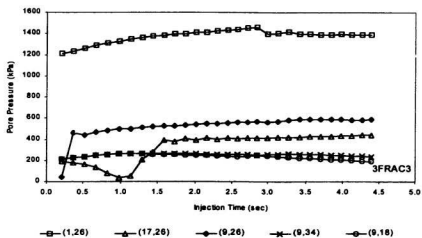
Figure A5.199. Pore pressure development during injection (3FRAC3)
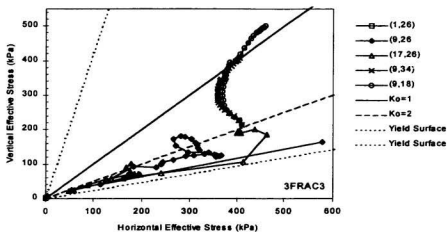

Figure A5.200. Stress paths during injection (3FRAC3)

593

Figure A5.202. Plastic strain contours at end of injection (3FRAC4)

JOB TITLE

FLAC (VERSION 3.30)

LEGEND

5/31/1999 11:46
step 31828
Cons. Time 4.500E+00
0.000E+00 <x< 7.000E-01
1.500E-01 <y< 4.800E-01

R_plastic
0.000E+00
1.00E-02
2.00E-02
3.00E-02
4.00E-02
5.00E-02
6.00E-02
7.00E-02
8.00E-02
9.00E-02
Contour interval= 5.00E-03
Boundary plot

0   2E-1

0.005

D. J. Waller

Figure A5.201. Extent of yield zone at end of injection (3FRAC4)

JOB TITLE

FLAC (VERSION 3.30)

LEGEND

5/31/1999 11:46
step 31828
Cons. Time 4.500E+00
0.000E+00 <x< 7.000E-01
1.500E-01 <y< 4.800E-01

Plasticity Indicator
* at yield in shear or vol.
X elastic, at yield in past
o at yield in tension
Boundary plot

0   2E-1

D. J. Waller

Figure A5.203. Change in horizontal effective stress (3FRAC4)
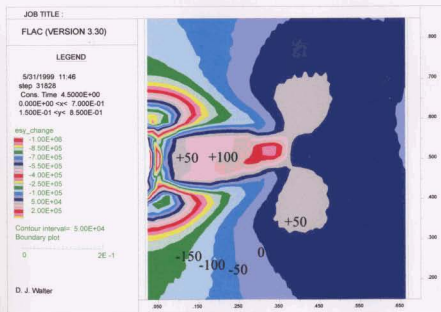
Figure A5.204. Change in vertical effective stress (3FRAC4)
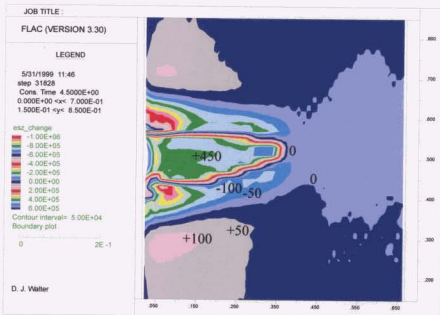
Figure A5.205. Change in tangential effective stress (3FRAC4)
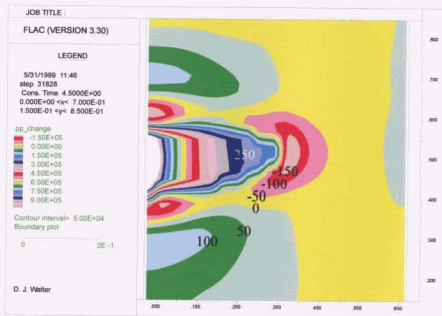
Figure A5.206. Change in pore pressure (3FRAC4)
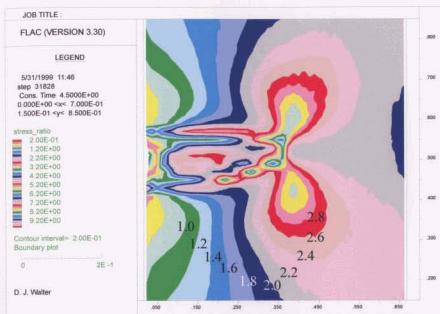
Figure A5.207. Stress ratio σ'_x/σ'_y (3FRAC4)
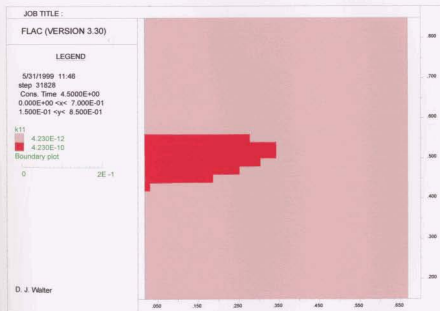
Figure A5.208. FLAC permeability (3FRAC4)
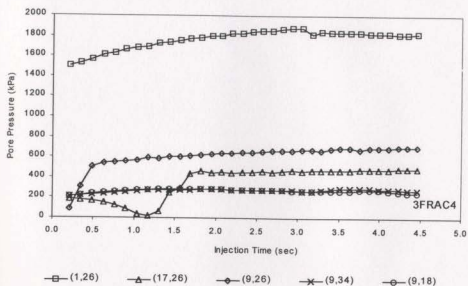
Figure A5.209. Pore pressure development during injection (3FRAC4)
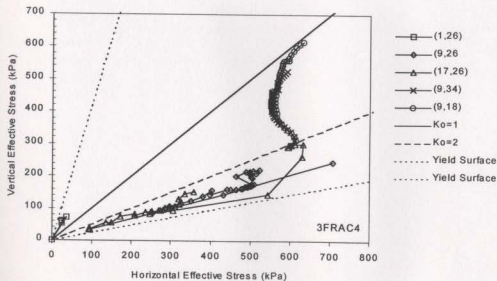
Figure A5.210. Stress paths during injection (3FRAC4)
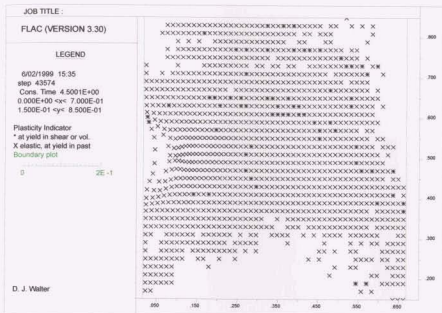
Figure A5.211. Extent of yield zone at end of injection (3FRAC5)
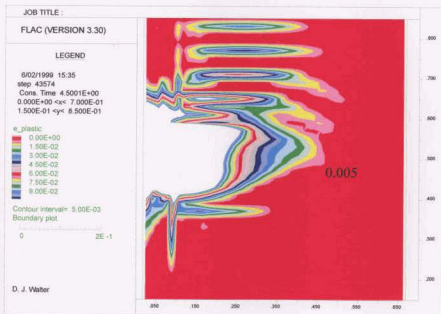
Figure A5.212. Plastic strain contours at end of injection (3FRAC5)
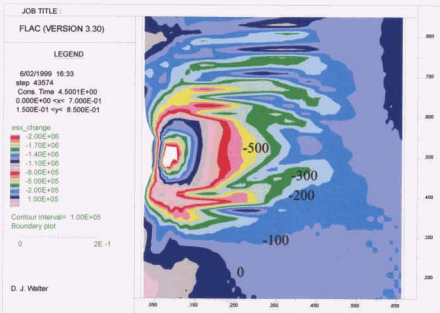
Figure A5.213. Change in horizontal effective stress (3FRAC5)
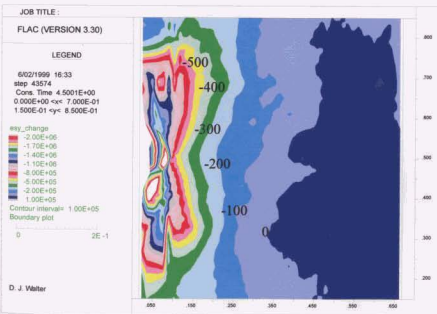
Figure A5.214. Change in vertical effective stress (3FRAC5)
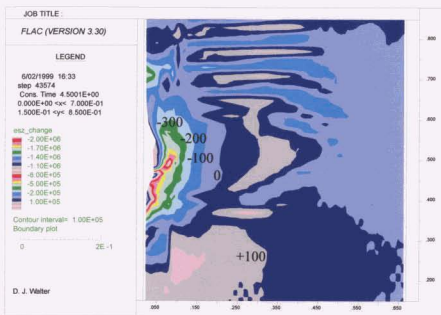
Figure A5.215. Change in tangential effective stress (3FRAC5)
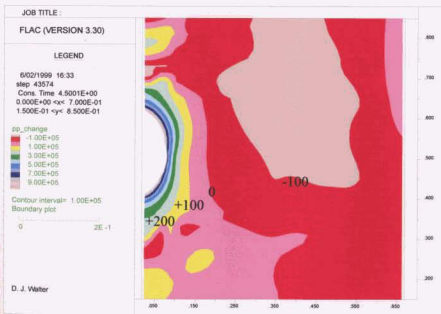
Figure A5.216. Change in pore pressure (3FRAC5)
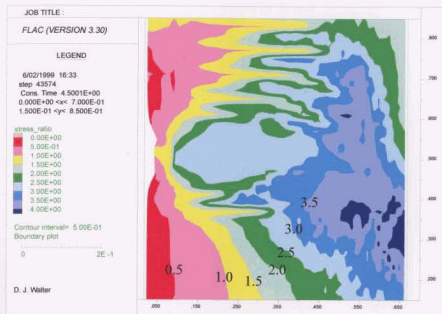
Figure A5.217. Stress ratio σ'$_x$/σ'$_y$ (3FRAC5)
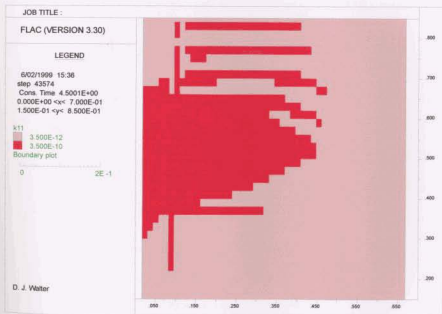
Figure A5.218. FLAC permeability (3FRAC5)
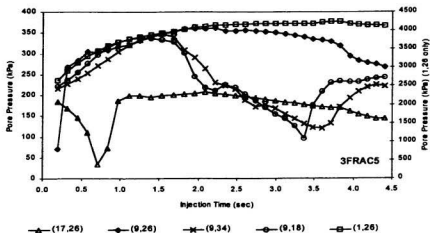
Figure A5.219. Pore pressure development during injection (3FRAC5)
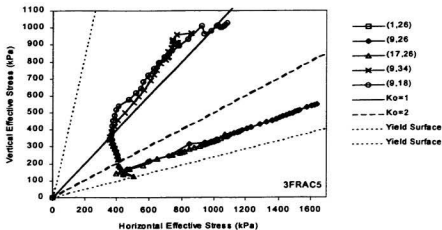
Figure A5.220. Stress paths during injection (3FRAC5)

603
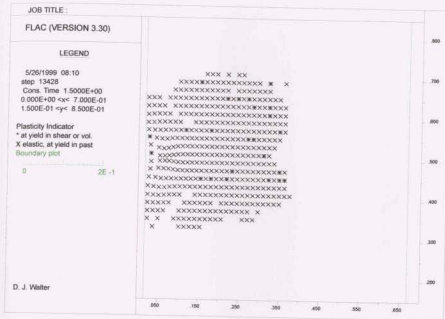
Figure A5.221. Extent of yield zone at end of injection (3FRAC6)
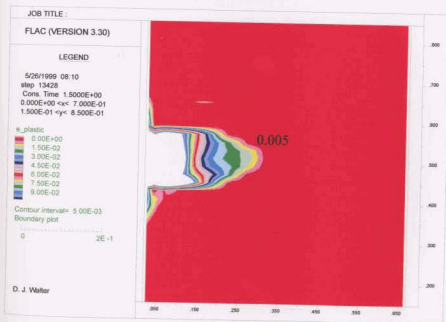
Figure A5.222. Plastic strain contours at end of injection (3FRAC6)
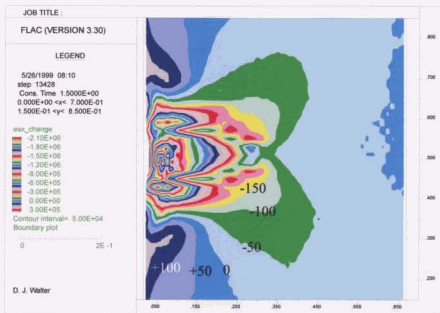
Figure A5.223. Change in horizontal effective stress (3FRAC6)
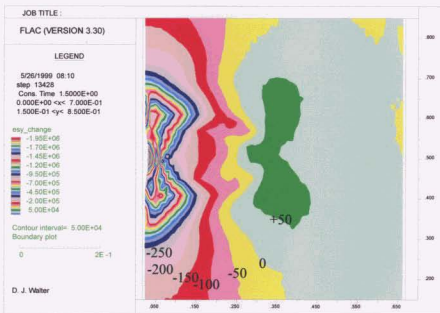
Figure A5.224. Change in vertical effective stress (3FRAC6)

Figure A5.226. Change in pore pressure (3FRAC6)

Figure A5.225. Change in tangential effective stress (3FRAC6)
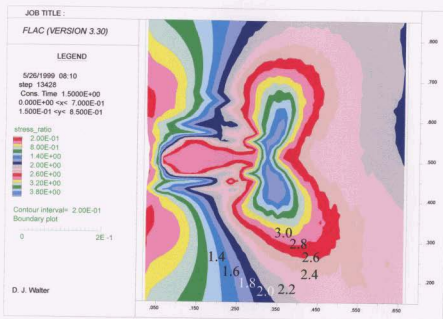
Figure A5.227. Stress ratio σ'$_x$/σ'$_y$ (3FRAC6)
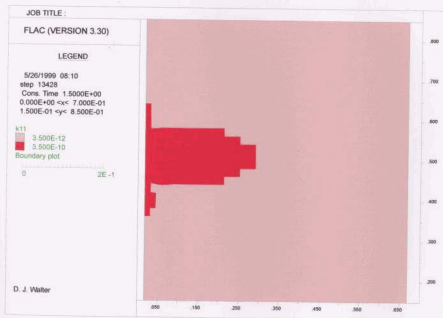
Figure A5.228. FLAC permeability (3FRAC6)
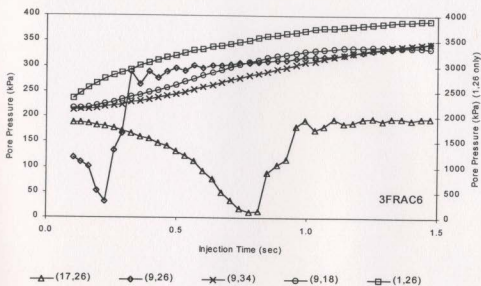
Figure A5.229. Pore pressure development during injection (3FRAC6)
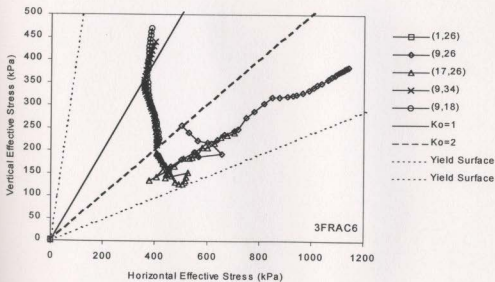
**Figure A5.230.** Stress paths during injection (3FRAC6)

A5.3   Field Tests
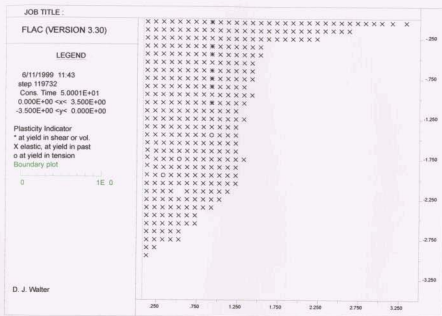
Figure A5.231. Extent of yield zone at t = 50 s (FLDTST1)
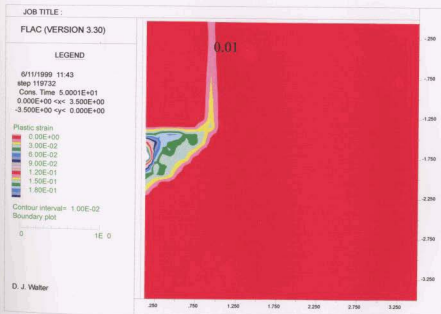
Figure A5.232. Plastic strain contours at t = 50 s (FLDTST1)
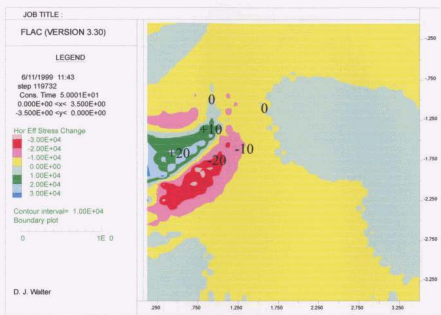
Figure A5.233. Change in horizontal effective stress at t = 50 s (FLDTST1)
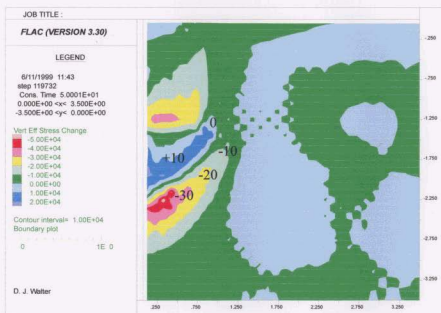
Figure A5.234. Change in vertical effective stress at t = 50 s (FLDTST1)
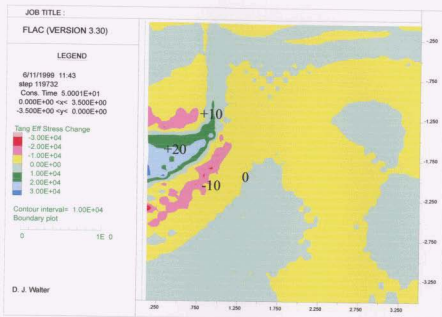
Figure A5.235. Change in tangential effective stress at t = 50 s (FLDTST1)
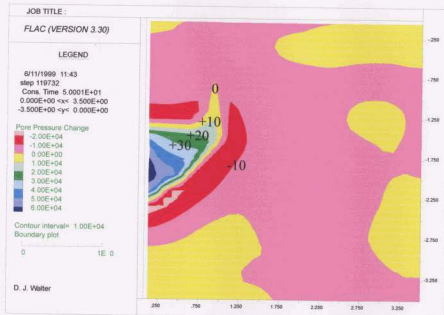
Figure A5.236. Change in pore pressure at t = 50 s (FLDTST1)
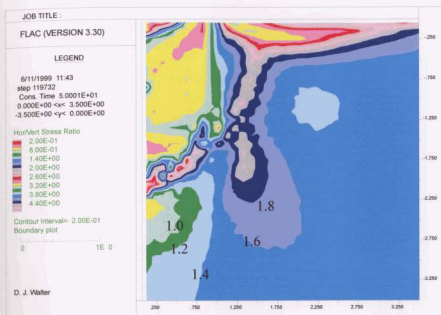
Figure A5.237. Stress ratio σ'_x/σ'_y at t = 50 s (FLDTST1)
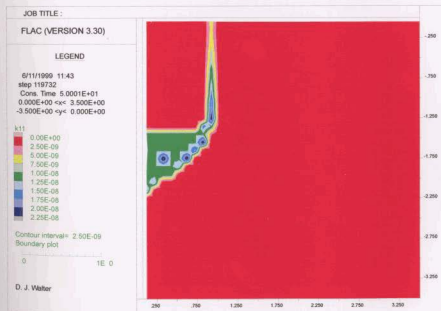
Figure A5.238. FLAC permeability at t = 50 s (FLDTST1)
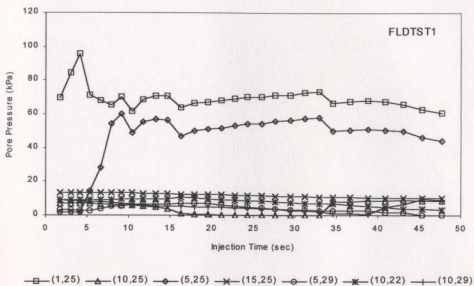
Figure A5.239. Pore pressure development during injection (FLDTST1)
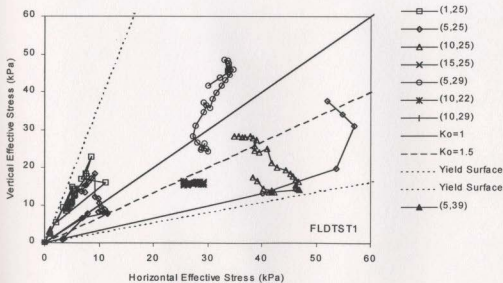
Figure A5.240. Stress paths during injection (FLDTST1)
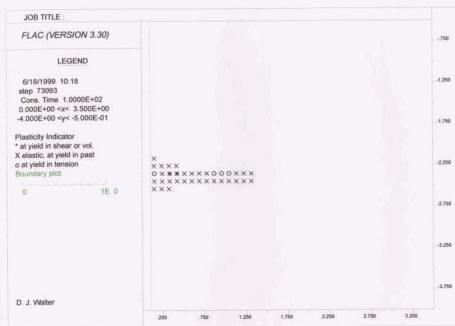
Figure A5.241. Extent of yield zone at t = 100 s (FLDTST2)
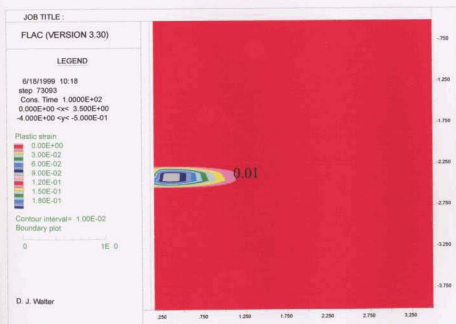
Figure A5.242. Plastic strain contours at t = 100 s (FLDTST2)
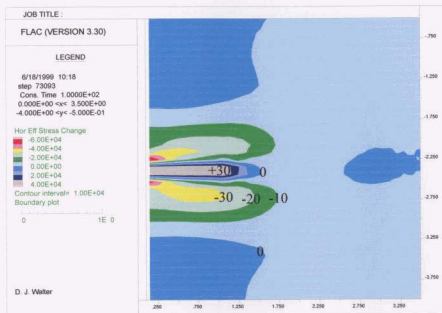
Figure A5.243. Change in horizontal effective stress at t = 100 s (FLDTST2)
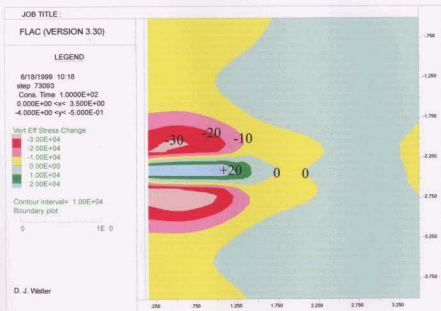
Figure A5.244. Change in vertical effective stress at t = 100 s (FLDTST2)
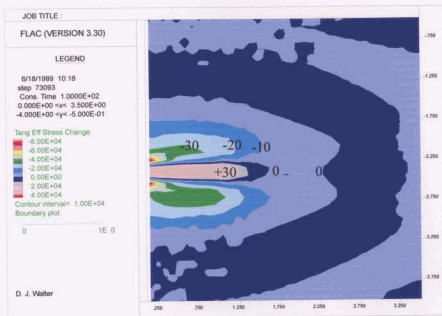
Figure A5.245. Change in tangential effective stress at t = 100 s (FLDTST2)
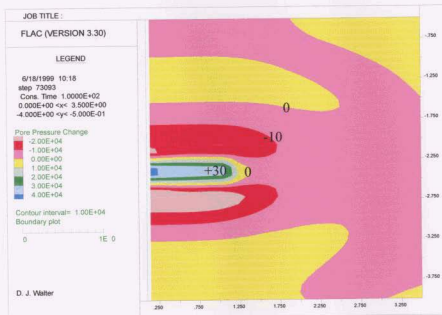
Figure A5.246. Change in pore pressure at t = 100 s (FLDTST2)
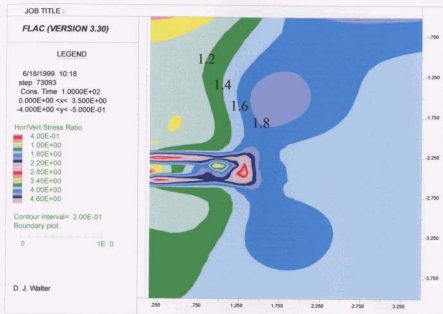
Figure A5.247. Stress ratio σ'$_x$/σ'$_y$ at t = 100 s (FLDTST2)
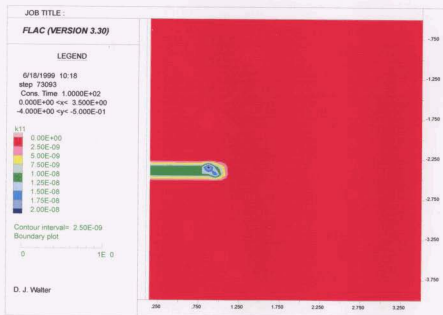
Figure A5.248. FLAC permeability at t = 100 s (FLDTST2)
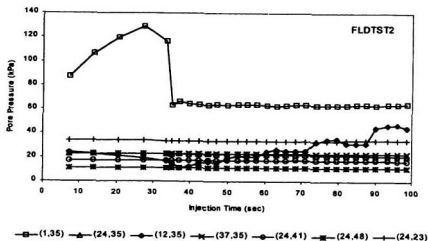
Figure A5.249. Pore pressure development during injection (FLDTST2)
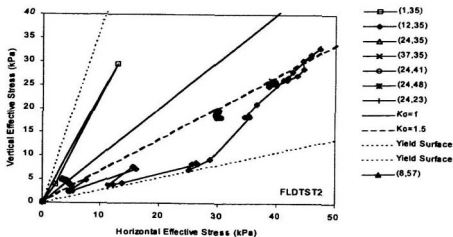
Figure A5.250. Stress paths during injection (FLDTST2)

619
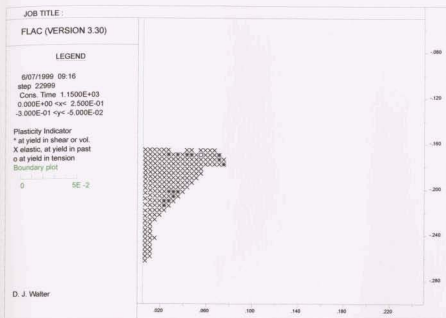
Figure A5.251. Extent of yield zone at end of injection (CCFS01A)
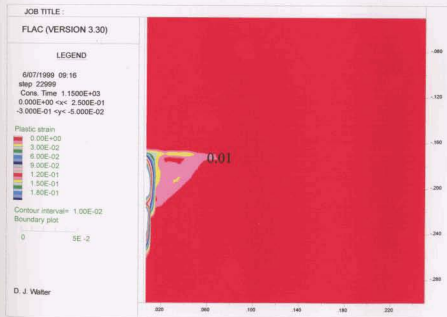
Figure A5.252. Plastic strain contours at end of injection (CCFS01A)
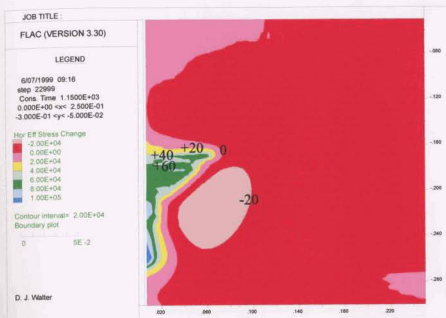
Figure A5.253. Change in horizontal effective stress (CCFS01A)
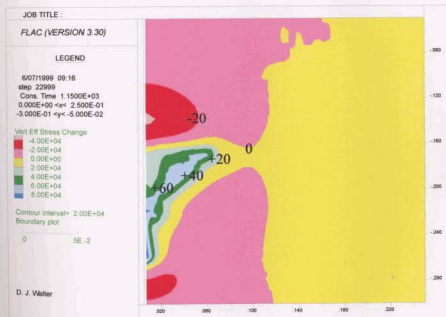
Figure A5.254. Change in vertical effective stress (CCFS01A)
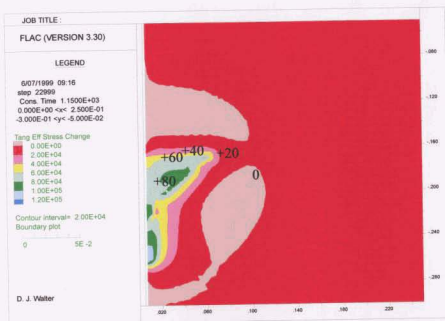
Figure A5.255. Change in tangential effective stress (CCFS01A)
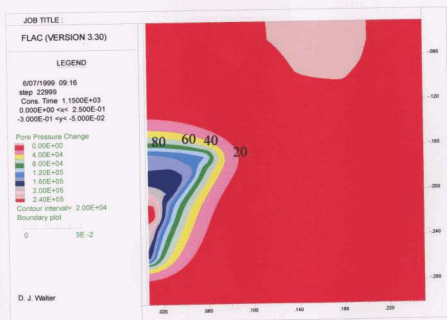
Figure A5.256. Change in pore pressure (CCFS01A)
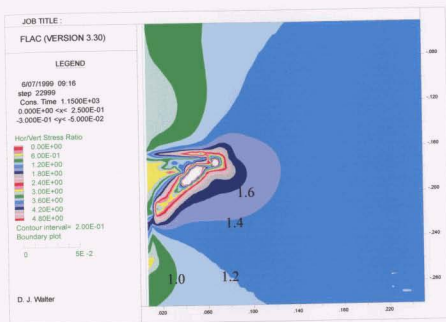
**Figure A5.257.** Stress ratio σ'ₕ/σ'ᵥ (CCFS01A)
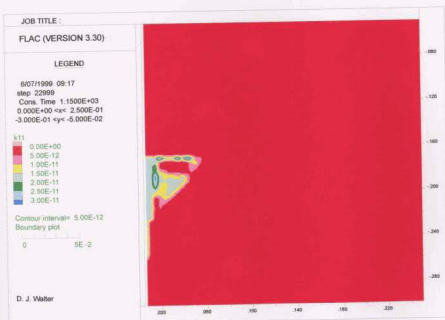
Figure A5.258. FLAC permeability (CCFS01A)
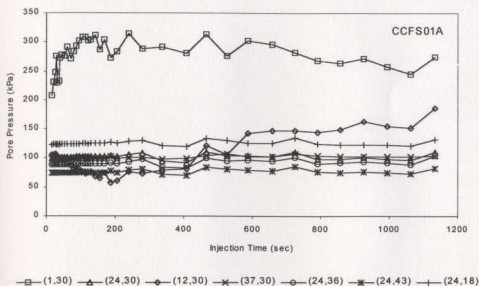
Figure A5.259. Pore pressure development during injection (CCFS01A)
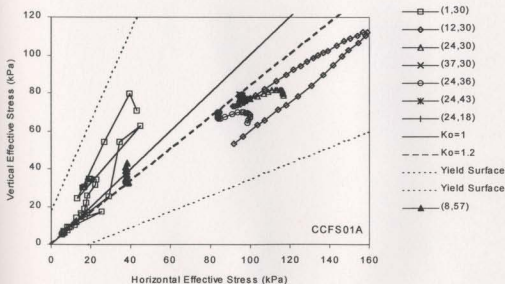
Figure A5.260. Stress paths during injection (CCFS01A)
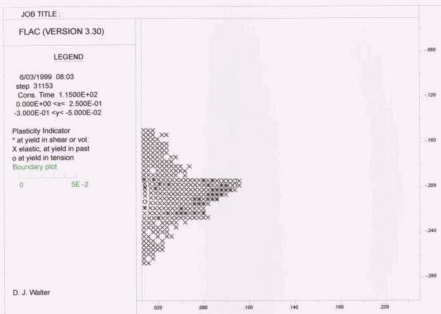
Figure A5.261. Extent of yield zone at end of injection (CCFS01B)
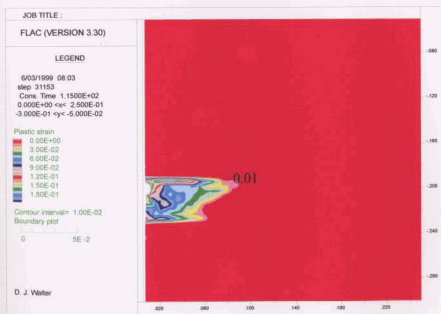
Figure A5.262. Plastic strain contours at end of injection (CCFS01B)
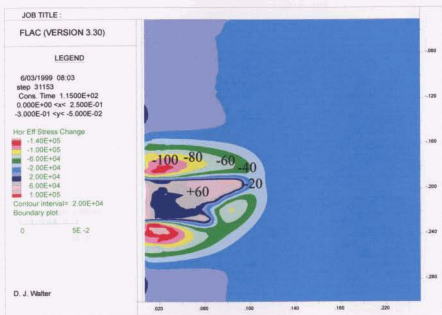
Figure A5.263. Change in horizontal effective stress (CCFS01B)
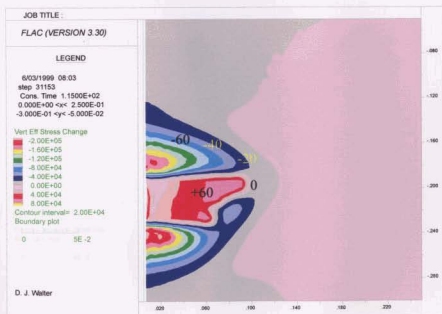
Figure A5.264. Change in vertical effective stress (CCFS01B)
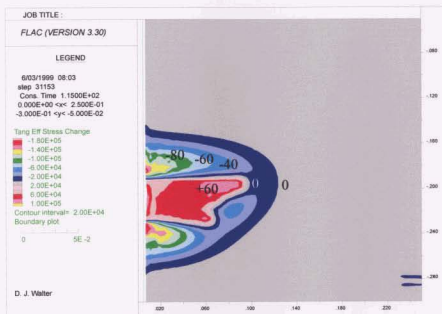
Figure A5.265. Change in tangential effective stress (CCFS01B)
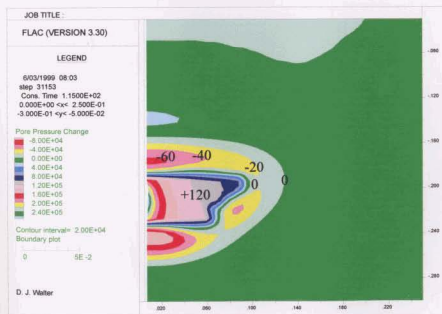
Figure A5.266. Change in pore pressure (CCFS01B)
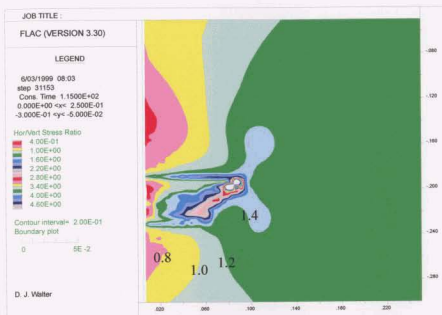
Figure A5.267. Stress ratio σ'_x/σ'_y (CCFS01B)
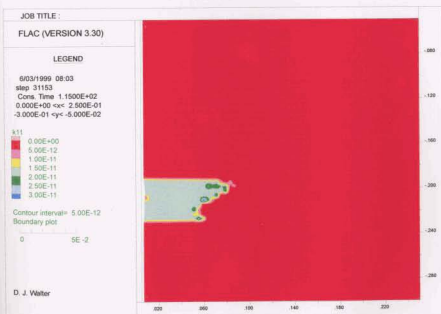
Figure A5.268. FLAC permeability (CCFS01B)
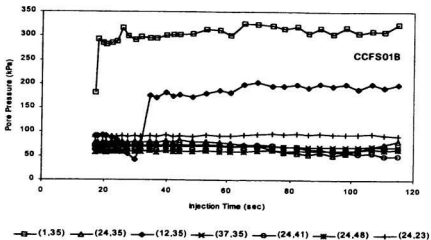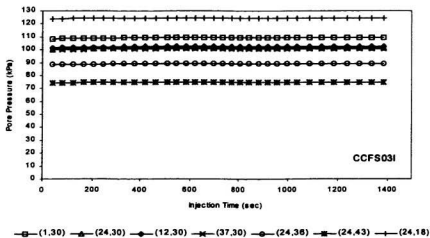
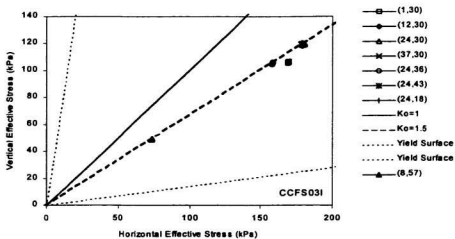**Figure A5.269.** Pore pressure development during injection (CCFS01B)
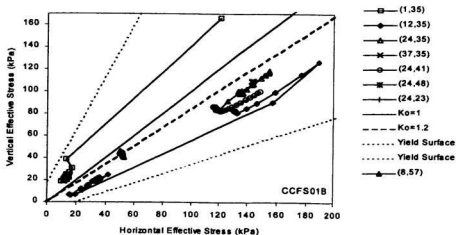
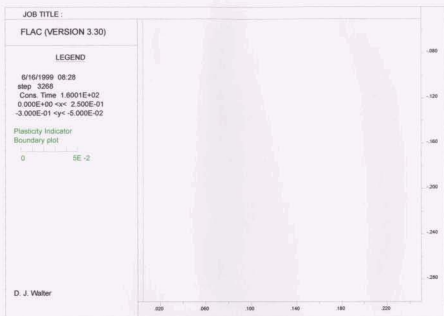**Figure A5.270.** Stress paths during injection (CCFS01B)
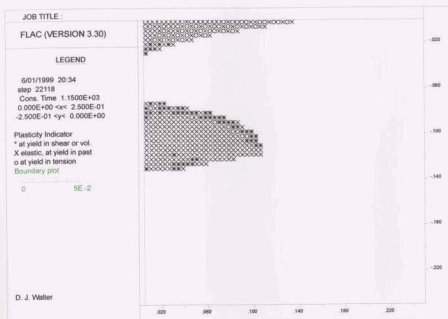
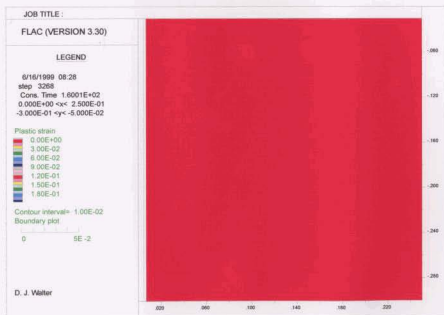**Figure A5.271.** Extent of yield zone at end of injection (CCFS01C)

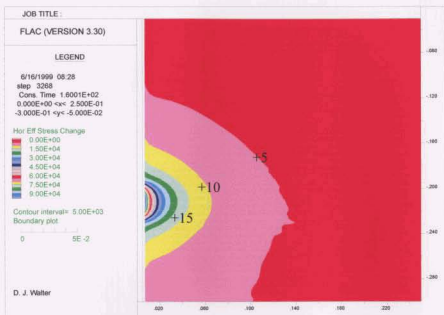**Figure A5.272.** Plastic strain contours at end of injection (CCFS01C)
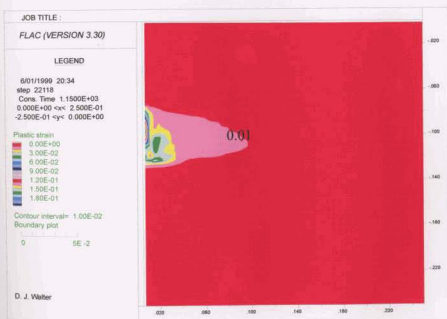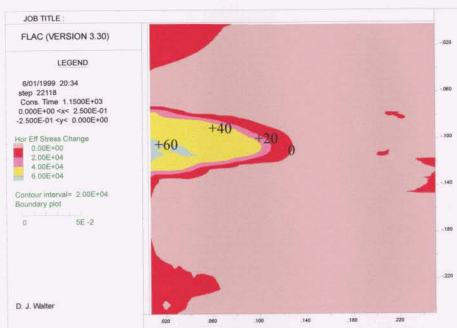
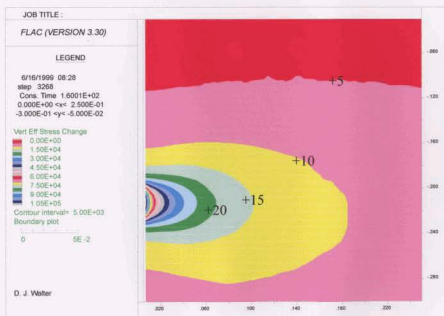**Figure A5.273.** Change in horizontal effective stress (CCFS01C)
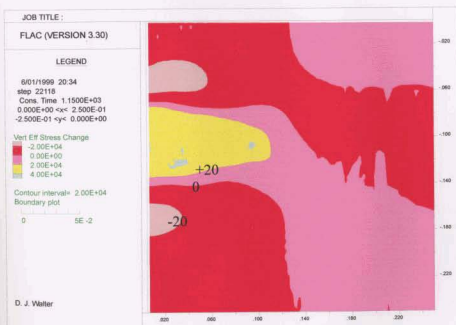
Figure A5.274. Change in vertical effective stress (CCFS01C)
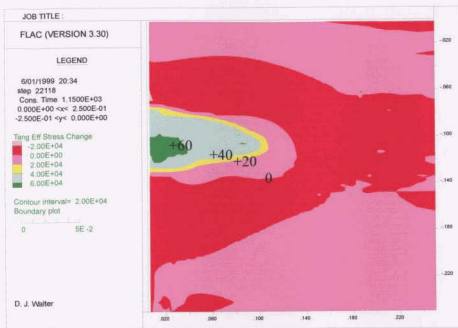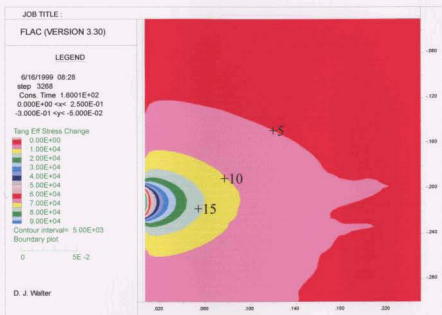
Figure A5.275. Change in tangential effective stress (CCFS01C)
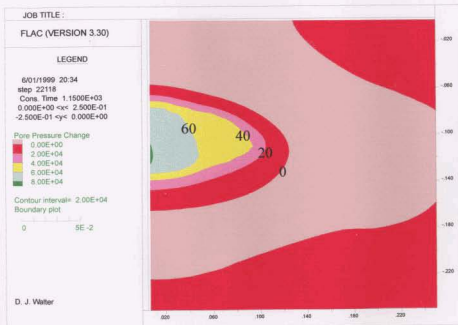
Figure A5.276. Change in pore pressure (CCFS01C)
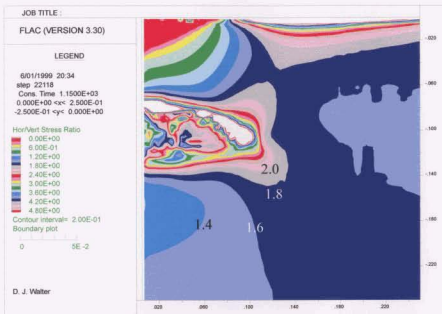
Figure A5.277. Stress ratio σ'_x/σ'_y (CCFS01C)
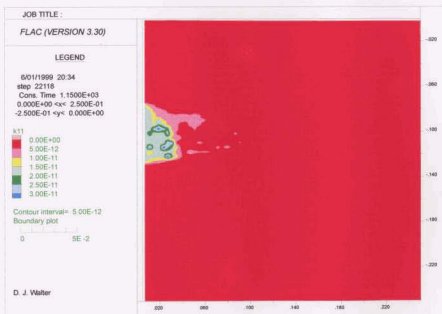
Figure A5.278. FLAC permeability (CCFS01C)
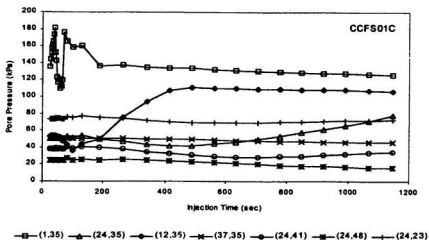
Figure A5.279. Pore pressure development during injection (CCFS01C)
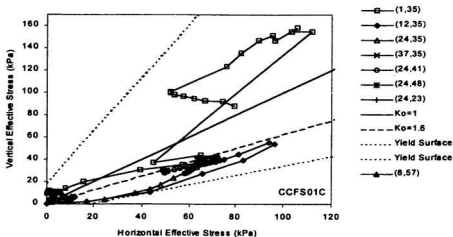
Figure A5.280. Stress paths during injection (CCFS01C)

635

JOB TITLE:

FLAC (VERSION 3.30)

LEGEND

6/01/1999 09:14
step 38223
Core Time 1.1500E+02
0.000E+00 <x< 2.500E-01
-2.500E-01 <y< 0.000E+00

Plastic strain
0.000E+00 <x< 2.500E-01
-2.500E-01 <y< 0.000E+00
Contour interval: 1.00E-02
0   5E -2

Contour interval: 1.00E-02
3.00E+00
3.00E-02
6.00E-02
6.00E-02
9.00E-02
1.20E-01
1.50E-01
1.80E-01

Boundary plot
0   5E -2

0.0

D. J. Walker

JOB TITLE:

FLAC (VERSION 3.30)

LEGEND

6/01/1999 09:14
step 38223
Core Time 1.1500E+02
0.000E+00 <x< 2.500E-01
-2.500E-01 <y< 0.000E+00

Plasticity indicator
X elastic, at yield in past
* at yield in shear or vol.
o at yield in tension

Boundary plot
0   5E -2

D. J. Walker
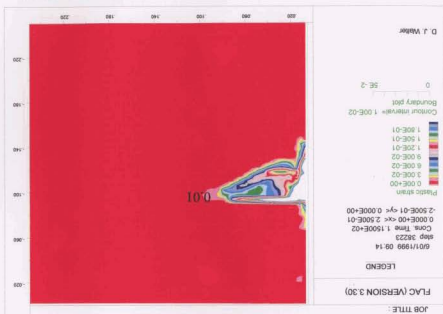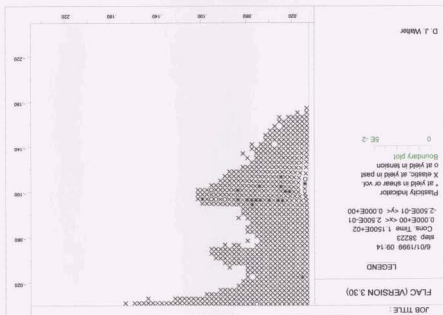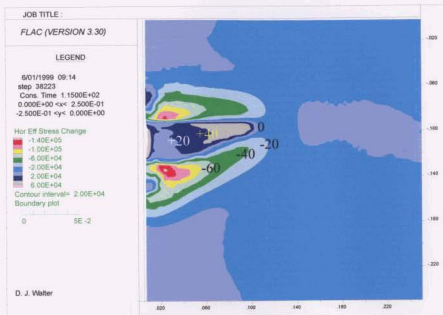
Figure A5.283. Change in horizontal effective stress (CCFS01D)
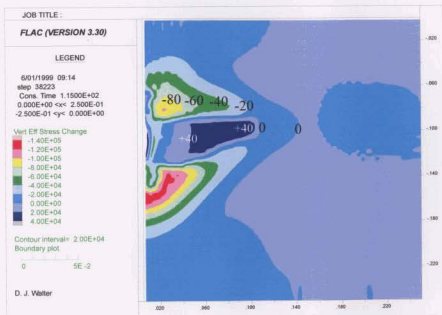
Figure A5.284. Change in vertical effective stress (CCFS01D)

**Figure A5.285.** Change in tangential effective stress (CCFS01D)
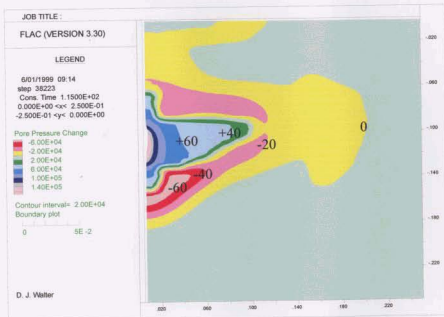

Figure A5.286. Change in pore pressure (CCFS01D)
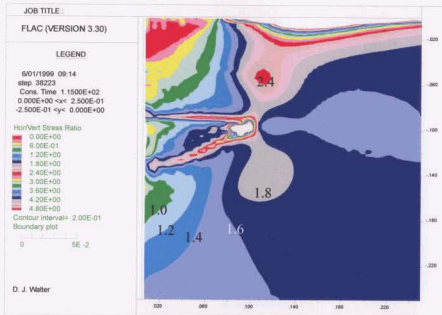
Figure A5.287. Stress ratio σ'_x/σ'_y (CCFS01D)
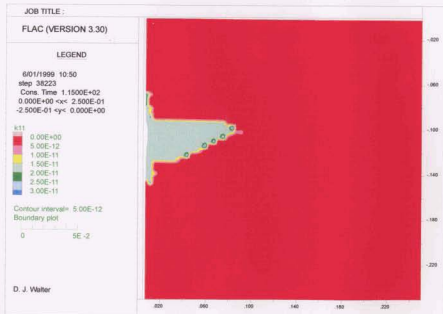
Figure A5.288. FLAC permeability (CCFS01D)
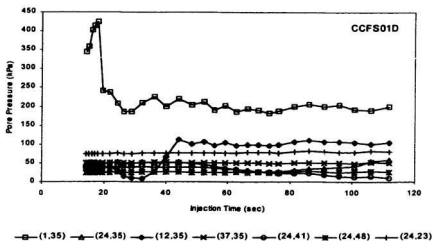
Figure A5.289. Pore pressure development during injection (CCFS01D)
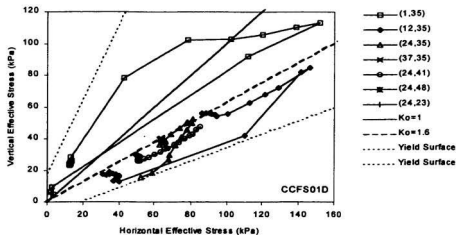
Figure A5.290. Stress paths during injection (CCFS01D)

Figure A5.291. Extent of yield zone at end of injection (CCFS02E)

Figure A5.292. Plastic strain contours at end of injection (CCFS02E)

Figure A5.293. Change in horizontal effective stress (CCFS02E)

Figure A5.294. Change in vertical effective stress (CCFS02E)

Figure A5.295. Change in tangential effective stress (CCFS02E)
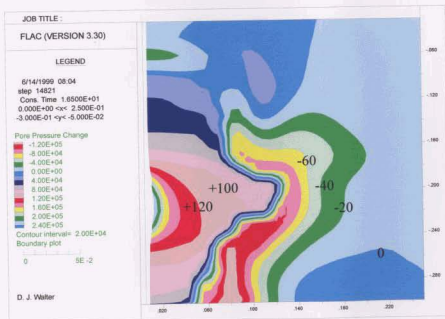
Figure A5.296. Change in pore pressure (CCFS02E)
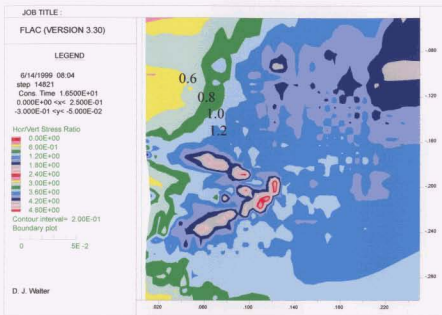
Figure A5.297. Stress ratio σ'_x/σ'_y (CCFS02E)
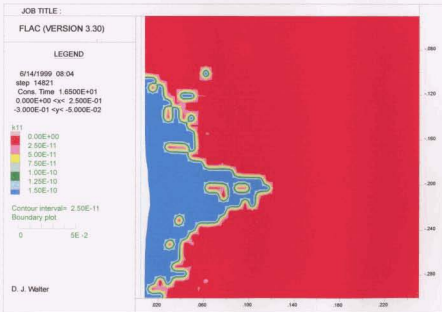
Figure A5.298. FLAC permeability (CCFS02E)
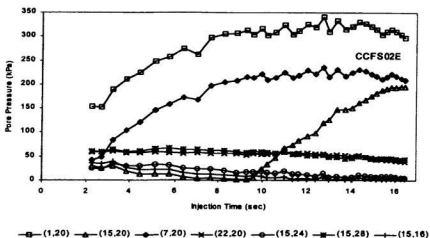
Figure A5.299. Pore pressure development during injection (CCFS02E)
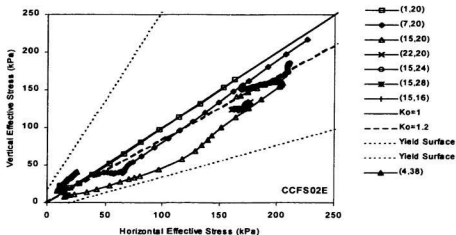
Figure A5.300. Stress paths during injection (CCFS02E)

645
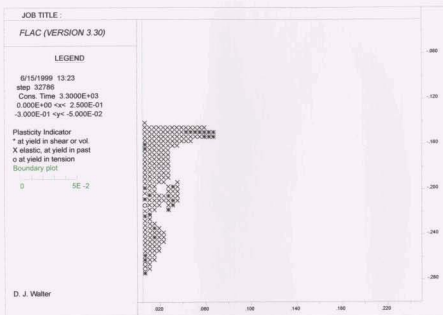
Figure A5.301. Extent of yield zone at end of injection (CCFS02F)
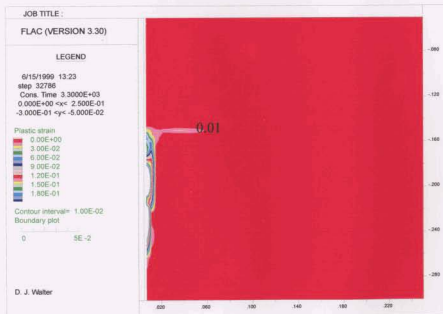
Figure A5.302. Plastic strain contours at end of injection (CCFS02F)
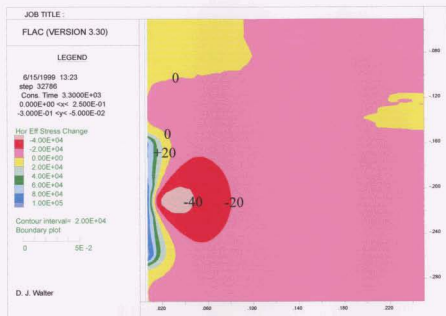
Figure A5.303. Change in horizontal effective stress (CCFS02F)

Figure A5.304. Change in vertical effective stress (CCFS02F)
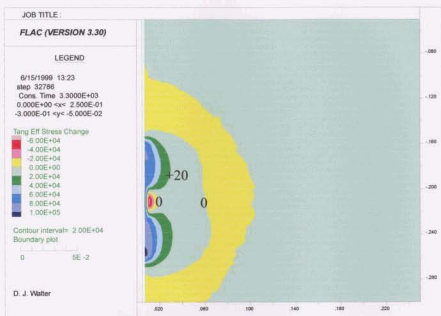
Figure A5.305. Change in tangential effective stress (CCFS02F)
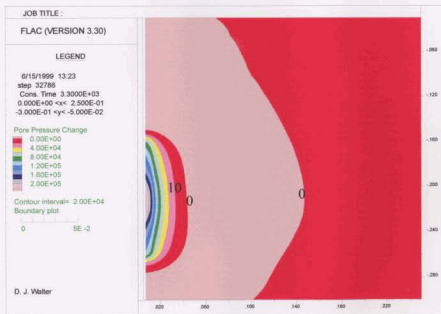
Figure A5.306. Change in pore pressure (CCFS02F)
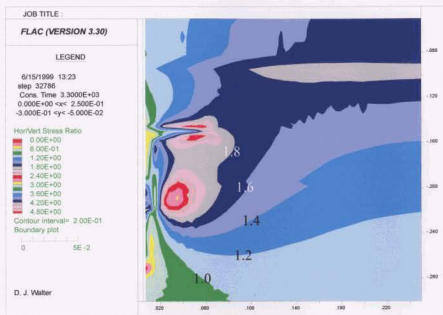
**Figure A5.307.** Stress ratio σ'_x/σ'_y (CCFS02F)
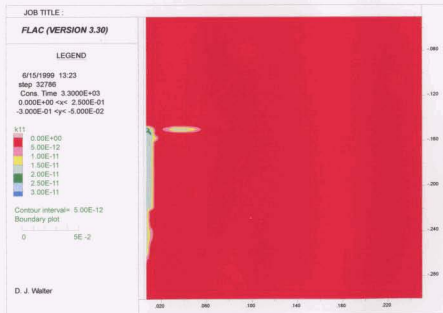
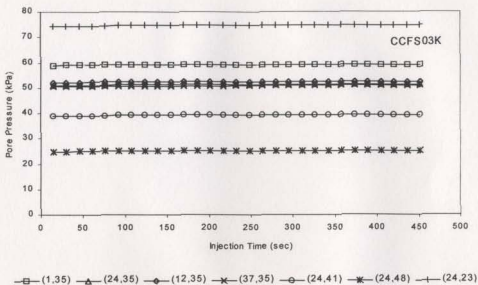**Figure A5.308.** FLAC permeability (CCFS02F)
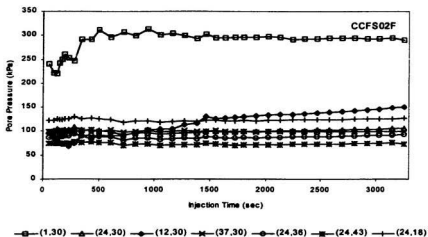
Figure A5.309. Pore pressure development during injection (CCFS02F)
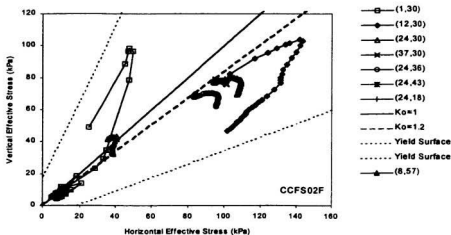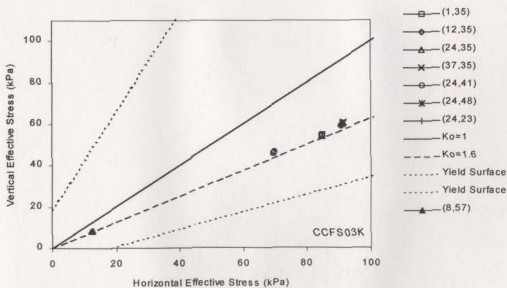

Figure A5.310. Stress paths during injection (CCFS02F)
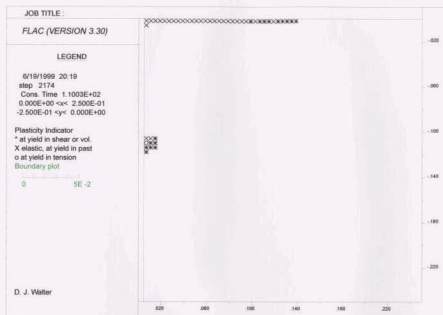
650
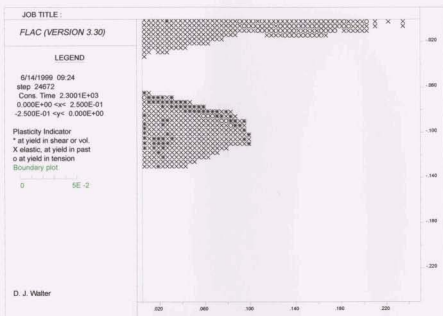
Figure A5.311. Extent of yield zone at end of injection (CCFS02G)
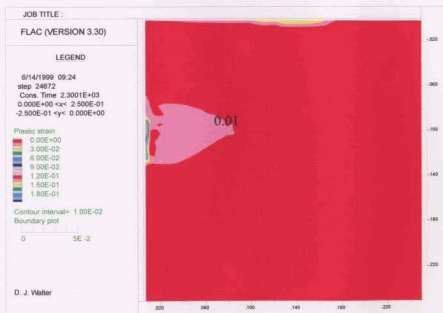
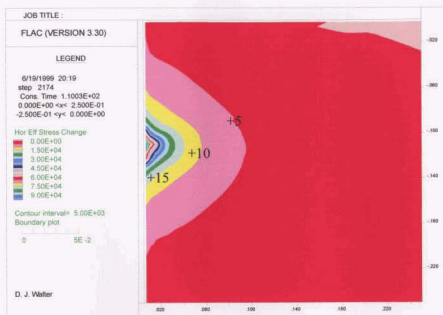**Figure A5.312.** Plastic strain contours at end of injection (CCFS02G)
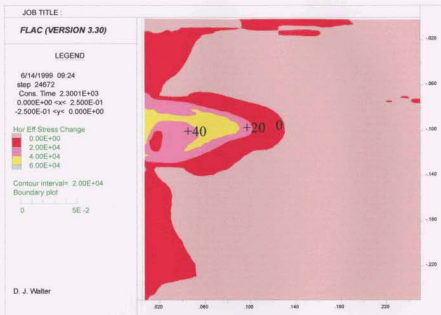
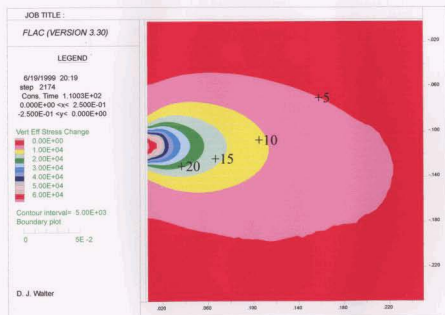**Figure A5.313.** Change in horizontal effective stress (CCFS02G)
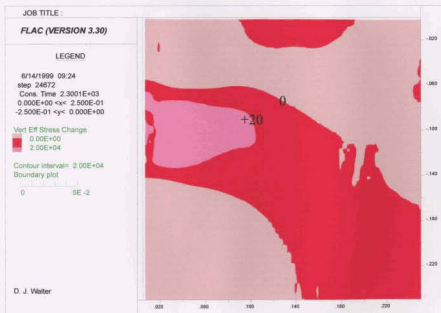
Figure A5.314. Change in verticaleffective stress (CCFS02G)
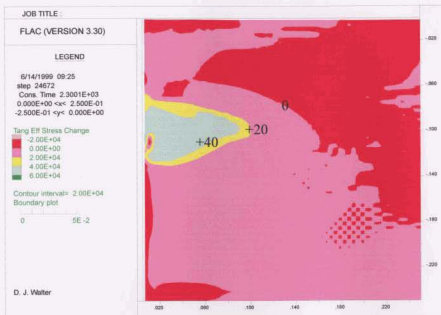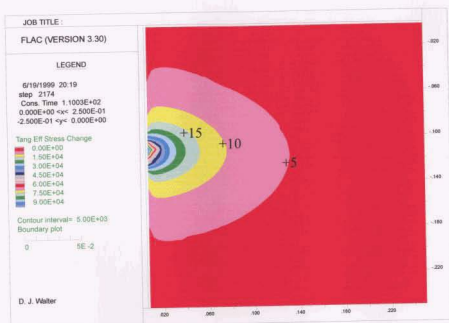
**Figure A5.315.** Change in tangential effective stress (CCFS02G)
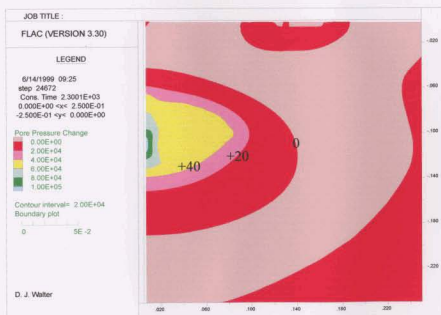
Figure A5.316. Change in pore pressure (CCFS02G)
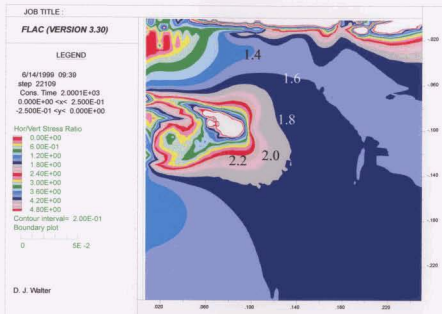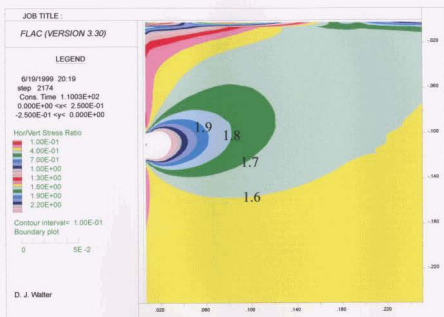
Figure A5.317. Stress ratio σ'$_x$/σ'$_y$ (CCFS02G)
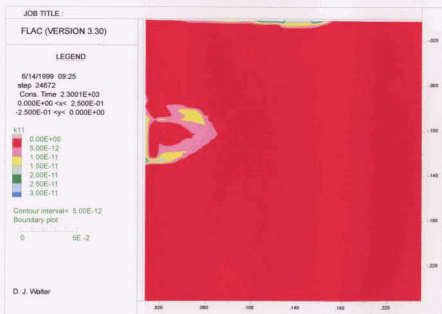
Figure A5.318. FLAC permeability (CCFS02G)
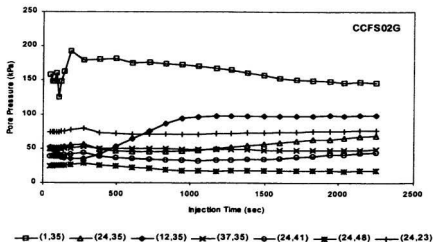
Figure A5.319. Pore pressure development during injection (CCFS02G)
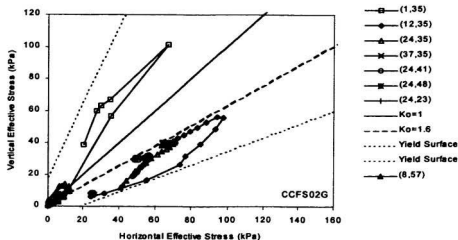
Figure A5.320. Stress paths during injection (CCFS02G)

655
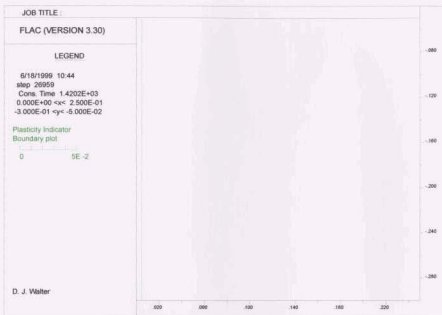
Figure A5.321. Extent of yield zone at t = 1420 s (CCFS03I)
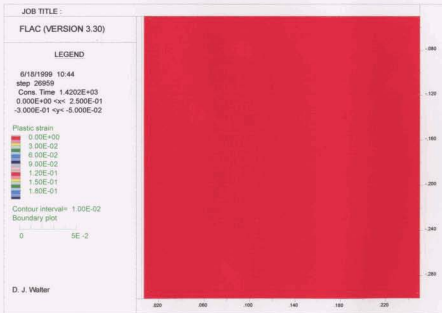
Figure A5.322. Plastic strain contours at t = 1420 s (CCFS03I)

Figure A5.323. Change in horizontal effective stress at t = 1420 s (CCFS03I)
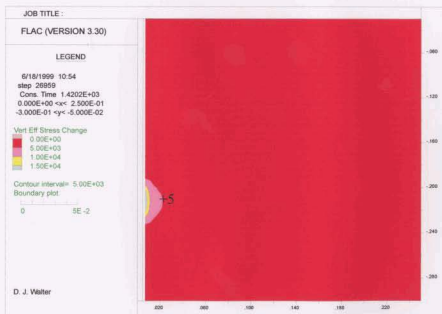
Figure A5.324. Change in vertical effective stress at t = 1420 s (CCFS03I)

Figure A5.325. Change in tangential effective stress at t = 1420 s (CCFS03I)
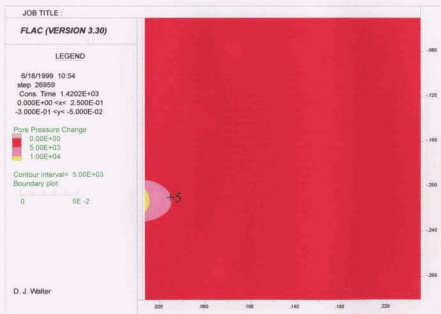
Figure A5.326. Change in pore pressure at t = 1420 s (CCFS03I)
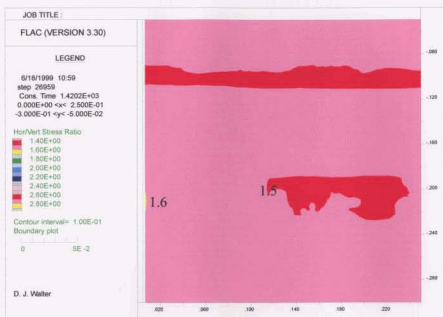
Figure A5.327. Stress ratio σ'_x/σ'_y at t = 1420 s (CCFS03I)
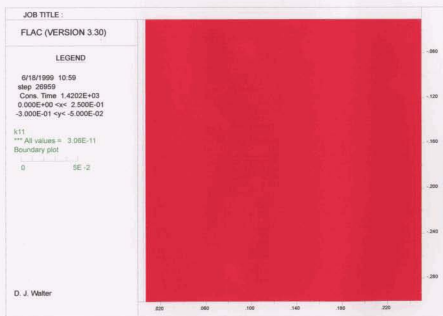
**Figure A5.328.** FLAC permeability at t = 1420 s (CCFS03I)

Figure A5.329. Pore pressure development during injection (CCFS03I)

Figure A5.330. Stress paths during injection (CCFS03I)

Figure A5.331. Extent of yield zone at end of injection (CCFS03J)

Figure A5.332. Plastic strain contours at end of injection (CCFS03J)

Figure A5.333. Change in horizontal effective stress (CCFS03J)

Figure A5.334. Change in vertical effective stress (CCFS03J)

Figure A5.335. Change in tangential effective stress (CCFS03J)
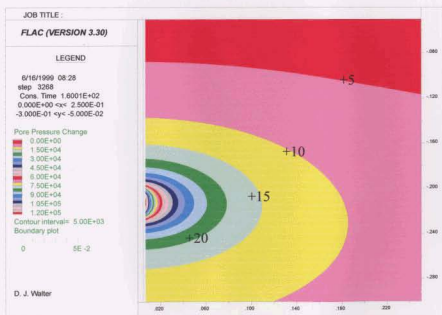
Figure A5.336. Change in pore pressure (CCFS03J)
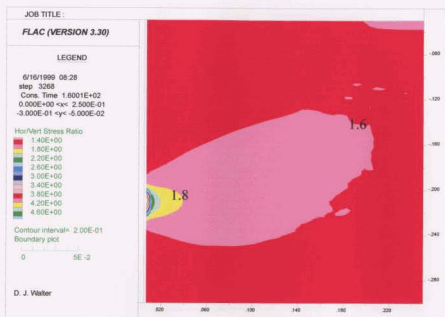
Figure A5.337. Stress ratio σ'_x/σ'_y (CCFS03J)
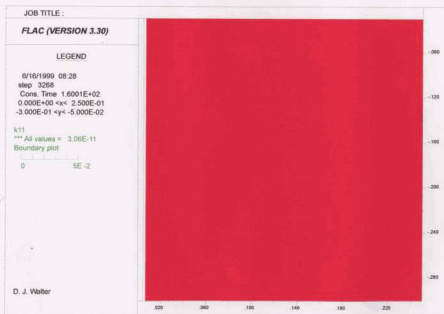
Figure A5.338. FLAC permeability (CCFS03J)
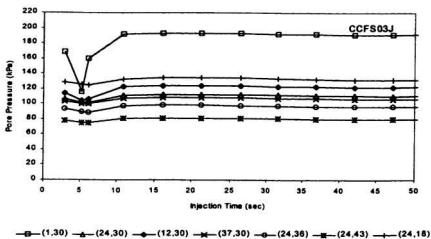
Figure A5.339. Pore pressure development during injection (CCFS03J)
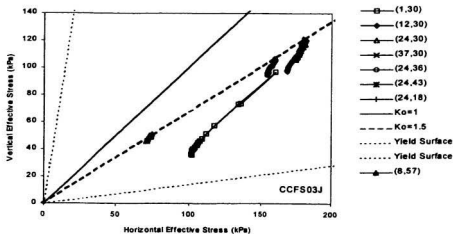

Figure A5.340. Stress paths during injection (CCFS03J)

665

**Figure A5.341.** Extent of yield zone at t = 457 s (CCFS03K)
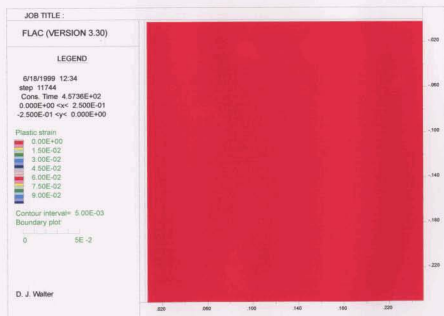
**Figure A5.342.** Plastic strain contours at t = 457 s (CCFS03K)
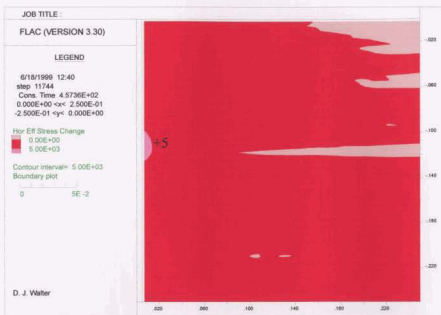
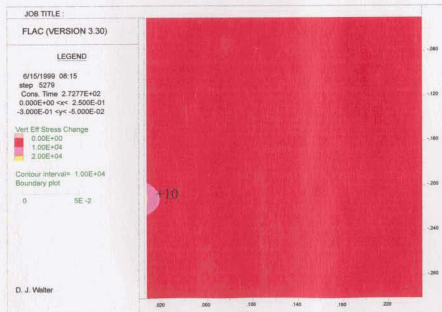**Figure A5.343.** Change in horizontal effective stress at t = 457 s (CCFS03K)
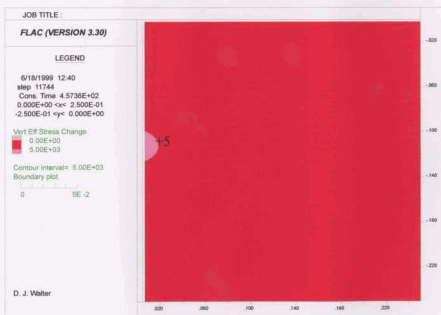
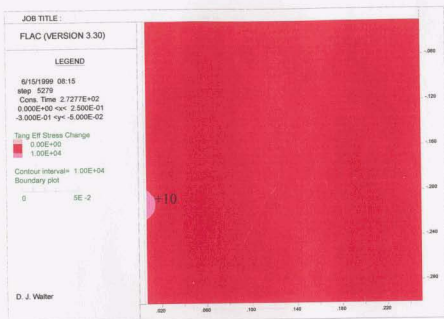**Figure A5.344.** Change in vertical effective stress at t = 457 s (CCFS03K)
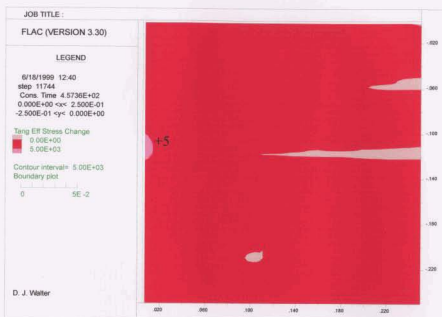
**Figure A5.345.** Change in tangential effective stress at t = 457 s (CCFS03K)
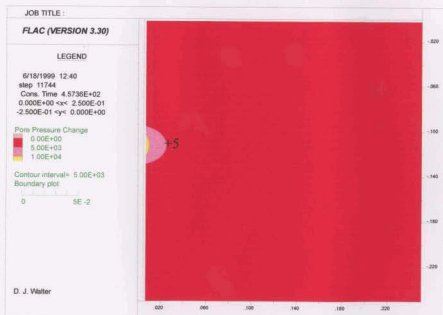
**Figure A5.346.** Change in pore pressure at t = 457 s (CCFS03K)
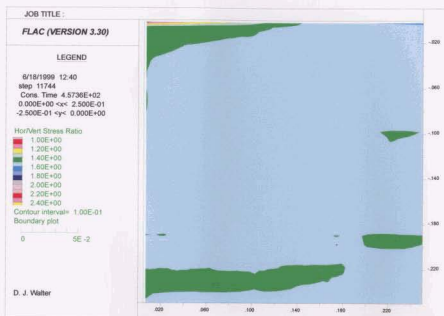
Figure A5.347. Stress ratio σ'_h/σ'_v at t = 457 s (CCFS03K)
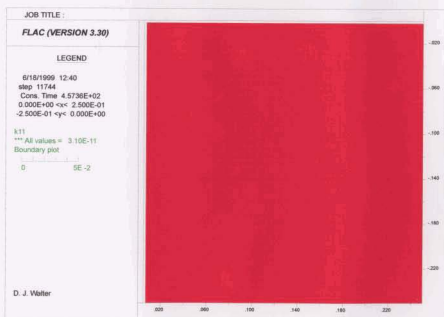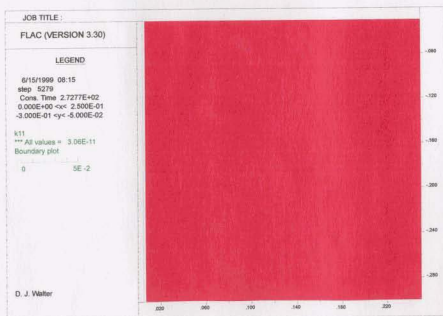

Figure A5.348. FLAC permeability at t = 457 s (CCFS03K)
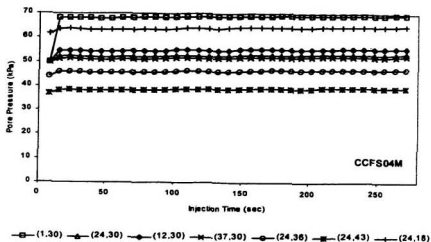
Figure A5.349. Pore pressure development during injection (CCFS03K)

Figure A5.350. Stress paths during injection (CCFS03K)

Figure A5.351. Extent of yield zone at end of injection (CCFS03L)

Figure A5.352. Plastic strain contours at end of injection (CCFS03L)

Figure A5.353. Change in horizontal effective stress (CCFS03L)

Figure A5.354. Change in vertical effective stress (CCFS03L)

Figure A5.355. Change in tangential effective stress (CCFS03L)
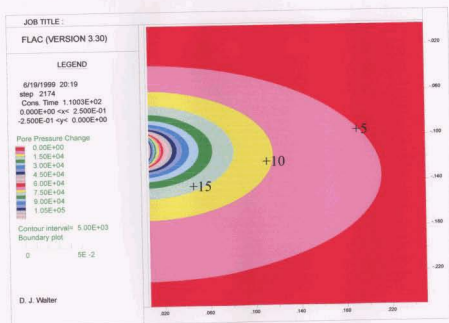
Figure A5.356. Change in pore pressure (CCFS03L)

Figure A5.357. Stress ratio σ'_x/σ'_y (CCFS03L)
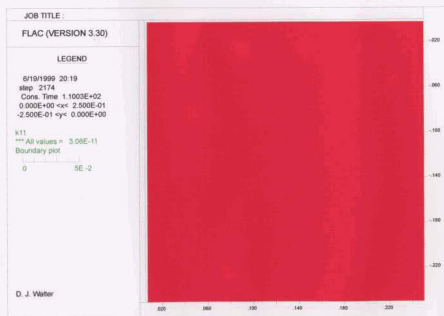
Figure A5.358. FLAC permeability (CCFS03L)
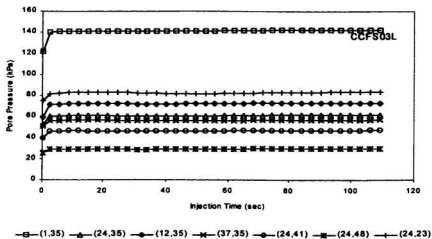
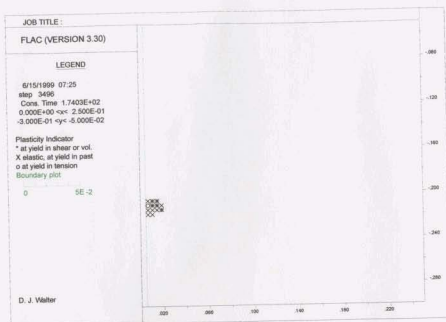**Figure A5.359.** Pore pressure development during injection (CCFS03L)
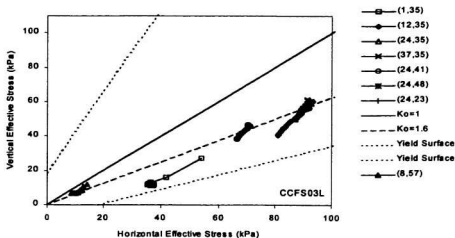
Figure A5.360. Stress paths during injection (CCFS03L)
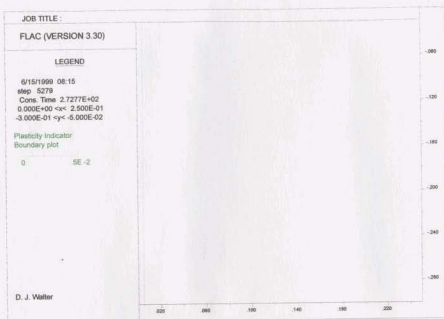
**Figure A5.361.** Extent of yield zone at t = 273 s (CCFS04M)
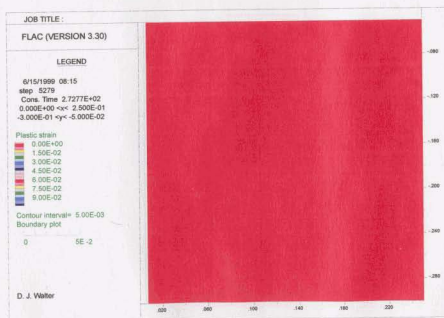
Figure A5.362. Plastic strain contours at t = 273 s (CCFS04M)
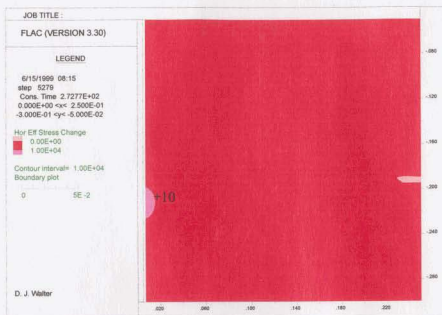
Figure A5.363. Change in horizontal effective stress at t = 273 s (CCFS04M)

Figure A5.364. Change in vertical effective stress at t = 273 s (CCFS04M)

Figure A5.365. Change in tangential effective stress at t = 273 s (CCFS04M)
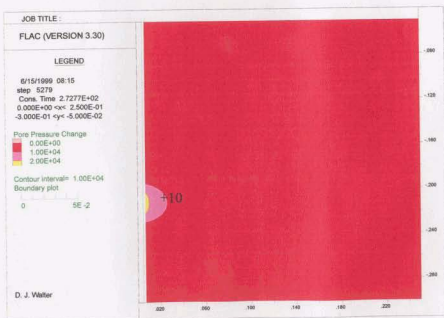
Figure A5.366. Change in pore pressure at t = 273 s (CCFS04M)
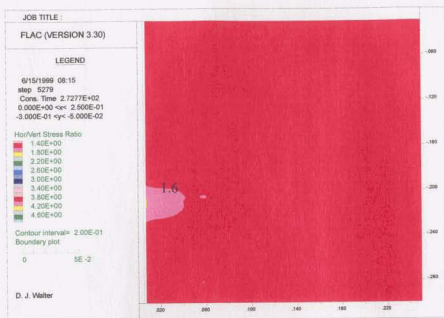
Figure A5.367. Stress ratio σ'$_x$/σ'$_y$ at t = 273 s (CCFS04M)

Figure A5.368. FLAC permeability at t = 273 s (CCFS04M)

Figure A5.369. Pore pressure development during injection (CCFS04M)
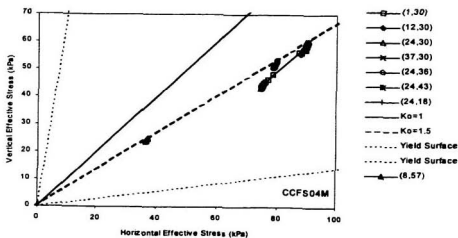
Figure A5.370. Stress paths during injection (CCFS04M)

Figure A5.371. Extent of yield zone at end of injection (CCFS04N)
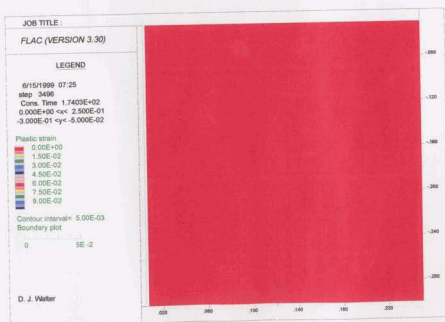
Figure A5.372. Plastic strain contours at end of injection (CCFS04N)
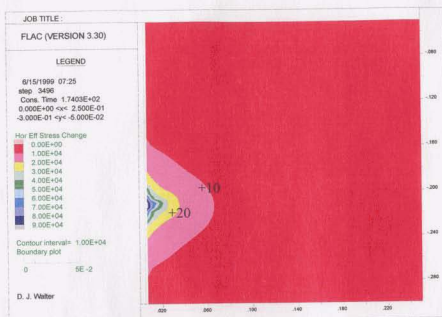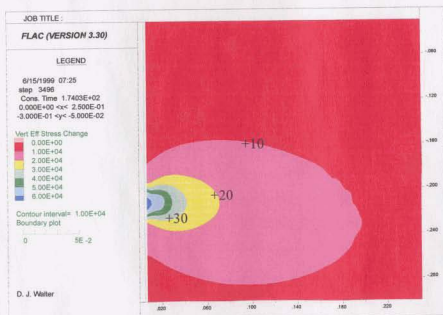
Figure A5.373. Change in horizontal effective stress (CCFS04N)

Figure A5.374. Change in vertical effective stress (CCFS04N)
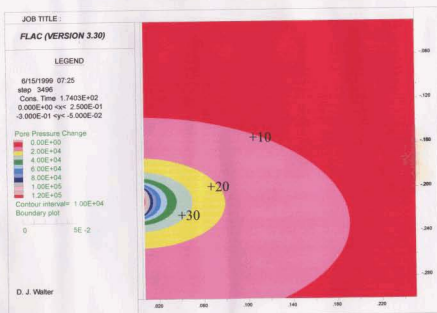
Figure A5.375. Change in tangential effective stress (CCFS04N)

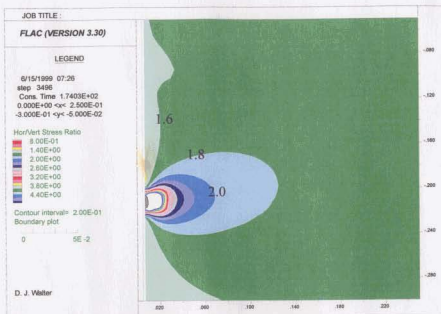

Figure A5.376. Change in pore pressure (CCFS04N)

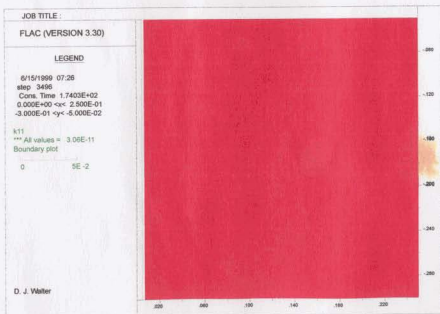**Figure A5.377.** Stress ratio σ'_x/σ'_y (CCFS04N)

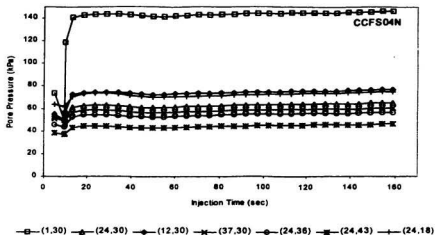**Figure A5.378.** FLAC permeability (CCFS04N)
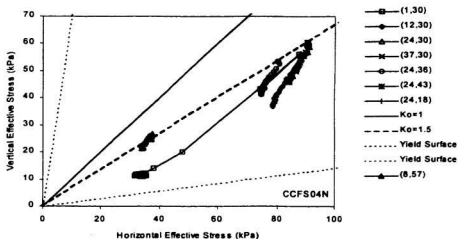
Figure A5.379. Pore pressure development during injection (CCFS04N)

Figure A5.380. Stress paths during injection (CCFS04N)

685